

Synthesis and Ion Exchange of
Germanate Materials

By

Ryan George

Supervisor: Dr J.A.Hriljac

A thesis submitted to the University of Birmingham for the degree of
DOCTOR OF PHILOSOPHY.

The School of Chemistry
College of Engineering and Physical Sciences
University of Birmingham
May 2019

UNIVERSITY OF
BIRMINGHAM

University of Birmingham Research Archive

e-theses repository

This unpublished thesis/dissertation is copyright of the author and/or third parties. The intellectual property rights of the author or third parties in respect of this work are as defined by The Copyright Designs and Patents Act 1988 or as modified by any successor legislation.

Any use made of information contained in this thesis/dissertation must be in accordance with that legislation and must be properly acknowledged. Further distribution or reproduction in any format is prohibited without the permission of the copyright holder.

Abstract

This work focuses on exploring new materials for potential effluent treatment with regards to caesium and strontium uptake. A germanate derivative of the natural mineral umbite has been investigated for potential ion exchange properties, this work explores the viability of this material as an exchanger and attempts to modify its exchange properties.

Subsequent ion exchange results shows both caesium and strontium uptake by zirconogermanate umbite ($K_2ZrGe_3O_9 \cdot H_2O$) but at low levels. This is substantially improved by chemical modification of the umbite structure with the replacement of Zr by 25% Nb/Sb at the octahedral site. High resolution synchrotron X-ray powder diffraction data shows complex structural behaviour of these doped materials when they undergo caesium exchange.

Further attempts at doping higher levels for Zr results in mixed phases with in formation of pharmacosiderite phases ($HK_3Ge_7O_{16} \cdot 4H_2O$ and $HK_3Ti_4Ge_3O_{16} \cdot 4H_2O$), with these also showing interesting ion exchange properties. The thermal decomposition products of the pharmacosiderite phases have also been analysed for potential wasteform candidates.

Acknowledgements

Firstly, I would like to thank Joe for all the help and guidance over the course of my PhD and tolerating my inability to correctly use GSAS. I would also like to thank the School of Chemistry and the ESPRC for funding this project. The experience gained from being part of the DISTINCTIVE consortium have been invaluable and the nights out are also worth a mention.

A special thanks to Hriljac group members past and present for all the discussions, help and insightful knowledge over the course of my PhD. A special thanks goes to Evin, who has been very helpful over the course of the last four or so years. The group outings, Christmas parties and general drinking sessions have always been a good laugh. Many thanks to Dr Jackie Deans whose technical support has been a great help to me and everyone on floor five.

I would also like to thank the 5th floor members past and present for all their help and the laughs we have had along the way, but mostly tolerating me for that long. The floor atmosphere has always made it an enjoyable and welcoming place to work and long may it continue.

TABLE OF CONTENTS

CHAPTER 1- INTRODUCTION	1
1.1 BACKGROUND.....	2
1.1.1 Waste types and disposal.....	2
1.2 IMMOBILISATION OPTIONS.....	4
1.2.1 Glass wasteforms.....	4
1.2.2 Ceramic Wasteforms	5
1.2.3 Cementation.....	7
1.3 MATERIALS FOR CAESIUM-137 AND STRONTIUM-90 UPTAKE	8
1.3.1 Zeolites, Clinoptilolite and SIXEP	10
1.3.2 Ammonium molybdophosphate	12
1.3.3 Prussian blue and Cs treat.....	13
1.3.4 Crystalline silicotitanate	14
1.3.4 Clays	16
1.4 NEW MATERIALS FOR ION EXCHANGE APPLICATIONS.....	17
1.4.1 Octahedral-tetrahedral silicates	18
1.5 GERMANATES - SCOPE OF THE WORK	24
CHAPTER 2- EXPERIMENTAL.....	25
2.1 HYDROTHERMAL SYNTHESIS	26
2.2 X-RAY DIFFRACTION	27
2.2.1 Fundamentals of crystallography.....	27
2.2.2 Diffraction fundamentals.....	29

2.2.3 X-ray generation	31
2.2.4 Filters, monochromators and detectors.....	33
2.2.5 Diffractometer geometry	33
2.2.6 Synchrotron X-ray diffraction	35
2.2.7 Powder Diffraction	36
2.3 RIETVELD REFINEMENT.....	39
2.4 X-RAY FLUORESCENCE SPECTROSCOPY (XRF).....	42
2.4.1 XRF geometry	43
2.4.2 XRF sample preparation.....	45
2.4.3 Fused bead preparation.....	45
2.5 TGA/DTA	46
CHAPTER 3- SYNTHESIS AND ION EXCHANGE OF $K_2ZrGe_3O_9 \cdot H_2O$	48
3.1 INTRODUCTION.....	49
3.2 EXPERIMENTAL.....	54
3.2.1 Synthesis of $K_2ZrSi_{3-x}Ge_xO_9 \cdot H_2O$	54
3.2.2 Synthesis of $K_2ZrGe_3O_9 \cdot H_2O$	54
3.2.3 Ion exchange studies.....	56
3.2.4 Proton exchange	56
3.2.5 NaCl reflux	56
3.3 RESULTS AND DISCUSSION.....	57
3.3.1 Mixed Silicon/Germanium umbite systems	57
3.3.2 Synthesis and optimisation of $K_2ZrGe_3O_9 \cdot H_2O$	62
3.3.3 Ion exchange.....	68

3.3.4 Reitveld refinements of Cs exchanged parent umbite	71
3.3.5 Sodium exchange of zirconogermanate umbite.....	75
3.3.6 Proton form of zirconogermanate umbite.....	82
3.3.7 Synthesis of Ti and Sn germanoumbites	86
3.3.8 Synthesis of ammonium zirconogermanate umbite, $(\text{NH}_4)_2\text{ZrGe}_3\text{O}_9 \cdot \text{H}_2\text{O}$	88
3.3.9 Synthesis of caesium form of zirconogermanate umbite, $\text{Cs}_2\text{ZrGe}_3\text{O}_9 \cdot \text{H}_2\text{O}$	92
3.3.10 Zirconogermanate umbite thermal conversion	94
3.4 CONCLUSIONS	97
CHAPTER 4- FRAMEWORK DOPING AND ION EXCHANGE OF $\text{K}_2\text{ZrGe}_3\text{O}_9 \cdot \text{H}_2\text{O}$	98
4.1 INTRODUCTION.....	99
4.2 EXPERIMENTAL.....	103
4.2.1 Synthesis of $\text{K}_{2-x}\text{Zr}_{1-x}\text{Nb}_x\text{Ge}_3\text{O}_9 \cdot \text{H}_2\text{O}$	103
4.2.2 Synthesis of $\text{K}_{2-x}\text{Zr}_{1-x}\text{Sb}_x\text{Ge}_3\text{O}_9 \cdot \text{H}_2\text{O}$	103
4.2.3 Ion exchange studies.....	104
4.3 RESULTS AND DISCUSSION.....	105
4.3.1 Synthesis of niobium doped umbite	105
4.3.2 Ion exchange of Niobium doped umbite	109
4.3.3 Examining XRF variability	111
4.3.4 Rietveld refinement of Nb doped umbites.....	113
4.3.5 Cs exchange of niobium doped zirconogermanate umbites	121
4.3.6 Antimony doping of zirconogermanate umbite, $\text{K}_{2-x}\text{Zr}_{1-x}\text{Sb}_x\text{Ge}_3\text{O}_9 \cdot \text{H}_2\text{O}$	136
4.3.7 Ion exchange of antimony doped umbite	145
4.3.8 Critical assessment of the observed ion exchange data.....	156

4.3.9 Thermal conversion of doped umbites	157
4.4 CONCLUSIONS	165
CHAPTER 5- ION EXCHANGE AND THERMAL CONVERSION OF PHARMACOSIDERITES.....	166
5.1 INTRODUCTION.....	167
5.2 EXPERIMENTAL.....	173
5.2.1 $K_3HGe_7O_{16} \cdot 4H_2O$ synthesis.....	173
5.2.2 $K_3HTi_4Ge_3O_{16} \cdot 4H_2O$ synthesis	173
5.2.3 $K_3HTi_4Si_3O_{16} \cdot 4H_2O$ synthesis	173
5.2.4 Ion exchange studies.....	174
5.3 RESULTS AND DISCUSSION.....	175
5.3.1 Synthesis and optimisation of Pharmacosiderites	175
5.3.2 $K_3HGe_7O_{16} \cdot 4H_2O$ ion exchange	187
5.3.3 $K_3HTi_4Ge_3O_{16} \cdot 4H_2O$ ion exchange	193
5.3.4 Titanosilicate pharmacosiderite thermal conversion	198
5.3.5 Thermal conversion of germanogermanium pharmacosiderites	204
5.3.6 Thermal conversion of titanogermanate pharmacosiderites	207
5.4 CONCLUSIONS	216
CHAPTER 6-CONCLUSIONS AND FURTHER WORK.....	217
6.1 CONCLUSIONS	218
6.1.1 Germanoumbites.....	218
6.1.2 Doped Germanoumbites	220
6.1.3 Pharmacosiderites.....	221

6.2 FURTHER WORK	223
6.2.1 Chapter 3	223
6.2.2 Chapter 4	224
6.2.3 Chapter 5	225
REFERENCES	226
APPENDICES	232

List of Figures

Figure 1.1: Structure of Clinoptilolite.	11
Figure 1.2: Structure of prussian blue	14
Figure 1.3: Structure of Na-CST	15
Figure 1.4: Structure of AV-7	19
Figure 1.5: The structure of AV-3	20
Figure 1.6: Structure of AV-13	21
Figure 1.7: Structure of AV-9	22
Figure 2.1: 7 crystal systems.	28
Figure 2.2: Graphical representation of diffraction between two planes.	30
Figure 2.3: Graphical representation of an X-ray tube.....	31
Figure 2.4: Graphical representation of diffractometer geometries	34
Figure 2.5: Graphical representation of powder diffraction and the origin of the Debye-Scherrer cones.....	36
Figure 2.6: Flow chart showing the available information that can be gathered from an XRD powder diffraction pattern [70].	38
Figure 2.7: Graphical representation of the fundamental principles behind X-ray Fluorescence Spectroscopy (XRF).	42
Figure 3.1: Crystal structure of the zirconosilicate umbite	50
Figure 3.2: Cs-exchanged umbite.....	51
Figure 3.3: Wadeite structure	52
Figure 3.4: X-ray diffraction pattern for the attempted replacement of Si by 25% Ge.....	58
Figure 3.5: X-ray diffraction pattern for the attempted replacement of Si by 50% Ge.....	59

Figure 3.6: X-ray diffraction pattern for the attempted replacement of Si by 75% Ge.....	60
Figure 3.7: X-ray diffraction pattern of the $K_2ZrGe_2O_7$ phase	61
Figure 3.8: Comparison between the diffraction patterns for the seven day and one day optimised synthesis of $K_2ZrGe_3O_9.H_2O$	63
Figure 3.9: Rietveld refinement for the parent $K_2ZrGe_3O_9.H_2O$ phase.....	64
Figure 3.10: Expanded view showing the peak splitting evident in the refinement of $K_2ZrGe_3O_9.H_2O$	67
Figure 3.11: Rietveld refinement for the Cs-exchanged zirconogermanate umbite phase.....	72
Figure 3.12: Rietveld refinement for the Cs-exchanged zirconogermanate umbite phase.....	73
Figure 3.13: X-ray diffraction patterns for the NaCl refluxed material and parent material, ..	77
Figure 3.14: X-ray diffraction patterns for the NaCl refluxed material and proton form of $K_2ZrGe_3O_9.H_2O$	79
Figure 3.15: X-ray diffraction patterns for the parent phase, NaCl refluxed material and the regenerated KCl refluxed material.	80
Figure 3.16: TGA analysis for the Parent and NaCl refluxed materials.	81
Figure 3.17: X-ray diffraction patterns for the parent material and the attempted synthesis of the proton exchanged form.	82
Figure 3.18: X-ray diffraction pattern for the attempted synthesis of $K_2TiGe_3O_9.H_2O$	86
Figure 3.19: X-ray diffraction pattern for the attempted synthesis of $K_2SnGe_3O_9.H_2O$	87
Figure 3.20: X-ray diffraction patterns for the attempted synthesis of ammonium umbite	89
Figure 3.21: Attempted Rietveld refinement of ammonium umbite using the $P2_12_12_1$ space group.....	90
Figure 3.22: X-ray diffraction pattern for the attempted synthesis of $Cs_2ZrGe_3O_9.H_2O$	92
Figure 3.23: Attempted Rietveld refinement of $Cs_2ZrGe_3O_9.H_2O$	93

Figure 3.24: VT XRD for the thermal conversion of umbite at 50 °C intervals.	95
Figure 3.25: X-ray diffraction data for the final phase assemblage of heated umbite.	96
Figure 4.1: Structure of Cs-exchanged Nb-CST	100
Figure 4.2: Local coordination environment for Sr ²⁺ in Nb-CST	101
Figure 4.3: X-ray diffraction patterns for the initial synthesis attempts of niobium doped zirconogermanate umbites with general formula K _{2-x} Zr _{1-x} Nb _x Ge ₃ O ₉ .H ₂ O.....	106
Figure 4.4: X-ray diffraction pattern for the attempted synthesis of x = 0.4 doped umbite. .	108
Figure 4.5: Rietveld refinement for K _{1.9} Zr _{0.9} Nb _{0.1} Ge ₃ O ₉ .H ₂ O.....	114
Figure 4.6: Rietveld refinement for K _{1.8} Zr _{0.8} Nb _{0.2} Ge ₃ O ₉ .H ₂ O	116
Figure 4.7: Rietveld refinement for K _{1.75} Zr _{0.75} Nb _{0.25} Ge ₃ O ₉ .H ₂ O.....	118
Figure 4.8: Example of peak splitting in the 0.1Nb doped umbite refinement	120
Figure 4.9: Peak splitting observed for the Cs-exchanged doped umbites.....	122
Figure 4.10: Attempted fitting of peak splitting using the exchanged Poojary model.....	124
Figure 4.11: Rietveld refinement of Cs-exchanged 0.1Nb umbite using the exchanged Poojary model.	125
Figure 4.12: 2 Phase refinement of Cs-exchanged 0.1Nb umbite.....	126
Figure 4.13: Expanded view of figure 4.12 showing fitting to the peak splitting observed. .	127
Figure 4.14: 2 Phase refinement of Cs-exchanged 0.2Nb umbite.....	129
Figure 4.15: Expanded view of figure 4.14 showing fitting to the peak splitting observed. .	130
Figure 4.16: 2 Phase refinement of Cs-exchanged 0.25Nb umbite.....	132
Figure 4.17: Expanded view of figure 4.16 showing fitting to the peak splitting observed. .	133
Figure 4.18: Rietveld refinement for K _{1.9} Zr _{0.9} Sb _{0.1} Ge ₃ O ₉ .H ₂ O.....	137
Figure 4.19: Rietveld refinement for K _{1.8} Zr _{0.8} Sb _{0.2} Ge ₃ O ₉ .H ₂ O.....	140
Figure 4.20: Rietveld refinement for K _{1.75} Zr _{0.75} Sb _{0.25} Ge ₃ O ₉ .H ₂ O.....	143

Figure 4.21: Peak splitting observed for the Cs-exchanged Sb doped umbites,	148
Figure 4.22: Rietveld refinement for Cs-exchanged $K_{1.9}Zr_{0.9}Sb_{0.1}Ge_3O_9 \cdot H_2O$	149
Figure 4.23: Expanded view of figure 4.22 showing fitting to the peak splitting observed. .	149
Figure 4.24: Rietveld refinement for Cs-exchanged $K_{1.9}Zr_{0.8}Sb_{0.2}Ge_3O_9 \cdot H_2O$	151
Figure 4.25: Expanded view of figure 4.24 showing fitting to the peak splitting observed. .	151
Figure 4.26: Rietveld refinement for Cs-exchanged $K_{1.9}Zr_{0.75}Sb_{0.25}Ge_3O_9 \cdot H_2O$	153
Figure 4.27: Expanded view of figure 4.26 showing fitting to the peak splitting observed. .	154
Figure 4.28: VT XRD for the thermal conversion of Cs-exchanged 0.25Nb umbite at 50 °C intervals.	160
Figure 4.29: X-ray diffraction data for the final phase assemblage of heated Cs-exchanged 0.25Nb umbite.	161
Figure 4.30: VT XRD for the thermal conversion of Cs-exchanged 0.25Sb umbite at 50 °C intervals.	162
Figure 4.31: X-ray diffraction data for the final phase assemblage of heated Cs-exchanged 0.25Sb umbite.	163
Figure 4.32: TGA and DTA data for the 0.25Sb and Nb doped umbites.	164
Figure 5.1: Structure of $M_3HGe_7O_{16} \cdot xH_2O$	168
Figure 5.2: Cubic super cell for $K_3HGe_7O_{16} \cdot 4H_2O$,	169
Figure 5.3: X-ray diffraction patterns for $K_3HGe_7O_{16} \cdot 4H_2O$, 45 ml synthesis and 125 ml scale up.	175
Figure 5.4: Rietveld refinement for $K_3HGe_7O_{16} \cdot 4H_2O$	177
Figure 5.5: Rietveld refinement for $K_3HGe_7O_{16} \cdot 4H_2O$ reduced range.	178
Figure 5.6: Expanded view from the Rietveld refinement for $K_3HGe_7O_{16} \cdot 4H_2O$ showing peak asymmetry.	181

Figure 5.7: X-ray diffraction pattern for $K_3HTi_4Ge_3O_{16} \cdot 4H_2O$	182
Figure 5.8: X-ray diffraction patterns for $K_3HTi_4Ge_3O_{16} \cdot 4H_2O$ two day and ten day syntheses	183
Figure 5.9: Rietveld refinement for $K_3HTi_4Ge_3O_{16} \cdot 4H_2O$	184
Figure 5.10: An example of the peak shoulders observed in the experimental data for $K_3HTi_4Ge_3O_{16} \cdot 4H_2O$	184
Figure 5.11: X-ray diffraction patterns for $K_3HX_4Ge_3O_{16} \cdot 4H_2O$, where X= Sn and Zr.	187
Figure 5.12: Rietveld refinement for the Cs-exchanged $K_3HGe_7O_{16} \cdot 4H_2O$	190
Figure 5.13: Rietveld refinement for Cs-exchanged $K_3HTi_4Ge_3O_{16} \cdot 4H_2O$	196
Figure 5.14: VT XRD data for $K_3HTi_4Si_3O_{16} \cdot 4H_2O$	200
Figure 5.15: X-ray diffraction pattern for the final phase assemblage of heated $K_3HTi_4Si_3O_{16} \cdot 4H_2O$	201
Figure 5.16: VT XRD pattern for Cs-exchanged $K_3HTi_4Si_3O_{16} \cdot 4H_2O$	203
Figure 5.17: X-ray diffraction pattern for the final phase assemblage of heated Cs-exchanged $K_3HTi_4Si_3O_{16} \cdot 4H_2O$	204
Figure 5.18: X-ray diffraction pattern for the final phase assemblage of heated $K_3HGe_7O_{16} \cdot 4H_2O$	205
Figure 5.19: X-ray diffraction data for the final phase assemblage of heated Cs-exchanged $K_3HGe_7O_{16} \cdot 4H_2O$	206
Figure 5.20: VT XRD data for $K_3HTi_4Ge_3O_{16} \cdot 4H_2O$	208
Figure 5.21: X-ray diffraction data for the final phase assemblage of heated $K_3HTi_4Ge_3O_{16} \cdot 4H_2O$	209
Figure 5.22: VT XRD data for Cs-exchanged $K_3HTi_4Ge_3O_{16} \cdot 4H_2O$	210

Figure 5.23 X-ray diffraction data for the final phase assemblage of heated Cs-exchanged $K_3HTi_4Ge_3O_{16} \cdot 4H_2O$	211
Figure 5.24: VT XRD data for Sr-exchanged $K_3HTi_4Ge_3O_{16} \cdot 4H_2O$	213
Figure 5.25: X-ray diffraction data for the final phase assemblage of heated Sr-exchanged $K_3HTi_4Ge_3O_{16} \cdot 4H_2O$	214

List of Tables

Table 2.1: The comparisons between the two different types of XRF spectrometer	44
Table 3.1: Synthesis optimisation of the umbite synthesis.....	55
Table 3.2: Lattice parameters, atomic positions, occupancy and thermal parameters for the refinement of $K_2ZrGe_3O_9.H_2O$	65
Table 3.3: Selected bond lengths from the refinement of $K_2ZrGe_3O_9.H_2O$	66
Table 3.4: Relative compositions for the Si and Ge umbite synthesis	68
Table 3.5: Fused bead XRF data for the parent and Cs-exchanged phases.....	69
Table 3.6: Loose powder XRF data for Na, Mg, Ca and Sr-exchange.....	70
Table 3.7: Exchange site atoms and occupancies for the unexchanged and exchanged zirconosilicate umbite.....	71
Table 3.8: Lattice parameters, atomic positions, occupancy and thermal parameters for the refinement of Cs-exchanged $K_2ZrGe_3O_9.H_2O$	74
Table 3.9: Selected bond lengths from the refinement of Cs-exchanged $K_2ZrGe_3O_9.H_2O$	75
Table 3.10: Loose powder XRF data before and after a NaCl reflux.....	78
Table 3.11: XRF loose powder results showing the regeneration of the parent umbite phase after a KCl reflux.....	80
Table 3.12: Loose powder XRF data showing zirconogermanate umbite before and after acid treatment for the attempted synthesis of the proton form.....	83
Table 3.13: Second attempted synthesis of the proton form showing pressed pellet XRF data before and after exchange.....	84
Table 3.14: Cs-exchange data for the proton form of $K_2ZrGe_3O_9.H_2O$	85

Table 3.15: XRF loose powder data for the assumed ammonium form of zirconogermanate umbite.....	91
Table 4.1: XRF data for the doped umbite materials	107
Table 4.2: XRF analysis of Cs-exchanged Nb doped umbites	109
Table 4.3: XRF analysis of Sr-exchanged 0.2Nb doped umbite	110
Table 4.4: XRF analysis for the Cs-exchanged 0.2Nb doped sample	112
Table 4.5: Lattice parameters, atomic positions, occupancy and thermal parameters for the refinement of $K_{1.9}Zr_{0.9}Nb_{0.1}Ge_3O_9 \cdot H_2O$	115
Table 4.6: Selected bond lengths from the refinement of $K_{1.9}Zr_{0.9}Nb_{0.1}Ge_3O_9 \cdot H_2O$	116
Table 4.7: Lattice parameters, atomic positions, occupancy and thermal parameters for the refinement of $K_{1.8}Zr_{0.8}Nb_{0.2}Ge_3O_9 \cdot H_2O$	117
Table 4.8: Selected bond lengths from the refinement of $K_{1.8}Zr_{0.8}Nb_{0.2}Ge_3O_9 \cdot H_2O$	118
Table 4.9: Lattice parameters, atomic positions, occupancy and thermal parameters for the refinement of $K_{1.75}Zr_{0.75}Nb_{0.25}Ge_3O_9 \cdot H_2O$	119
Table 4.10: Selected bond lengths from the refinement of $K_{1.75}Zr_{0.75}Nb_{0.25}Ge_3O_9 \cdot H_2O$	120
Table 4.11: Lattice parameters, caesium occupancies and weight fractions from the two phase Rietveld refinement of Cs-exchanged 0.1Nb umbite.	128
Table 4.12: Lattice parameters, caesium occupancies and weight fractions from the two phase Rietveld refinement of Cs-exchanged 0.2Nb umbite.	131
Table 4.13: Lattice parameters, caesium occupancies and weight fractions from the two phase Rietveld refinement of Cs-exchanged 0.25Nb umbite.	134
Table 4.14: Summary table for the refinements of Cs-exchanged Nb doped umbites.....	135
Table 4.15: Lattice parameters, atomic positions, occupancy and thermal parameters for the refinement of $K_{1.9}Zr_{0.9}Sb_{0.1}Ge_3O_9 \cdot H_2O$	138

Table 4.16: Selected bond lengths from the refinement of $K_{1.9}Zr_{0.9}Sb_{0.1}Ge_3O_9 \cdot H_2O$	139
Table 4.17: Lattice parameters, atomic parameters, occupancy and thermal parameters for the refinement of $K_{1.8}Zr_{0.8}Sb_{0.2}Ge_3O_9 \cdot H_2O$	141
Table 4.18: Selected bond lengths from the refinement of $K_{1.8}Zr_{0.8}Sb_{0.2}Ge_3O_9 \cdot H_2O$	142
Table 4.19: Lattice parameters, atomic parameters, occupancy and thermal parameters for the refinement of $K_{1.75}Zr_{0.75}Sb_{0.25}Ge_3O_9 \cdot H_2O$	144
Table 4.20: Selected bond lengths from the refinement of $K_{1.75}Zr_{0.75}Sb_{0.25}Ge_3O_9 \cdot H_2O$	145
Table 4.21: XRF analysis of Cs-exchanged Sb doped umbites.....	146
Table 4.22: Variation in XRF data shown for the caesium uptake in the 0.25Sb doped sample repeat syntheses.	146
Table 4.23: XRF analysis of Cs-exchanged Sb doped umbites.....	147
Table 4.24: Lattice parameters, caesium occupancies and weight fractions from the two phase Rietveld refinement of Cs-exchanged 0.1Sb umbite	150
Table 4.25: Lattice parameters, caesium occupancies and weight fractions from the two phase Rietveld refinement of Cs-exchanged 0.2Sb umbite	152
Table 4.26: Lattice parameters, caesium occupancies and weight fractions from the two phase Rietveld refinement of Cs-exchanged 0.25Sb umbite.	154
Table 4.27: Summary table for the refinements of Cs-exchanged Sb doped umbites.	155
Table 5.1: Composition, space group and lattice parameters for the known germanate pharmacosiderite phases.	171
Table 5.2: Lattice parameters, atomic positions, occupancy and thermal parameters for the reduced range refinement of $K_3HGe_7O_{16} \cdot 4H_2O$	179
Table 5.3: Selected bond lengths from the refinement of $K_3HGe_7O_{16} \cdot 4H_2O$	180

Table 5.4: Lattice parameters, atomic positions, occupancy and thermal parameters for the refinement of $K_3HTi_4Ge_3O_{16} \cdot 4H_2O$	185
Table 5.5: Selected bond lengths from the refinement of $K_3HTi_4Ge_3O_{16} \cdot 4H_2O$	186
Table 5.6: XRF data of pressed pellets for $K_3HGe_7O_{16} \cdot 4H_2O$	188
Table 5.7: XRF data of fused beads for $K_3HGe_7O_{16} \cdot 4H_2O$	189
Table 5.8: Lattice parameters, atomic positions, occupancy and thermal parameters for the refinement of Cs-exchanged $K_3HGe_7O_{16} \cdot 4H_2O$	191
Table 5.9: Selected bond lengths from the refinement of Cs-exchanged $K_3HGe_7O_{16} \cdot 4H_2O$	192
Table 5.10: XRF data of pressed pellets for $K_3HTi_4Ge_3O_{16} \cdot 4H_2O$	193
Table 5.11: XRF data of fused beads for $K_3HTi_4Ge_3O_{16} \cdot 4H_2O$	194
Table 5.12: Lattice parameters, atomic positions, occupancy and thermal parameters for the refinement of Cs-exchanged $K_3HTi_4Ge_3O_{16} \cdot 4H_2O$	197
Table 5.13: Selected bond lengths from the refinement of Cs-exchanged $K_3HTi_4Ge_3O_{16} \cdot 4H_2O$	198

Abbreviations

XRD - X-Ray Diffraction

VTXRD – Variable temperature x-ray diffraction

XRF- X-Ray Fluorescence

AMP – Ammonium molybdophosphate

AV – Aveiro materials

CST- Crystalline silicotitanate

DTA – Differential thermal analysis

GDF – Geological disposal facility

HLW – High level waste

ILW – Intermediate level waste

LLW – Low level waste

PAN – Polyacrylonitrile

PB - Prussian blue

PTFE - Polytetrafluoroethylene

SIXEP- Sellafield ion exchange effluent plant

TGA – Thermal gravimetric analysis

Chapter 1- Introduction

1.1 Background

The UK has ambitious targets of reducing net carbon emissions by 80% by 2050 and to meet the international goal of being carbon neutral by 2100. Nuclear power currently equates to approximately 21% of UK power generation, with renewable energy contributing a smaller percentage. The reliance on fossil fuels must be reduced in order to meet these targets and prevent global temperature rises; as a result the power generation future of the UK looks set to combine predominantly renewable power with nuclear energy [1-4].

Nuclear energy is an issue which splits opinion, with foreign investment, reactor location and overall cost being offset by job creation and reliable power generation. However nuclear waste remains the largest issue that surrounds the use of nuclear energy and the need to deal with nuclear waste has been of the utmost importance in the 20th and 21st centuries. The emergence of nuclear power as an alternative to more conventional carbon producing methods of power generation in the early 20th century has resulted in the widely debated issue centred on what to do with the waste produced. Coupled to this is the testing and decommissioning of nuclear weaponry and nuclear accidents such as Chernobyl in 1986 and Fukushima in 2011 [5-7]. The result of all of this is a worldwide research effort focusing not only on immobilisation and storage of nuclear waste but also on environmental remediation.

1.1.1 Waste types and disposal

By the end of the next decade, seven of the eight current nuclear power stations in the UK fleet will undergo decommissioning [8]. The reprocessing of the spent fuel involves dissolving the rods in nitric acid, the resulting mixture then undergoes a solvent extraction

process to remove any remaining uranium and plutonium that is formed during the fission process [9]. The waste from these reactors can be placed under three categories low level waste (LLW), intermediate level waste (ILW) and high level waste (HLW)

LLW consists of low level alpha and beta/ gamma emitters which can be managed at a surface disposal facility. Usually stored in large metal drums, LLW accounts for the largest volume of all waste types however produces the least amount of radioactivity [10]. ILW consists of waste with greater beta/gamma activity which requires managed disposal, example of which include materials used to clad the reactor and some of the materials used to build the plant.

HLW consists of all the spent fuel and fission products from the power generation process.

HLW and ILW are often placed in temporary storage until long term storage is available [9].

It is HLW which provides the greatest contributor to the overall radiation output when decommissioning a reactor and the general fission process. Short lived isotopes decay to harmless levels during storage of spent fuel in water cooled ponds; radioactive species with high activities and with half-lives on a human timescale present the biggest risk. The radioactivity of nuclear waste decreases with increasing time after its production and range from approximately 10,000 to 1 Ci/L for HLW, from 10 to 10^{-3} Ci/L for ILW and 10^{-3} to 10^{-6} Ci/L for LLW [10].

The waste is managed in different ways depending on radioactivity and material type, current and future safe disposal of HLW presents the greatest challenge for research groups worldwide. As a result a wide range of methods have been suggested for the immobilisation of nuclear wastes.

Immobilization of radionuclide and other waste materials from the various stages of power generation and decommissioning has resulted in various different methods of waste

processing, with these final wasteforms destined to be placed in geological disposal facilities (GDF) for long term storage. As a result robust chemically, thermally and radiation stable wasteforms are required whilst occupying the minimal possible volume for disposal [11].

1.2 Immobilisation options

1.2.1 Glass wasteforms

The immobilisation of radionuclides in glasses by vitrification has been widely investigated as a potential disposal method for the last 40 years. The amorphous nature of glasses and the resultant structural flexibility allows for the encapsulation of a wide range of radioactive species, providing a solid in which these species are chemical bonded to the glass framework [12-13]. The optimisation of these glass wasteforms, with the view of increasing loading, physical/chemical properties and storage properties, has resulted in a wide range of different compositions.

Silicate glasses have been used for the immobilisation of HLW, the flexibility of these materials with respect to waste composition and property optimisation has resulted in it being the preferred immobilisation method worldwide. The addition of boric oxide to silica allows for lower processing temperatures and glass workability with minor additions of other modifying oxides gives a wide range of borosilicate glass compositions for waste immobilisation [9].

Borosilicate glass matrices can accommodate high levels of alkali and alkali earth cations; however formation conditions need to be optimised to prevent the volatilisation of species such as caesium. Actinide and lanthanide radionuclides can also be incorporated into these glass

phases with lower oxidation state species more easily integrated, an example being 1% wt loading of Pu⁴⁺ compared to 4 % wt Pu³⁺ in more reducing conditions [14-15]. Generally the increase in incorporation rate is inversely proportional to oxidation state, however certain metal such as Pd, Ru and Rh are insoluble in borosilicate glasses and will precipitate out, affecting the glass formation process [12].

Interest in phosphate glasses started during the early studies into immobilization materials due to low formation temperature and high solubility for metal oxides. However low thermal and chemical stability relative to borosilicate glasses meant that early phosphate glass compositions were less useful for waste immobilisation. Newer glass compositions, such as lead iron phosphate glasses developed at Oak Ridge National lab, have increased the usefulness of phosphate glasses. Lead iron phosphate glasses show good thermal, chemical [9] and radiation stability [16] and can be prepared at temperatures ranging from 800-1000 °C, around 100-250 °C lower than borosilicate glasses [17].

There are many other types of glass which can be used to immobilise HLW, a commercial lanthanide borosilicate glass called Löffler glass has been suggested as a potential candidate for immobilisation of actinide species such as U, Pu and Am [18]. Formation of glass wastefoms by sintering, mixing HLW with a glass frit under pressure provides an alternative to standard vitrification methods. The benefits of this method are lower reaction temperatures and as a result reduced volatisation of radionuclides such as Cs, Mo and Tc[19].

1.2.2 Ceramic Wastefoms

The use of ceramic wastefoms for long term immobilisation has been widely investigated; the principle behind this involves synthetic analogues of mineral phases in which HLW is

immobilised. The benefit to this is the preservation of these types of phases on a geological timescale observed in nature and as a result a compatibility with future storage methods such as a GDF.

A method for waste immobilisation was developed by Ringwood *et al.* in the 1970's, this was based on immobilisation of radionuclides in mineral type phases in a synthetic rock (Synroc). Synroc is mainly composed of perovskite (CaTiO_3), zirconolite ($\text{CaZrTi}_2\text{O}_7$) and hollandite ($\text{BaAl}_2\text{Ti}_6\text{O}_{16}$) in which the radionuclides are incorporated into these ceramic phases. The benefit of using synroc is that the wastefrom phase assemblage is dictated by the different mineral components and as a result radionuclides distribute in low concentrations across the various phases, much like they would in natural conditions [20-23].

The perovskite phase, general formula ABX_3 , can accommodate a wide range of different elements into stable solid solutions. The structural flexibility of the perovskite system allows for various combinations at the A and B sites. Examples of which are Sr^{2+} being substituted for Ca^{2+} at the A site and a range of tetravalent elements that can replace Ti^{4+} at the B site. The CaTiO_3 phase has been suggested as a host matrix for lanthanide and actinide elements due to low leach rates and the facile incorporation of these elements into its crystal structure [24].

Zirconolite ($\text{CaZrTi}_2\text{O}_7$) is one of the other major phases found in synroc, depending on the nature of the waste species and subsequent substitution into the zirconolite structure it can form various polymorphs [25]. As a result zirconolite is capable to incorporate a wide range of radionuclides of varying valence and ionic radii. The use of CeO_2 as a surrogate for tetravalent actinide elements is common and the replacement of Zr by up to 50% Ce has been

shown in zirconolite, the resultant ceramic wastefrom showed good aqueous stability with low Ce leach rates [26].

The removal of silicates and higher titanium content from the original synroc preparation allowed for the formation of a hollandite phase. In natural hollandite ($\text{BaMn}_8\text{O}_{16}$) manganese can have varying oxidation states and there are a wide range of structural isotypes, in the synroc phase manganese is replaced by Al^{3+} and Ti^{4+} . The Hollandite in synroc ($\text{BaAl}_2\text{Ti}_6\text{O}_{16}$) is a key component of the overall assemblage due to leaching resistance but also its structural flexibility, with the potential to incorporate a wide range of elements at both the Ba and Al/Ti sites [20]. ^{137}Cs decays into ^{137}Ba and the replacement of Cs for Ba in hollandite phases has been widely investigated. Due to the size of the Cs cation the maximum limit of substitution was 0.3 Cs per unit cell, increased Cs substitution resulted in the deformation of the hollandite structure [27]. Variation of the Al/Ti site has allowed for the optimisation of Cs uptake, the most promising of which is the facile incorporation of Cs into Cr/Ti hollandites with the mixed chromium systems showing high caesium retention and durability [28-29].

1.2.3 Cementation

The advantages of cement as a wastefrom are the relatively low cost, simple and low production temperature of these materials [30]. However cementation has often been restricted to LLW and ILW waste, increased levels of radioactivity can cause radiolysis of water in the cement and result in the evolution of hydrogen gas. Also the range of different constituents in waste streams can affect the setting properties of the cement resulting in a less robust final material.

Additional problems arise due to the microporous nature of cement and its alkaline character. This can lead to the precipitation of alkaline insoluble species; these can then be leached out of the cement by leachants of different pH. Despite this, various cements, concretes and cement-based composites have been suggested as immobilization options for HLW [9, 30].

The disposal and long term storage in geological disposal facilities (GDF) originated in the US in 1950's as a permanent solution to the management of nuclear wastes. The concept of a GDF has been based upon a multi-barrier system where engineered and natural barriers contain radionuclides and associated wastefoms. The materials which are placed underground must remain undisturbed by both human interaction and natural processes, with the environment inside a GDF varying over a geological time length. As a result the safety of a GDF has to be considered over a long time period with the risk decreasing as the radionuclide species decay, the effective containment and isolation of the radioactive species is paramount especially during the early period of operation. Locations for GDF's have been suggested worldwide and these will be the final destination for HLW for many countries [31]. Other alternative are recycling of nuclear waste for the use in future reactors for power generation and the reuse of waste in industrial applications [32].

1.3 Materials for Caesium-137 and Strontium-90 uptake

Caesium-137 and strontium-90 are two products of the fission process; these radionuclides are of significant interest as ion exchange targets. The reason for this is the potential health hazards that these radionuclides present due to similarities in biological behaviour as other elements in the body, specifically potassium and calcium, respectively. Caesium-137 can find

its way into soft tissue whereas strontium-90 can find its way into bones, with the radioactivity of these species presenting a significant health risk in those affected. These radionuclides are distributed by nuclear weapons testing and nuclear accident; as a result they find their way into the environment. This presents a contamination risk and as result radioactive species can then be taken into the body. [33].

Due to the high mobility of these species the distribution of radionuclides is not homogenous over the area affected by discharge into the environment. An example of this is after the Fukushima event, complex currents off the coast and seasonal variations resulted in varied deposition of radiocaesium in the surrounding sea [34]. Atmospheric transport models showed that deposition of radiocaesium could have occurred as far away as North America and Eurasia [33]. The removal of these radionuclides from waste feeds in of high importance and example of this is process used by the Sellafield nuclear waste processing plant in the United Kingdom.

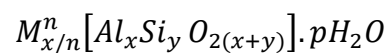
An ion exchange process is used to remove radioactive caesium and strontium isotopes from the Sellafield waste streams. Ion exchange involves the exchange of ions between a solution and a complex, commonly an organic exchange resin or inorganic open-framework material. The preference for one ion over another is described as the selectivity of an exchange material, ideally the specific ion targeted for exchange will be the only ion taken up by the exchange material. However this is rarely the case due to competition and similarities in properties between the ions in solution, especially for alkali and alkali earth cations. As caesium and strontium are present in very low concentrations, relative to cations such as sodium in the waste streams, high selectivity is required to successfully remove the radionuclides. The selectivity of a material is often described by the distribution coefficient (K_d), the distribution of ions in the solid against those in solution, with the larger the number

for the target ion the better. A second way of showing ion exchange properties is cation exchange capacity, which is a measure of the total uptake of a material; this is often shown as a simple percentage or milliequivalents per gram (mEq/g).

The effectiveness of an ion exchange is usually determined by both its selectivity and total exchange uptake however factors such a rate of uptake and exchanger stability in varying pH must be considered. As a result the selection of a material for exchange processes is usually a compromise of all the factors mentioned above.

1.3.1 Zeolites, Clinoptilolite and SIXEP

Zeolites are large family hydrated aluminosilicate materials with the general formula:



Where M is an alkali and/or alkali earth cation and n is cation charge [35]

Zeolites structurally consist of a framework of connected aluminium and silicon tetrahedra which form a system of cavities and channels. The aluminium tetrahedron is responsible for the net negative framework charge which is charge balanced by extra-framework cations, these are located in the channels alongside zeolitic water. The porous nature of zeolites and the wide range of different structures and compositions, both natural and synthetic, have made them widely used in industry as ion exchangers.

Clinoptilolite is the most abundant zeolite in nature and is mined in over 16 different countries, commonly found in sedimentary rock, Figure 1.1 [36].

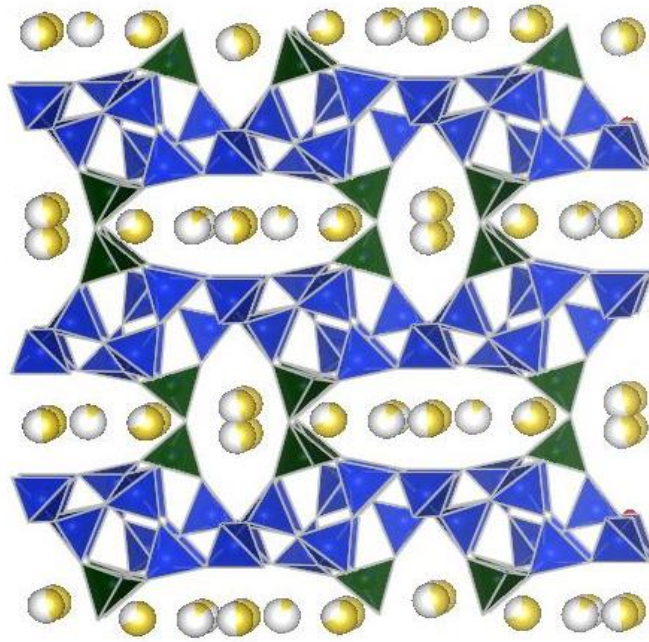


Figure 1.1: Structure of Clinoptilolite consisting of corner shared silicon (Blue) and aluminium (Green) tetrahedra. Sodium cations (Yellow spheres) are shown with site occupancies indicated by the amount of coloured shading.

Clinoptilolite is mostly studied as a material for ion exchange, primarily for use in the nuclear industry. Its use in the removal of radioactive cations, primarily caesium and strontium from nuclear aqueous waste, is central to the site ion exchange and effluent plant (SIXEP) at Sellafield, UK. Over the last 25 years SIXEP has been removing caesium and strontium radioisotopes from pond water, removing radioactive sources from the plant effluent and discharging cleaned water [37]. The material used on the SIXEP plant is mined in Mud Hills, California, this minimises plant performance variability. As clinoptilolite is a natural zeolite it has impurity phases such as quartz [38] calcite and feldspar [36]; these impurities can reduce the ion exchange capacity of the material. However Clinoptilolite used at SIXEP shows high selectivity towards caesium and strontium with it capable of removing 20 mol of Cs^+ and 1 mol of Sr^{2+} in the presence of 7.5×10^5 mol of Na^+ and 5×10^3 mol of Ca^{2+} . The cation

exchange capacity for clinoptilolite is 2.2 mEq/g however in practice this value is reduced due to impurities [37]. The exchanged clinoptilolite can then be encapsulated in cement for long term storage [36].

SIXEP clinoptilolite is unique in that it exhibits both high Cs^+ and Sr^{2+} selectivity, when compared to clinoptilolite mined elsewhere. Whilst this is a large positive for nuclear applications in the UK and explains its successful application for over 30 years, it is also a finite resource. Location dependant variations in the materials ion exchange properties and lack of compositional control through synthesis have led to investigation into alternatives.

The disadvantage in the use of natural zeolites extends beyond just clinoptilolite but all natural materials. Inclusion of impurities, post processing to purify the material, differences in composition from variations in their formation environments [35] can have an effect on the ion exchange properties. That is why a considerable amount of research is focused on other materials, which allow for greater control over composition but also access to a range of different structures and related ion exchange properties.

1.3.2 Ammonium molybdophosphate

One of the most extensively studied ion exchangers is ammonium 12-molybdophosphate (AMP), $(\text{NH}_4) \text{PMo}_{11}\text{O}_{40}$. AMP has been shown to exhibit good cation exchange in acidic conditions by Thistlethwaite *et al.* [39] and further work examining the caesium uptake was reported in nature by Smit *et al.* [40]. The high caesium selectivity relative to sodium and potassium of AMP outperformed the ammonium form of Dowex® 50 ion exchange resin. K_d values for Cs^+ uptake by AMP are in the region of 6000 ml/g, compared to K_d values of 3.4 and ~0 for potassium and sodium respectively [40], indicating high Cs^+ selectivity.

Due to these properties AMP is still heavily studied with much research focusing on the design of composite AMP systems which look to improve the processing properties of AMP. Sebesta *et al.* showed that composites composing of polyacrylonitrile (PAN) had very little impact on the properties of AMP with further work showing high Cs^+ and Sr^{2+} uptake across a large pH range. AMP/ SiO_2 composites have been shown to have high chemical stability, radiation resistance and when mixed with the zeolite mordenite, low caesium leachability [41-44].

1.3.3 Prussian blue and Cs treat

The pigment Prussian blue (PB), $\text{Fe}_4[\text{Fe}_3(\text{CN})_6]_3$ as shown by Figure 1.2, was used medicinally during the Goiania incident for the treatment of radiocaesium poisoning [45], this is due to the crystal cage size of PB being similar to that of a caesium cation [46]. The ability of the material to uptake Cs^+ has meant PB can be applied outside of medical applications, focusing on environmental remediation and nuclear waste treatment.

Research into composite systems such as PB coated magnetic nanoparticles, which enable facile removal of exchanged materials by magnetic separation, are of great interest for exchange column applications [47].

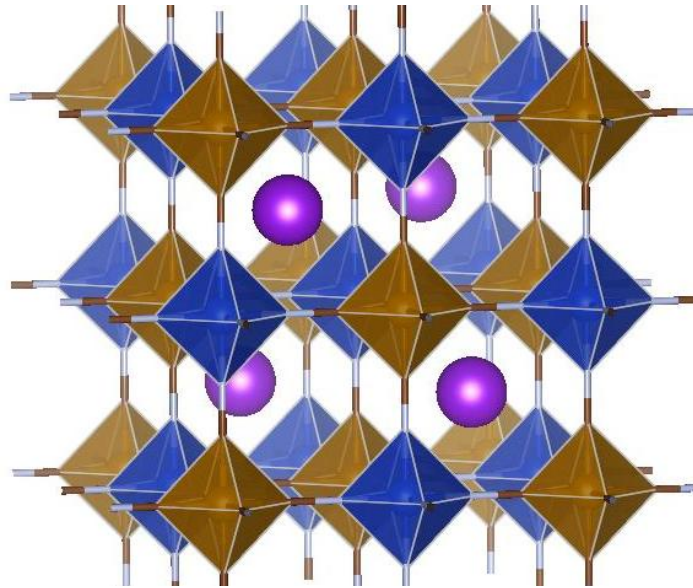


Figure 1.2: Structure of prussian blue, consisting of $\text{Fe}^{2+}/\text{Fe}^{3+}$ polyhedral (Blue and Brown) which are connected by cyano linkers. Cation sites are shown by the purple spheres and are located in the framework cavity.

Cs Treat[®], a potassium cobalt hexacyanoferrate, has been extensively used for caesium removal in the nuclear industry as it shows very high Cs^+ selectivity in alkaline salt loaded radwaste solutions. Column exchange experiments report K_d values for caesium uptake to be in the region of 9.2×10^4 ml/g in high sodium solutions [48] and stable over multiple exchange cycles.

1.3.4 Crystalline silicotitanate

Crystalline silicotitanate (CST), ideal formula $\text{Na}_2\text{Ti}_2\text{O}_3\text{SiO}_4 \cdot 2\text{H}_2\text{O}$, was hydrothermally synthesised by Poojary *et al.* The structure CST consists of clusters of titanium octahedra connected by linear arrangement of alternating Si and Na atoms, the arrangement of Ti

octahedra and Si tetrahedra produces a channel, Figure 1.3. There are two distinct sodium environments in the structure of Na-CST, one of which is tightly bound to the framework and the other located in the channel, which is exchangeable for both Cs^+ and Sr^{2+} [49-50].

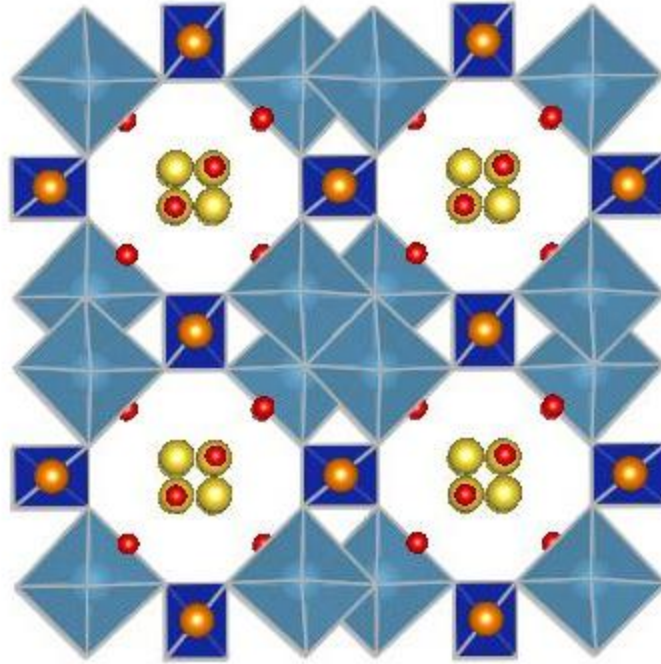


Figure 1.3: Structure of Na-CST consisting of Ti clusters (Light Blue) connected by silicon tetrahedra (Blue). The two sodium environments are shown using coloured spheres, the tightly bound framework sodium (Orange) and exchangeable pore sodium (Yellow), water molecules are shown using red spheres.

Cs^+ exchange occurs at mildly acidic to basic conditions with approximately 25% of Na^+ replaced by Cs^+ at pH range 2-9. However Cs^+ uptake occurs at very low levels in highly basic nuclear solutions due to competition with Na^+ and K^+ , with K_d values for Cs^+ in an excess of Na^+ of approximately 3000 ml/g.

Ion exchange properties of Na-CST can be improved by the replacement of Ti^{4+} by Nb^{5+} , the result is much higher ion exchange capacity and improved caesium selectivity, K_d value of 17640 ml/g, then the parent material in waste solutions [52]. The ion exchange properties of

CST can be further improved by the reduction of the crystallinity of the material. Clearfield *et al.* show that poorly crystalline Na-CST shows much improved Strontium uptake, especially in basic conditions due to the uptake of $\text{Sr}(\text{OH})^+$. This trend was also observed for Nb-Na-CST with improved caesium uptake when compared to the crystalline derivative [53]. The effectiveness of the niobium doped Na-CST ion exchange has resulted in the commercialisation of the material as IONSIV IE-911.

1.3.4 Clays

One extensively researched family of inorganic materials are naturally occurring clay materials, with much research focusing their ion exchange properties. Clays such as kaolinite and monmorillonite have been suggested for use in environmental remediation due their affinity for metal ions. These materials contain sheets of silicon tetrahedra and aluminium octahedra in either a 1:1 or 2:1 ratio. The isomorphous substitution of Si^{4+} by Al^{3+} in the tetrahedral sheet and Al^{3+} by Mg^{2+} in the octahedral sheet generates net negative charge in the structure [54-55]. This negative charge is compensated by cations located in the interlamellar gap and as a result clay materials can ion exchange a range of metal ions [56-57]. High exchange capacity, low cost and high natural abundance are properties that make clays so interesting but industrial ion exchange applications are limited due to mechanical disadvantages and composition variations [58].

1.4 New materials for ion exchange applications

The synthesis and properties of open framework inorganic materials is a continually expanding area of inorganic chemistry. The abundance of natural open-framework materials alongside the design of novel architectures has resulted in a very diverse family of materials. The exploration of both physical and chemical properties of these materials has led to a wide range of potential applications. These open-framework materials are characterised by three-dimensional structure with a system of pores and channels. This channel system and variation in pore size has meant open framework inorganic material have found uses in catalysis, separation and in ion exchange. The established methodology for removing Cs and Sr has been highlighted in previous sections and the design of materials capable of incorporating Cs and Sr has expanded beyond those currently in use.

Nature often provides us with a starting point with a wide range of minerals which exhibit the structural characteristics already outlined and as a result synthetic derivatives of these minerals are also to be considered. The challenges extend beyond the synthesis of these mineral phases but also establishing a greater structural understanding and insight into ion exchange properties. A large and well studied family of open-framework materials are silicates, these materials are made up of SiO_n repeat units and account for around 10% of all known structures. Silicates can consist of connected tetrahedra-tetrahedra much like zeolites or consist of mixed coordination frameworks, with the silicon occupying one of the tetrahedral sites.

1.4.1 Octahedral-tetrahedral silicates

A framework consisting of a tetravalent octahedra metal and silicon tetrahedra are commonly known as octahedral-tetrahedral materials (OT materials), unlike zeolites these minerals are much rarer in nature, however they are easily synthetically accessible. The atom that occupies the octahedral site can vary and this results in the formation of a wide range of microporous materials. However it has been of great interest to introduce a wide range of different metal atoms into the framework in order to develop materials that can be of use industrially as cation-exchangers for the removal of radionuclides.

Altering the composition of these metal silicates by isomorphous substitution affects the properties, making it a great tool for modification of the product. Using isomorphous substitution allows for the introduction of a range of metals such as Zr, Sn and Ti into the silicate framework and as a result a large range of compositional variation [59-60].

Rocha *et al.* have synthesised and reported a large group of these OT materials, designated AV materials, which are analogues of natural systems with potential to ion exchange. AV-7 ($\text{Na}_{0.5}\text{K}_{1.5}\text{SnSi}_3\text{O}_9 \cdot \text{H}_2\text{O}$) is a stannosilicate which has the structure of the zirconosilicate mineral kostylevite, Figure 1.4.

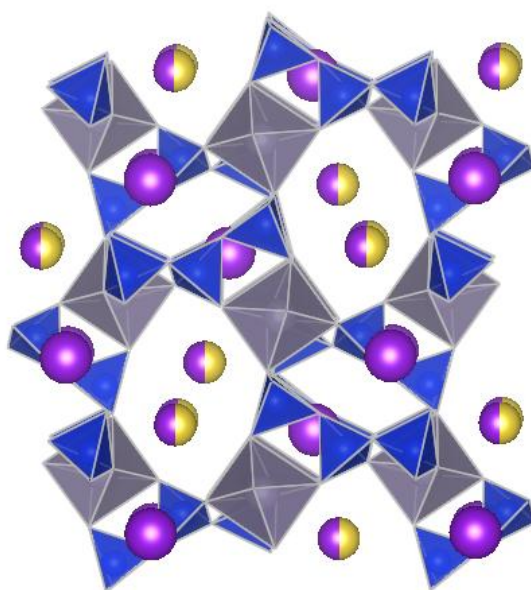


Figure 1.4: Structure of AV-7 consisting of corner sharing Sn octahedra (Grey) and silicon tetrahedra (Blue). The extra-framework cations are shown as purple (Potassium) and yellow (Sodium) spheres.

AV-7 consists of six-membered rings of SiO_4 and SnO_6 octahedra, where each SnO_6 octahedra connects to six SiO_4 tetrahedra on the six-membered rings, resulting in the formation of long channels which contain seven-membered rings. The two extra-framework cation sites are occupied by either K^+ alone, or K^+ and Na^+ . The K^+ cation is coordinated to four oxygens in the seven-membered rings located in the channel and two of the oxygens on the nearby six-membered ring. The K^+ and Na^+ site is coordinated to six framework oxygens and water molecules [60]. The ion exchange properties have been studied, however uptake of Cs^+ and Sr^{2+} has been shown to be minimal [61].

AV-3 ($\text{Na}_5\text{Zr}_2\text{Si}_6\text{O}_{18}(\text{Cl},\text{OH})\cdot 2\text{H}_2\text{O}$) is structurally analogous to the mineral petarisite consisting of a three-dimensional open-framework with corner sharing six-membered silicate rings and ZrO_6 octahedra, Figure 1.5.

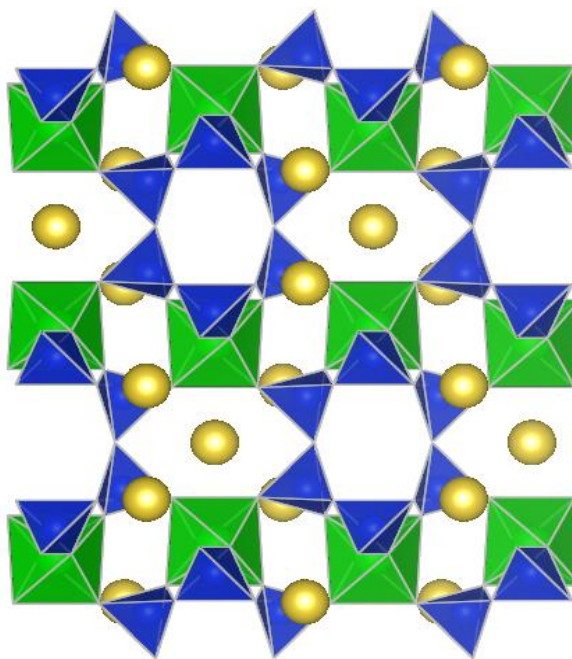


Figure 1.5: The structure of AV-3 consisting of corner sharing zirconium octahedra (Green) and sodium tetrahedra (Blue), sodium cations shown by yellow spheres.

Two channels with pore openings of $3.5 \times 5.5 \text{ \AA}$ are defined by mixed six-membered rings, one of which consists of pairs of SiO_4 tetrahedra linked by ZrO_6 octahedra. The other channel system is limited by six-membered silicate rings in which sodium, chloride, hydroxyl ions and the water molecules reside within the channels. Despite the presence of exchangeable cations in extendable pore systems, little work has been done to investigate ion exchange properties of the petarasite structure [62]. Other AV systems have been shown to ion exchange with the umbite system in particular being very well studied, this will be covered in Chapter 3.

AV-13 is a novel has a three-dimensional framework structure with corner sharing MO_6 octahedra where M can be either tin, zirconium or hafnium and SiO_4 tetrahedra. Silicon forms six-membered $(\text{Si}_6\text{O}_{18})^{12-}$ rings which are interconnected by corner sharing octahedra [63].

The overall structure is described by Ferreira *et al.* as a “knots” and “crosses” structure,

Figure 1.6. This is due to distorted metal cubes in which a six-membered silicate ring and sodium ions are located; these cages are accessed through a small $2.3 \times 3.2 \text{ \AA}$ pore.

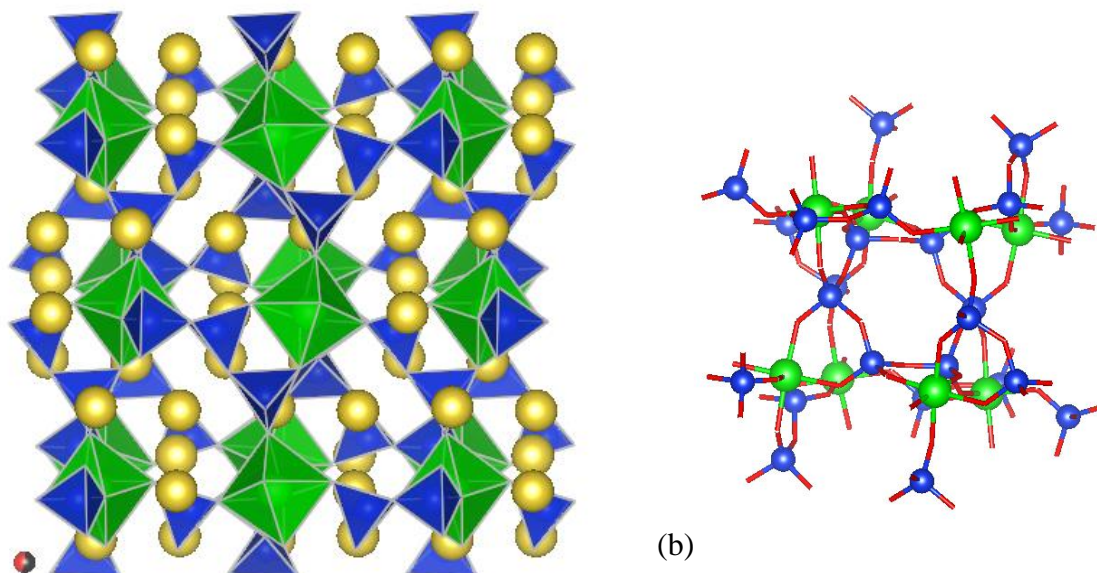


Figure 1.6: Structure of AV-13 consisting of metal octahedra (Green), silicon tetrahedra (Blue) and extra-framework sodium as yellow spheres. Knots and crosses structure shown in Figure 1.6b, the distorted metal cube (Knot) contains a silicon 6MR (Crosses). This motif alternates throughout the structure; the sodium ions are located inside this unit.

The local sodium environment inside the structure is disordered, with sodium cations inside the metal cubes connected to three framework oxygen's and to two other ligands, either water or a different anion [63]. Previous to this work, Cocoran *et al.* incorrectly characterised this material but reported its ion exchange properties, with it able to exchange all alkali metals [64]. Further interest in this material focuses on the potential anion exchange properties of the AV-13 structure or anion trapping via synthesis routes.

Variation of the octahedral component is not limited to transition metals, the incorporation of lanthanides has allowed for the functionalisation of these materials with regards to radionuclide uptake. The montregianite structure, $\text{Na}_2\text{KRESi}_8\text{O}_{19} \cdot 5\text{H}_2\text{O}$ (RE= rare earth),

consists of alternating sheets, a silicate sheet with four and eight-membered rings and an open octahedral sheet consisting of YO_6 and $\text{NaO}_4(\text{H}_2\text{O})_2$ octahedra. Potassium is ten-coordinate and found in the channels formed by the eight-membered rings. The montregianite structure allows for the incorporation of a range of rare earths, AV-1 (RE=Y) [65] and AV-5 (RE=Ce) [66] are examples; with further benefit to using rare earths being the interesting optical properties they exhibit. The transitions between 4f orbitals of the photoluminescent centre and the subsequent influence exerted on the rare earth by other nearby species allows them to be used as sensors. AV-9 a mixed Tb-Eu montregianite has been suggested as a potential qualitative and even quantitative Cs sensor, Figure 1.7.

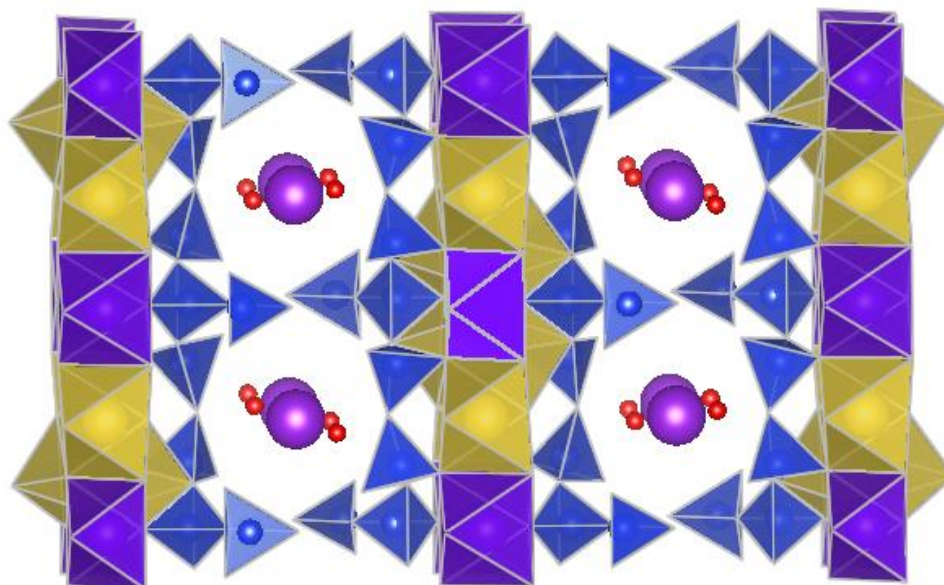


Figure 1.7: Structure of AV-9 with alternating RE (Purple) and sodium octahedra connected by silicon tetrahedra linkers (Blue). Potassium cations, shown by purple spheres, are located in the channel system alongside water molecules (Red spheres).

Figueiredo *et al.* showed that the photoluminescence spectrum vary dependant on effective caesium loading, with emission intensity decreasing with increasing caesium concentration.

AV-9 also shows fast ion exchange kinetics with the removal of approximately 70% of caesium from solution and equilibrium reached within one hour [67].

1.5 Germanates - Scope of the work

Despite the range of established and potential ion exchange materials reported above, matching the performance of SIXEP clinoptilolite has been difficult to achieve. Finding materials which can exchange both caesium and strontium, whilst showing good uptake capacity and kinetics, is of vital importance to future nuclear waste applications.

The synthesis of mixed octahedral-tetrahedral materials began with purely structural work however an understanding of their ion exchange properties was very soon developed. The purpose of this work focuses on combination of the work mentioned above, open framework ion exchange materials and wastefoms. In this case the work will focus on the direct conversion of an ion exchanger to a potential wastefom phase through thermal conversion via an ion exchanged intermediate; this should hopefully lock any alkali or alkali earth cations in a ceramic phase. The benefit to using mixed framework silicates is some of them can be thermally converted directly to a denser phase; a good example is the umbite type materials which will be covered in greater detail in the following chapters.

The compositional variation of OT materials focuses on the substitution of the octahedral component, the purpose of this work is to vary the tetrahedral site and see how this impacts ion exchange properties. The ionic radii for Ge^{4+} (0.39\AA) is larger than that of Si^{4+} (0.26\AA), it is hoped that by increasing the larger unit cell of OT germanates may allow for more facile exchange of the large caesium cation. The most common use of germanium is in optics and electronics, with only a small number of open-framework germanate materials reported. Examples such as pharmacosiderites have been investigated for their ion exchange properties, these materials will be covered in greater detail in later chapters.

Chapter 2- Experimental

2.1 Hydrothermal synthesis

Hydrothermal synthesis is a solution based methodology designed to mimic the mineral formation conditions in nature. This is done by heating a gel or liquid in a sealed vessel in order to generate pressure which causes crystallisation of a material from solution. The most common solvent used is water however solvothermal synthesis, in which solvents such as alcohols are used, is also common. The pressure generated by the reaction vessel is autogenous, the vapour pressure of the solvent coupled with the level of filling dictate the pressure generated at a given temperature. Great care must be taken when using solvents other than water due to the vapour pressure generated, the amount of solvent used must be adjusted so that the pressure generated remains within the operating parameters of the vessel.

A typical hydrothermal reaction vessel consists of a stainless steel shell in which a Polytetrafluoroethylene (PTFE) insert is located. The maximum operating temperature of this assembly is approximately 250 °C after which the PTFE begins to denature, however the excellent chemical stability of PTFE make it the ideal choice for the highly corrosive starting solutions usually used. The steel shell consists of a series of pressure release systems to allow for safe depressurisation if operating pressure is exceeded. Operating temperatures above 250 °C can be achieved with the PTFE commonly replaced by a borosilicate glass insert; solvothermal work typically uses glass inserts due to the porosity of PTFE and subsequent solvent absorption.

The benefit to using a hydrothermal synthesis technique is the ability to access different phases from traditional solid state methods. The inclusion of water often results in the formation of materials with lower density than those made by solids state methods and as a result is a valuable methods of accessing open-framework materials such as zeolites and

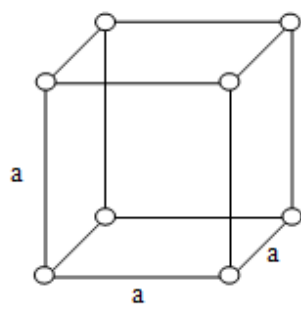
AlPO's. Crystal growth in a hydrothermal system is extremely complicated and is a combination of a range of factors such as temperature, pressure, composition and concentration of the starting solution, but also more subtle factors such as crystal growth zones, mass transport and nucleation. The additions of mineralisers such as OH⁻ and F⁻ also greatly affect the crystallisation process. The combination of these factors allows for the formation of phases and crystal morphology inaccessible by other synthesis methods.

Throughout this work Parr (model 4749, 4744 and 4748) acid digestion vessels with PTFE liners were used for all synthesis reported in this work.

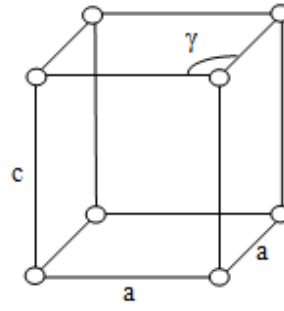
2.2 X-ray diffraction

2.2.1 Fundamentals of crystallography

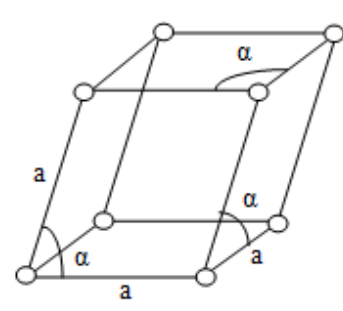
Matter is commonly classified into three states, gaseous, liquid and solid. The relationship between these states is dependent on the thermal energy of the constituent molecules. An ordered arrangement of molecules in a solid corresponds to a lower energy state and this ordering is called the crystalline state. A distinctive property of the crystalline state is the regular repetition in three-dimensions, made of molecules or groups of molecules, extending over a distance corresponding to thousands of molecular dimensions. The smallest repeat unit that represents this periodicity is called the unit cell, which can be described using lattice parameters. The dimensions of the unit cell are described as a , b and c , and the angles between the unit cell edges are α , β and γ . The relationship between these lattice parameters results in seven crystal systems, as shown in Figure 2.1 [68]:



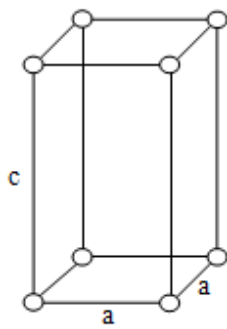
Cubic
 $(a=b=c, \alpha=\beta=\gamma=90^\circ)$



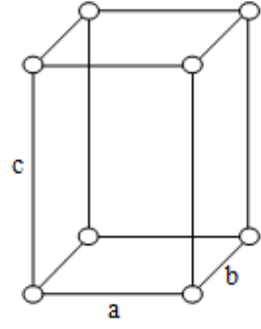
Hexagonal
 $(a=b \neq c, \alpha=\beta=90^\circ, \gamma=120^\circ)$



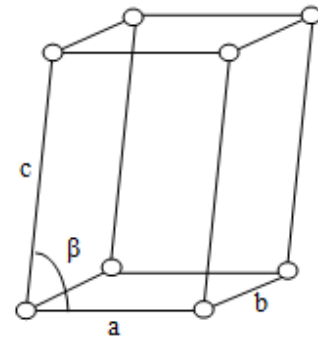
Rhombohedral
 $(a=b=c, \alpha=\beta=\gamma \neq 90^\circ)$



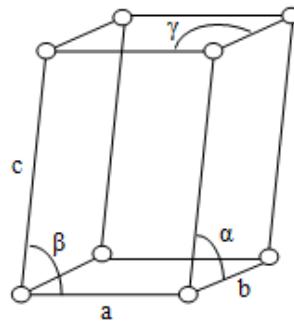
Tetragonal
 $(a=b \neq c, \alpha=\beta=\gamma=90^\circ)$



Orthorhombic
 $(a \neq b \neq c, \alpha=\beta=\gamma=90^\circ)$



Monoclinic
 $(a \neq b \neq c, \alpha=\gamma=90^\circ, \beta \neq 90^\circ)$



Triclinic
 $(a \neq b \neq c, \alpha \neq \beta \neq \gamma)$

Figure 2.1: 7 crystal systems.

Each crystal system has an associated primitive cell; each of these primitive cells defines a lattice type. However there are also other types of lattices, based on non-primitive cells, which cannot be related to the previous ones such as body-centred (*I*) or face-centred (*F*). The combination of the seven crystal systems and lattice types result in the derivation of 14 Bravais lattice types.

The 32 crystallographic point groups, which describe the symmetry elements possible in three dimensions, can be combined with the 14 Bravais lattices to generate 230 crystallographic space groups to which any three-dimensional crystal unit cell must correspond. Crystals are constructed of crystallographic planes which intersect the three crystallographic axes; the reciprocal of the intercept of these three axes can be described by Miller indices. Miller indices are a series of integers labelled as the (*hkl*) for the described plane, for example (100).

2.2.2 Diffraction fundamentals

Crystal structure analysis is usually based on diffraction phenomena caused by interactions between matter and X-rays, neutrons or electrons. A simple method was derived for obtaining the conditions required for diffraction, as described by W.L.Bragg in 1913 [69], this is shown by Figure 2.2 and Equation 2.1.

$$n\lambda = 2d_{hkl}\sin\theta$$

Equation 2.1: Braggs law

Where;

λ is the wavelength of the X-ray

d_{hkl} is the spacing between crystal layers

θ is the incident angle

n is an integer

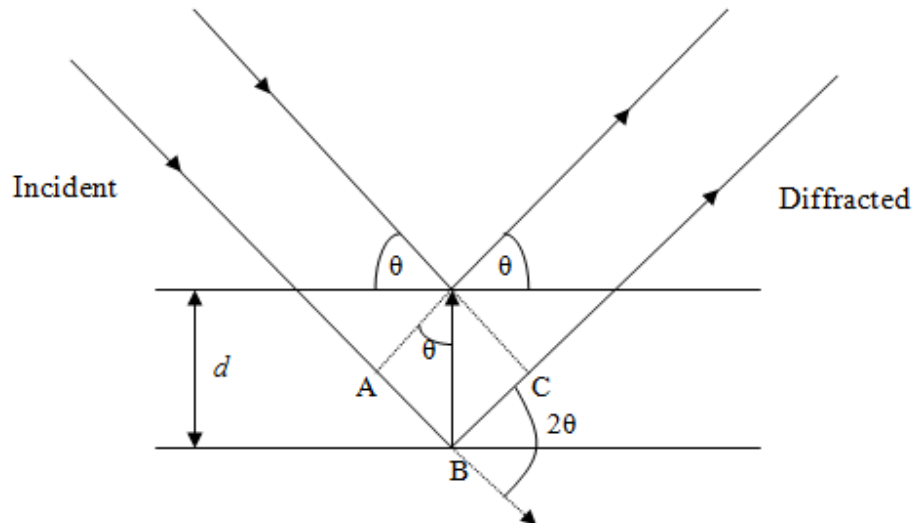


Figure 2.2: Graphical representation of diffraction between two planes.

The reflection of the incident beam by parallel lattice planes that are separated by a distance d , at an angle θ , results in constructive and destructive interference. The difference in path between the waves scattered by the parallel lattice planes is equal to $AB + BC = 2d \sin \theta$. If this is equal to an integer value for the number of wavelengths constructive interference is the result, satisfying Bragg's law. Where there is constructive interference between lattice planes,

a peak in intensity of the reflected beams is observed. The intensities resulting from satisfying of Bragg's law allows for the characterisation of a crystal structure [68].

2.2.3 X-ray generation

A conventional X-ray generator consists of a sealed tube in which a high voltage is applied across anode and cathode, held under vacuum. The voltage applied is element dependent with approximately 36 kV required for a copper source, molybdenum for example would require a higher voltage. A schematic for X-ray generation is shown in Figure 2.3, which consists of a cathode with a filament that emits electrons that are accelerated by the high voltage into a target anode metal.

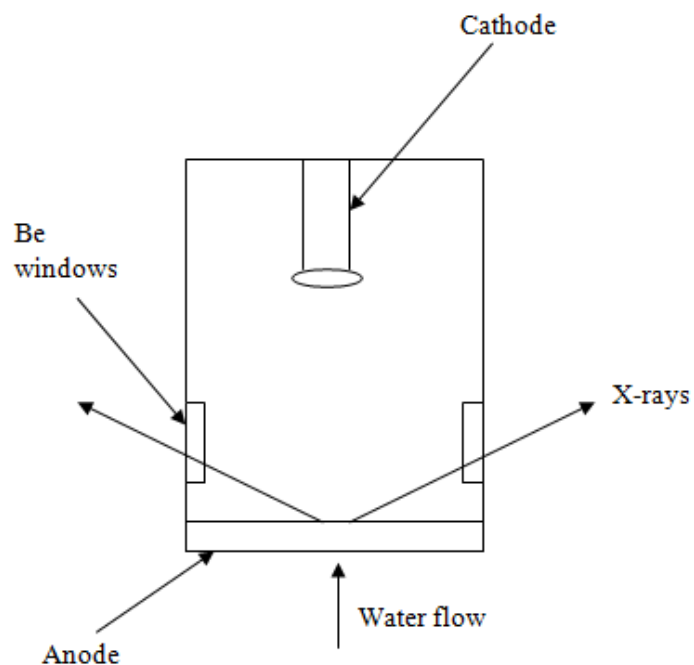


Figure 2.3: Graphical representation of an X-ray tube.

A vacuum is required because electrons colliding with gas molecules in the tube reduce the efficiency of the generation process. The generation of X-rays is highly inefficient due to much of the energy of the system lost through heat dissipation; as a result water cooling is required to prevent the melting of the target metal. Heat production and water cooling efficiency dictate the maximum power that can be applied to the X-ray tube. The X-rays generated in the tube leave through four perpendicular beryllium windows with a take-off angle commonly in the range 4-8°.

The X-rays generated consist of two combined components, the first being a continuous spectrum of white radiation called Bremsstrahlung. Bremsstrahlung are generated from the rapid deceleration of electrons by collisions with the metal target, the energy loss observed occurs after multiple events is converted to radiation. The second component of the generated X-rays is produced from the so called characteristic spectrum of the target element. This spectrum consists of sharp lines which appear at very distinct wavelengths alongside the continuous white radiation background. Electrons with high enough energy are capable of ionizing the target element by exciting an electron from an inner shell. An electron from a higher atomic energy level can move in to fill the vacancy and a characteristic X-ray photon is emitted with wavelength depending on the difference in energy between the two. Alpha (α) radiation is emitted when two energy levels are adjacent and Beta (β) emitted when there is an energy level that separates the two. The characteristic frequency and subsequent energy increases proportionally with atomic number, for example Cu $K_{\alpha} = 1.5418 \text{ \AA}$ compared to the Mo $K_{\alpha} = 0.7107 \text{ \AA}$ [68].

2.2.4 Filters, monochromators and detectors

Diffraction experiments require the energy of the radiation be limited to a wavelength range as narrow as possible. Preferably the radiation should consist of photons of only a single wavelength, this is can be done by using X-ray optics. Filters allow the required wavelength through and absorb the unwanted radiation, the element used for the filter is chosen so that its absorption edge falls in between the K_{α} and the K_{β} peaks of the anode element. For example, a nickel filter will absorb the Cu K_{β} and only have a small impact on the intensity of the K_{α} required for the experiment. A single crystal monochromator can also be used to select a single wavelength, resulting in monochromatic radiation. The simplest crystal monochromator can be set at a specific angle to the X-ray beam which is equivalent to selecting a particular wavelength from the spectrum. Intensity loss when using a monochromator is significant, so an effort must be made to correctly orientate crystal to minimise this intensity loss [68].

The most common types of detectors are scintillation counters and position sensitive detectors (PSD). A Scintillation counter is a doped phosphor, commonly thallium doped sodium iodide, which convert X-ray photons into light. The light emission is amplified and converted into an electrical signal by means of a photomultiplier tube where the resulting signal is proportional to the incident photon energy. PSD operate as an array of point detectors which allows for the simultaneous collection of diffraction data, the advantage of this being substantially improved data collection rates.

2.2.5 Diffractometer geometry

Laboratory diffractometers can be orientated in two different geometries, transmission and reflection, as shown in Figure 2.4. Transmission geometry is best for analysing samples with

relatively low absorption; heavily absorbing samples require an absorption correction to be applied before data analysis. Due to the flexibility of the types of sample preparation that can be used, transmission geometry also allows for facile study of air sensitive samples. In reflection geometry a flat surface is required for the best data quality data however it is more easily adapted for other diffraction applications.

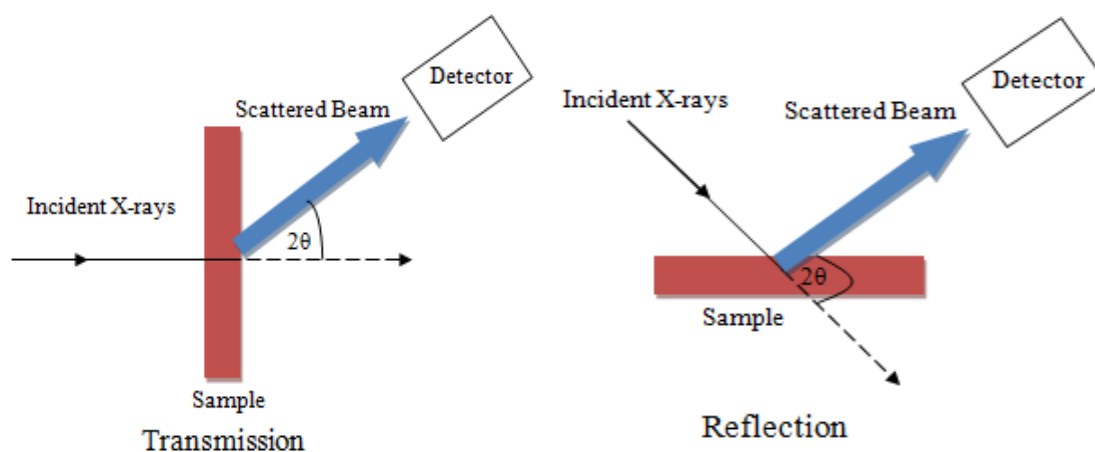


Figure 2.4: Graphical representation of diffractometer geometries

For this work the powder diffraction data was measured using a Bruker D8 diffractometer in both geometries. In transmission geometry a copper X-ray source and a germanium crystal monochromator were used to give Cu K_{α} radiation at a wavelength of 1.5406 Å. The samples were prepared by grinding in a pestle and mortar and isolating between two pieces of Scotch™ tape, with the mounted sample being rotated throughout data collection.

Reflection geometry used a non-monochromatic copper source with samples mounted using zero-background sample holders. Due to the sample rotation and stage tilting the powder was held in place by a minimal amount of petroleum jelly, which contributes a minimal background. In both cases the diffraction pattern was produced electronically.

2.2.6 Synchrotron X-ray diffraction

Charged particles under the influence of an accelerating field generate electromagnetic radiation, where the energy of the radiation is dependent on velocity. When accelerating electrons to near the speed of light, the radiation spectrum extends into the high energy region including the X-ray range. Synchrotron sources utilise this property by accelerating electrons through a closed trajectory, typically circular, from which X-rays are generated. The electron beam is often held under vacuum in a storage ring, with magnets used to control beam direction and maintain a narrow beam. The X-rays are channelled down beam lines to experimental workstations; these are tangential to the beam trajectory. The characteristics of the radiation supplied to the beam lines can be altered using insertion devices called wigglers and undulators. Insertion devices can be efficiently used to increase the flux naturally emitted by a synchrotron and to optimize the spectral range. The produced X-rays are of high intensity and highly collimated allowing for higher quality data, with much reduced collection time, compared to laboratory diffraction experiments [68].

As a result a wide range of different experiments can be undertaken at synchrotron sources, making them invaluable in material science.

Synchrotron data shown in this work was collected at station I11, Diamond Light Source, UK. Samples were firmly packed into glass capillaries (0.5 mm in diameter) and sealed. The sealed capillaries were fixed onto brass magnetic holders and pre-aligned before data was collected. The wavelength of the radiation used was determined from silicon standards before the experiment.

2.2.7 Powder Diffraction

Powders are polycrystalline materials composed of a large number of crystallites which are randomly orientated. Each of these crystallites diffracts independently of one another, as a result for any given value for d-spacing there will be a number of crystallites which can satisfy Bragg's law. The diffracted beams with the same d-spacing produce a cone, so called Debye-Scherrer cones, as shown in Figure 2.5.

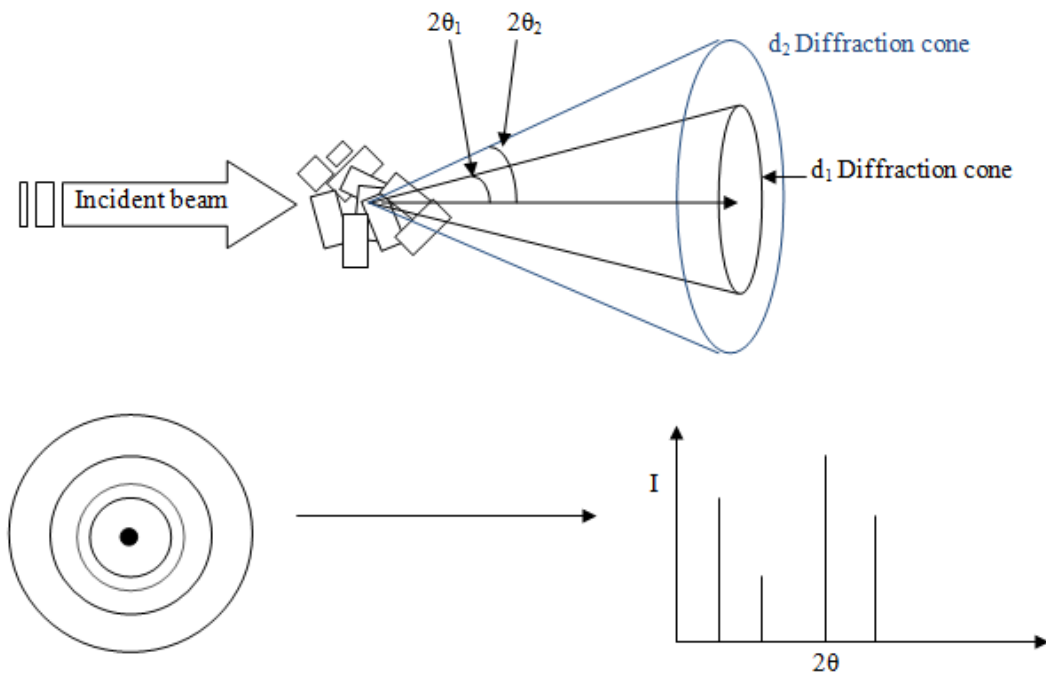


Figure 2.5: Graphical representation of powder diffraction and the origin of the Debye-Scherrer cones.

The cones can be recorded by the detectors of diffractometers, however a simple representation is a line which simply records the position and the intensity of the diffracted beam on a particular section of the cones. In an ideal powder crystallite distribution in the sample is isotropic; therefore the diffracted intensity on each recorded ring is homogeneous.

As a result the measurement of a random section of the diffraction cones is representative of the reflection intensities. If the orientation of the crystallites in the sample is not totally random, the pattern obtained will not be isotropic. If this is the case then the powder sample can be appropriately rotated so that each crystallite adopts many different orientations during data collection, resulting in a much more homogenous diffraction pattern [70].

Therefore sample preparation is highly important to the collection of high quality powder diffraction data. Other factor such as number of crystallites (amount of sample analysed) and preferred orientation can impact the quality of data recorded. The resultant diffractions pattern and the information contained, such as peak positions and intensities, allows for qualitative phase analysis using wide range of different structural databases available. Figure 2.6 shows the different features of powder diffraction pattern and the information that can be garnered from the technique.

Wavelengths used for diffraction experiments in this work are Cu $K\alpha = 1.5406 \text{ \AA}$ for laboratory sources and 0.82525 \AA for high resolution experiments.

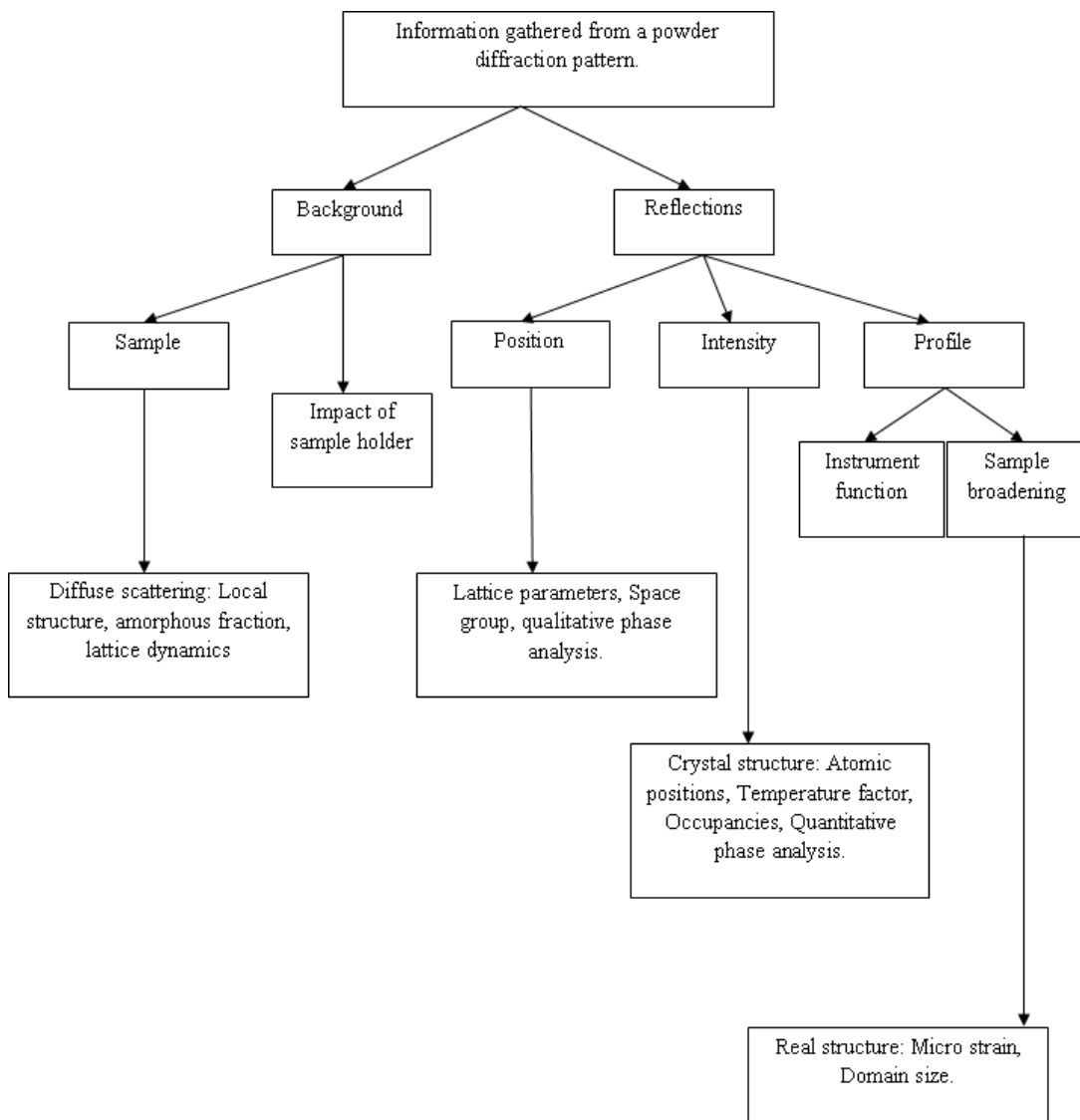


Figure 2.6: Flow chart showing the available information that can be gathered from an XRD powder diffraction pattern [70].

2.3 Rietveld refinement

Rietveld refinement [71-72] allows for the elucidation of an accurate crystal structure from powder diffraction data by using a “whole pattern fitting” method. The concept involves the calculation of a diffraction pattern using a selection of parameters which can be refined or fixed by the user. In order to start a Rietveld refinement a suitable model is required consisting of lattice parameters, space group, atomic positions and instrument parameters such as the wavelength used. The model is then used to calculate a pattern, with refinable of parameters used to minimise the difference between experimental and calculated patterns by a least-squares method, Equation 2.2.

$$S_y = \sum_j w_i (y_i - y_{ci})^2$$

Equation 2.2 Residual

Where S_y is the residual, the quantity minimised by the Rietveld refinement, w_i the weighting factor, y_i the observed intensity and y_{ci} and calculated intensities at the i^{th} step.

The calculated intensity can be described as follows in Equation 2.3 and is a sum of Bragg reflection in a specified range.

$$y_{ci} = S \sum_j L_{(hkl)} |F_{(hkl)}|^2 \phi_i(2\theta_i - 2\theta_k) P_{(hkl)} A + y_{bi}$$

Equation 2.3 Calculated intensity

Where;

S is the scale factor

$L_{(hkl)}$ is the Lorentz polarization factor

$F_{(hkl)}$ is the structure factor

Φ_i is the reflection profile function

$P_{(hkl)}$ is the preferred orientation function

A is the absorption factor

y_{bi} is the background intensity

An accurate description of peak shape (profile) is required for a successful refinement, with peak shapes observed resulting from a combination of factors. These factors are both sample related (defects, stress/strain effects and crystallite size) and instrumental (radiation, geometry slit size) which varies as a function of 2θ . Once a robust model has been derived and suitable starting points for background, scaling and profile have been achieved, refinement of structural parameters can be considered. Refinement of structural parameters is non-trivial, as such constraints and restraints can be applied to improve the stability of the structural fit and improve the fit quality. The measure of the agreement between experimental and calculated fit can be expressed using multiple function as described by equations 2.4 to 2.6

$$R_{wp} = \left\{ \frac{\sum_i w_i [y_i - y_{ci}]^2}{\sum_i w_i [y_i]^2} \right\}^{1/2}$$

Equation 2.4 Weighted profile value

$$R_{exp} = \left\{ \frac{(N - P)}{\sum_i^N w_i [y_i]^2} \right\}^{1/2}$$

Equation 2.5 R expected

$$\chi^2 = \left(\frac{R_{wp}}{R_{exp}} \right)^2$$

Equation 2.6 Goodness-of-fit

Where;

w is the weighting factor

y_i and y_{ci} are the observed and calculated intensities at the i^{th} step.

These factors provide an indication of the quality of the fit mathematically, however chemical sense must be applied to further confirm the quality of the fit achieved, this includes sensible values for bond lengths, bond angles and occupancies. All refinements shown in the work use the GSAS code implemented with the EXPGUI interface [73-74], however other Rietveld refinement tools are available.

2.4 X-ray Fluorescence Spectroscopy (XRF)

XRF is an analytical technique used to determine the chemical composition of a range of different materials both qualitatively and quantitatively. When a core electron is excited by an X-ray of sufficient energy a vacancy is left in the shell which can be filled by an electron from a higher level shell, as demonstrated in Figure 2.7.

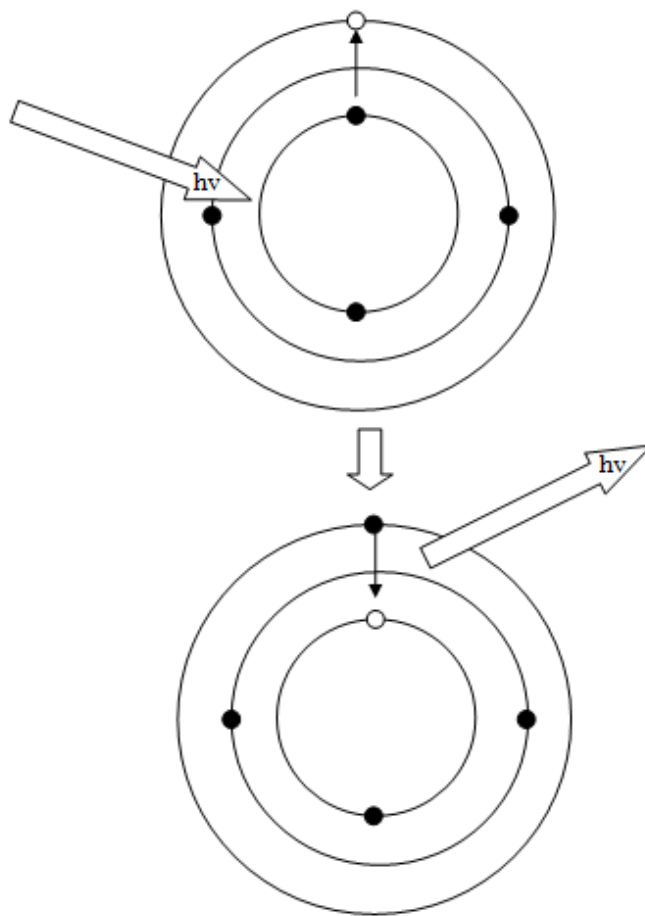


Figure 2.7: Graphical representation of the fundamental principles behind X-ray Fluorescence Spectroscopy (XRF).

The electron from the higher shell has higher energy and as a result the energy surplus is emitted as an X-ray photon, this is recorded in the XRF spectrum as a line. The energy levels

of each individual element vary so the radiation emitted is characteristic of that particular element, with the collection of lines considered a fingerprint of the elements analysed. The fluorescent yield is dependent on atomic number with the heavier the element the stronger intensity of the line recorded, as a result lighter elements can be more difficult to measure accurately [75].

Matrix effects also need to be considered as they have a direct impact on the measured intensities; this can be broken down into two contributing factors, the absorption and enhancement of the characteristic radiation produced. Both incoming and emitted X-rays must pass through the sample, the magnitude of absorption is dependant the energy of the radiation, the path length and sample density. Absorption increases with sample density and atomic number of atoms contained in the sample, as a result it is possible that in extreme examples emitted fluorescence is unable to leave the sample and only the surface is measured. Enhancement occurs when emitted fluorescence, called primary fluorescence, excites a second element in the sample resulting in secondary fluorescence. The impact of the matrix effect is sample dependant and the relationship between the contained elements and their characteristic fluorescence must be considered [75].

2.4.1 XRF geometry

Fluorescence can be measured in two different ways, WDXRF (wavelength dispersive) which separates the X-rays according to their wavelengths or EDXRF (energy dispersive) which directly measures the different energies of the emitted fluorescence X-rays from the sample. EDXRF can have two different geometries with optics in either a 2D or 3D configuration. 2D EDXRF is the simplest configuration, in which the sample is directly irradiated and the

resultant fluorescence measured by an energy dispersive detector. In this configuration scattered tube radiation can reach the detector resulting in a significant background and as a result low concentrations are difficult to determine. This can be improved by having a 3D optics in which the tube irradiates a secondary target which scatters the X-rays and irradiates the sample. The advantage of 3D EDXRF is that tube radiation cannot reach the detector allows for better determination of low concentrations due to significantly less background. WDXRF has a different detection system to EDXRF, samples are irradiated in a similar way to 2D EDXRF however the detection system consists of collimators, diffraction crystal and a detector. X-rays coming from the sample are diffracted by the crystal at different wavelengths and intensities measured by the detector. Sequential spectrometers measure the independent intensities one at a time and simultaneous spectrometers measure all in coming radiation at the same time [75]. Table 2.1 gives an overview of the differences between the different geometries.

Table 2.1: The comparisons between the two different types of XRF spectrometer

	EDXRF	WDXRF
Elemental range	Na- U	Be - U
Resolution	Poor for light elements Good for heavy elements	Good for light elements Reasonable for heavy elements
Sensitivity	Poor for light elements Good for heavy elements	Reasonable for light elements Good for heavy elements
Detection limit	Good for heavy elements	Good for all elements
Cost	Relatively inexpensive	Expensive
Detector	simultaneous	Sequential/simultaneous

All results shown in this work were collected using a WDXRF Bruker S8 Tiger and result analysis done using the packaged Bruker quantitative analysis software.

2.4.2 XRF sample preparation

There are 3 widely used methods of preparing samples for XRF analysis these are loose powder, pressed pellets and fused beads. The analysis of loose powder samples is done by placing the sample inside mylar film lined sample cup, this allows for the analysis of small sample amounts and sample recovery. However this introduces significant errors due to particle size and sample inhomogeneity. Mixing a sample with a binding material such as wax which is not detectable by XRF and pressing it into a pellet improves data quality. However errors are still introduced by sample inhomogeneity and grain size effects, so a better method is required to remove these errors.

Fused beads remove sample inhomogeneity and grain size effects due the vitrification of the sample allowing for more accurate XRF analysis. This is done by using a fluxing agent at a 10:1 flux to sample ratio and a high temperature treatment, to allow effective mixing of the sample and flux. This results in the reduction of matrix effects, relative to other sample preparations, due to the dilution of the sample. A wide range of different borate flux materials are available, with the 66:34 lithium tetraborate:metaborate mixed flux used for all samples in this study. All samples are treated at 1050 °C in a platinum/gold crucible with a releasing agent added, commonly iodides or bromides, to aid in the release of the glass bead [76-77].

2.4.3 Fused bead preparation

All samples were treated at 800 °C (12 hours with a 10 °C/min ramp rate) before fusion to remove any combustibles and water which can affect the quality of the bead produced. 0.35 g of the sample was well mixed with 3.5 g of 66:34 lithium tetraborate:metaborate flux and placed in a platinum/gold crucible. The crucible was heated to 1050 °C for ten minutes to

allow sufficient time for melt formation. Ammonium iodide releasing agent is added under rapid swirling to remove any bubbles in the melt, this was then heated for a further seven minutes. Any further bubbles were once again removed by swirling the crucible and the melt heated for a further two minutes. After cooling at room temperature the resultant bead is removed from the crucible and analysed by XRF.

2.5 TGA/DTA

Thermal gravimetric analysis (TGA) is an analytical technique which allows for the characterisation of a material by studying its thermal properties. Typically this involves analysing the variation of the sample mass over time, with a temperature gradient, in a controlled atmosphere. From this a range of physical and chemical information can be determined for the material, such as thermal stability, redox chemistry, reaction kinetics and moisture/volatile content as examples. A typical TGA consists of a highly sensitive precision balance inside a sealed heating stage which can be exposed to a range of different atmospheres. Commonly a TGA will be used in conjunction with other analysis tools, such as mass spectrometry, which can analyse any evolved products resulting from the thermal reactions of a material. This information can be correlated to a specific time and temperature allowing for greater understanding of sample breakdown, dehydration and the evolution of other volatiles. Differential thermal analysis can also be used to study further thermal changes in a material as a function of time and temperature. Changes in the material relative to an inert reference can give further information on the exothermic and endothermic processes occurring during sample heating. Information such as crystallisation, phase changes and melting point can be determined from the DTA curve.

In this work, all the experiments were undertaken on a NETZSCH STA 449F1 Jupiter (TGA) and NETZSCH 403 C (QM).

Chapter 3- Synthesis and Ion

Exchange of $K_2ZrGe_3O_9 \cdot H_2O$

3.1 Introduction

The study of mixed octahedral-tetrahedral materials tends to focus on the diversity of structures and variations in composition. The facile hydrothermal synthesis of these materials allows for chemical modification of these structures either by low level doping or isomorphous substitution of the metal octahedra. This is especially highlighted in the Umbite system, general formula $K_2MSi_3O_9 \cdot H_2O$, where M is a tetravalent metal cation. The formula for the mineral phase has zirconium located on the octahedral site however titanium substitution for zirconium does occur, this shows the flexibility of the material and as a result the interest in synthetic derivatives which contain different M^{4+} octahedra.

Very often a systematic approach is applied to synthesising novel silicate phases, this is highlighted by Lin *et al.* [78]. They reported the synthesis of four novel titanosilicates, designated AM-1 through 4, which were synthesised hydrothermally with only small variations in gel compositions and the same reaction conditions. Lin found that these AM materials were often present as impurity phases in the synthesis of previously known titanosilicates ETS-10, ETS-4 and synthetic nenadkevichite. AM-1 and AM-4 were novel titanosilicate materials where as AM-2 and AM-3 were synthetic analogues of umbite and penkvilksite respectively [78].

This was the first time a titanium pure derivative of umbite was reported and it started a trend towards the synthesis of umbite with differing octahedra. The synthesis of the mineral umbite phase was reported by Poojary *et al.* [79] and this was soon followed by a stannosilicate umbite, AV-6, reported by Lin *et al.* [80].

The interest in umbite is same as other octahedral–tetrahedral materials previously mentioned; high chemical and thermal stability and an extended pore system with exchangeable cations.

The structure itself consists of silicate polymeric chains which are connected by metal octahedra, resulting in a three-dimensional structure which contains of two distinct potassium environments. The first has a larger eight-membered ring pore opening and a potassium cation coordinated to the framework and a water molecule (M1). The second has a smaller eight-membered ring pore opening where potassium is bound only to the framework (M2), as shown in Figure 3.1 [79,81].

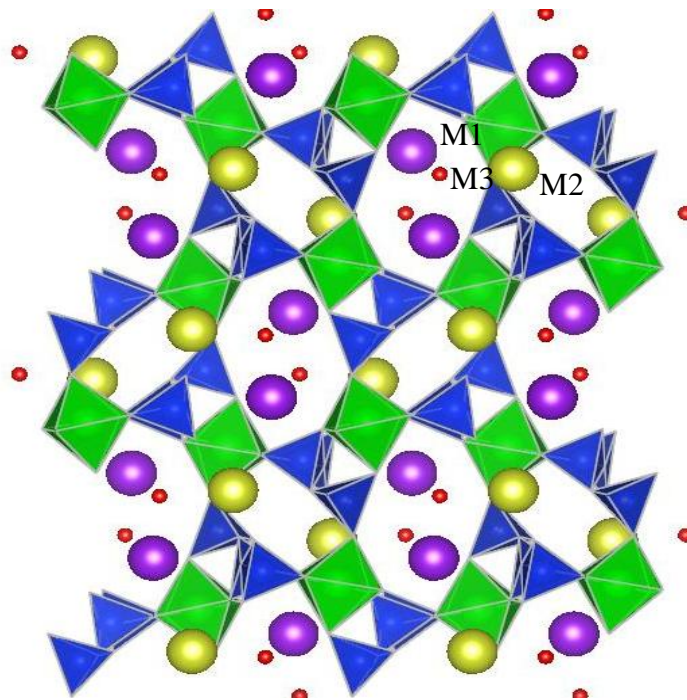


Figure 3.1: Crystal structure of the zirconosilicate umbite, Zr octahedra are shown in green and Si tetrahedra in blue. The two potassium cation sites are shown using two different colour spheres (M1 = purple and M2 = yellow) with the water oxygen shown by the smaller red spheres

The pore system of umbite has led to interest in any potential ion exchange properties; extensive studies by Poojary *et al.* shows synthetic umbite, $K_2ZrSi_3O_9 \cdot H_2O$, to be a good exchanger with respect to caesium [79]. The initial replacement of 50% of K^+ by Cs^+ increases to 75% after an additional exchange cycle. It was shown that Cs occupies two sites in the umbite structure, replacing potassium in the M2 cation site but also replacing a small

amount of the interapore water in site M1, designated M3. Further caesium exchange results in the cation site M2 being fully occupied by Cs^+ , with once again interapore water being replaced by Cs^+ , site M1 remains potassium rich as shown by Figure 3.2 [79].

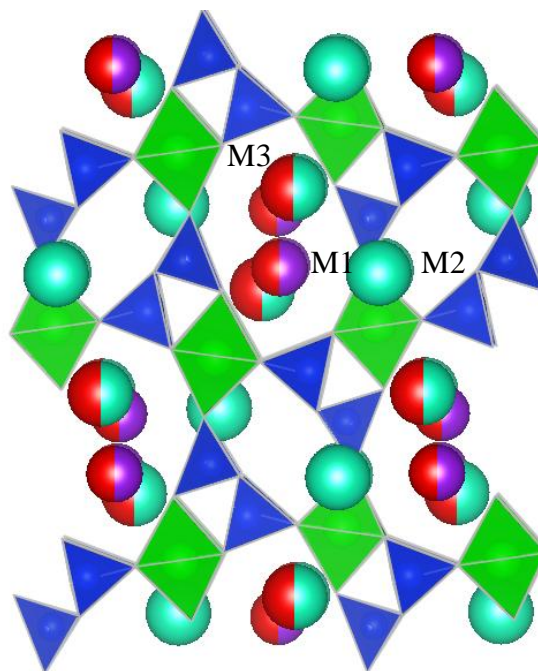


Figure 3.2: Cs-exchanged umbite where M2 site is fully occupied by Cs (Turquoise spheres). The mixed occupancy of M1/M3 is shown by the two tone spheres where water is shown in red, Cs in turquoise and potassium in purple.

The zirconosilicate umbite can also undergo facile sodium exchange with the complete replacement of K^+ by Na^+ . $\text{Na}_2\text{ZrSi}_3\text{O}_9 \cdot \text{H}_2\text{O}$ also exchanges with caesium to similar levels as the potassium form, albeit with greater selectivity [79].

Further work by Celestian *et al.* explored the exchange mechanism in umbite using in-situ X-ray diffraction studies, the monoclinic proton form ($\text{H}_{1.22}\text{K}_{0.78}\text{ZrSi}_3\text{O}_9 \cdot 2.16\text{H}_2\text{O}$), was used due to faster rate of uptake [82]. Potassium occupies cation site M2, whilst M1 is fully occupied by protons. A two step exchange process of the K^+ cations occurs to facilitate Cs^+ uptake, the first process involves Cs^+ occupying site M2 which displaces K^+ to site M1. This initial step is

slow and cation disorder at site M2 is the likely cause for the transition of the structure from monoclinic to orthorhombic space group which describes the umbite family. Caesium uptake then increases rapidly in the second step fully occupying site M2, with Cs^+ once again occupying site M3 and K^+ moving through the channel system to site M1. It is suggested by the author that multi step ion exchange is fundamental to the properties umbite and other microporous three-dimensional materials [82].

The thermal conversion of synthetic umbite is into a potential ceramic wastefrom type phase after ion exchange is also of interest. Poojary *et al.* reported the conversion of synthetic umbite to a wadeite type phase at elevated temperatures [79]. The rare natural mineral wadeite ($\text{K}_2\text{ZrSi}_3\text{O}_9$) is a hexagonal cyclosilicate with a framework composed of three membered (Si_3O_9) rings of (SiO_4) tetrahedra and isolated (ZrO_6) octahedra, with K^+ ions located in the cavities, Figure 3.3 [83-84].

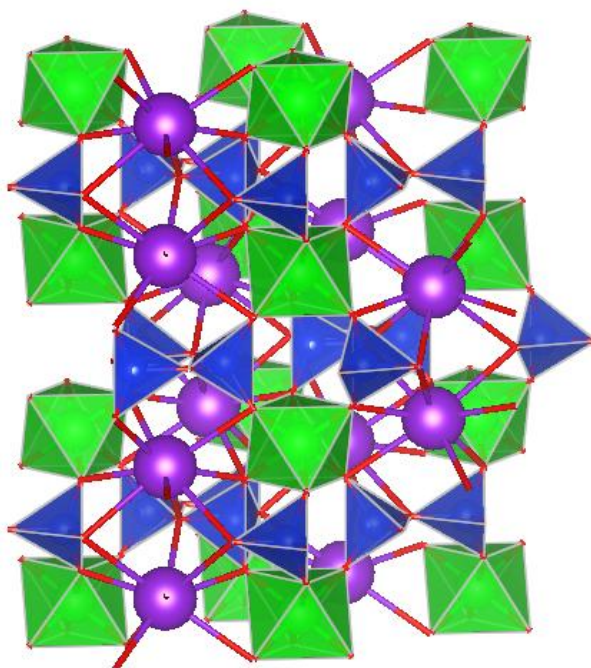


Figure 3.3: Wadeite structure where Si tetrahedra are shown in blue, Zr octahedra in green and the encapsulated potassium shown by purple spheres bound to the framework.

The $\text{Cs}_2\text{ZrSi}_3\text{O}_9$ wadeite type phase has been investigated as a potential wasteform, with the aqueous durability shown to vary depending on pH. Leachability studies have shown that at neutral pH aqueous durability of this material is very high however at higher pH dissolution of the silicate network occurs resulting in caesium release. The channel openings are smaller than a caesium cation and as a result this prevents the release of Cs^+ in aqueous environments [85]. The umbite system has been shown to be a capable ion exchange material but through thermal conversion a robust wasteform.

The aim of this chapter is to further explore umbite synthesis with the hope of accessing a wider range of umbite materials with germanium substitution for which the ion exchange properties can be explored. The reason for substitution of germanium at the tetrahedral site have already been discussed, germanium containing umbite phases have been explored by Plevert *et al.* In this work a range of organocation containing materials were synthesised alongside $\text{K}_2\text{ZrGe}_3\text{O}_9 \cdot \text{H}_2\text{O}$ as reference material. The $\text{K}_2\text{ZrGe}_3\text{O}_9 \cdot \text{H}_2\text{O}$ material is structurally analogous to the silicate phase reported by Poojary *et al.* and it is also reported to undergo the same transformation at elevated temperatures. The exploration of ion exchange properties of the zirconogermanate umbite is limited; it is reported to be able to exchange sodium for potassium whereas the organocation derivatives do not ion exchange [86].

In this chapter, we initially focus on the synthesis of mixed Si/Ge phases and moves onto the optimisation of the synthesis of germanium pure umbite. Ion exchange properties and thermal conversion of this material are also examined.

3.2 Experimental

3.2.1 Synthesis of $K_2ZrSi_{3-x}Ge_xO_9 \cdot H_2O$

Typical synthesis for $x = 0.75$

The mixed silicon/germanium umbite was prepared by mixing 0.435 g of germanium dioxide (Gerald wise and co), 0.75 g of fumed silica (Aldrich) and 3.75 g of potassium hydroxide (85%, Sigma) in 10.5 ml of deionised water. To the stirring mixture 1.66 g of zirconyl chloride octahydrate (98%, Sigma) was added until dissolved. The mixture is then stirred for a further hour to allow it to homogenise.

The resulting mixture was then transferred to a 45 ml Teflon liner and placed in a Parr autoclave at 200 °C for 5 days. The resulting product was then filtered and washed in deionised water before being dried overnight at 60 °C.

3.2.2 Synthesis of $K_2ZrGe_3O_9 \cdot H_2O$

The zirconogermanate umbite was prepared by mixing 1.52 g of germanium dioxide (Gerald wise and co) and 1.66 g of potassium hydroxide (85%, Sigma) in 20 ml of deionised water. To the stirring mixture 1.50 g of zirconyl chloride octahydrate (98%, Sigma) was added until dissolved. The mixture is then stirred for a further hour to allow it to homogenise.

The resulting mixture was then transferred to a 45 ml Teflon liner and placed in a Parr autoclave at 200 °C for 24 hours. The resulting product was then filtered and washed in deionised water before being dried overnight at 60 °C.

All compounds synthesised were analysed using Powder X-ray diffraction (XRD) on a Bruker D8 Advance using a Cu K α source at room temperature. Phase matching was performed using the EVA software from known databases.

Table 3.1: Synthesis optimisation of the umbite synthesis

	KOH (g)	GeO ₂ (g)	ZrOCl ₂ .8H ₂ O (g)	H ₂ O(ml)	Time(days)
1	0.26	0.2	0.19	10	7
2	0.26	0.2	0.18	10	5
3	0.44	0.38	0.38	20	5
4	0.44	0.38	0.38	10	6
5	0.43	0.38	0.38	10	3
6	0.43	0.38	0.38	10	2
7	0.43	0.38	0.38	10	1
8	0.43	0.38	0.38	5	1
9	0.88	0.77	0.78	10	1
10	1.69	1.52	1.53	20	1

3.2.3 Ion exchange studies

0.1 M solutions of strontium nitrate (98%, Alfa Aesar) or caesium nitrate (99.8%, Alfa Aesar) were added to 0.2-0.5 g of sample with an overall w/v ratio of 1:100. This was then shaken for 24 hours before being filtered, washed and dried overnight at 60 °C. Elemental analysis was undertaken using X-ray fluorescence (XRF) on a Bruker S8 Tiger with the samples prepared as either a loose powder, pressed pellet or fused bead.

3.2.4 Proton exchange

200 ml of 0.1M solution of acetic acid (Glacial, Fisher) was added to 2 g of sample with an overall w/v ratio of 1:100. This was then stirred for 24 hours to keep sample agitated before being filtered, washed with copious amounts of deionised water and dried overnight at 60 °C. Elemental analysis was undertaken using X-ray fluorescence (XRF) on a Bruker S8 Tiger with the samples prepared as either a loose powder, pressed pellet or fused bead.

3.2.5 NaCl reflux

100 ml of 1 M solution of sodium chloride (98%, Sigma) was added to 1 g of sample with an overall w/v ratio of 1:100. This was then refluxed for 24 hours before being left to cool, filtered, washed with copious amounts of deionised water and dried overnight at 60 °C. Elemental analysis was undertaken using X-ray fluorescence (XRF) on a Bruker S8 Tiger with the samples prepared as either a loose powder, pressed pellet or fused bead.

3.3 Results and discussion

3.3.1 Mixed Silicon/Germanium umbite systems

The synthesis of mixed silicon/germanium umbite materials was initially attempted by replacing SiO_2 with GeO_2 during synthesis. With the facile variation of the metal octahedra it was hoped that a range of mixed Si/Ge materials could be synthesised, with the variation in unit cell due to the larger germanium cation (Si 0.26 Å vs Ge 0.39Å, Shannon radii) varying ion exchange properties relative to the zirconosilicate umbite phase.

This would hopefully introduce some degree of compositional control, allowing us to tune Cs^+ uptake or selectivity by variation of the stoichiometry, providing our hypothesis is correct. Figure 3.4 shows the high-resolution powder diffraction pattern for the attempted replacement of Si by 25% Ge, the result was the target umbite phase and an impurity phase, $\text{K}_2\text{ZrGe}_2\text{O}_7$.

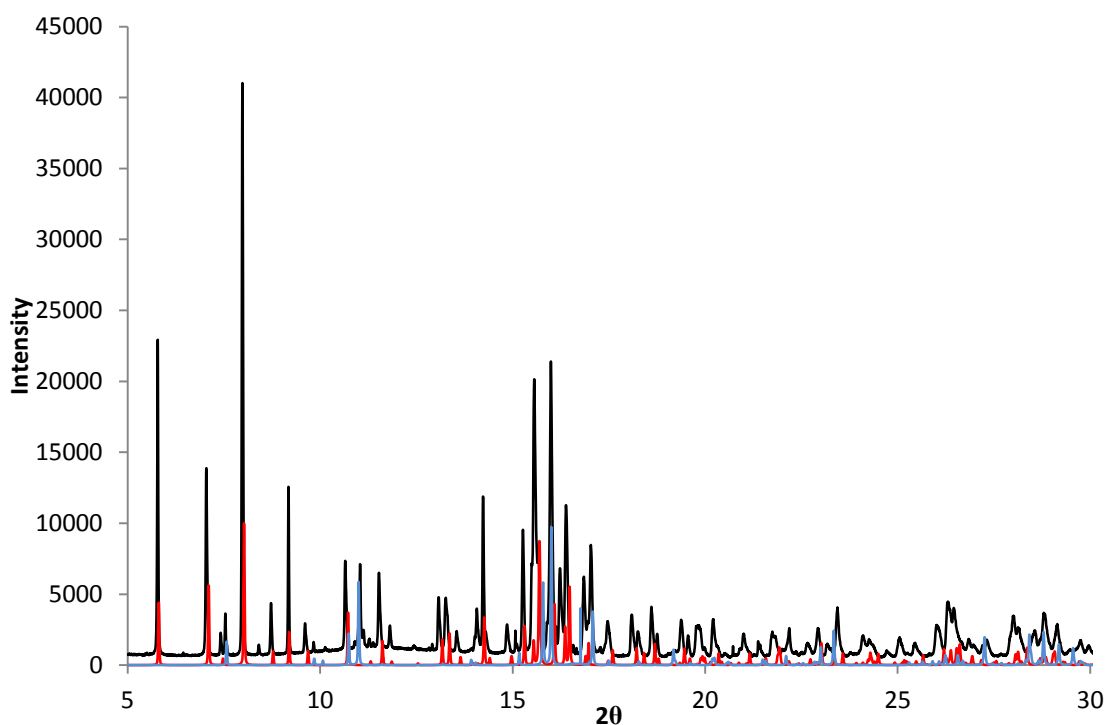


Figure 3.4: X-ray diffraction pattern ($\lambda = 0.82525 \text{ \AA}$) for the attempted replacement of Si by 25% Ge. Reference patterns for $\text{K}_2\text{ZrSi}_3\text{O}_9 \cdot \text{H}_2\text{O}$ (Red) and $\text{K}_2\text{ZrGe}_2\text{O}_7$ (Blue) have been added for comparison.

The impurity is part of an extended K-Zr-Ge-O phase map as described by Ilyushin *et al.*[87]. From this it is possible to infer that the addition of germanium to the reaction mixture is enough to cause a secondary reaction to occur resulting in the $\text{K}_2\text{ZrGe}_2\text{O}_7$ phase. An inhomogeneous distribution of GeO_2 in the starting gel, which could be the result of the poor solubility of GeO_2 , would explain this side reaction as it would result in germanium rich areas and the formation of $\text{K}_2\text{ZrGe}_2\text{O}_7$. The formation of the $\text{K}_2\text{ZrGe}_2\text{O}_7$ impurity phase is also observed when replacing Si by 50% Ge as shown by Figure 3.5.

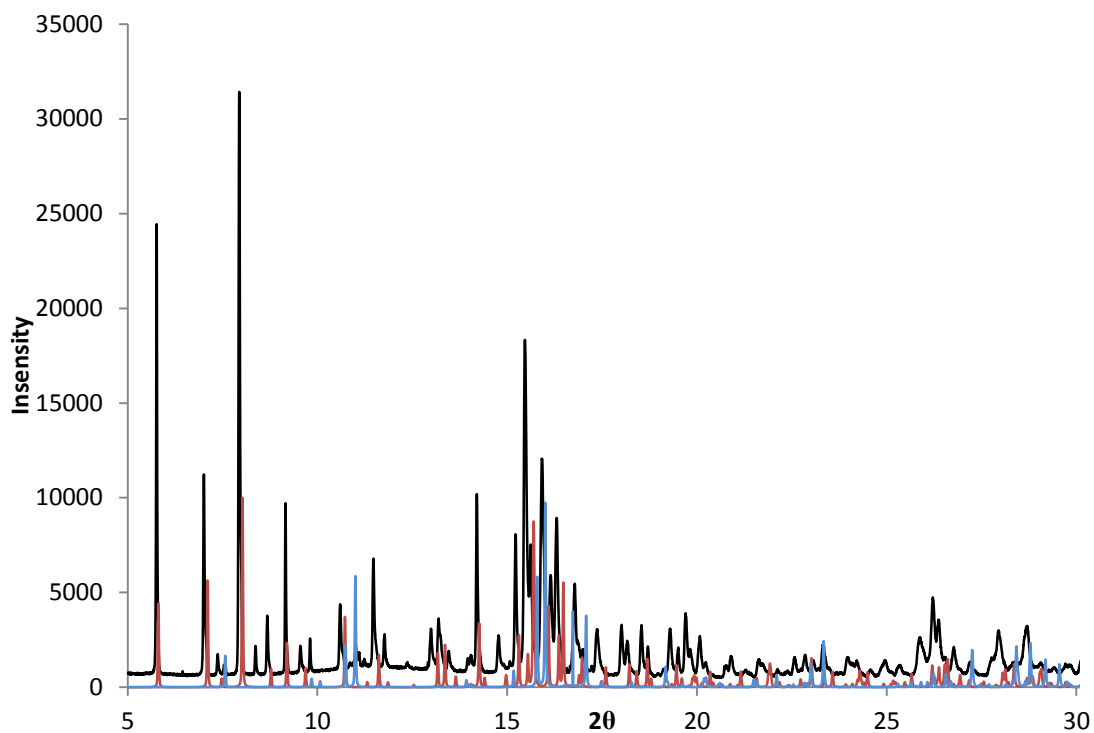


Figure 3.5: X-ray diffraction pattern ($\lambda = 0.82525 \text{ \AA}$) for the attempted replacement of Si by 50% Ge. Reference patterns for $\text{K}_2\text{ZrSi}_3\text{O}_9 \cdot \text{H}_2\text{O}$ (Red) and $\text{K}_2\text{ZrGe}_2\text{O}_7$ (Blue) have been added for comparison.

A minimal shift from the reference umbite pattern can be observed in Figure 3.5, which could suggest a small amount of germanium doping into the silicate umbite however germanium would appear to preferentially form $\text{K}_2\text{ZrGe}_2\text{O}_7$. The replacement of Si by 75% Ge was attempted, however this once again proved to be unsuccessful with the same impurity phase formed alongside an umbite phase, as shown by Figure 3.6.

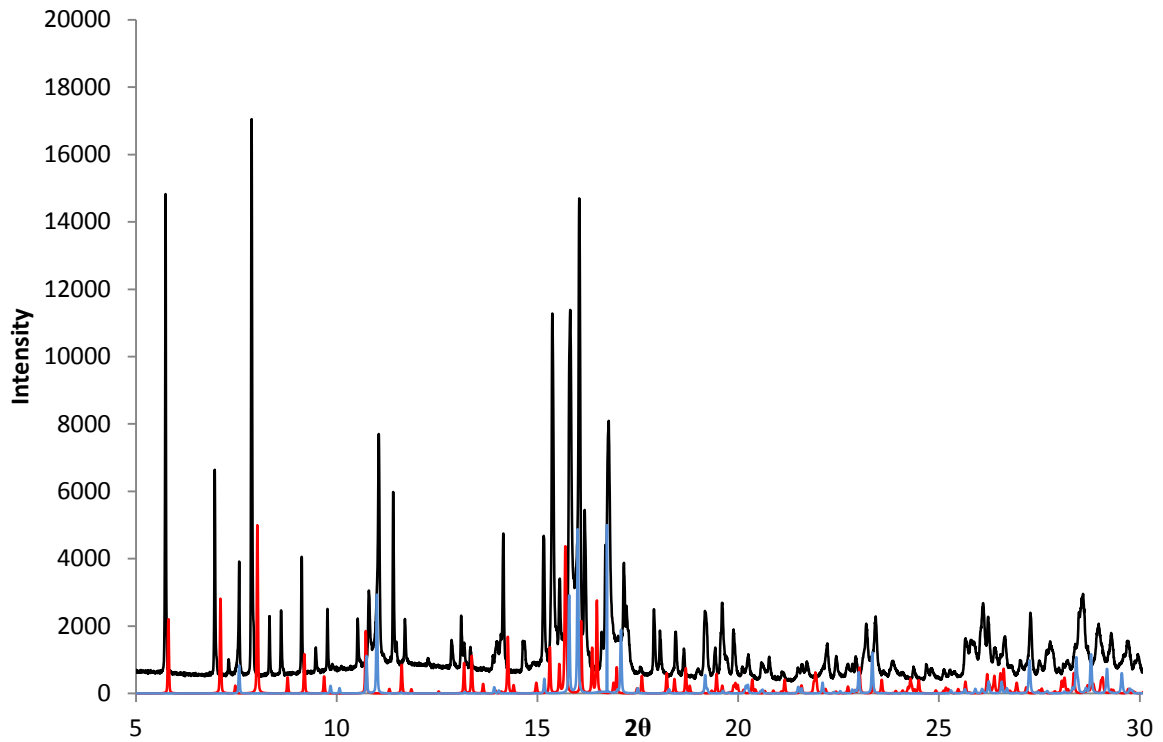


Figure 3.6: X-ray diffraction pattern ($\lambda = 0.82525 \text{ \AA}$) for the attempted replacement of Si by 75% Ge. Reference patterns for $\text{K}_2\text{ZrSi}_3\text{O}_9 \cdot \text{H}_2\text{O}$ (Red) and $\text{K}_2\text{ZrGe}_2\text{O}_7$ (Blue) have been added for comparison.

The impurity phase, $\text{K}_2\text{ZrGe}_2\text{O}_7$, is also the product when SiO_2 is fully replaced by GeO_2 when synthesising umbite using the methodology outlined in Section 3.2.1. Figure 3.7 shows the resultant diffraction pattern in which no umbite phase is present.

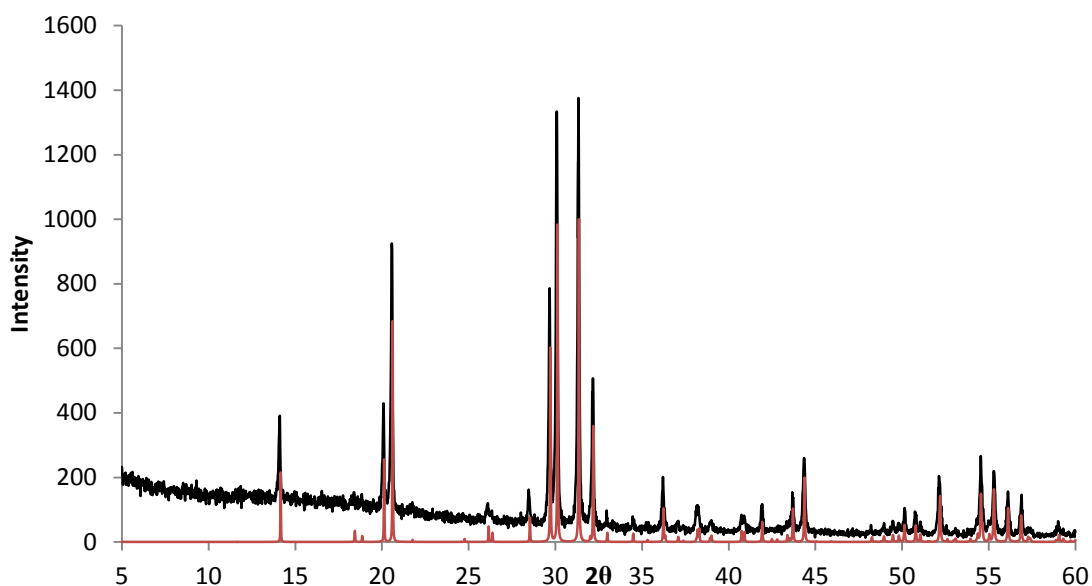


Figure 3.7: X-ray diffraction pattern ($\lambda = 1.5406 \text{ \AA}$) of the $\text{K}_2\text{ZrGe}_2\text{O}_7$ phase confirmed using Bruker phase matching software, as shown by calculated diffraction pattern (Red).

$\text{K}_2\text{ZrGe}_2\text{O}_7$ itself has been investigated for ion exchange by Clearfield *et al.*, it has a three-dimensional lattice of ZrO_6 and GeO_4 layers connected by germanate linkers resulting in a condensed structure. Exchange for potassium in the structure was shown to be minimal as the cation is strongly held inside of a narrow channel system and as a result was of no interest for further study [88]. The reported synthesis for this phase is very similar to that of umbite, interestingly the more condensed phase forms at lower temperature at $180 \text{ }^\circ\text{C}$ than umbite at $200 \text{ }^\circ\text{C}$. This would suggest that the $\text{K}_2\text{ZrGe}_2\text{O}_7$ phase may form first and as a result prevent the formation of umbite as shown by Figure 3.7.

Determining the actual germanium content of the above mixed umbite phases would prove to be very difficult due to the different phases present and the potential substitution into the impurity phases. Due to the mixed Ge/Si umbite phases not being pure, no ion exchange properties were determined for the different germanium doping levels, due to the potential

impact the impurity phases may have on the uptake by the umbite material. The unsuccessful doping of germanium into the zirconosilicate umbite meant the focus was shifted to the synthesis $K_2ZrGe_3O_9 \cdot H_2O$ phase and potential silicon doping into this material.

3.3.2 Synthesis and optimisation of $K_2ZrGe_3O_9 \cdot H_2O$

As discussed in Section 3.1, Plevert *et al.* reported the synthesis of $K_2ZrGe_3O_9 \cdot H_2O$ [86], however the synthesis time of four days and the small yield of sample would have been insufficient for further work. This synthesis was successfully repeated and would act as basis for further synthesis scale up, the result being a highly crystalline $K_2ZrGe_3O_9 \cdot H_2O$ phase. The reduction of the water content from that of the literature synthesis allowed for the maximisation of fill in the Parr autoclaves used and as a result an increase in yield, with the synthesis time reduced down to 24 hours to maximise sample output. Figure 3.8 shows the diffraction patterns for the first attempted seven day synthesis of the material and the optimised 24 hour synthesis.

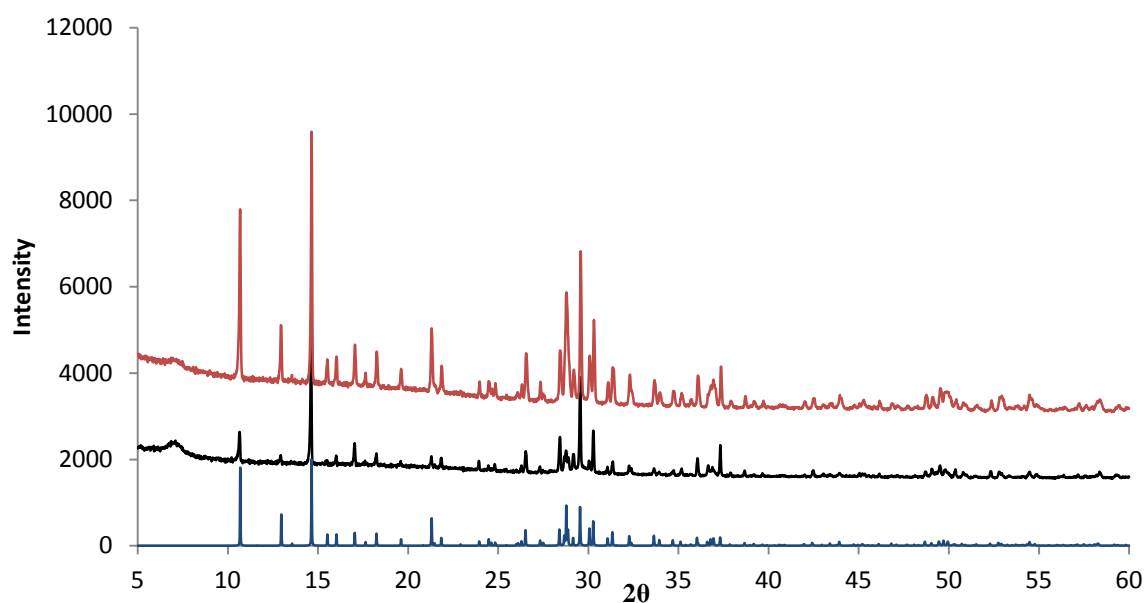


Figure 3.8: Comparison between the diffraction patterns ($\lambda = 1.5406 \text{ \AA}$) for the seven day (Black) and one day optimised synthesis (Red) of $\text{K}_2\text{ZrGe}_3\text{O}_9 \cdot \text{H}_2\text{O}$, umbite reference pattern (Blue) shown for comparison.

Table 3.1 summarises the composition variations used to optimise the synthesis in experimental Section 3.2.2. Rietveld refinement of the $\text{K}_2\text{ZrGe}_3\text{O}_9 \cdot \text{H}_2\text{O}$ phase confirms the work of Plevrt *et al.*, with it crystallising in an orthorhombic space group, $P2_12_12_1$, Figure 3.9. Restraints were applied to Ge-O and Zr-O bonds of 1.74 \AA and 2.07 \AA respectively, calculated from the sum of the ionic radii.

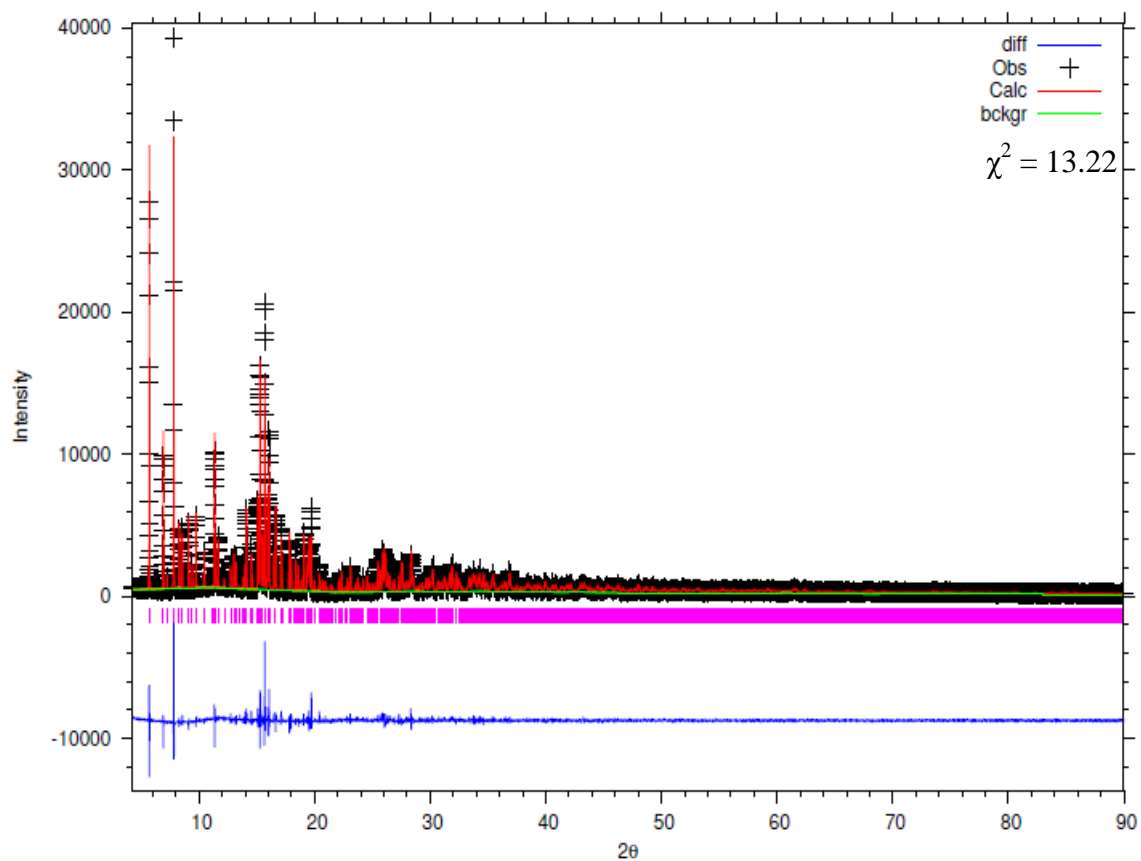


Figure 3.9: Rietveld refinement for the parent $K_2ZrGe_3O_9 \cdot H_2O$ phase.

Table 3.2: Lattice parameters, atomic positions, occupancy and thermal parameters for the refinement of $\text{K}_2\text{ZrGe}_3\text{O}_9 \cdot \text{H}_2\text{O}$. Thermal parameters are grouped by element.

$\lambda/\text{\AA}$	0.82525				
$a/\text{\AA}$	10.3898(1)				
$b/\text{\AA}$	13.6479(1)				
$c/\text{\AA}$	7.4254(1)				
$V/\text{\AA}^3$	1053.92(2)				
<i>Space Group</i>	$P2_12_12_1$				
R_{wp}	0.1079				
R_{exp}	0.0297				
χ^2	13.22				
<i>Site</i>	<i>x</i>	<i>y</i>	<i>z</i>	<i>Occupancy</i>	U_{iso}
Zr1	0.4564(2)	0.2095(1)	0.2649(3)	1	0.0070(5)
Ge1	0.1878(2)	0.1715(2)	-0.0099(3)	1	0.0019(3)
Ge2	0.0315(2)	0.0450(1)	0.7256(3)	1	0.0019(3)
Ge3	0.6365(2)	0.3380(2)	0.5972(3)	1	0.0019(3)
O1	0.4179(9)	0.3637(6)	0.2377(18)	1	0.0109(13)
O2	0.3396(9)	0.1869(10)	0.0348(14)	1	0.0109(13)
O3	0.5285(10)	0.0674(6)	0.2835(16)	1	0.0109(13)
O4	0.5513(12)	0.2398(7)	0.5039(15)	1	0.0109(13)
O5	0.6315(10)	0.2230(8)	0.1139(15)	1	0.0109(13)
O6	0.3001(10)	0.1849(10)	0.4359(13)	1	0.0109(13)
O7	0.0867(10)	0.1438(8)	0.1769(13)	1	0.0109(13)
O8	0.0812(11)	0.0544(8)	0.4992(14)	1	0.0109(13)
O9	0.1732(10)	0.0696(8)	0.8466(15)	1	0.0109(13)
K1	0.2166(5)	0.6270(3)	0.1232(6)	1	0.0201(11)
K2	0.4403(4)	0.0812(3)	0.7087(7)	1	0.0201(11)
O10	0.6915(12)	0.0642(8)	0.8765(16)	1	0.0109(13)

Table 3.3: Selected bond lengths from the refinement of $K_2ZrGe_3O_9 \cdot H_2O$.

<i>Bond</i>	<i>Distance (Å)</i>		<i>Bond</i>	<i>Distance (Å)</i>
Ge1-O2	1.63(2)		Zr-O1	2.15(2)
Ge1-O5	1.73(1)		Zr-O2	2.12(1)
Ge1-O7	1.78(1)		Zr-O3	2.08(2)
Ge1-O9	1.76(1)		Zr-O4	2.07(1)
			Zr-O5	2.15(2)
Ge2-O1	1.74(1)		Zr-O6	2.09(1)
Ge2-O3	1.71(1)			
Ge2-O8	1.76(1)		Av K1-O	3.14
Ge2-O9	1.76(1)			
			Av K2-O	2.994
Ge3-O4	1.75(1)			
Ge3-O6	1.75(2)			
Ge3-O7	1.77(1)			
Ge3-O8	1.73(1)			

The starting point for the refinement was a modified Clearfield zirconosilicate umbite model, replacing the three silicon environments with germanium and using the unit cell parameters derived by Plevert *et al.* as a starting point. Due to the highly crystallinity of the sample, discrepancies between the simulated and experimental intensities are evident. There is potentially a small amount of peak splitting, which is evident at higher 2θ as shown in Figure 3.10. This splitting is only very subtle and is not modelled when using an orthorhombic $P2_12_12_1$ space group.

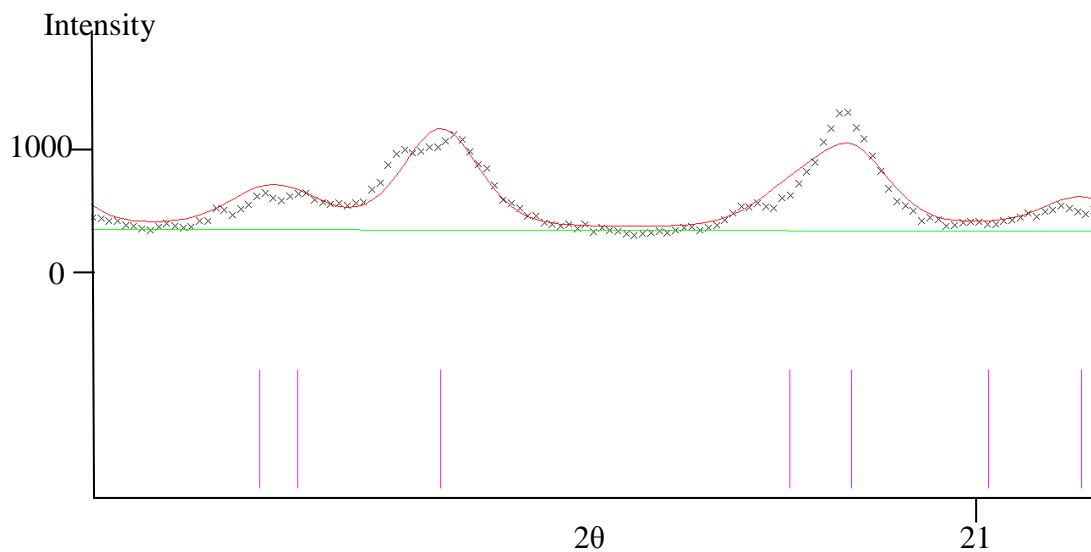


Figure 3.10: Expanded view showing the peak splitting evident in the refinement of $\text{K}_2\text{ZrGe}_3\text{O}_9 \cdot \text{H}_2\text{O}$

This would suggest that we have a reduction in symmetry albeit with only a small variation from the parent orthorhombic cell, however attempts to fit to a modified version of the related monoclinic *Celestian et al.* proton form resulted in a poor quality of fit. As the orthorhombic cell provides the best fit to the parent zirconogermanate umbite phase, it was decided to continue with the $P2_12_12_1$ cell with work deriving a new model to better fit the experimental data ongoing.

With the successful synthesis of $\text{K}_2\text{ZrGe}_3\text{O}_9 \cdot \text{H}_2\text{O}$, Si doping to access mixed phases was again attempted however this resulted in an amorphous phase being formed. From this we can determine that the synthesis of a mixed phase from either end member is not possible by the addition of silica or germanium dioxide into the reaction mixture. A possible reason for inability to vary the tetrahedral cation is the differences in synthesis composition; the germanium containing synthesis is much more dilute than the silicon equivalent as shown in Table 3.4 and as a result relative solubility may have large role in dictating the successfulness of doping.

Table 3.4: Relative compositions for the Si and Ge umbite synthesis normalised to zirconium.

	K	Si	Ge	Zr	H ₂ O
K ₂ ZrSi ₃ O ₉ .H ₂ O	12.97	3.22	-	1	113
K ₂ ZrGe ₃ O ₉ .H ₂ O	6.27	-	3.07	1	235

As the synthesis of the germanate parent material, K₂ZrGe₃O₉.H₂O, had been optimized and with the ion exchange properties only briefly covered by Plevert *et al.* it was decided to further study the ion exchange properties of this material.

3.3.3 Ion exchange

In order to further understand the ion exchange properties of zirconogermanate umbite it was decided to test the material against a range of alkali and alkali earth cations. All exchanges were done in bulk with a large excess and enough time was allowed for the exchanges to reach equilibrium, this would determine the maximum uptake of the material. Initial ion exchanges focused on Cs⁺ with analysis performed using XRF and it was discovered that the uptake of these cations was very poor, as shown in Table 3.5.

Table 3.5: Fused bead XRF data for the parent and Cs-exchanged phases, molar ratios are normalised to germanium.

	Parent molar ratios	Cs exchange molar ratios
K	0.71	0.68
Ge	1	1
Zr	0.41	0.41
Cs	-	0.02

Zirconogermanate umbite shows negligible levels of Cs⁺ uptake especially when considering the ability of the zirconosilicate to ion exchange, in this case it appears as if increasing the unit cell volume has subsequently reduced cation uptake. Further exchanges using Mg²⁺, Ca²⁺, Sr²⁺ and Na⁺ showed the same trend with once again negligible calcium and strontium uptake and no sodium and magnesium uptake, Table 3.6.

Table 3.6: Loose powder XRF data for Na, Mg, Ca and Sr-exchange, molar ratios are normalised to germanium.

Elements	Na Ex molar ratio	Mg Ex molar ratio	Ca Ex molar ratio	Sr Ex molar ratio
K	0.57	0.63	0.67	0.54
Ge	1	1	1	1
Zr	0.51	0.42	0.43	0.48
Na	0	-	-	-
Mg	-	0	-	-
Ca	-	-	0.006	-
Sr	-	-	-	0.008

The differences observed for the molar ratios in Table 3.6 are symptomatic of using loose powder preparations when analysing by XRF and should be considered more qualitatively. As a result the values in Table 3.6 cannot be compared to the results shown in Table 3.5, however what is evident is the ion exchange properties are incredibly poor regardless.

Assuming a similar exchange process to that suggested by Celestian *et al.* [82], the rate limiting step is removal of potassium from site M2. If potassium is too tightly bound to the framework during this initial step then it would be unfavourable for caesium to replace potassium, this would prevent Cs^+ diffusing into the structure and occupying the second cation site. This could also explain the poor divalent exchange with it being even less favourable to remove two monovalent cations for each divalent cation.

3.3.4 Reitveld refinements of Cs-exchanged parent umbite

As previously described in Section 3.3.3 the reported caesium uptake of this material from XRF is incredibly low. Synchrotron XRD data was used to further analyse the caesium uptake hopefully confirming what was observed using XRF. As described by Poojary *et al.*, caesium occupies a different position in the channel to potassium and this would likely provide the best starting model for the caesium exchanged parent phase assuming similar behaviour. However it was decided to try both the caesium exchanged umbite and unexchanged umbite as starting points, the differences in cation sites are summarised in Table 3.7.

Table 3.7: Exchange site atoms and occupancies for the unexchanged and exchanged zirconosilicate umbite

Cation Sites	$K_2ZrSi_3O_9 \cdot H_2O$	$Cs_{1.1}K_{0.9}ZrSi_3O_9 \cdot H_2O$
Exchange site 1	K1 = 1 O10 = 1	K1 = 0.7 O10 = 0.3
Exchange site 2	K2 = 1	K2 = 0.2 Cs1 = 0.8
Exchange site 3	-	O11 = 0.7 Cs2 = 0.3

Reitveld refinement of high-resolution powder diffraction data ($\lambda = 0.82525 \text{ \AA}$), using the Poojary exchanged model as a starting point, gave a poor fit relative to the parent as seen in Figure 3.11. Restraints were applied to Ge-O and Zr-O bonds of 1.74 \AA and 2.07 \AA respectively. Cation occupancies were refined under constraints, with the total occupancy for each cation site constrained to one.

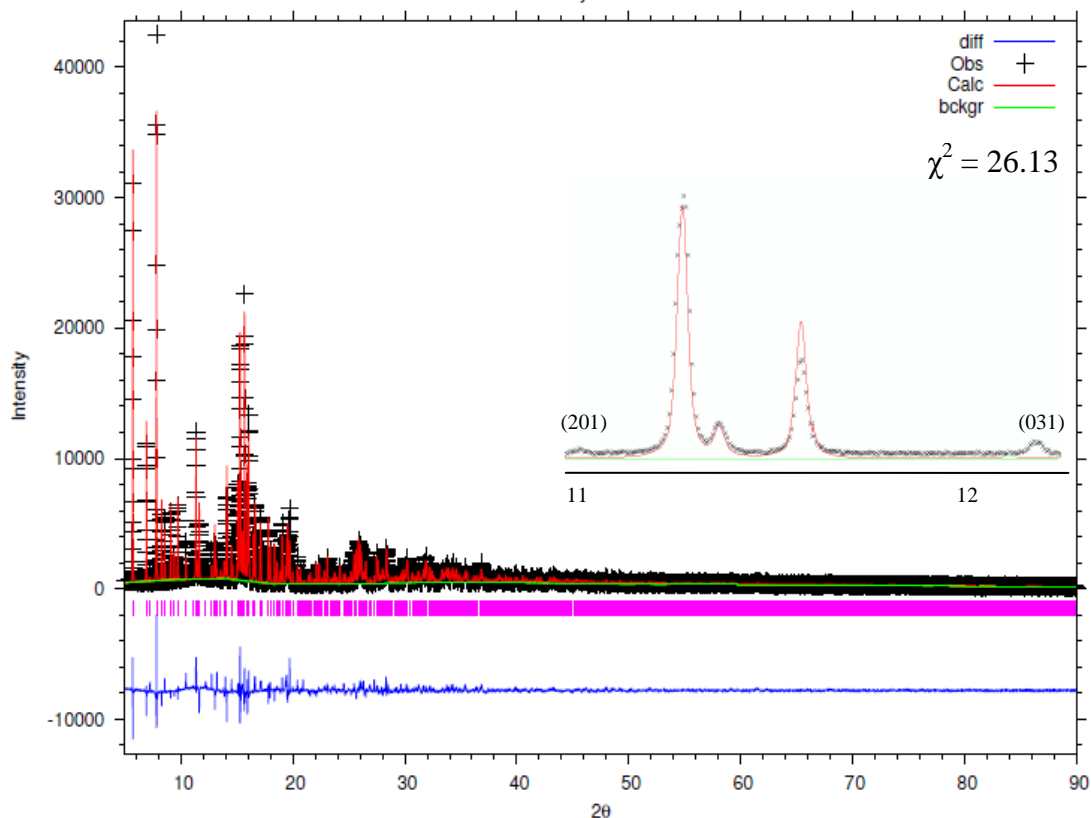


Figure 3.11: Rietveld refinement for the Cs-exchanged zirconogermanate umbite phase. Insert shows the poor fitting of the low intensity peaks when using the Poojary Cs-exchanged zirconosilicate umbite model.

This relatively poor fit is reflected by a high χ^2 value of 26.13 for this refinement using the exchanged model. The refinement was unstable, especially when refining occupancies for the cation sites, with the model over calculating the amount of caesium present as approximately 0.2 caesiums per unit cell. This model is also unable to fit to the lower intensity peaks such as the (201) and (031) as shown in Figure 3.11. As this model was derived from a caesium rich phase, it is possible that it will only accurately fit phases which are substantially more caesium rich than the zirconogermanate umbite, hence the over calculation of the caesium content, from the refinement.

The exchange umbite phase is much more closely related to the unexchanged sample and this is reflected in the quality of the refinement. Using the unexchanged model, assuming caesium

occupies the same site as potassium instead of a separate site, gives a much more representative caesium content which is in better agreement with the XRF data. It also provides a much better fit for the low intensity phases mentioned previously, as shown in Figure 3.12. This is reflected by a χ^2 value of 9.55, which is substantially lower than calculated for the refinement in Figure 3.11. Restraints were applied to Ge-O and Zr-O bonds of 1.74 Å and 2.07 Å respectively. Cation occupancies were refined under constraints, with the total occupancy for each cation site constrained to one.

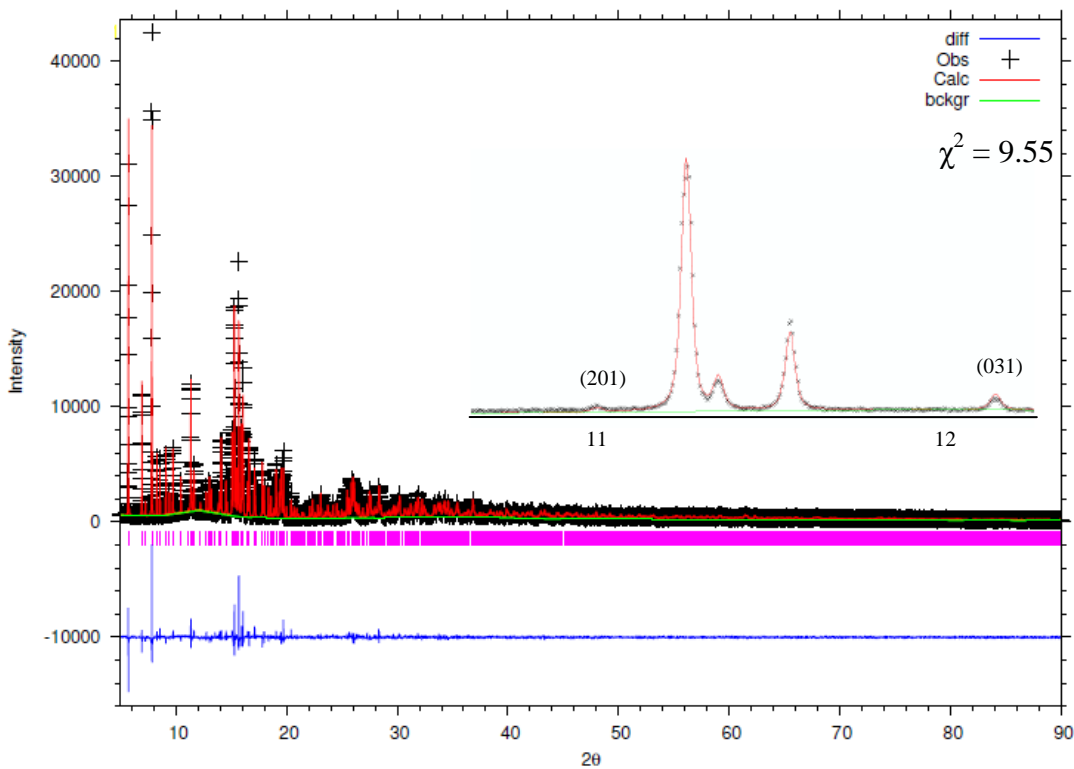


Figure 3.12: Rietveld refinement for the Cs-exchanged zirconogermanate umbite phase. Insert shows peak fitting for low intensity peaks when using the parent zirconosilicate umbite as the starting model.

Table 3.8: Lattice parameters, atomic positions, occupancy and thermal parameters for the refinement of Cs-exchanged K₂ZrGe₃O₉.H₂O. Thermal parameters are grouped by element and cation site.

$\lambda / \text{\AA}$	0.82525				
$a / \text{\AA}$	10.4001(1)				
$b / \text{\AA}$	13.6517(1)				
$c / \text{\AA}$	7.4302(1)				
$V / \text{\AA}^3$	1055.00(2)				
<i>Space Group</i>	$P2_12_12_1$				
R_{wp}	0.0870				
R_{exp}	0.0282				
χ^2	9.55				
Site	x	y	z	Occupancy	U_{iso}
Zr1	0.4565(2)	0.2095(1)	0.2652(2)	1	0.0059(4)
Ge1	0.1872(2)	0.1718(2)	-0.0080(3)	1	0.0022(2)
Ge2	0.0315(2)	0.0455(1)	0.7254(3)	1	0.0022(2)
Ge3	0.6357(2)	0.3377(2)	0.5969(3)	1	0.0022(2)
O1	0.4179(9)	0.3637(6)	0.2377(16)	1	0.0080(11)
O2	0.3408(9)	0.1836(6)	0.0351(13)	1	0.0080(11)
O3	0.5341(9)	0.0642(6)	0.2767(15)	1	0.0080(11)
O4	0.5500(11)	0.2421(7)	0.5022(14)	1	0.0080(11)
O5	0.6281(9)	0.2243(7)	0.1108(13)	1	0.0080(11)
O6	0.2964(10)	0.1833(9)	0.4384(12)	1	0.0080(11)
O7	0.0840(9)	0.1422(7)	0.1795(12)	1	0.0080(11)
O8	0.0770(9)	0.0526(8)	0.4967(14)	1	0.0080(11)
O9	0.1736(9)	0.0681(7)	0.8471(13)	1	0.0080(11)
K1	0.2164(4)	0.6262(3)	0.1212(5)	0.942(2)	0.0559(17)
K2	0.4391(4)	0.0802(3)	0.7095(6)	0.969(2)	0.0262(15)
O10	0.6955(12)	0.0705(8)	0.8818(16)	1	0.0382(43)
Cs1	0.2164(4)	0.6262(3)	0.1212(5)	0.058(2)	0.0559(17)
Cs2	0.4391(4)	0.0802(3)	0.7095(6)	0.031(2)	0.0262(15)

Table 3.9: Selected bond lengths from the refinement of Cs-exchanged $K_2ZrGe_3O_9 \cdot H_2O$

<i>Bond</i>	<i>Distance (Å)</i>		<i>Bond</i>	<i>Distance (Å)</i>
Ge1-O2	1.64(1)		Zr-O1	2.16(1)
Ge1-O5	1.72(1)		Zr-O2	2.12(1)
Ge1-O7	1.80(1)		Zr-O3	2.14(1)
Ge1-O9	1.78(1)		Zr-O4	2.06(1)
			Zr-O5	2.13(1)
Ge2-O1	1.72(1)		Zr-O6	2.13(1)
Ge2-O3	1.69(1)			
Ge2-O8	1.76(1)		Av M1-O	3.14
Ge2-O9	1.76(1)			
			Av M2-O	2.99
Ge3-O4	1.73(1)			
Ge3-O6	1.75(1)			
Ge3-O7	1.77(1)			
Ge3-O8	1.76(1)			

Assuming that Poojary *et al.* accurately describes ion exchange in umbite, the poor fit achieved relative to the unexchanged model could be down to deficiencies in the derived model, this will be further explored in Chapter 4.

3.3.5 Sodium exchange of zirconogermanate umbite

The synthesis of a sodium form of the zirconogermanate umbite is a potential method to improve the ion exchange properties; this is based on previous work by Poojary and co-workers on the zirconosilicate analogue [79]. The relative size of sodium compared to potassium means it is less thermodynamically favourable for the smaller sodium cation to occupy a pore site in the umbite framework. The improved selectivity for caesium by the sodium form of the zirconosilicate originates from the minimal pore rearrangement required during ion exchange; potassium and caesium occupy very different positions in the pore and

as a result must undergo a large change in position making it less favourable. This combination of unfavourable cation-framework bonding and ideal pore position allow for the facile replacement with a larger cation [79].

The formation of a sodium form can be achieved using two different methods, direct hydrothermal synthesis and ion exchange. The direct hydrothermal synthesis of a sodium form of both the zirconosilicate and zirconogermanate is not possible, likely due to unfavourable sodium bond length which would be even more unfavourable in the zirconogermanate due to the expanded framework.

Accessing a sodium form by exchange can be achieved by two methods, single or multiple exchange cycles and by using forcing conditions. Plevart *et al.* report that the zirconogermanate umbite is able to undergo sodium exchange however as reported in Section 3.3.3 no sodium exchange is observed. The exchanges were single cycles at room temperature using 0.1 M solution made from a range of sodium salts, this was sufficient for the reported synthesis of $\text{Na}_2\text{ZrSi}_3\text{O}_9 \cdot \text{H}_2\text{O}$ albeit at a higher concentration.

Due to no observed sodium uptake in the zirconogermanate it is unlikely higher concentration or multiple exchange cycles would yield $\text{Na}_2\text{ZrGe}_3\text{O}_9 \cdot \text{H}_2\text{O}$. So the use of forcing conditions, in this case a concentrated NaCl reflux, was used force sodium into the zirconogermanate pore system. The diffraction pattern for this material appears slightly different to the parent umbite phase; this variation is shown in Figure 3.13.

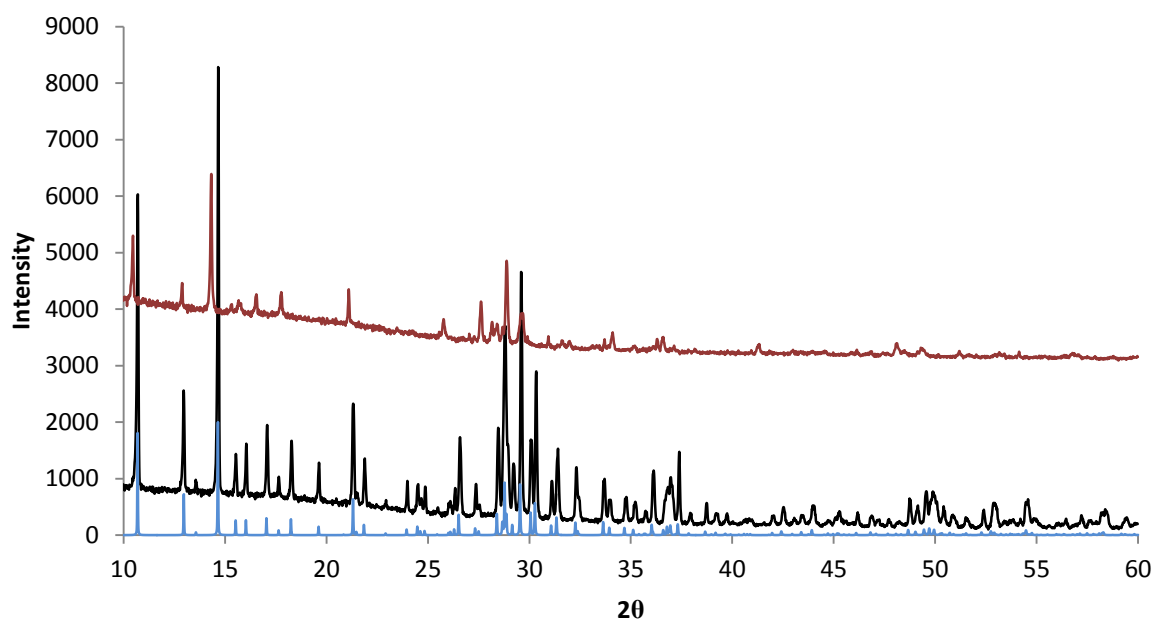


Figure 3.13: X-ray diffraction patterns ($\lambda = 1.5406 \text{ \AA}$) for the NaCl refluxed material (Red) and parent material (Black), umbite reference pattern (Blue) added for comparison.

When comparing the two diffraction patterns shown in Figure 3.13, subtle variation of intensities is observed alongside a noticeable peak shift. Crystallinity of the material has been reduced when exchanging by reflux, due to the more extreme conditions used, relative to the conditions used in normal ion exchange methods. A smaller unit cell would be expected if sodium had completely or partially replaced potassium, however a shift to lower 2θ is observed, indicating a larger unit cell.

Elemental analysis by XRF, Table 3.10, showed that the zirconogermanate umbite was unable to uptake sodium, interestingly the XRF data also showed significantly less potassium than the parent material before reflux.

Table 3.10: Loose powder XRF data before and after a NaCl reflux, ratios are normalised to germanium.

K	0.65	0.15
Ge	1	1
Zr	0.48	0.48
Na	-	0

Due to the lack of sodium in the XRF data, reduced potassium content and differences in diffraction pattern further analysis was required to understand what was happening to the material during the reflux process.

Due to the reduction of potassium observed in the XRF data and subsequent loss of extra framework cations from the material charge balancing must occur. As seen in the XRF data there are no other elements present outside of Ge, Zr and K, however charge balancing must still occur, suggesting another cation has replaced potassium in the pore system. Only elements below sodium in the periodic table are invisible using the Bruker S8 Tiger. As a result it was hypothesised that it could be protons replacing the potassium in the pore system. The small expansion of unit cell also agrees with the literature, with an increase of lattice parameters for the proton zirconosilicate umbite.

The proton form of the zirconogermanate has been synthesised in this work and will be covered in greater detail in Section 3.3.6, however the XRD patterns can be compared between the two materials. The diffraction pattern for the NaCl refluxed material shows some similarities to the synthesised proton form of zirconogermanate umbite as shown in Figure 3.14.

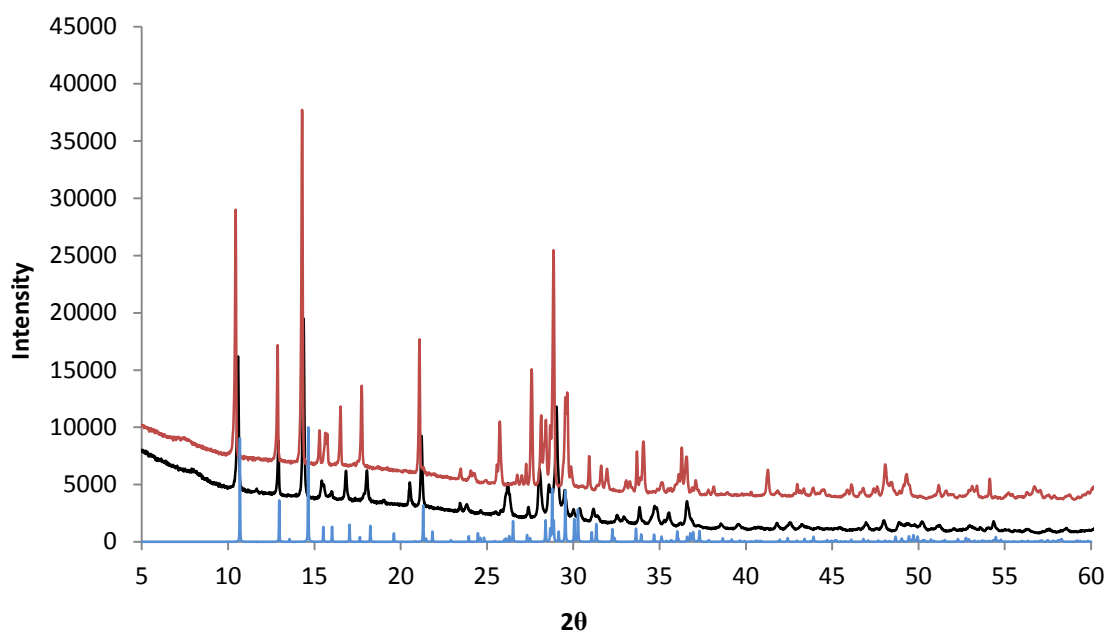


Figure 3.14: X-ray diffraction patterns ($\lambda = 1.5406 \text{ \AA}$) for the NaCl refluxed material (Red) and proton form of $K_2ZrGe_3O_9 \cdot H_2O$ (Black). A reference pattern (Blue) for the parent umbite phase has been added for comparison.

Interestingly this material can also be regenerated using a potassium chloride reflux, back to the original umbite phase, confirming that the unknown species is located in the channel system can be fully exchanged back out of the framework, as shown by Figure 3.15.

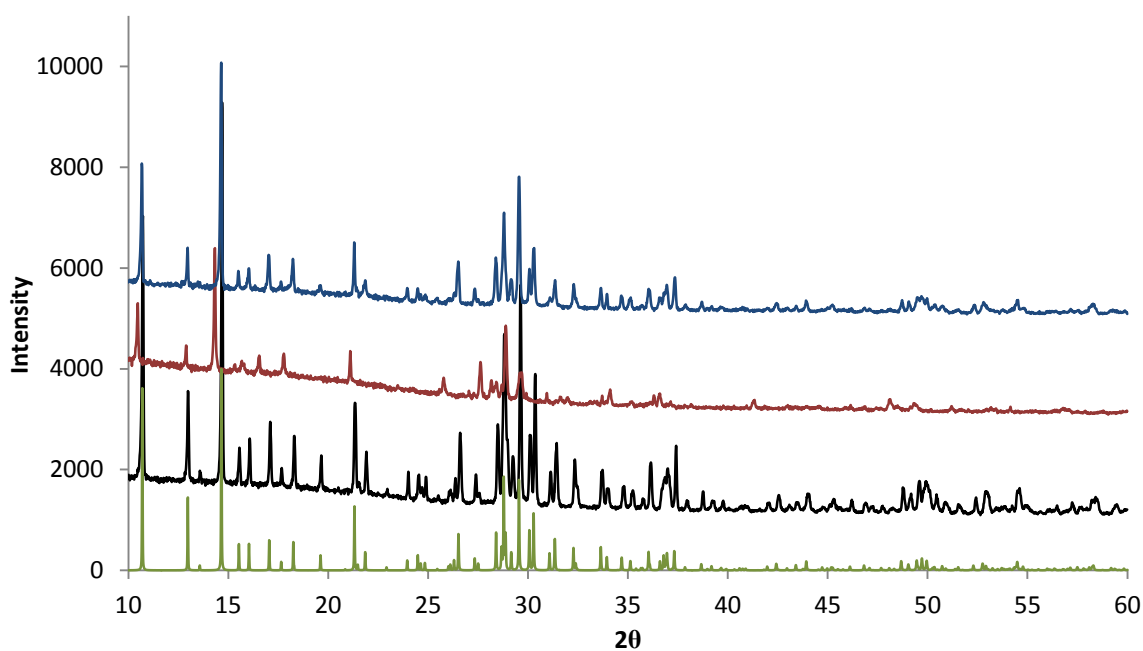


Figure 3.15: X-ray diffraction patterns ($\lambda = 1.5406 \text{ \AA}$) for the parent phase (Black), NaCl refluxed material (Red) and the regenerated KCl refluxed material (Blue). A reference (Green) for the parent umbite phase has been added for comparison.

XRF analysis further confirms the regeneration of the parent phase, as shown in Table 3.11, with the observed amount of potassium returning to pre-NaCl reflux levels.

Table 3.11: XRF loose powder results showing the regeneration of the parent umbite phase after a KCl reflux, all molar ratios are normalised to germanium.

Element	Parent molar ratios	NaCl reflux molar ratios	KCl reflux molar ratios
K	0.65	0.15	0.65
Ge	1	1	1
Zr	0.48	0.48	0.49
Na	-	0	0

TGA analysis of the refluxed sample, Figure 3.16, shows increased mass loss relative to the parent material. The mass loss appears to be approximately double at 400 °C in the refluxed sample and this can be attributed to the dehydration of the material; as a result it would be reasonable to assume double the water content relative to the parent. This agrees with the increased water content in the proton form characterised by Celestian *et al.* [82]. The evidence gathered points towards the NaCl reflux forming the proton form of umbite; however why this occurs is currently unknown.

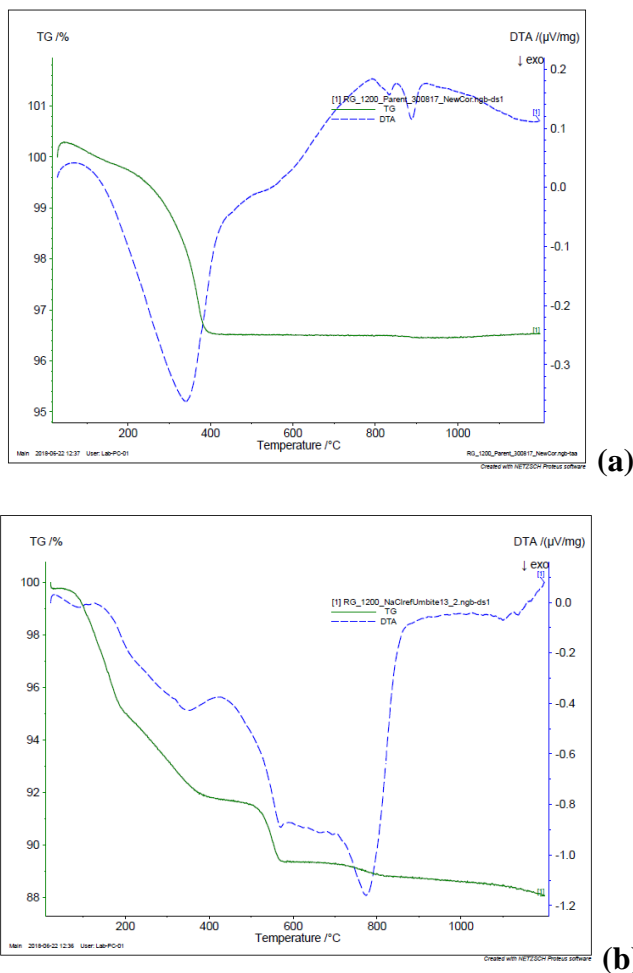


Figure 3.16: TGA analysis for the Parent (a) and NaCl refluxed (b) materials.

3.3.6 Proton form of zirconogermanate umbite

Another second way of improving ion exchange is by the synthesis of the proton form of a material, this strategy has already been applied to umbite materials as outlined by Celestian *et al.* [82] and CST [51]. The replacement of potassium from the channel systems for protons may allow for improved caesium uptake, as it is less favourable to have protons in the channels. The synthesis of the proton form of zirconogermanate umbite is described in Section 3.2.4, the use of a weak acid is pivotal to the success of this synthesis due to the acid solubility of germanium. Increasing the concentration to 1 M acetic acid or using other stronger acids such as nitric acid results in the dissolution of the sample. Figure 3.17 shows the diffraction pattern for the proton exchanged material, where a decrease in sample quality is observed relative to the parent material.

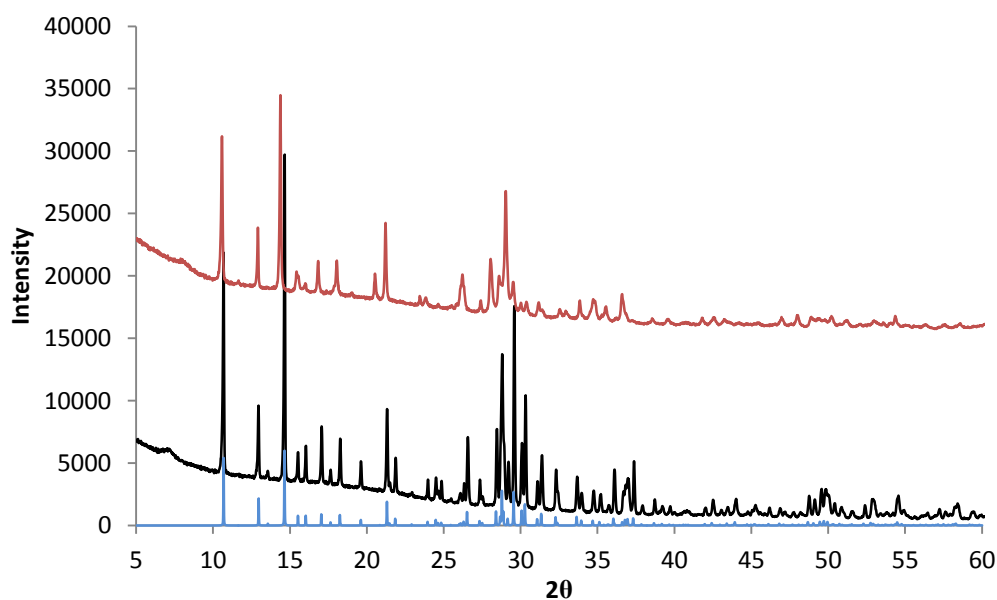


Figure 3.17: X-ray diffraction patterns ($\lambda = 1.5406 \text{ \AA}$) for the parent material (Black) and the attempted synthesis of the proton exchanged form (Red). A reference pattern (Blue) for the parent umbite phase has been added for comparison.

Despite the reduction of sample quality, there is a noticeable shift to lower 2θ and variations in relative intensities. This is to be expected due to the reported shift to a monoclinic unit cell reported for the zirconosilicate umbite assuming similar behaviour for the zirconogermanate. A reduction of crystallinity is also observed which will due to the conditions used, it is worth noting the yield of sample after the synthesis is much less than that expected for other exchanges reported. XRF data, Table 3.12, shows much reduced potassium content and it can be assumed that this is due to the successful proton exchange.

Table 3.12: Loose powder XRF data showing zirconogermanate umbite before and after acid treatment for the attempted synthesis of the proton form. Molar ratios are normalised to germanium.

Element	Parent molar ratios	Proton form molar ratios
K	0.61	0.15
Ge	1	1
Zr	0.48	0.58

As with the zirconosilicate total replacement of potassium for protons was not possible after a single exchange cycle and as a result a second more concentrated 0.5 M exchange was used. Due to the acid solubility of the zirconogermanate umbite the second higher concentration exchange dissolved the sample completely.

On closer inspection the zirconium content appears to be substantially higher than what was expected, subsequent repetitions of the synthesis yielded also showed a variation in the amount of potassium removed during the exchange. Zirconium is still higher than expected when compared to the unexchanged parent material as shown in Table 3.13. A potential

explanation for this could be that, on sample dissolution, germanium stays in solution and zirconium forms a solid impurity that is not observed by XRD.

Table 3.13: Second attempted synthesis of the proton form showing pressed pellet XRF data before and after exchange. Molar ratios are normalised to germanium.

Element	Parent molar ratios	Proton form molar ratios
K	0.63	0.29
Ge	1	1
Zr	0.46	0.69

For the first proton form synthesised preliminary uptake caesium and strontium exchange by XRF shows significantly greater caesium uptake relative to the parent material, however due to the large errors in the XRF data it is difficult to estimate total uptake. Subsequent repetition of the caesium exchange resulted in significantly different calculated molar ratios as shown in Table 3.14.

Table 3.14: Cs-exchange data for the proton form of $K_2ZrGe_3O_9 \cdot H_2O$, XRF data normalised to germanium

Element	Cs-Ex proton form loose powder molar ratios	Cs-Ex proton form pressed pellet molar ratios
K	0	0
Ge	1	1
Zr	1.1	0.71
Cs	0.21	0.36

For both sets of XRF data no potassium is shown to be present however it would not be possible to assume full caesium exchange due to hydrogen not being visible by XRF but also the poor data acquired. Strontium uptake also appears higher than the parent material however once again it is difficult to assess the actual uptake due to poor XRF data.

The high zirconium content from XRF seems to be intrinsic to the proton form synthesis, such extreme germanium/zirconium ratios are not observed for any other umbite samples analysed. These large errors could originate from sample preparation methods however comparison of loose powder and pressed pellet data still show a high zirconium content. The nonsensical data, if analysed qualitatively, shows caesium uptake. However the inconsistency observed in the XRF data reduces the reliability of proton form synthesis for the improvement of ion exchange in germanate umbite. It is highly likely that the sample is slowly being dissolved, which would explain the reduced yield and nonsensical XRF data, even in the weak acid. Reproducibility is critical to understanding ion exchange characteristics and as a result the synthesis of the proton form of the zirconogermanate is not a viable method of improving uptake characteristics.

3.3.7 Synthesis of Ti and Sn germanoumbites

The literature has already shown that the synthesis of both the titano and stannosilicate umbite is possible. The titanosilicate is reported to show different ion exchange properties to the zirconosilicate and for this reason the synthesis of a titano and stannogermanate umbite were attempted. This was done by replacing the zirconyl chloride octahydrate with suitable Ti and Sn sources, titanium isopropoxide and tin chloride pentahydrate respectively, in the standard zirconogermanate umbite synthesis. The titanium synthesis did not result in an umbite phase, but instead a different octahedral tetrahedral framework material analogous to the mineral pharamcosiderite, Figure 3.18. This material has been studied in the literature for ion exchange applications and will be covered in greater detail in Chapter 5.

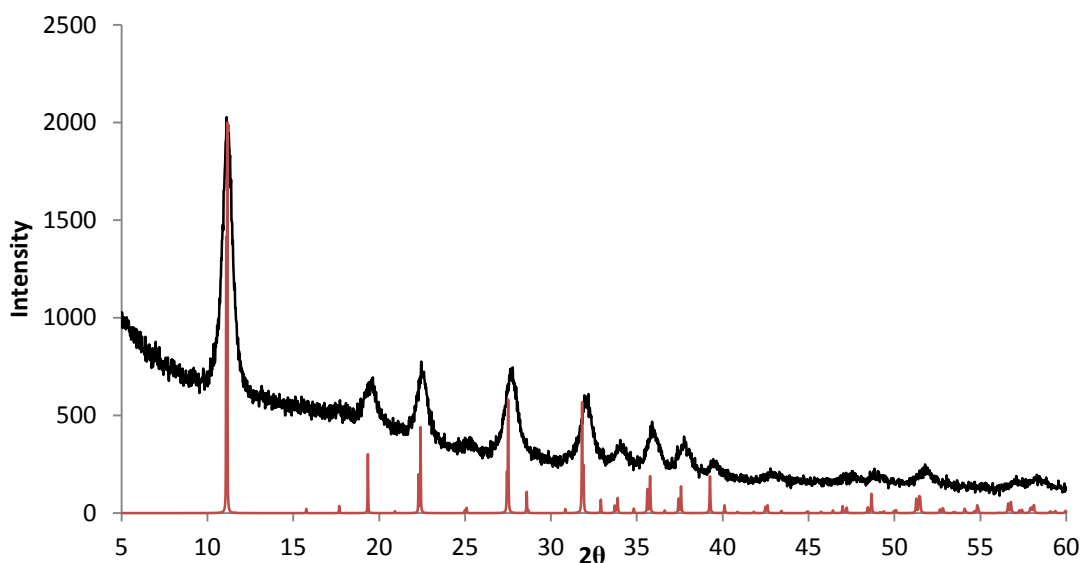


Figure 3.18: X-ray diffraction pattern ($\lambda = 1.5406 \text{ \AA}$) for the attempted synthesis of $\text{K}_2\text{TiGe}_3\text{O}_9 \cdot \text{H}_2\text{O}$. Resultant phase was a titanogermanate pharamcosiderite $\text{HK}_3\text{Ti}_4\text{Ge}_3\text{O}_{16} \cdot 4\text{H}_2\text{O}$, confirmed using Bruker phase matching software, shown by calculated diffraction pattern (Red).

The tin synthesis also resulted in a different pharamcosiderite phase, $\text{HK}_3\text{HGe}_7\text{O}_{16} \cdot 4\text{H}_2\text{O}$, alongside an umbite phase as shown in Figure 3.19.

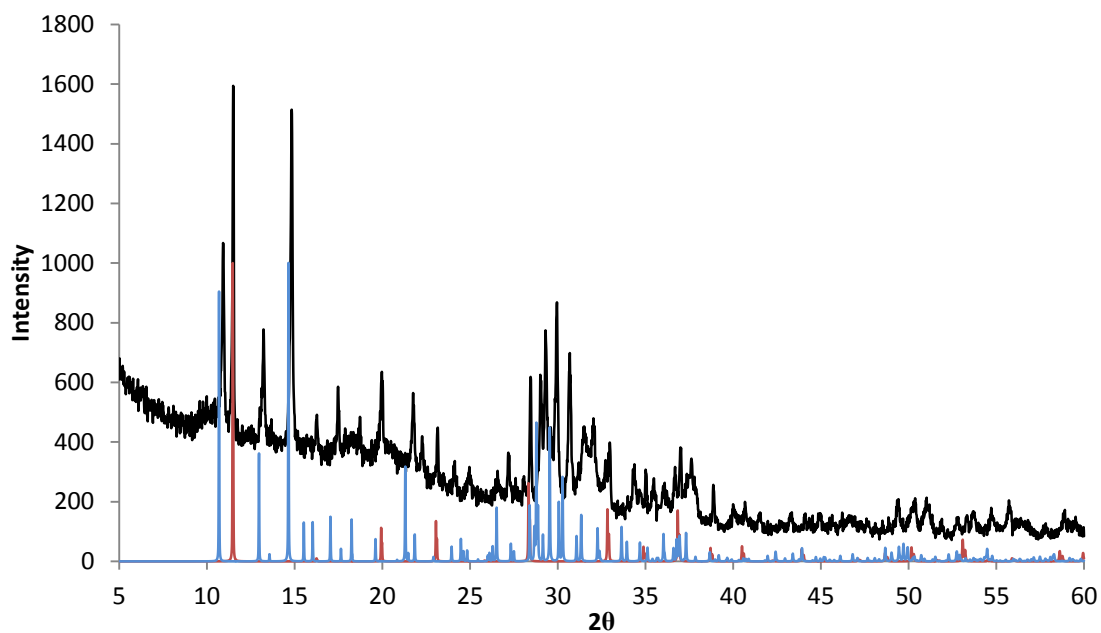


Figure 3.19: X-ray diffraction pattern ($\lambda = 1.5406 \text{ \AA}$) for the attempted synthesis of $\text{K}_2\text{SnGe}_3\text{O}_9 \cdot \text{H}_2\text{O}$. Peaks corresponding to the germanogermanate pharmacosiderite $\text{HK}_3\text{Ge}_7\text{O}_{16} \cdot 4\text{H}_2\text{O}$, are shown by the calculated reference pattern (Red) and umbite (Blue).

Attempts to alter the gel compositions for both titanium and tin synthesis methods would not result in pure umbite type phases. The relative flexibility of the silicate when compared to the germanate is surprising, as many of the octahedral tetrahedral materials show variability in composition. Zirconogermanate umbite occupies a very narrow phase boundary and due to similar synthesis conditions for the pharmacosiderite phases it is possible to access multiple phases with only small variation in gel composition.

3.3.8 Synthesis of ammonium zirconogermanate umbite, $(\text{NH}_4)_2\text{ZrGe}_3\text{O}_9\cdot\text{H}_2\text{O}$

As previously described in Section 3.3.5 the synthesis of a sodium form of zirconogermanate was not possible, this was attributed to the potential size mismatch between cation size and the size of the expanded germanate framework. As the only reported direct synthesis of umbites contain potassium it was decided to try and synthesise an ammonium form directly, due the similarity in size between the potassium and ammonium cations (1.51 Å vs 1.54 Å). This was done hydrothermally, modifying the methodology in Section 3.2.2, replacing potassium hydroxide with ammonium hydroxide solution.

Due to the water content of ammonium hydroxide solution, the added extra water was reduced to maintain the same level of fill for the autoclave. Germanium dioxide solubility in this solution was limited, potentially due to the lower pH of solution compared to the KOH solution normally used. XRD analysis using a Bruker D8 in transmission geometry showed a highly crystalline product which did not match any phases using Bruker phase matching software.

Comparison of the diffraction patterns potential ammonium form and potassium form shows some similarities between diffraction patterns, Figure 3.20.

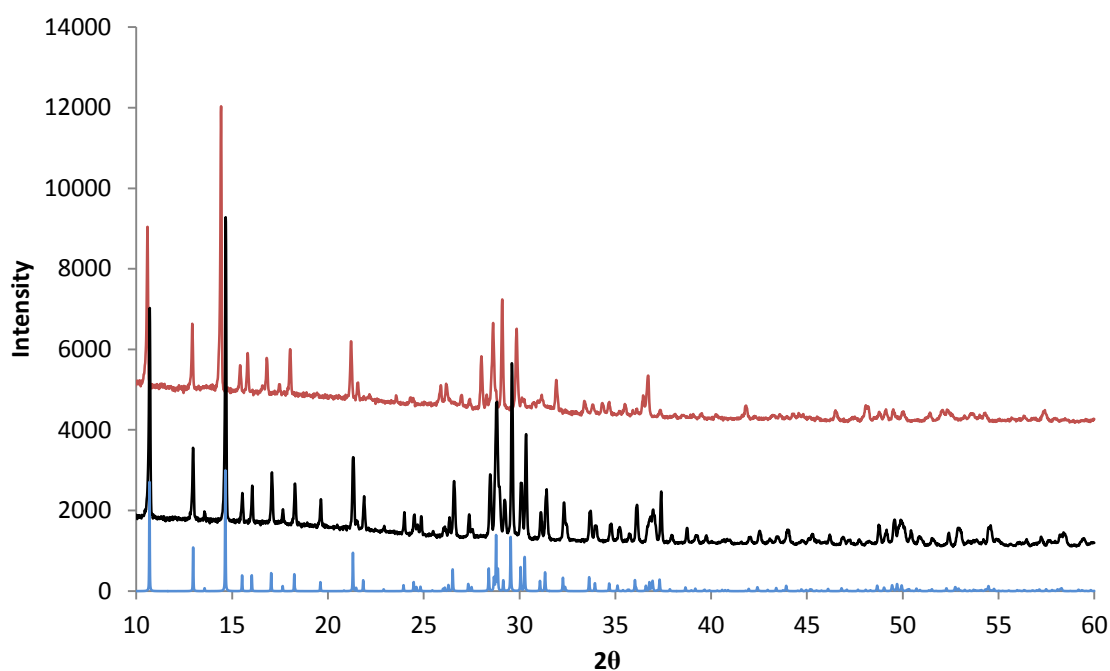


Figure 3.20: X-ray diffraction patterns ($\lambda = 1.5406 \text{ \AA}$) for the attempted synthesis of ammonium umbite (Red) with the parent material shown for comparison (Black). Umbite reference pattern (Blue) added for comparison.

However attempts to refine diffraction data collected using a Bruker D8 in reflection geometry ($\lambda = 1.5406 \text{ \AA}$ and 1.5444 \AA), for both the orthorhombic ($P2_12_12_1$) and Celestian proton monoclinic ($P2_1/c$) umbite models, resulted in poor quality refinements.

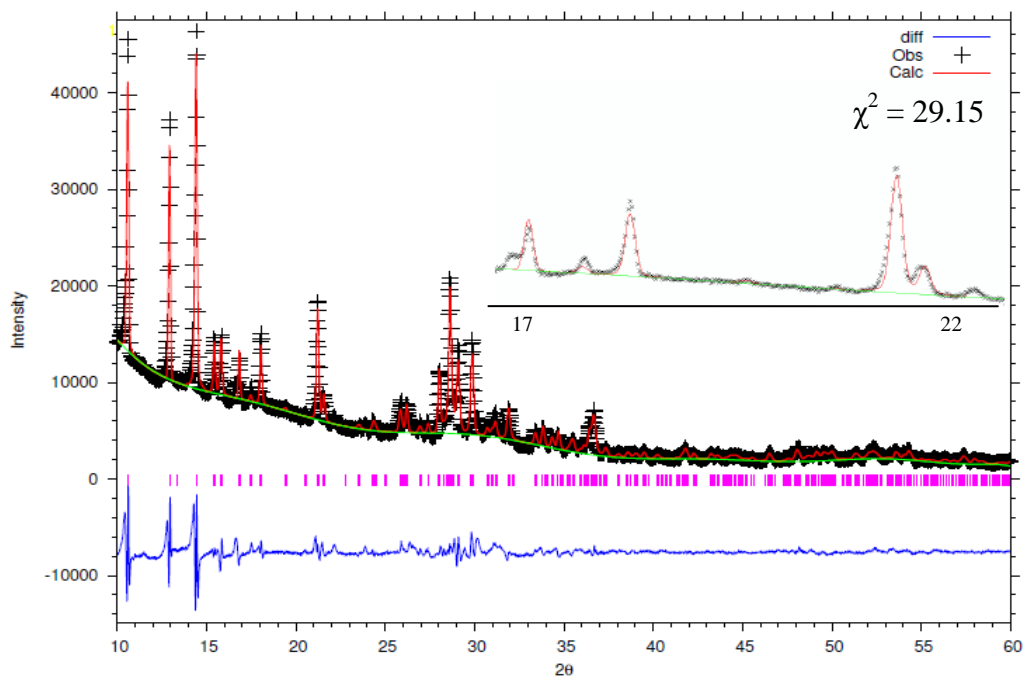


Figure 3.21: Attempted Rietveld refinement of ammonium umbite using the $P2_12_12_1$ space group, insert shows poor peak fitting.

For both models low angle peak shape proved difficult to fit correctly alongside additional peaks at 15-25° 2θ not being matched in the experimental data, this is demonstrated in Figure 3.21. At this point it is possible that there may be some unidentified impurity phase, but peak splitting and as a result a different space group cannot be ruled out. Assuming the material was related to umbite ion exchange tests were done to see if the material can indeed exchange, once again using 0.1 M solution for 24 hours at room temperature. Table 3.15 shows the ion exchange data recorded on loose powders which shows an increase in caesium and strontium uptake compared to the parent phase, showing this material has some degree of ion exchange ability, albeit still relatively poor.

Table 3.15: XRF loose powder data for the assumed ammonium form of zirconogermanate umbite, all molar ratios are normalised to germanium.

Element	Ammonium form Cs- Ex molar ratios	Ammonium form Sr- Ex molar ratios
Ge	1	1
Zr	0.52	0.51
Cs	0.07	-
Sr	-	0.08

Further work, such as the use of neutron diffraction to study ammonium location in the structure and potentially a full structural solution, must be done to characterise this material fully. However it is possible that this could be a novel ammonium derivative of umbite of which there are none reported in the literature.

3.3.9 Synthesis of caesium form of zirconogermanate umbite, $\text{Cs}_2\text{ZrGe}_3\text{O}_9\cdot\text{H}_2\text{O}$

It has been shown that caesium incorporation into the zirconogermanate umbite structure by ion exchange is limited. However in order to determine whether the structure can accept caesium or whether it is due to ion exchange factors, such as kinetics and selectivity, the synthesis of a caesium form of the material was attempted. This was done by the modification of the standard umbite synthesis from Section 3.2.2, replacing potassium hydroxide for caesium hydroxide. Synthesis length was increased to 5 days at 200 °C to allow substantial crystallisation time. Figure 3.22 shows the diffraction pattern recorded on a Bruker D8 in transmission geometry for the synthesised material, sample crystallinity is very low when compared to the highly crystalline parent material.

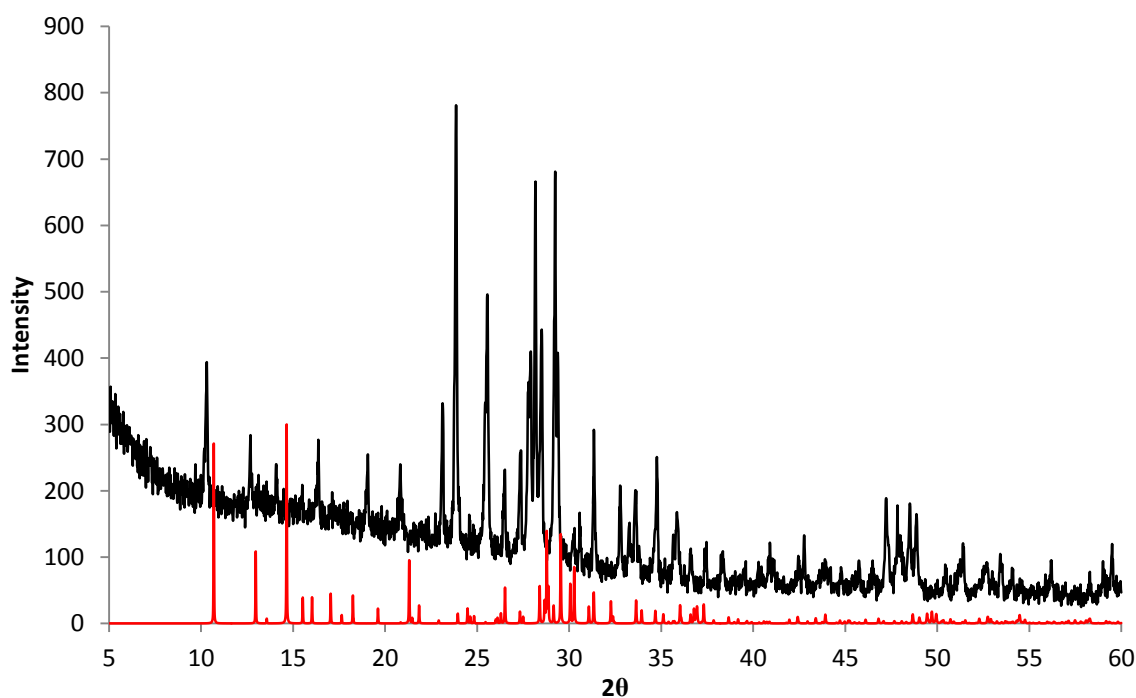


Figure 3.22: X-ray diffraction pattern ($\lambda = 1.5406 \text{ \AA}$) for the attempted synthesis of $\text{Cs}_2\text{ZrGe}_3\text{O}_9\cdot\text{H}_2\text{O}$. A reference pattern (Red) for the parent umbite phase has been added for comparison.

Phase identification using known Bruker software did not successfully identify the synthesised phase; this was expected due to the caesium form of umbite not being reported for both the zirconosilicate and zirconogermanate in the literature. Attempts to refine data recorded on a Bruker D8 in reflection geometry ($\lambda = 1.5406 \text{ \AA}$ and 1.5444 \AA), resulted in a suitable fit to a caesium form of the orthorhombic $P2_12_12_1$ space group, Figure 3.23. Restraints were applied to Ge-O and Zr-O bonds of 1.74 \AA and 2.07 \AA respectively.

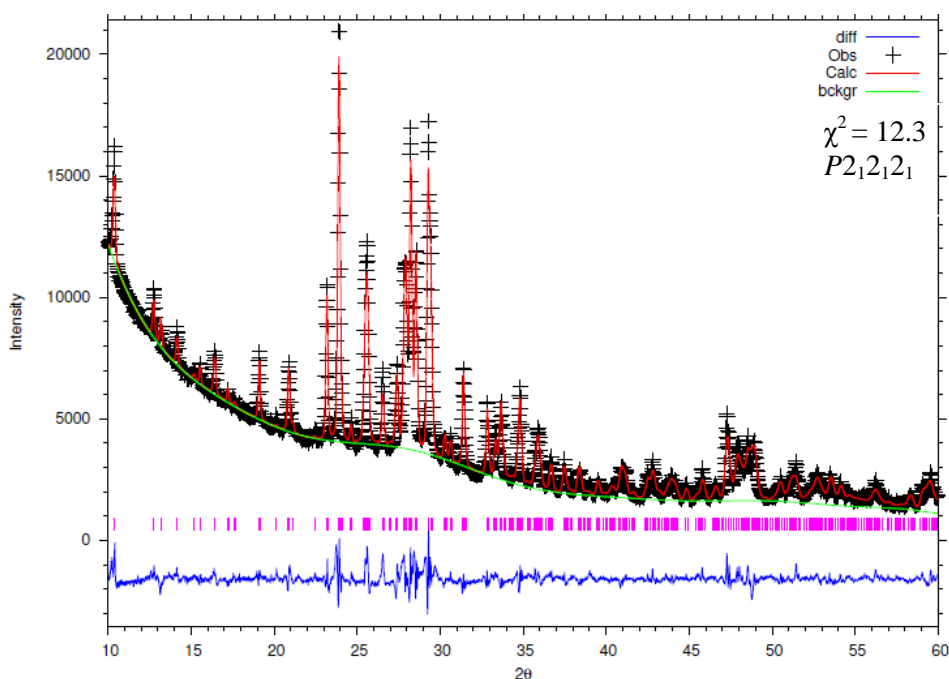


Figure 3.23: Attempted Rietveld refinement of $\text{Cs}_2\text{ZrGe}_3\text{O}_9 \cdot \text{H}_2\text{O}$.

However further improvement of the refinement has proved difficult to the poor quality of data recorded despite lengthy scan times, with low angle peak shape and the background being poorly fit. Further work must be undertaken to fully characterise the material, higher quality data would be required to allow for a more reliable Rietveld refinement and increased confidence in the model suggested.

3.3.10 Zirconogermanate umbite thermal conversion

Plevert *et al.* report that the thermal conversion product for the zirconogermanate umbite is a wadeite analogue, however this is not explicitly shown in the literature. The intention was to exchange the material and analyse the caesium containing phases, this is clearly not possible with this material. However studying the thermal conversion of the parent material will give a much greater understanding of the zirconogermanates thermal behaviour especially in comparison to the silicate.

Variable temperature XRD using a Bruker D8 ($\lambda = 1.5406 \text{ \AA}$) with an Anton Parr heating stage was used to analyse the sample with a scan recorded at 50 °C intervals up to 1100 °C, shown in Figure 3.24. The umbite structure is stable up to 750 °C after which the material undergoes a rapid phase transition at approximately 800 °C to a different phase which is stable up to a minimum of 1100 °C. Figure 3.25 shows the result of phase identification, using Bruker phase matching software, on the room temperature scan after the heating cycle. The formation of wadeite is confirmed [89] however the scheelite phase, ZrGeO_4 , which was reported to form by Plevert *et al.* is not observed.

The minor peaks, which could not be phase matched using Bruker software, are unidentified. Many of these additional peaks are not visible in the 1100 °C scan which suggests formation of minor phases on cooling. The shown phase transition occurs at lower temperature than the reported conversion in the silicate material, which occurs at approximately 900 °C [79, 86].

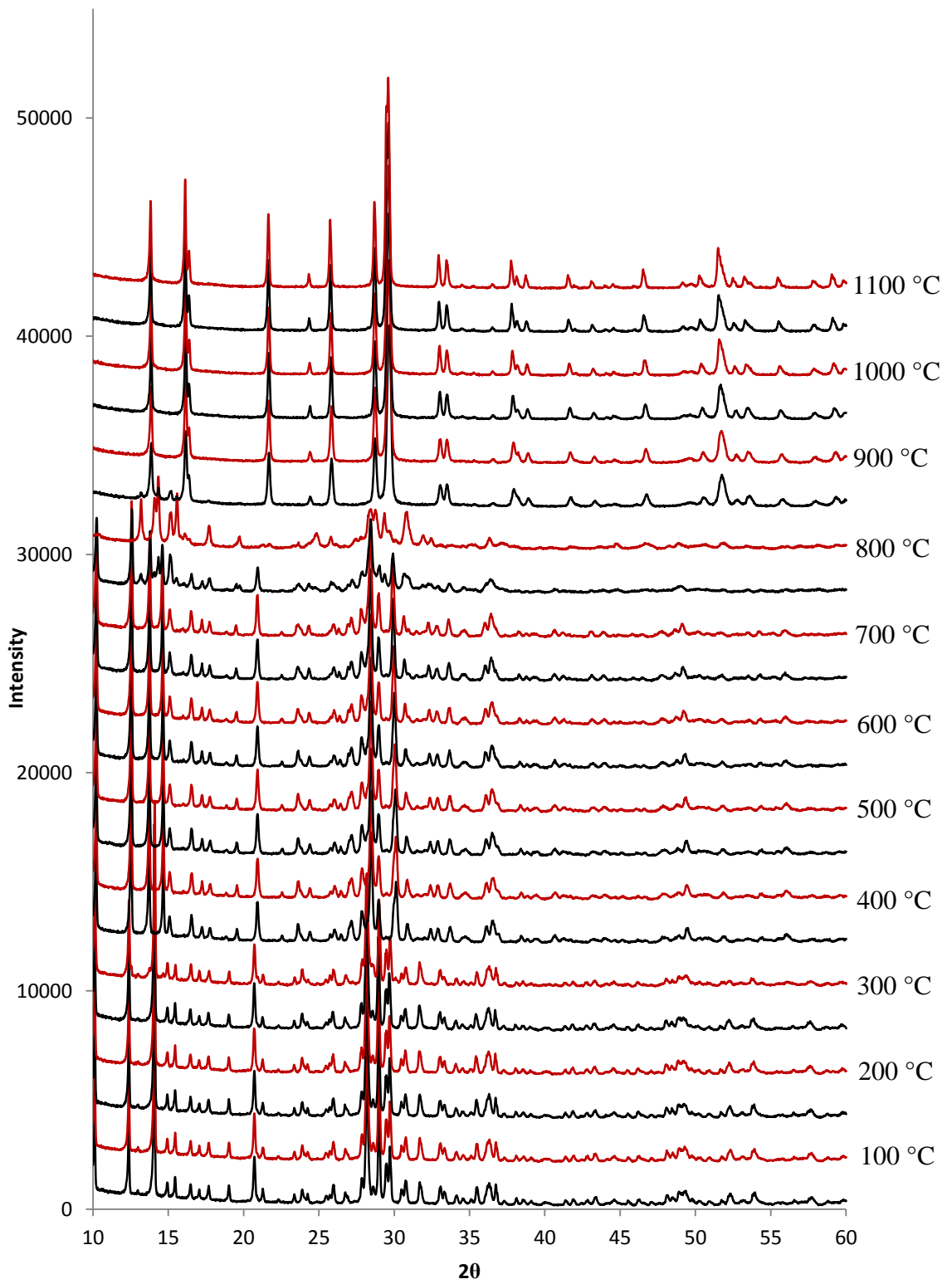


Figure 3.24: VT XRD for the thermal conversion of umbite at 50 °C intervals.

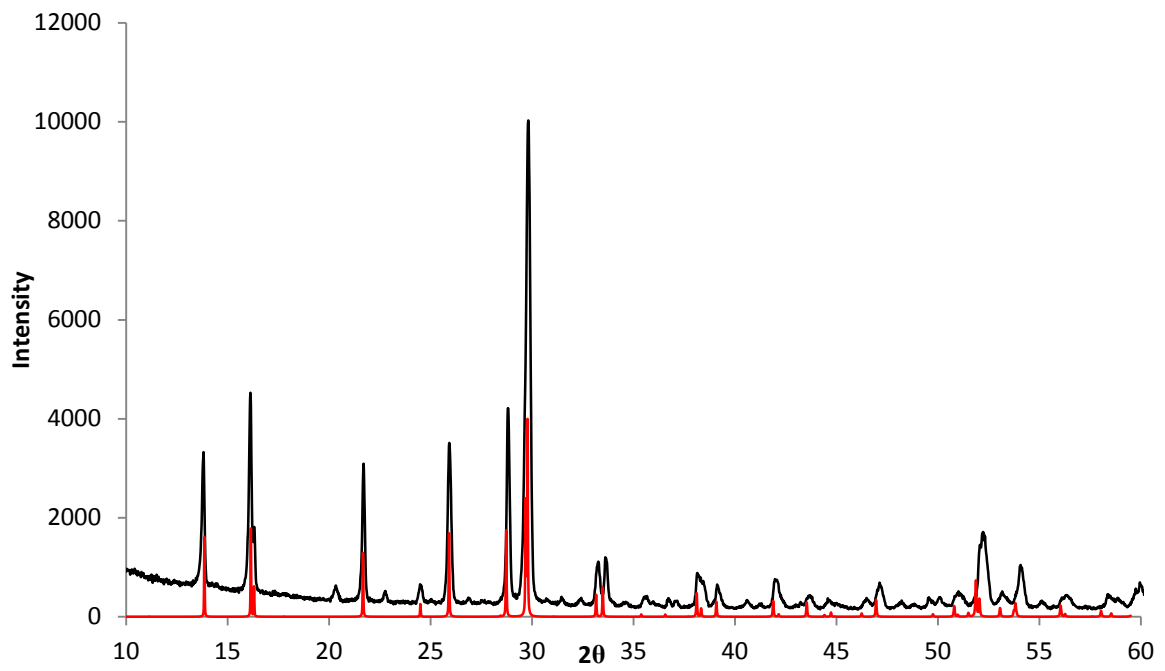


Figure 3.25: X-ray diffraction data ($\lambda = 1.5406 \text{ \AA}$) for the final phase assemblage of heated umbite. Wadeite reference pattern (Red) added for comparison.

3.4 Conclusions

The successful synthesis and subsequent optimisation of a zirconogermanate umbite has allowed for further investigation into the materials ion exchange properties. The caesium and strontium uptake by zirconogermanate umbite is extremely low and is far worse than the zirconosilicate umbite reported by Poojary *et al.* The attempted synthesis of a sodium form through both hydrothermal and ion exchange methods in order to try and improve exchange properties was not possible, with zirconogermanate umbite showing no sodium uptake even when using forcing reflux conditions.

The synthesis of the proton form was possible and this resulted in improved cation exchange relative to the parent material especially for caesium. However sample quality was extremely poor and reproducibility of sample preparation was difficult, this is due to the relatively low acid stability of germanium oxide relative to silicon oxides. Attempts to make other germanate umbites containing titanium and tin resulted in the formation of pharmacosiderite phases and mixed germanium/silicon umbites could not be synthesised phase pure.

Zirconogermanate umbite exists in a very narrow phase boundary which can be easily affected variations in gel composition with respect to dopants, highlighting the framework inflexibility. Most post synthesis methods from the literature have been exhausted to try and improve the incredibly poor uptake characteristics of the zirconogermanate umbite. A different methodology must be considered and that is modification during synthesis, this is explored in greater detail in Chapter 4.

Chapter 4- Framework Doping and
Ion Exchange of $K_2ZrGe_3O_9 \cdot H_2O$

4.1 Introduction

Unfortunately not all materials exhibit useful ion exchange properties as highlighted by the work in Chapter 3. However this allows for further work on the alteration of ion exchange properties, with a focus on the improvement of selectivity, kinetics and cation exchange capacity. The most common method to do this is framework modification by doping which can be implemented in two different ways.

1. Modification of framework charge and subsequent removal of charge balancing cations, such as the replacement of a 4^+ cation for a 5^+ cation, an example of this is niobium doping into CST.
2. Variation of unit cell parameters by the substitution of elements with larger ionic radii and the subsequent impact on pore size and volume, as explored in Chapter 3.

Both of the above methods allow for the tailoring of optimum ion exchange properties, with niobium doping showing the most prevalence in the literature. The composition of the natural mineral sitinakite suggests that Nb can substitute for Ti in the structure. The substitution of Nb^{5+} for Ti^{4+} in the framework reduces the amount of charge balancing cations required in the channel system and as a result can modify ion exchange behaviour. Luca *et al.* showed that Cs^+ selectivity increases with niobium content up to a maximum of 40% Nb, with Cs distribution coefficient (K_d) values being over double for the doped material [52]. This was further explored by Tripathi *et al.* with regards to the origins of the selectivity for Nb-CST. It was suggested that the removal of cations from the tunnels allows for the uptake of extra water, potentially as a hydrated Cs complex. As the quantity of Cs^+ increases, protons/hydronium ions are displaced from the channels which results in a modification of coordination with regards to Cs^+ . It was observed that additional bonds were formed between

Cs^+ and water molecules, from eight coordinate in undoped material to 12-coordinate in the Nb doped material. This gives a more thermodynamically favourable environment for Cs^+ to occupy and hence increased Cs uptake [90]. Figure 4.1 shows the positions that Cs^+ occupies in the channel system of Nb-CST and the local bonding environment for Cs^+ in the channel.

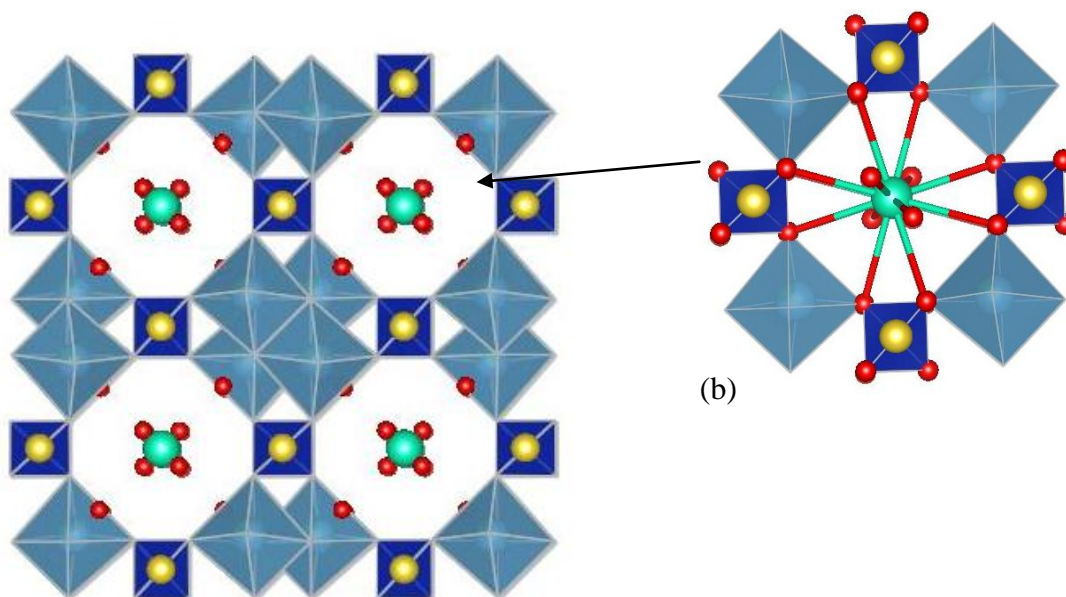


Figure 4.1: Structure of Cs-exchanged Nb-CST, where Cs^+ cations (Turquoise) and inter pore water (Red) are shown by coloured spheres. Figure 4.1b shows the local bonding environment for the 12-coordinate Cs^+ cation.

The reverse is true for Sr^{2+} uptake which is higher in the undoped material, in which the Sr complex is ten-coordinate compared to the seven in Nb-CST [90]. This variation in coordination number was further studied by Tripathi *et al.* It was observed that by varying the niobium content it is possible to alter the coordination of Sr^{2+} in the channels, reporting that in the 16% Nb phase Sr^{2+} coordination is nine [91]. Once again the coordination environment of the cation is dependent on the number of bonds formed to water in the channel. The author believes that despite the available space in the channel increasing, the doping of niobium reduces the number of Sr- H_2O bonds. This results in a less thermodynamically favourable

environment and hence reducing selectivity [92] however it is not fully explained why this is the case in the literature. Figure 4.2 shows the site occupied by strontium in the Nb-CST channel system. The location of Sr^{2+} in the channel system is very different to that of Cs^+ as shown in Figure 4.1, with Sr^{2+} occupying a position much closer to the framework.

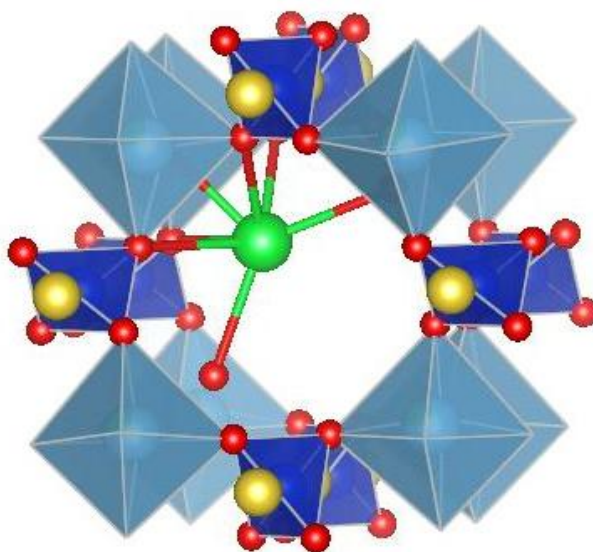


Figure 4.2: Local coordination environment for Sr^{2+} in Nb-CST, where Sr^{2+} is shown by a green sphere with a coordination of seven.

Radioisotope work undertaken by Clearfield *et al.* explored the kinetics of caesium and strontium uptake from waste stimulants for both Nb-CST and CST. Due to the size of the caesium cation, uptake by Nb-CST occurred at a slower rate relative to strontium uptake in CST however this can be improved by reducing the crystallinity as mentioned in Chapter 1. The smaller particle size means many more unit cells are on or near the surface and, as a result, readily available for ion exchange. The author suggests that a single mix of poorly crystalline CST and Nb-CST may well be used to remove both Cs^+ and $\text{Sr}(\text{OH})^+$ from current waste solutions simultaneously [53].

As described above the optimisation of ion exchange properties is substantially more complex than simply altering the framework of a material and attention has to be given to interaction between the framework and the cation. The selectivity of an ion exchange material is controlled by the strength and number of bonds formed by exchange reactions. In this chapter niobium doping has been used to try and improve the poor ion exchange properties shown by zirconogermanate umbite.

4.2 Experimental

4.2.1 Synthesis of $K_{2-x}Zr_{1-x}Nb_xGe_3O_9 \cdot H_2O$

Typical synthesis for $x = 0.25$

The zirconogermanate umbite was prepared by mixing 1.52 g of germanium dioxide (Gerald wise and co) and 1.67 g of potassium hydroxide (85%, Sigma) in 20 ml of deionised water.

To the stirring mixture 0.3144 g of niobium chloride (99%, Sigma) was added with 1.125 g of zirconyl chloride octahydrate (98%, Sigma) until dissolved. The mixture is then stirred for a further hour to allow it to homogenise.

The resulting mixture was then transferred to a 45 ml Teflon liner and placed in a Parr autoclave at 200 °C for 24 hours. The resulting product was then filtered and washed in deionised water before being dried overnight at 60 °C.

4.2.2 Synthesis of $K_{2-x}Zr_{1-x}Sb_xGe_3O_9 \cdot H_2O$

Typical synthesis for $x = 0.25$

The zirconogermanate umbite was prepared by mixing 1.52 g of germanium dioxide (Gerald wise and co) and 1.67 g of potassium hydroxide (85%, Sigma) in 20 ml of deionised water.

To the stirring mixture 0.1882 g antimony oxide (99.995%, Aldrich) was added with 1.125 g of zirconyl chloride octahydrate (98%, Sigma) until dissolved. The mixture is then stirred for a further hour to allow it to homogenise.

The resulting mixture was then transferred to a 45 ml Teflon liner and placed in a Parr autoclave at 200 °C for 24 hours. The resulting product was then filtered and washed in deionised water before being dried overnight at 60 °C.

All compounds synthesised were analysed using Powder X-ray diffraction (XRD) on a Bruker D8 Advance using a Cu K α source at room temperature. Phase matching was performed using the EVA software from known databases.

4.2.3 Ion exchange studies

0.1 M solutions of strontium nitrate (98%, Alfa Aesar) or caesium nitrate (99.8%, Alfa Aesar) were added to 0.2-0.5 g of sample with an overall w/v ratio of 1:100. This was then shaken for 24 hours before being filtered, washed and dried overnight at 60 °C. Elemental analysis was undertaken using X-ray fluorescence (XRF) on a Bruker S8 Tiger with the samples prepared as either a loose powder, pressed pellet or fused bead.

4.3 Results and discussion

4.3.1 Synthesis of niobium doped umbite

As described in Section 4.1 niobium doping can allow for the modification of the ion exchange properties of a material. It was reported in Chapter 3 that the zirconogermanate umbite shows negligible ion exchange, especially when considering the good ion exchange properties shown by the silicate derivative. In order to promote ion exchange, a range of mixed Nb⁵⁺/Zr⁴⁺ materials were proposed, firstly to determine the maximum amount of niobium incorporation possible but to also study how cation uptake varies with niobium content.



For every niobium doped into the framework potassium from the channel system should be lost in order to balance framework charge. This would result in materials with general formula K_{2-x}Zr_{1-x}Nb_xGe₃O₉.H₂O, with initial targeted niobium content of x = 0.1, 0.2, 0.3 and 0.4. As was shown in Chapter 3, doping into the zirconogermanate structure is difficult at both the octahedral and tetrahedral site; however the accommodation of low doping levels may be possible.

The doped niobium zirconogermanates were hydrothermally synthesised using the same conditions for the undoped material, the use of niobium(V) chloride as the niobium source was preferred due its higher solubility relative to the oxide. Initial synthesis attempts of 0.1Nb and 0.2Nb doping resulted in the formation of umbite phases. However the incorporation of niobium is difficult to confirm by XRD, as it is possible niobium could be occupying an amorphous phase, which would not be visible in the collected diffraction patterns. The

synthesis of the 0.3Nb doped material once again resulted in single phase umbite however subsequent attempts to try and repeat this synthesis failed. Due to the lack of reproducibility further exploration of ion exchange properties for the 0.3Nb material were no longer considered. Figure 4.3 shows the initial synthesis attempts of the doped materials, with minimal variation of diffraction pattern relative to the undoped parent.

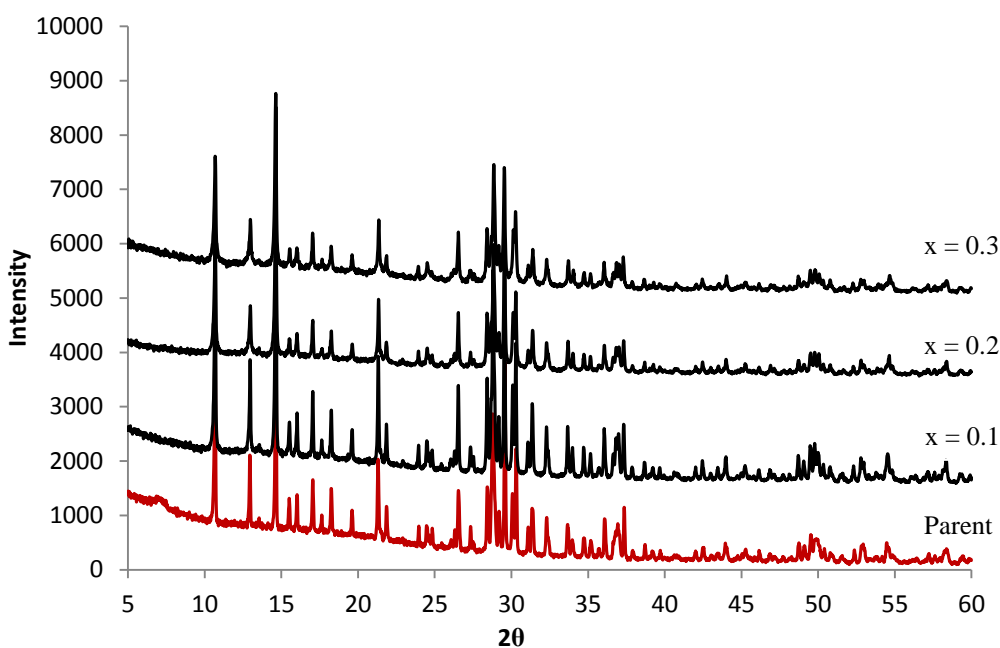


Figure 4.3: X-ray diffraction patterns ($\lambda = 1.5406 \text{ \AA}$) for the initial synthesis attempts of niobium doped zirconogermanate umbites with general formula $\text{K}_{2-x}\text{Zr}_{1-x}\text{Nb}_x\text{Ge}_3\text{O}_9 \cdot \text{H}_2\text{O}$. Parent pattern (Red) added for comparison.

It is observed that except for some peak broadening, presumably due to loss of crystallinity, very little else changes and there are no significant shift in peak positions indicating the unit cell dimensions are not affected by the doping. Elemental analysis of the doped samples by XRF, Table 4.1, showed niobium in the synthesised materials. However this does not confirm successful doping as it is not possible to distinguish the phase niobium is occupying.

The expected reduction in the relative amount of potassium, if niobium doping has been successful, is also not observed despite preparing the samples as fused beads.

Table 4.1: XRF data for the doped umbite materials, samples prepared as fused beads and molar ratios are normalised to germanium. Loose powder data for 0.3Nb added for comparison.

Element	Parent molar ratios	0.1Nb molar ratios	0.2Nb molar ratios	0.25Nb molar ratios	0.3Nb Molar ratios
K	0.71	0.75	0.77	0.73	0.68
Ge	1	1	1	1	1
Zr	0.41	0.35	0.33	0.32	0.33
Nb (Expected)	-	0.04 (0.033)	0.08 (0.066)	0.10 (0.083)	0.12 (0.099)

Due to the lack of reproducibility for the 0.3Nb doped material, a lower level doping of 0.25Nb was attempted and successfully synthesised, this became the upper limit for niobium incorporation. To further confirm successful doping, ion exchange properties would need to be explored. Any differences in ion exchange properties for the doped material relative to the parent phase would provide evidence for successful niobium incorporation into the umbite structure; this will be covered in further detail in Section 4.3.2.

The synthesis of a 0.4Nb doped material was attempted however the resultant product is no longer the single phase, with a mixture of both an umbite phase and germanogermanium pharmacosiderite ($\text{HK}_3\text{Ge}_7\text{O}_{16}\cdot 4\text{H}_2\text{O}$), as shown by Figure 4.4.

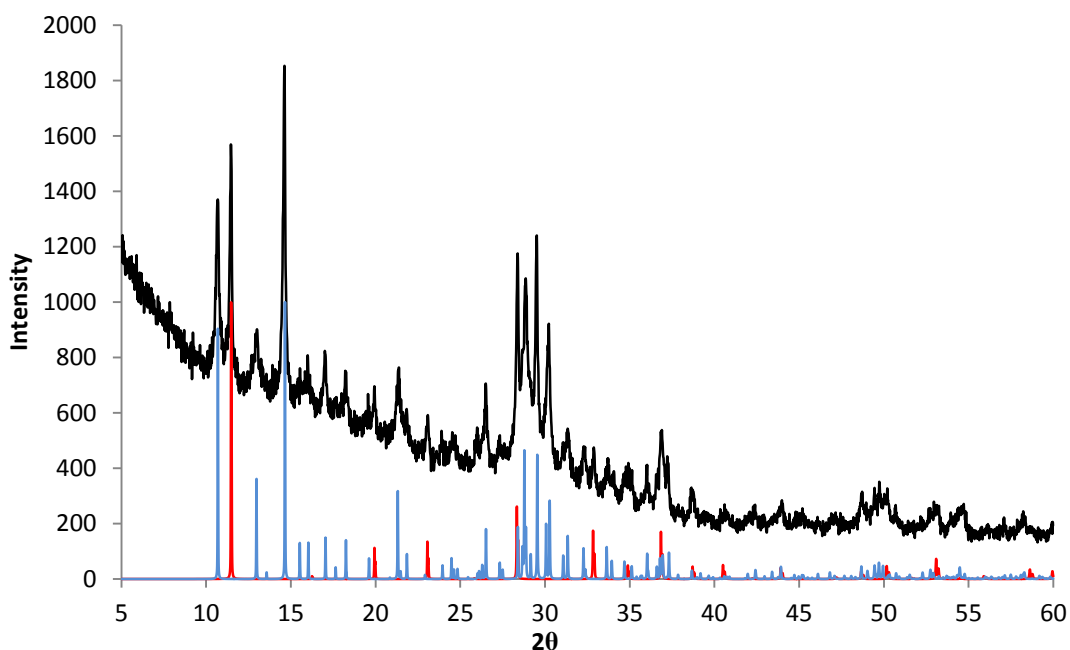


Figure 4.4: X-ray diffraction pattern ($\lambda = 1.5406 \text{ \AA}$) for the attempted synthesis of $x = 0.4$ doped umbite. Peaks corresponding to the germanogermanate pharmacosiderite, $\text{HK}_3\text{Ge}_7\text{O}_{16}\cdot 4\text{H}_2\text{O}$, are shown by the calculated reference pattern (Red) and umbite (Blue).

Clearly niobium incorporation at this level perturbs umbite formation as was observed for the isomorphous substitution of Ti and Sn. This again highlights the inflexibility of the zirconogermamate umbite framework however doping of other elements, excluding those already covered in this work, at low levels could still be a possibility. This is unlike the stannosilicate umbite which shows a great degree of framework flexibility with a range of dopants being incorporated into its structure at both coordination sites [61]. Octahedral site doping of 5^+ and subsequent $5^+/3^+$ combinations have shown to be possible and tetrahedral site doping of germanium for silicon for has also been successful, albeit at low levels. This flexibility reflected by differences in exchange characteristics with relative uptake of both caesium and strontium varying depending on the dopant [61].

4.3.2 Ion exchange of Niobium doped umbite

All materials were exchanged against strontium and caesium using nitrate solutions in a large excess, this would allow for the measuring of maximum uptake. As shown in Table 4.2, elemental analysis by XRF on the samples shows a large increase of caesium content relative to the parent material reported in Chapter 3 Section 3.3.3. The caesium content increases proportionally to the niobium content of the samples. A substantial increase is observed between 0.2 and 0.25Nb incorporation.

Table 4.2: XRF analysis of Cs-exchanged Nb doped umbites, samples were prepared as fused beads and molar ratios normalised to germanium.

Element	0.1Nb Cs-exchange Molar ratio	0.2Nb Cs-exchange Molar ratio	0.25Nb Cs-exchange Molar ratio	Parent Cs-exchange Molar ratio
K	0.54	0.56	0.28	0.68
Ge	1	1	1	1
Zr	0.36	0.33	0.32	0.41
Nb	0.04	0.08	0.1	-
Cs	0.16	0.17	0.39	0.02

The elemental ratios shown in Table 4.2 are normalised to germanium with great care taken to select the correct lines to give reasonable molar ratios, which are more representative of stoichiometry expected. Due to the mass of caesium, selection of the $K\alpha$ line has a significant impact on the reported weight percentages, resulting in a severe overestimation of the calculated caesium content relative to the other elements in the sample. As stated in Chapter 2

Section 2.4.2 sample thickness also impacts the calculated weight percentages, the required penetration depth of caesium for this sample is significantly larger than the other elements. This would often lead to total sample weight percentage of all elements to be considerably above 100% which is incorrect. Selection of sample preparation is vital due to relatively high molar masses of the elements in exchanged zirconogermanate umbite and as a result fused beads were the preferred preparation method. Limitations in using fused beads stem from the dilution factor and sample/flux relationship, however this is not an issue for the heavier elements analysed in this work. The strategy adopted for the XRF data was a combination of using fused beads and the selection of the $L\alpha_1$ line for caesium which gave more representative weight fractions and subsequent molar ratios. Table 4.3 shows that strontium uptake is still incredibly poor and as a result will no longer be studied.

Table 4.3: XRF analysis of Sr-exchanged 0.2Nb doped umbite, sample was prepared as loose powders and molar ratios normalised to germanium

Element	Molar Ratio
K	0.61
Ge	1
Zr	0.34
Nb	0.08
Sr	0.006

4.3.3 Examining XRF variability

In order to gain a greater understanding of XRF as a technique and greater trust in the reported results, the variability in the recorded data was examined. The caesium content reported for the 0.2Nb sample was lower than what was expected and did not agree with the trend observed in the preliminary loose powder data recorded. As a result a larger batch of the sample was ion exchanged by the same method as outlined in Section 4.2.3 and from this ion exchange sample three separate fused beads were made. Theoretically the exchange should be consistent across the whole sample, so the three beads should give very similar results when analysed. Each of these beads was also analysed in triplicate, which gives a much greater understanding of data variation from both the sample and the instrument. These results are shown in Table 4.4, once again all molar ratios have been normalised to germanium and the $L\alpha_1$ line has been selected for caesium.

Table 4.4: XRF analysis for the Cs-exchanged 0.2Nb doped sample, where three fused beads were analysed in triplicate. Molar ratios are normalised to germanium.

Elements	Fused Bead 1 Molar ratios		Fused Bead 2 Molar ratios		Fused Bead 3 Molar ratios
K	0.49		0.49		0.49
Ge	1		1		1
Zr	0.34		0.34		0.34
Nb	0.08		0.08		0.08
Cs	0.24		0.24		0.24
Second analysis					
K	0.50		0.49		0.48
Ge	1		1		1
Zr	0.34		0.33		0.34
Nb	0.08		0.08		0.08
Cs	0.23		0.24		0.24
Third analysis					
K	0.50		0.50		0.49
Ge	1		1		1
Zr	0.34		0.34		0.33
Nb	0.08		0.08		0.08
Cs	0.23		0.24		0.24

The resultant XRF data shows very good agreement between both the different beads and the analysis in triplicate, with very little variation in the calculated molar ratios. The three separately formed beads are in good agreement with one another, especially considering the fused bead formation process would contribute substantially to any errors in the data observed. The caesium molar ratio for each bead is consistent at 0.23 relative to germanium; this is higher than the reported value in table 4.2 for the 0.2Nb doped umbite. This much better fits the expected trend and as a result the caesium uptake shown in Table 4.3 is believed to be more representative of the uptake for 20% niobium doped umbite.

4.3.4 Rietveld refinement of Nb doped umbites

As previously established in Section 4.3.1, confirmation of niobium doping is inconclusive from the analysis already described. However it has been shown that niobium has been successfully incorporated due to the increase in observed caesium uptake. In order to gain greater understanding of how niobium doping impacts the umbite structure, high-resolution powder diffraction data was collected for each of the doping levels up to $x = 0.25$. Figures 4.5-4.7 show the Rietveld refinements for these materials, as Nb^{5+} and Zr^{4+} are isoelectronic the occupancies were not refined and were fixed to the as synthesised doping level. The total cation occupancy was split evenly between the two cation sites, for example the total cation occupancy for 0.1Nb is 1.9, meaning each cation site had a starting occupancy of 0.95. This was then allowed to refine with the sum of the two sites constrained to a total of 1.9. This strategy was applied to the other doping levels with total occupancies for 0.2Nb and 0.25Nb being 1.8 and 1.75 respectively. Restraints were applied to Ge-O and Zr-O bonds of 1.74 Å and 2.07 Å respectively.

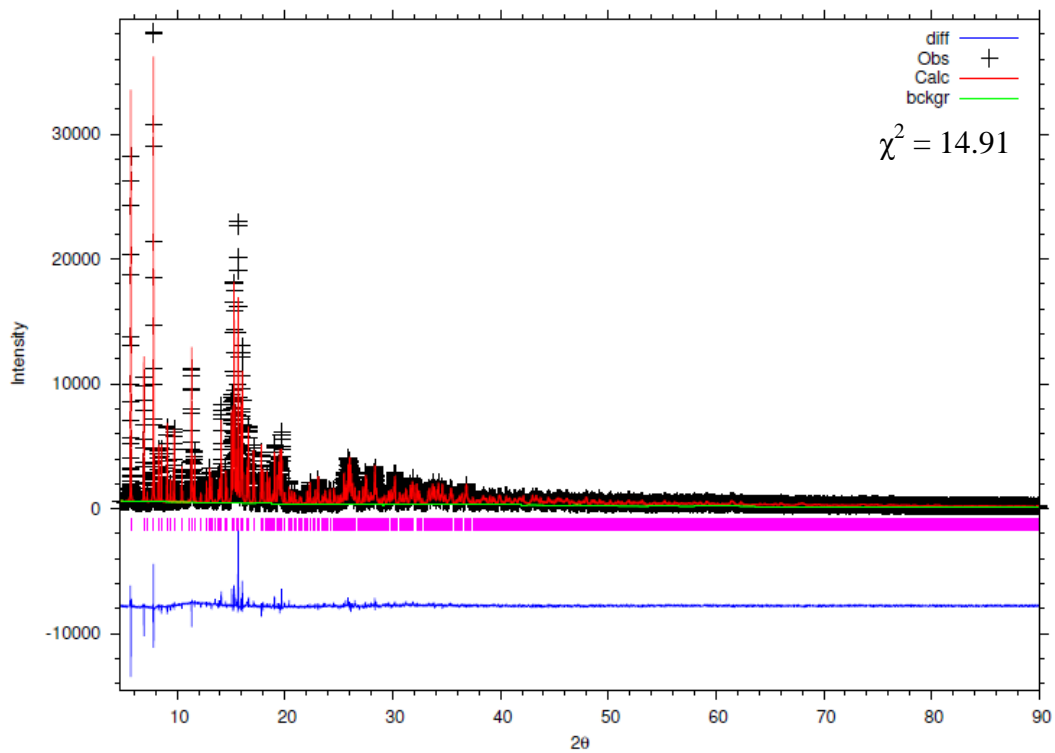


Figure 4.5: Rietveld refinement for $\text{K}_{1.9}\text{Zr}_{0.9}\text{Nb}_{0.1}\text{Ge}_3\text{O}_9 \cdot \text{H}_2\text{O}$.

Table 4.5: Lattice parameters, atomic positions, occupancy and thermal parameters for the refinement of $\text{K}_{1.9}\text{Zr}_{0.9}\text{Nb}_{0.1}\text{Ge}_3\text{O}_9\cdot\text{H}_2\text{O}$. Thermal parameters are grouped by element.

$\lambda/\text{\AA}$	0.82525				
$a/\text{\AA}$	10.3979(1)				
$b/\text{\AA}$	13.6467(1)				
$c/\text{\AA}$	7.4337(1)				
$V/\text{\AA}^3$	1054.81(2)				
<i>Space Group</i>	$P2_12_12_1$				
R_{wp}	0.1050				
R_{exp}	0.0272				
χ^2	14.91				
<i>Site</i>	<i>x</i>	<i>y</i>	<i>z</i>	<i>Occupancy</i>	<i>U_{iso}</i>
Zr1	0.4562(2)	0.2096(2)	0.2648(3)	0.9	0.0052(5)
Ge1	0.1875(2)	0.1722(2)	-0.0098(3)	1	0.0012(3)
Ge2	0.0313(2)	0.0451(1)	0.7253(3)	1	0.0012(3)
Ge3	0.6360(2)	0.3377(2)	0.5957(3)	1	0.0012(3)
O1	0.4238(7)	0.3570(3)	0.2392(16)	1	0.0062(10)
O2	0.3470(9)	0.1931(9)	0.0394(9)	1	0.0062(10)
O3	0.5246(8)	0.0701(3)	0.2819(15)	1	0.0062(10)
O4	0.5529(10)	0.2374(6)	0.4992(10)	1	0.0062(10)
O5	0.6233(7)	0.2241(6)	0.1191(13)	1	0.0062(10)
O6	0.3018(5)	0.1834(9)	0.4288(9)	1	0.0062(10)
O7	0.0944(8)	0.1418(7)	0.1796(7)	1	0.0062(10)
O8	0.0782(10)	0.0535(5)	0.4981(9)	1	0.0062(10)
O9	0.1682(7)	0.0698(6)	0.8534(13)	1	0.0062(10)
K1	0.2186(5)	0.6230(3)	0.1242(7)	0.920(3)	0.0117(10)
K2	0.4411(4)	0.0801(3)	0.7076(7)	0.980(3)	0.0117(10)
O10	0.6963(11)	0.0622(8)	0.8797(15)	1	0.0062(10)
Nb1	0.4562(2)	0.2096(2)	0.2648(3)	0.1	0.0052(5)

Table 4.6: Selected bond lengths from the refinement of $K_{1.9}Zr_{0.9}Nb_{0.1}Ge_3O_9 \cdot H_2O$.

<i>Bond</i>	<i>Distance (Å)</i>		<i>Bond</i>	<i>Distance (Å)</i>
Ge1-O2	1.72(5)		Zr/Nb-O1	2.05(4)
Ge1-O5	1.76(5)		Zr/Nb-O2	2.04(4)
Ge1-O7	1.76(5)		Zr/Nb-O3	2.04(4)
Ge1-O9	1.74(5)		Zr/Nb-O4	2.05(4)
			Zr/Nb-O5	2.06(4)
Ge2-O1	1.76(5)		Zr/Nb-O6	2.05(4)
Ge2-O3	1.73(5)			
Ge2-O8	1.76(5)		Av K1-O	3.18
Ge2-O9	1.75(5)			
			Av K2-O	3.01
Ge3-O4	1.77(5)			
Ge3-O6	1.76(5)			
Ge3-O7	1.75(5)			
Ge3-O8	1.75(5)			

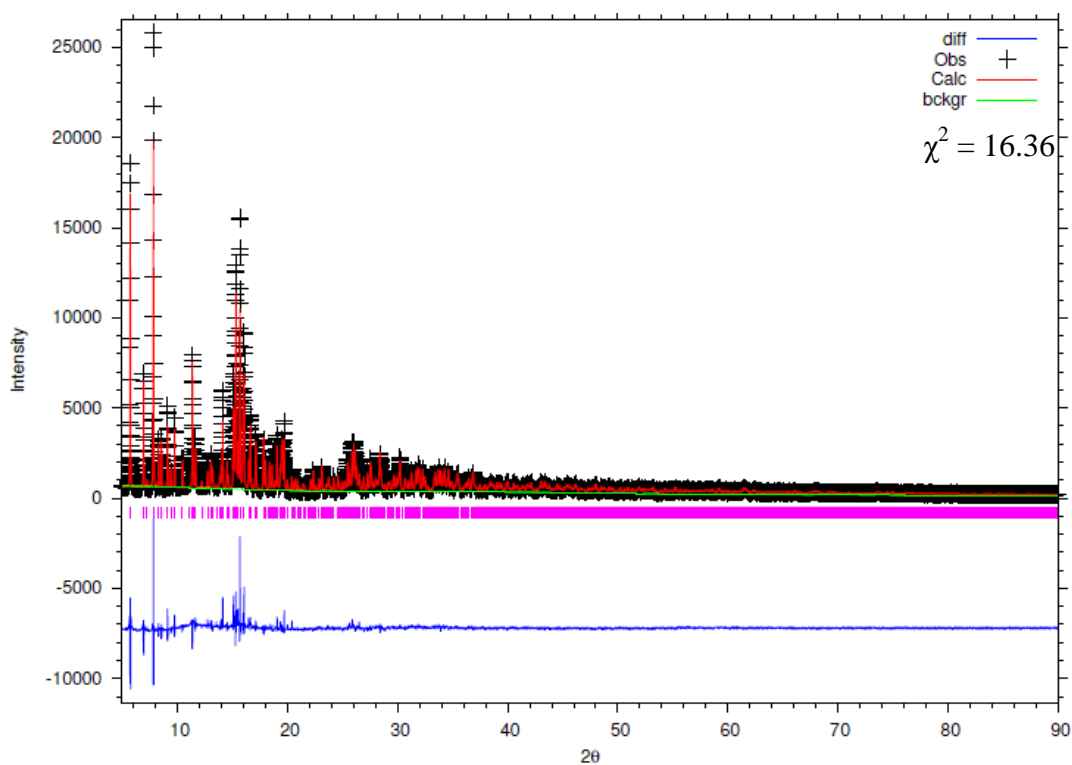


Figure 4.6: Rietveld refinement for $K_{1.8}Zr_{0.8}Nb_{0.2}Ge_3O_9 \cdot H_2O$

Table 4.7: Lattice parameters, atomic positions, occupancy and thermal parameters for the refinement of $\text{K}_{1.8}\text{Zr}_{0.8}\text{Nb}_{0.2}\text{Ge}_3\text{O}_9 \cdot \text{H}_2\text{O}$. Thermal parameters are grouped by element.

$\lambda / \text{\AA}$	0.82525				
$a / \text{\AA}$	10.3941(2)				
$b / \text{\AA}$	13.6321(2)				
$c / \text{\AA}$	7.4352(1)				
$V / \text{\AA}^3$	1053.53(3)				
<i>Space Group</i>	$P2_12_12_1$				
R_{wp}	0.1159				
R_{exp}	0.0287				
χ^2	16.36				
<i>Site</i>	<i>x</i>	<i>y</i>	<i>z</i>	<i>Occupancy</i>	U_{iso}
Zr1	0.4567(2)	0.2097(2)	0.2649(4)	0.8	0.0059(6)
Ge1	0.1878(3)	0.1718(2)	-0.0099(4)	1	0.0017(4)
Ge2	0.0312(3)	0.0442(2)	0.7253(4)	1	0.0017(4)
Ge3	0.6359(3)	0.3376(2)	0.5946(4)	1	0.0017(4)
O1	0.4230(9)	0.3573(3)	0.2395(22)	1	0.0059(13)
O2	0.3477(7)	0.1974(12)	0.0377(10)	1	0.0059(13)
O3	0.5257(10)	0.0705(3)	0.2789(20)	1	0.0059(13)
O4	0.5546(14)	0.2356(7)	0.4999(12)	1	0.0059(13)
O5	0.6240(9)	0.2237(7)	0.1185(17)	1	0.0059(13)
O6	0.3023(6)	0.1854(12)	0.4310(11)	1	0.0059(13)
O7	0.0967(10)	0.1412(10)	0.1807(8)	1	0.0059(13)
O8	0.0802(13)	0.0524(6)	0.4984(10)	1	0.0059(13)
O9	0.1666(9)	0.0671(7)	0.8600(17)	1	0.0059(13)
K1	0.2187(6)	0.6223(4)	0.1259(9)	0.862(4)	0.0060(12)
K2	0.4424(5)	0.0805(4)	0.7080(8)	0.938(4)	0.0060(12)
O10	0.6960(14)	0.0581(10)	0.8756(19)	1	0.0059(13)
Nb1	0.4567(2)	0.2097(2)	0.2649(4)	0.2	0.0059(6)

Table 4.8: Selected bond lengths from the refinement of $\text{K}_{1.8}\text{Zr}_{0.8}\text{Nb}_{0.2}\text{Ge}_3\text{O}_9 \cdot \text{H}_2\text{O}$.

<i>Bond</i>	<i>Distance (Å)</i>		<i>Bond</i>	<i>Distance (Å)</i>
Ge1-O2	1.74(5)		Zr/Nb-O1	2.05(4)
Ge1-O5	1.77(6)		Zr/Nb-O2	2.04(4)
Ge1-O7	1.76(6)		Zr/Nb-O3	2.03(4)
Ge1-O9	1.74(6)		Zr/Nb-O4	2.05(4)
			Zr/Nb-O5	2.06(4)
Ge2-O1	1.76(6)		Zr/Nb-O6	2.05(4)
Ge2-O3	1.72(5)			
Ge2-O8	1.77(6)		Av K1-O	3.18
Ge2-O9	1.76(6)			
			Av K2-O	3.02
Ge3-O4	1.77(6)			
Ge3-O6	1.77(5)			
Ge3-O7	1.74(6)			
Ge3-O8	1.75(6)			

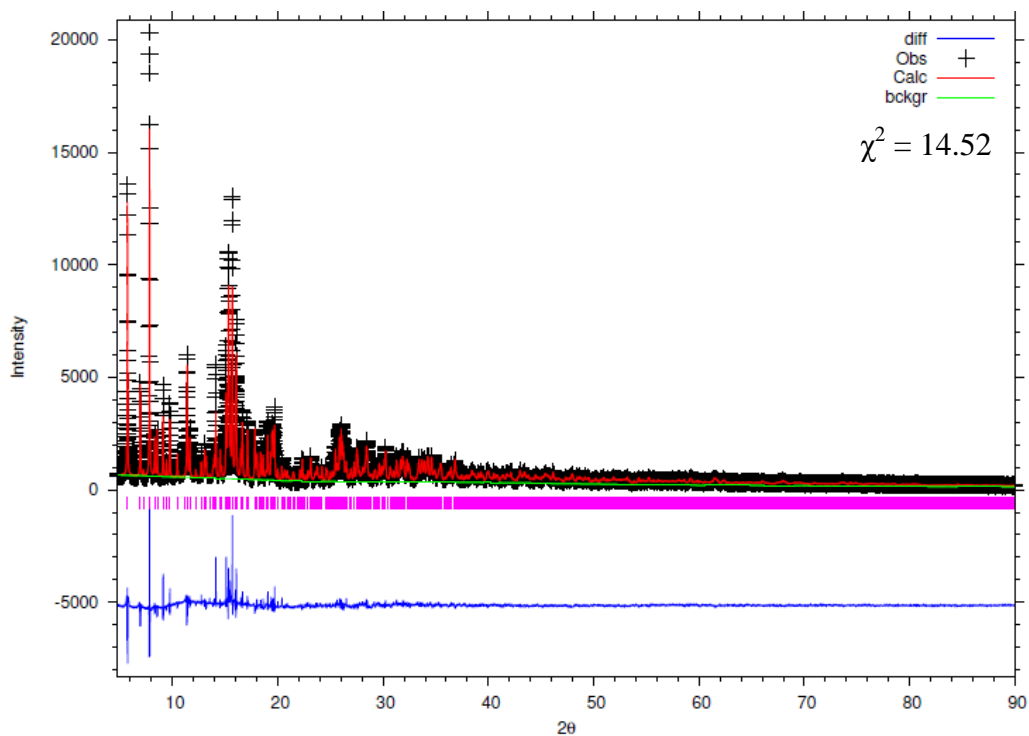


Figure 4.7: Rietveld refinement for $\text{K}_{1.75}\text{Zr}_{0.75}\text{Nb}_{0.25}\text{Ge}_3\text{O}_9 \cdot \text{H}_2\text{O}$.

Table 4.9: Lattice parameters, atomic positions, occupancy and thermal parameters for the refinement of $\text{K}_{1.75}\text{Zr}_{0.75}\text{Nb}_{0.25}\text{Ge}_3\text{O}_9 \cdot \text{H}_2\text{O}$. Thermal parameters are grouped by element.

$\lambda/\text{\AA}$	0.82525				
$a/\text{\AA}$	10.4006(2)				
$b/\text{\AA}$	13.6245(3)				
$c/\text{\AA}$	7.4414(1)				
$V/\text{\AA}^3$	1054.47(4)				
<i>Space Group</i>	$P2_12_12_1$				
R_{wp}	0.1097				
R_{exp}	0.0288				
χ^2	14.52				
<i>Site</i>	<i>x</i>	<i>y</i>	<i>z</i>	<i>Occupancy</i>	<i>U_{iso}</i>
Zr1	0.4571(3)	0.2100(2)	0.2647(4)	0.75	0.0049(6)
Ge1	0.1876(3)	0.1720(2)	-0.0091(4)	1	0.0024(4)
Ge2	0.0316(3)	0.0442(2)	0.7257(4)	1	0.0024(4)
Ge3	0.6365(3)	0.3374(3)	0.5946(4)	1	0.0024(4)
O1	0.4255(9)	0.3573(3)	0.2346(22)	1	0.0042(14)
O2	0.3456(8)	0.2056(13)	0.0393(11)	1	0.0042(14)
O3	0.5264(9)	0.0710(3)	0.2747(22)	1	0.0042(14)
O4	0.5538(14)	0.2359(7)	0.5001(13)	1	0.0042(14)
O5	0.6230(9)	0.2244(7)	0.1178(18)	1	0.0042(14)
O6	0.3036(6)	0.1851(13)	0.4321(11)	1	0.0042(14)
O7	0.0964(10)	0.1434(10)	0.1816(7)	1	0.0042(14)
O8	0.0857(13)	0.0521(6)	0.5016(11)	1	0.0042(14)
O9	0.1662(10)	0.0672(7)	0.8614(17)	1	0.0042(14)
K1	0.2205(7)	0.6197(5)	0.1233(9)	0.823(4)	0.0040(12)
K2	0.4424(6)	0.0800(5)	0.7089(9)	0.927(4)	0.0040(12)
O10	0.6973(15)	0.0533(11)	0.8802(20)	1	0.0042(14)
Nb1	0.4571(3)	0.2100(2)	0.2647(4)	0.25	0.0049(6)

Table 4.10: Selected bond lengths from the refinement of $K_{1.75}Zr_{0.75}Nb_{0.25}Ge_3O_9 \cdot H_2O$.

<i>Bond</i>	<i>Distance (Å)</i>		<i>Bond</i>	<i>Distance (Å)</i>
Ge1-O2	1.73(5)		Zr/Nb-O1	2.05(4)
Ge1-O5	1.76(5)		Zr/Nb-O2	2.04(4)
Ge1-O7	1.76(5)		Zr/Nb-O3	2.03(4)
Ge1-O9	1.74(5)		Zr/Nb-O4	2.05(4)
			Zr/Nb-O5	2.05(4)
Ge2-O1	1.76(5)		Zr/Nb-O6	2.05(4)
Ge2-O3	1.72(5)			
Ge2-O8	1.76(6)		Av K1-O	3.21
Ge2-O9	1.76(5)			
			Av K2-O	3.04
Ge3-O4	1.77(5)			
Ge3-O6	1.78(5)			
Ge3-O7	1.74(5)			
Ge3-O8	1.75(6)			

The Rietveld refinements shown in Figures 4.5 through 4.7 results in a similar quality of fit as the parent $K_2ZrGe_3O_9 \cdot H_2O$ phase in Chapter 3. Better quality fits would be preferred however very subtle peak splitting could be present in the doped umbite materials, as shown by Figure 4.8.

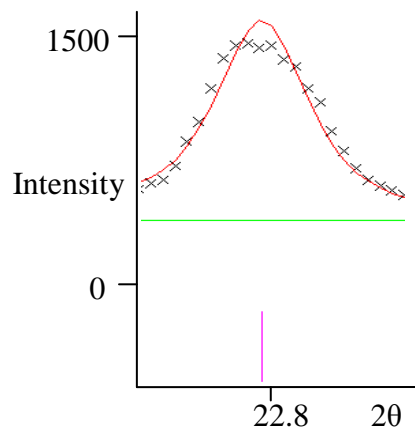


Figure 4.8: Example of peak splitting in the 0.1Nb doped umbite refinement

This provides more evidence that zirconogermanate umbites may not crystallise in an orthorhombic space group, probably better described by a monoclinic cell. Unfortunately deriving a model which better fits the experimental data, has as of yet, been unsuccessful.

Tables 4.5, 4.7 and 4.9 give much better understanding of the impact of niobium doping on the umbite structure. Unit cell parameters remain fairly consistent, confirming what was observed in the minimal variation in the initial lab data collected, as shown in Figure 4.3. A greater understanding on the impact of niobium doping on the two cation environments in the umbite structure can also be explored. The occupancies were initially set as even for both cation sites however this changes on refinement. Cation site one, where potassium is bound to inter pore water and the framework with a coordination of seven, refines to a lower occupancy. Cation site two, in which potassium is bound to only the framework with a coordination of eight, refines to a higher occupancy.

This is consistent across all the doped materials with the majority of the vacancies, created by niobium doping, being found at cation site one. A possible reason for this could be the difficulty of removing potassium at cation site two, which is fully bound to the framework, with a calculated average bond length closer to the expected K-O bond length of approximately 3 Å. Potassium at cation site one is bound to both the framework and extra framework water and could result in a less favourable environment for potassium, reflected by the longer K-O bonds observed.

4.3.5 Cs-exchange of niobium doped zirconogermanate umbites

Analysis of the Cs-exchange was further probed with high resolution powder diffraction ($\lambda = 0.82525 \text{ \AA}$). A significant amount of peak splitting was observed for the exchanged samples

and a significantly more complicated diffraction pattern when compared to the unexchanged samples, as shown by Figure 4.9.

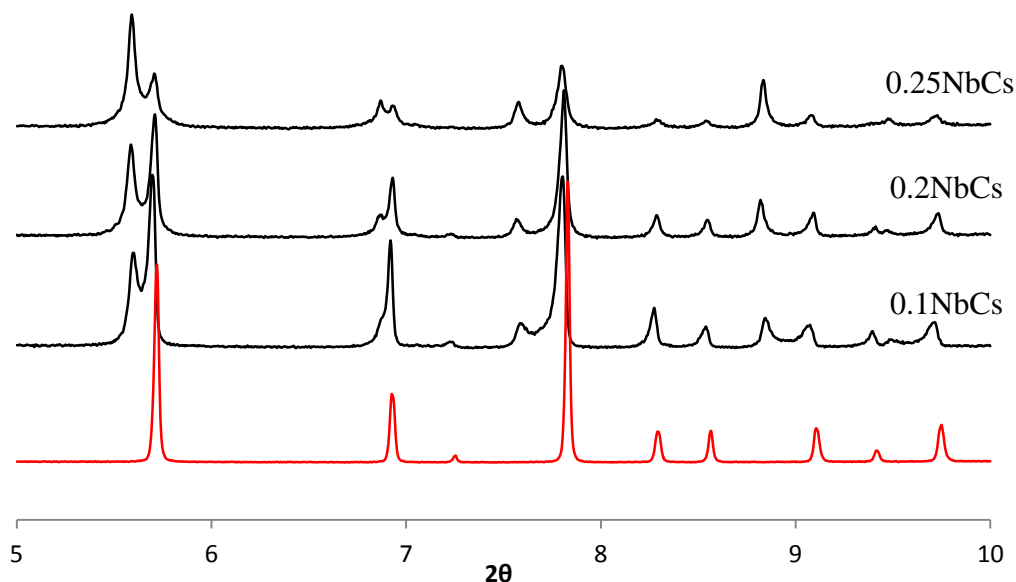


Figure 4.9: Peak splitting observed for the Cs-exchanged doped umbites, parent umbite pattern (Red) added for comparison.

The peak splitting could be described by a reduction of symmetry and the introduction of a non 90° angle. Monoclinic behaviour has been observed in umbite before, as described in Section 3.1 and this was initially explored for the exchanged samples. However the splitting was not accurately modelled by a monoclinic cell, with no stable models derived to fit the experimental data.

The peak splitting observed varies in relative intensity with increasing niobium content and subsequent increased caesium uptake, as shown in Figure 4.9. As the caesium content increases the intensity of the split peak at lower 2θ increases, which suggests that this phase is caesium rich, as you would expect a larger unit cell due to the larger caesium cation. This

would suggest that there are two distinct phases in the diffraction data and not a single exchanged phase.

As the parent material exchange is substantially worse exchanger than the doped material, it is possible that the two phases observed are the undoped parent and a niobium doped caesium exchanged phase. If this was the case then it would be difficult to tell from diffraction data due to the small variation in lattice parameter. It is more likely that it is a combination of a caesium and potassium rich exchanged phases, this would also explain the variation in relative intensities observed, the 0.25Nb phase has a higher uptake from XRF and as a result the caesium rich phase is the major phase.

Refinement of Cs-exchanged 0.1Nb umbite

As covered in Section 3.3.4 there are two potential models, derived by Poojary *et al.*, which can be used as a basis for the refinement;

1. Unexchanged parent phase ($\text{K}_2\text{ZrSi}_3\text{O}_9 \cdot \text{H}_2\text{O}$)
2. Cs-exchanged phase ($\text{Cs}_{1.1}\text{K}_{0.9}\text{ZrSi}_3\text{O}_9 \cdot \text{H}_2\text{O}$)

It has been shown that modifying the parent unexchanged phase allows for a relatively good fit for both the parent phase and the unexchanged doped phases. This model also provided a good fit for the Cs-exchanged parent as shown in Section 3.3.4.

In this case, the Cs-exchange model derived by Poojary *et al.* [79] did not provide a suitable fit for the reported exchanged data in Chapter 3; however it should more accurately represent high caesium umbites from which it was derived. In order to achieve the best possible refinement it was decided to try several different combinations of starting models for the exchanged 0.1Nb doped sample. It was initially assumed that there is a combination of two

exchanged phases, with one phase having substantially more caesium than the other. The Poojary *et al.* caesium exchanged model poorly fits the assumed caesium rich phase and is complicated by the variations in water occupancies for cation site one and three. This is reflected in the poor fitting to the observed peak splitting, as shown by Figure 4.10. For each two phase refinement, the blue tick marks indicate the Cs-rich phase and the pink tick marks the K-rich phase.

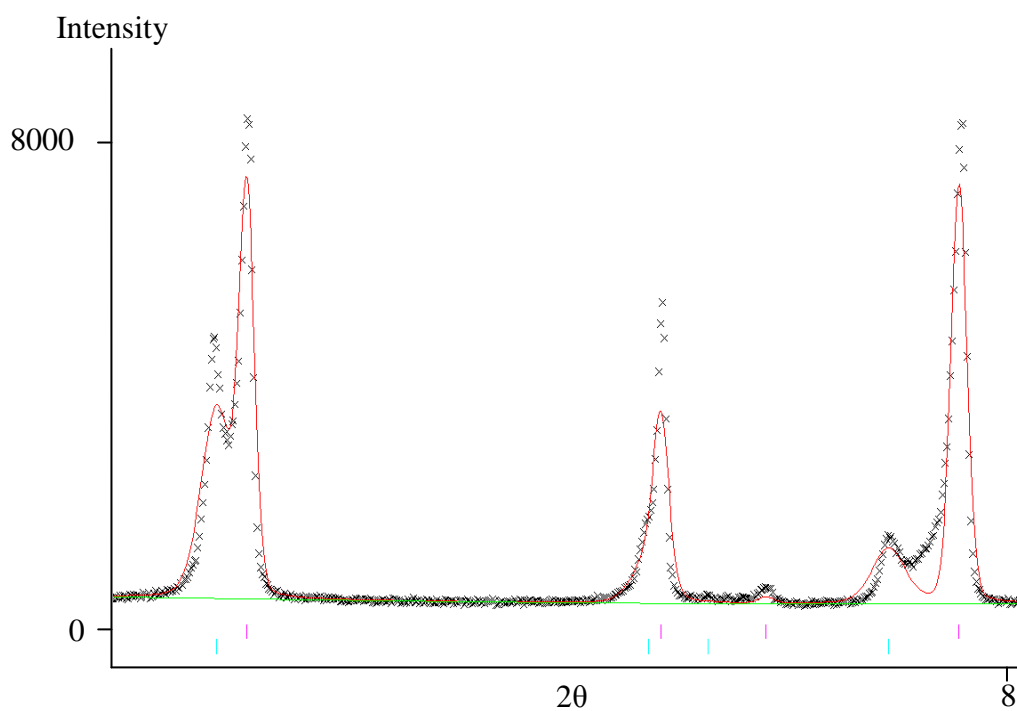


Figure 4.10: Attempted fitting of peak splitting using the exchanged Poojary model.

Applying this model to the potassium rich phase resulted in a poor quality fit to the experimental data and, as reported in Chapter 3, does not accurately fit the lower intensity peaks. This combination of models did not accurately represent the expected two phase model, resulting in a poor refinement, as shown in Figure 4.11.

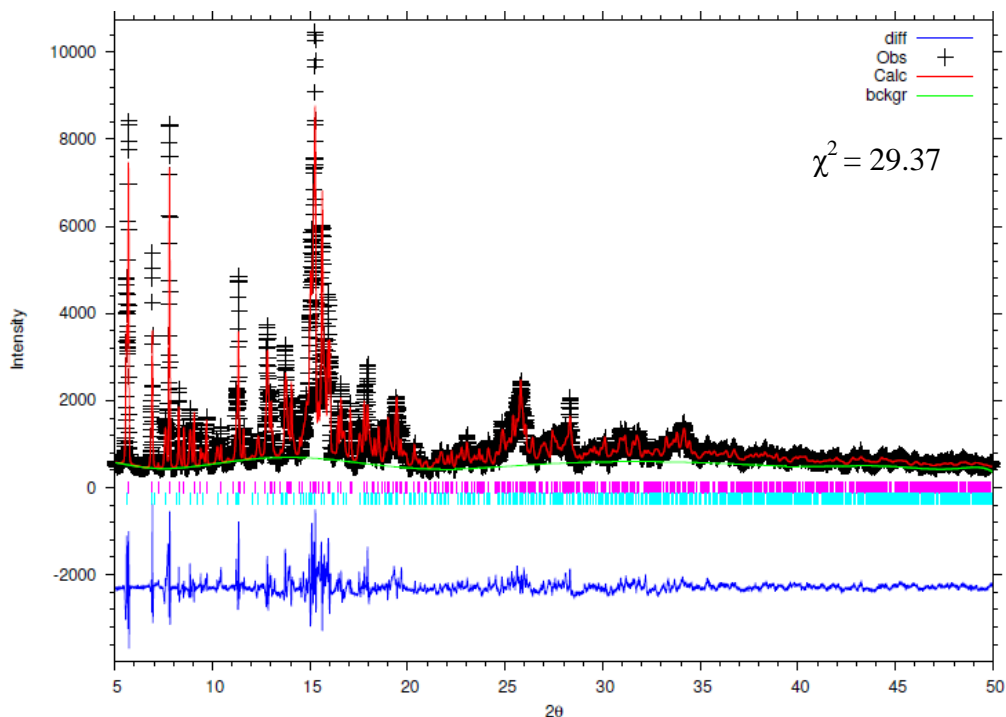


Figure 4.11: Rietveld refinement of Cs-exchanged 0.1Nb umbite using the exchanged Poojary model.

A two phase refinement using the modified zirconosilicate model, as discussed in Chapter 3, resulted in a better quality fit and the most stable refinement. For both phases caesium was added and the cation occupancies were allowed to refine under constraints, with cation occupancy at each site dictated by the refined values from Table 4.5. Restraints were applied to Ge-O and Zr-O bonds of 1.74 Å and 2.07 Å respectively.

Figure 4.12 shows the refinement for the 0.1Nb Cs-exchanged sample, the quality of fit can be improved however the combination of phases has provided the most stable refinement, with much better modelling of peak splitting, Figure 4.13. Peak shape is still an issue despite the use of asymmetry terms to better fit the peaks, with the complex region around 15° 2θ being poorly fit, however this is consistent across all umbite refinements shown in this work.

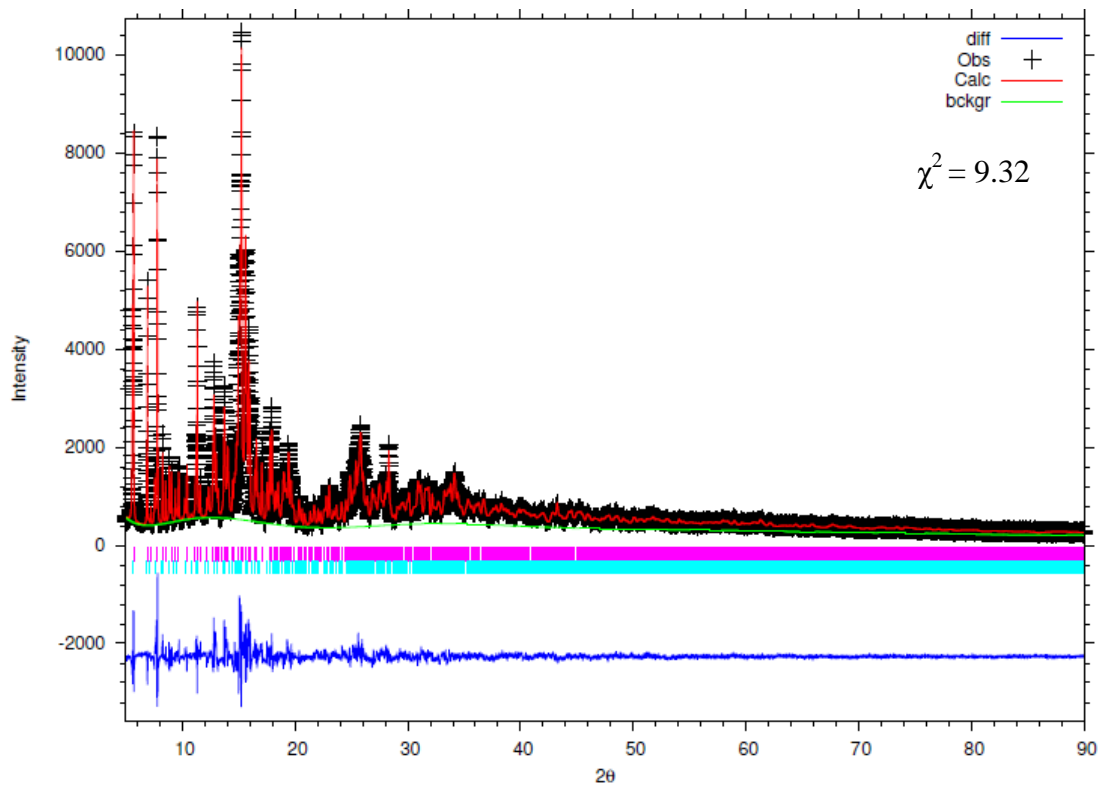


Figure 4.12: 2 Phase refinement of Cs-exchanged 0.1Nb umbite

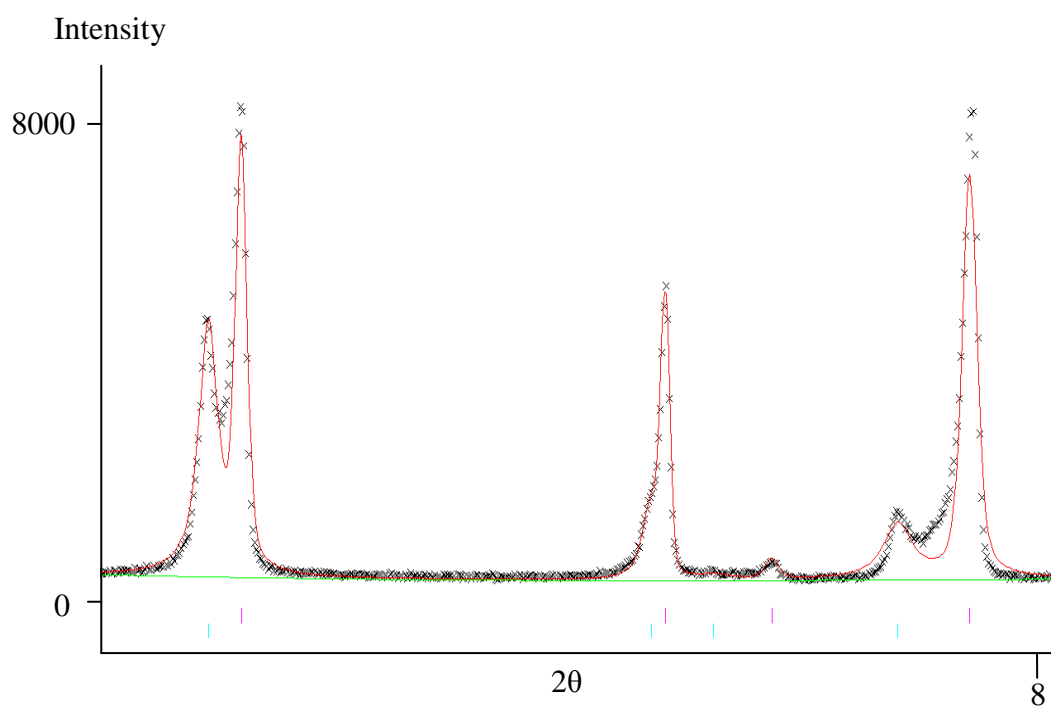


Figure 4.13: Expanded view of figure 4.12 showing fitting to the peak splitting observed.

From this caesium occupancy can be estimated for both the phases and weight fractions can be determined. The caesium occupancies, Table 4.11, show almost complete exchange at cation site two and partial exchange for potassium at cation site one for the more exchanged phase. This gives a formula of approximately $\text{Cs}_{1.20}\text{K}_{0.70}\text{Zr}_{0.9}\text{Nb}_{0.1}\text{Ge}_3\text{O}_9 \cdot \text{H}_2\text{O}$ with over half of the total potassium cations being exchanged for caesium.

Table 4.11: Lattice parameters, caesium occupancies and weight fractions from the two phase Rietveld refinement of Cs-exchanged 0.1Nb umbite.

Formula $X=\text{Zr}_{0.9}\text{Nb}_{0.1}\text{Ge}_3\text{O}_9\cdot\text{H}_2\text{O}$	$\text{Cs}_{0.27}\text{K}_{1.63}\text{X}$	$\text{Cs}_{1.20}\text{K}_{0.70}\text{X}$
$a / \text{Å}$	10.4476(5)	10.6848(4)
$b / \text{Å}$	13.6689(3)	13.7514(6)
$c / \text{Å}$	7.4538(2)	7.6728(4)
$V / \text{Å}^3$	1064.45(7)	1127.37(8)
Weight fraction	0.48	0.52
Cs occupancy site 1	0.202(6)	0.330(8)
Cs occupancy site 2	0.067(5)	0.866(9)

Weight fractions for both of the phases are very similar, suggesting equal amounts of both phases in this sample. The exchange mechanism determined by Celestian *et al.* for umbite, as covered in Chapter 3, suggests exchange occurs preferentially at cation site two which then allows diffusion into the channel system. This is supported by calculated occupancies for the doped zirconogermanate, with substantially lower caesium occupancy for cation site one. This is in good agreement with the caesium occupancies of zirconosilicate from the literature, as described by Table 3.7.

Refinement of Cs-exchanged 0.2Nb umbite

This strategy has also been applied to the 0.2Nb Cs-exchanged high-resolution powder diffraction data, once again providing a much more stable model and a slightly better refinement than that achieved with the exchanged 0.1Nb, as shown in Figure 4.14. For both phases caesium was added and the cation occupancies were allowed to refine under

constraints, with total cation occupancy at each site dictated by the refined values from Table 4.7. Restraints were applied to Ge-O and Zr-O bonds of 1.74 Å and 2.07 Å respectively. Figure 4.15 shows the quality of fit for the peak splitting using the two phase model.

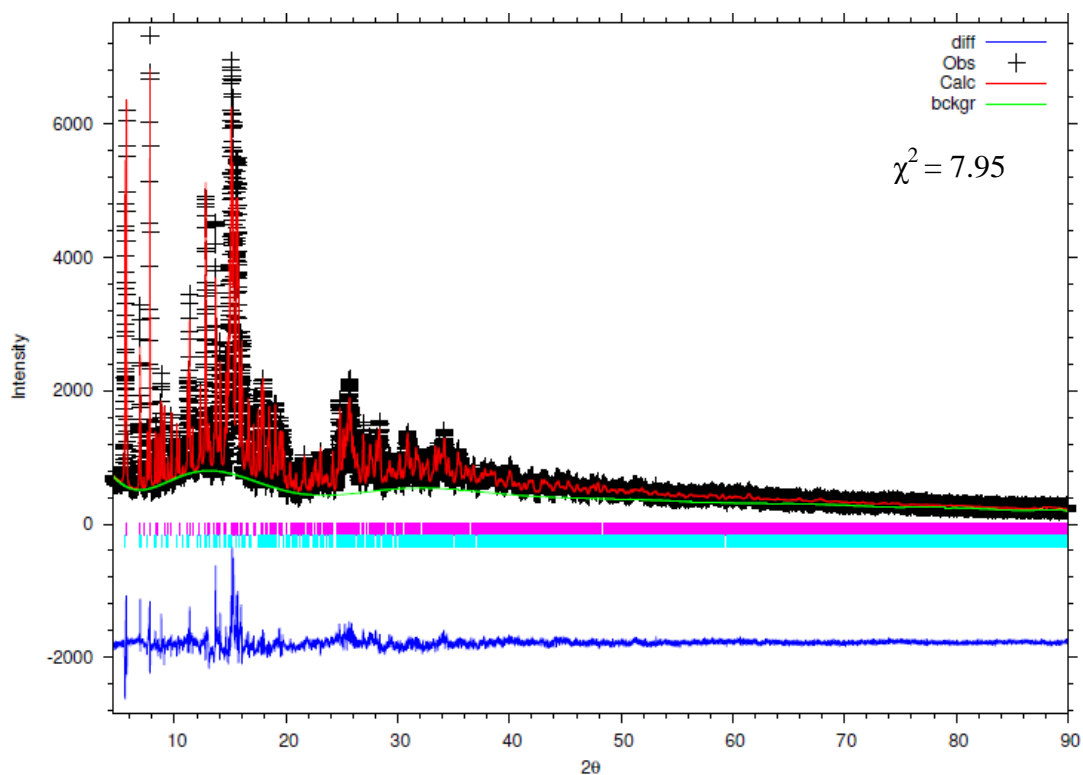


Figure 4.14: 2 Phase refinement of Cs-exchanged 0.2Nb umbite

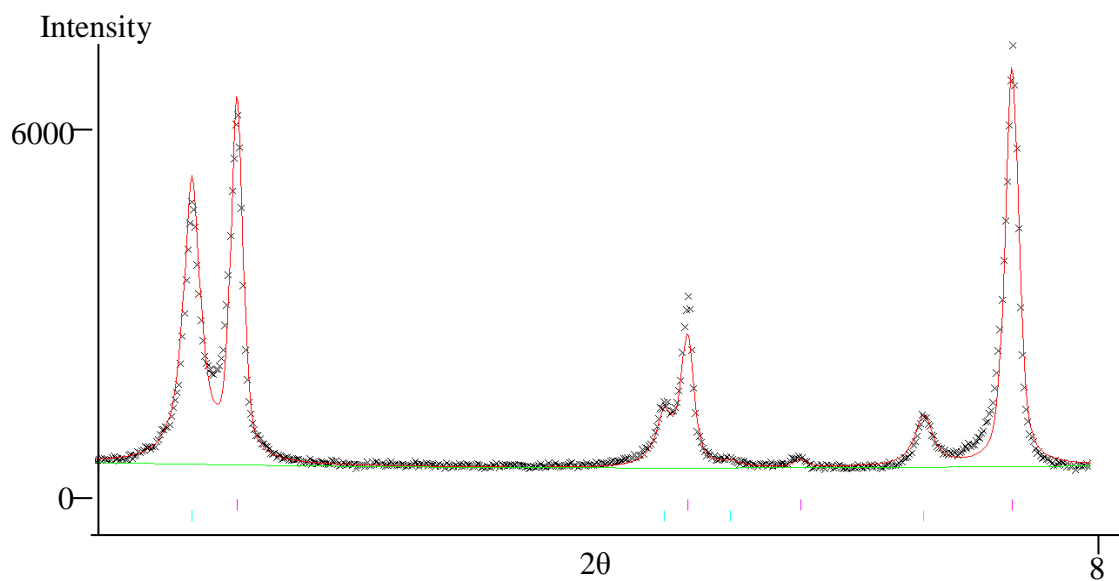


Figure 4.15: Expanded view of figure 4.14 showing fitting to the peak splitting observed.

The occupancies in Table 4.12 show that cation site two is almost fully occupied with caesium and cations site one is once again partially exchanged but to a higher caesium occupancy than the 0.1Nb material.

Table 4.12: Lattice parameters, caesium occupancies and weight fractions from the two phase Rietveld refinement of Cs-exchanged 0.2Nb umbite.

Formula $X=\text{Zr}_{0.8}\text{Nb}_{0.2}\text{Ge}_3\text{O}_9\cdot\text{H}_2\text{O}$	$\text{Cs}_{0.20}\text{K}_{1.6}\text{X}$	$\text{Cs}_{1.31}\text{K}_{0.49}\text{X}$
$a / \text{Å}$	10.4164(3)	10.7229(3)
$b / \text{Å}$	13.6491(3)	13.7714(4)
$c / \text{Å}$	7.4454(2)	7.6886(2)
$V / \text{Å}^3$	1058.53(4)	1135.38(4)
Weight fraction	0.40	0.60
Cs occupancy site 1	0.117(7)	0.446(4)
Cs occupancy site 2	0.081(6)	0.866(5)

This gives a formula of approximately $\text{Cs}_{1.31}\text{K}_{0.49}\text{Zr}_{0.8}\text{Nb}_{0.2}\text{Ge}_3\text{O}_9\cdot\text{H}_2\text{O}$ for the caesium rich phase and weight fraction showing that this is the major phase.

Refinement of Cs-exchanged 0.25Nb umbite

Figures 4.16 and 4.17 demonstrate the quality of the refinement for the 0.25Nb exchange using a two phase fit. For both phases caesium was added and the cation occupancies were allowed to refine under constraints, with total cation occupancy at each site dictated by the refined values from Table 4.9. Restraints were applied to Ge-O and Zr-O bonds of 1.74 Å and 2.07 Å respectively.

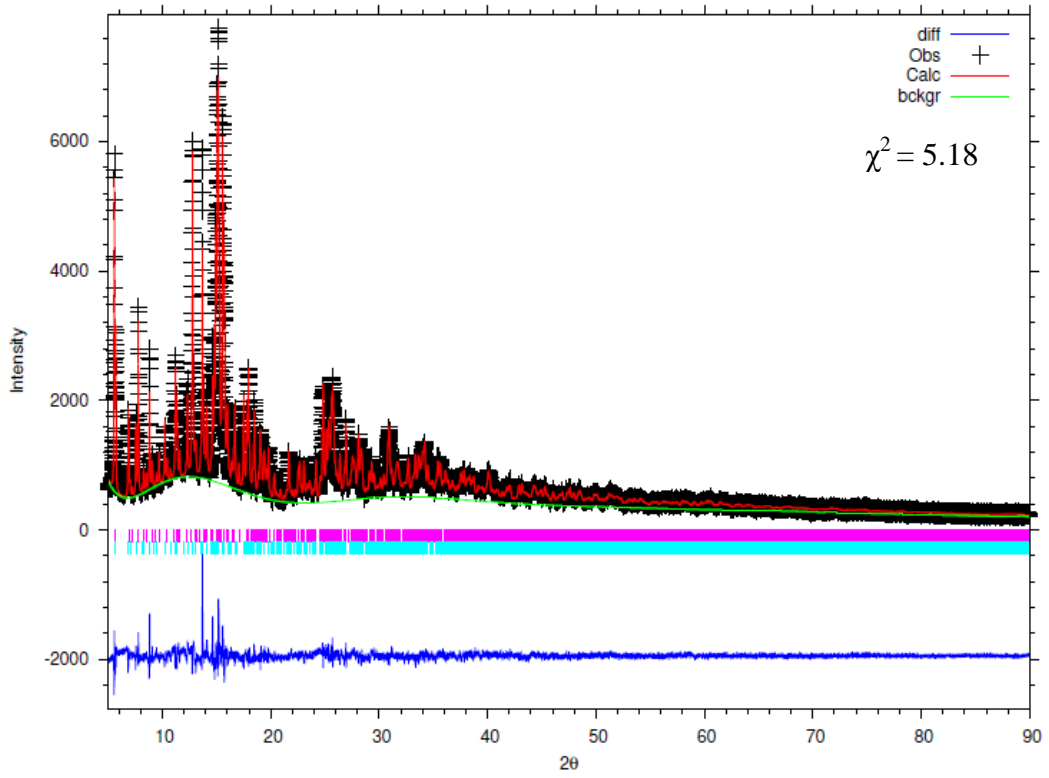


Figure 4.16: 2 Phase refinement of Cs-exchanged 0.25Nb umbite

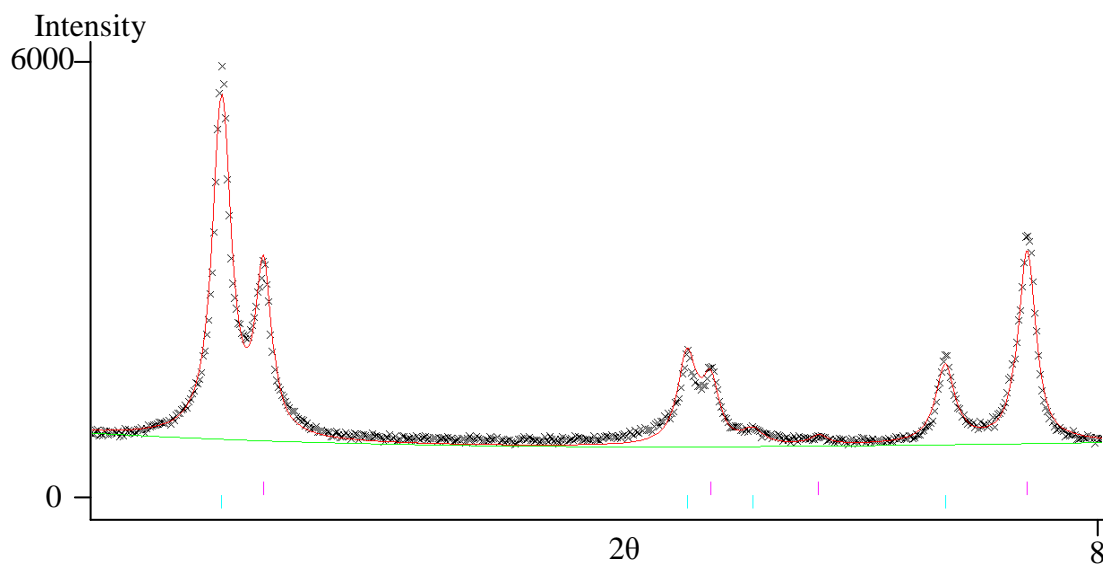


Figure 4.17: Expanded view of figure 4.16 showing fitting to the peak splitting observed.

The results of the refinement results are shown in Table 4.13, with occupancies for the caesium phase similar to those shown in Table 4.12; however the potassium rich phase contains substantially more caesium than in the other doped materials.

Table 4.13: Lattice parameters, caesium occupancies and weight fractions from the two phase Rietveld refinement of Cs-exchanged 0.25Nb umbite.

Formula	$\text{Cs}_{0.40}\text{K}_{1.35}\text{X}$	$\text{Cs}_{1.34}\text{K}_{0.41}\text{X}$
$\text{X}=\text{Zr}_{0.75}\text{Nb}_{0.25}\text{Ge}_3\text{O}_9\cdot\text{H}_2\text{O}$		
$a / \text{Å}$	10.4241(5)	10.7090(2)
$b / \text{Å}$	13.6416(6)	13.7683(2)
$c / \text{Å}$	7.4545(4)	7.6822 (1)
$V / \text{Å}^3$	1060.06(6)	1132.70(2)
Weight fraction	0.27	0.73
Cs occupancy site 1	0.204(8)	0.473(3)
Cs occupancy site 2	0.200(6)	0.870(4)

The 0.25Nb exchanged sample shows increased Cs uptake relative to the other doped materials, matching the trend observed in the XRF data. Once again cation site 2 is nearly fully occupied by caesium, which is consistent across all doped material with very similar occupancies observed in each case. The differences between them originate from the relative weight fractions and the occupancy of cation site one, which increased with niobium doping. As shown in Table 4.13 the majority of the sample is the exchanged form and cation site one is approximately half occupied by caesium. Possible reasons for this will be explored in Section 4.3.8. Table 4.14 summarises the refined weight fractions and Cs occupancies for the niobium doped samples.

Table 4.14: Summary table for the refinements of Cs-exchanged Nb doped umbites.

	10Nb		20Nb		25Nb	
	Cs _{0.27} K _{1.63}	Cs _{1.20} K _{0.70}	Cs _{0.20} K _{1.60}	Cs _{1.31} K _{0.49}	Cs _{0.40} K _{1.35}	Cs _{1.34} K _{0.41}
Weight fraction (%)	48	52	40	60	27	73
Cation site one - Cs occupancy	0.202(6)	0.330(8)	0.117(7)	0.446(4)	0.204(8)	0.473(3)
Cation site two - Cs occupancy	0.067(5)	0.866(9)	0.081(6)	0.866(5)	0.200(6)	0.870(4)

4.3.6 Antimony doping of zirconogermanate umbite, $K_{2-x}Zr_{1-x}Sb_xGe_3O_9 \cdot H_2O$

To explore whether the doping of umbite and subsequent interesting ion exchange behaviour is unique to niobium, it was decided to try and dope the umbite structure with another 5^+ metal and compare the ion exchange behaviour. Antimony was chosen as the dopant as it has a 5^+ oxidation state which occupies a six coordination geometry and is a similar size to niobium (0.64\AA Nb vs 0.6\AA Sb). A modified synthesis outlined in Section 4.2.2 was used with the oxide being chosen as the antimony source due to ease of use compared to the pentachloride, this however would present some issues due to the limited solubility of Sb_2O_5 in the weakly basic umbite synthesis. The targeted doping levels are once again $x = 0.1, 0.2$ and 0.25 for zirconium, with the assumption that $0.25Sb$ is the maximum doping level possible in the umbite structure.

Analysis of these materials by high-resolution powder diffraction data shows these materials are all single phase up to $0.25Sb$, with Rietveld refinements once again fitting best to a modified $P2_12_12_1$ orthorhombic cell, as shown in Figures 4.18 to 4.20.

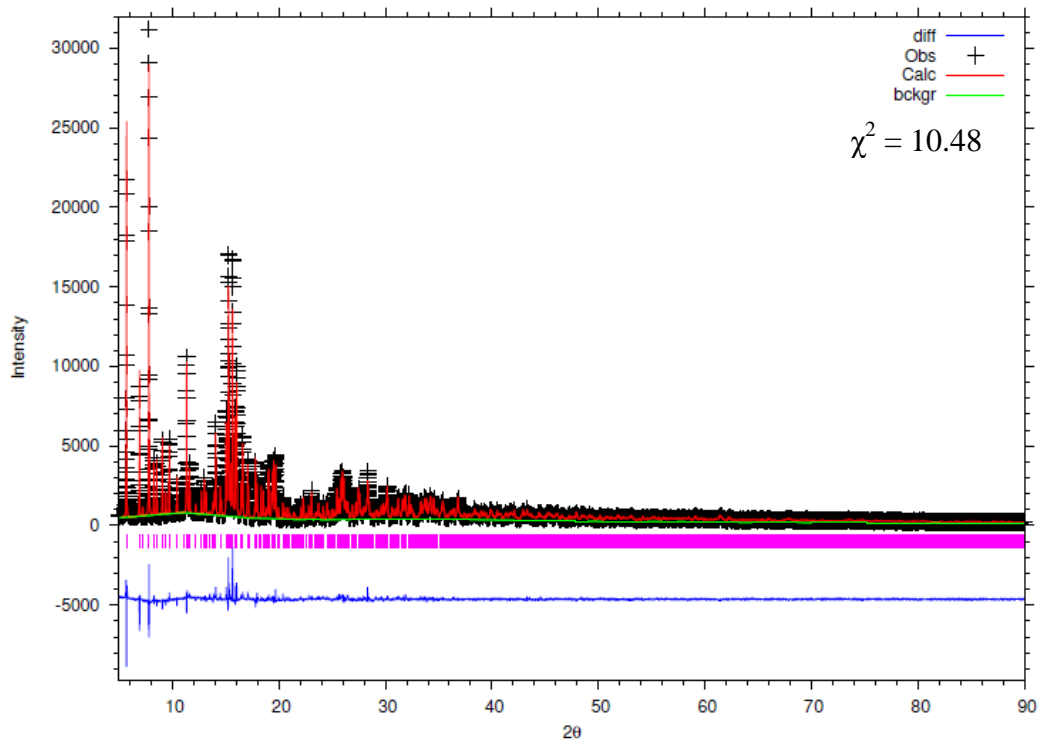


Figure 4.18: Rietveld refinement for $\text{K}_{1.9}\text{Zr}_{0.9}\text{Sb}_{0.1}\text{Ge}_3\text{O}_9\cdot\text{H}_2\text{O}$.

The quality of the Rietveld refinement is similar to both Nb doping and the parent, however it is of note that careful use of restraints was required to prevent substantial lengthening of Ge-O bonds. Restraints were applied to Ge-O and Zr-O bonds of 1.74 Å and 2.07 Å respectively. This bond lengthening worsens with increasing antimony content, improving the χ^2 however reducing chemical viability of the refinement. This is shown in bond length tables for the Rietveld refinements, where the Ge-O bond lengths range from 1.66 to 1.80 Å, suggesting some degree of distortion of the tetrahedra. This is also reflected by the increasing errors in the bond lengths; however this is made significantly worse if the refinement is not carefully restrained. Cation occupancies were refined under constraints with total cation content fixed by doping level.

Table 4.15: Lattice parameters, atomic positions, occupancy and thermal parameters for the refinement of $\text{K}_{1.9}\text{Zr}_{0.9}\text{Sb}_{0.1}\text{Ge}_3\text{O}_9 \cdot \text{H}_2\text{O}$. Thermal parameters are grouped by element.

$\lambda / \text{\AA}$	0.82525				
$a / \text{\AA}$	10.4166(1)				
$b / \text{\AA}$	13.6567(1)				
$c / \text{\AA}$	7.4394(1)				
$V / \text{\AA}^3$	1058.29(2)				
<i>Space Group</i>	$P2_12_12_1$				
R_{wp}	0.0849				
R_{exp}	0.0262				
χ^2	10.48				
<i>Site</i>	<i>x</i>	<i>y</i>	<i>z</i>	<i>Occupancy</i>	U_{iso}
Zr1	0.4567(2)	0.2101(1)	0.2644(3)	0.9	0.0057(5)
Ge1	0.1877(2)	0.1718(2)	-0.0090(3)	1	0.0029(3)
Ge2	0.0310(2)	0.0451(1)	0.7248(3)	1	0.0029(3)
Ge3	0.6367(2)	0.3377(2)	0.5943(3)	1	0.0029(3)
O1	0.4248(7)	0.3570(3)	0.2365(17)	1	0.0110(12)
O2	0.3456(6)	0.1951(10)	0.0425(8)	1	0.0110(12)
O3	0.5246(7)	0.0712(3)	0.2772(16)	1	0.0110(12)
O4	0.5551(10)	0.2381(2)	0.4949(10)	1	0.0110(12)
O5	0.6219(7)	0.2254(5)	0.1194(13)	1	0.0110(12)
O6	0.3030(5)	0.1842(10)	0.4279(9)	1	0.0110(12)
O7	0.0944(7)	0.1426(8)	0.1812(6)	1	0.0110(12)
O8	0.0820(10)	0.0528(5)	0.4998(8)	1	0.0110(12)
O9	0.1688(7)	0.0697(6)	0.8519(13)	1	0.0110(12)
K1	0.2195(5)	0.6226(3)	0.1260(6)	0.909(3)	0.0121(10)
K2	0.4408(4)	0.0797(3)	0.7077(6)	0.991(3)	0.0121(10)
O10	0.7023(11)	0.0625(8)	0.8784(15)	1	0.0110(12)
Sb1	0.4567(2)	0.2101(1)	0.2644(3)	0.1	0.0057(5)

Table 4.16: Selected bond lengths from the refinement of $K_{1.9}Zr_{0.9}Sb_{0.1}Ge_3O_9 \cdot H_2O$.

<i>Bond</i>	<i>Distance (Å)</i>		<i>Bond</i>	<i>Distance (Å)</i>
Ge1-O2	1.72(4)		Zr/Sb-O1	2.04(3)
Ge1-O5	1.77(4)		Zr/Sb-O2	2.03(3)
Ge1-O7	1.76(4)		Zr/Sb-O3	2.03(3)
Ge1-O9	1.75(5)		Zr/Sb-O4	2.03(3)
			Zr/Sb-O5	2.04(3)
Ge2-O1	1.76(4)		Zr/Sb-O6	2.04(3)
Ge2-O3	1.73(4)			
Ge2-O8	1.76(5)		Av K1-O	3.20
Ge2-O9	1.75(4)			
			Av K2-O	3.03
Ge3-O4	1.77(4)			
Ge3-O6	1.77(4)			
Ge3-O7	1.75(4)			
Ge3-O8	1.75(5)			

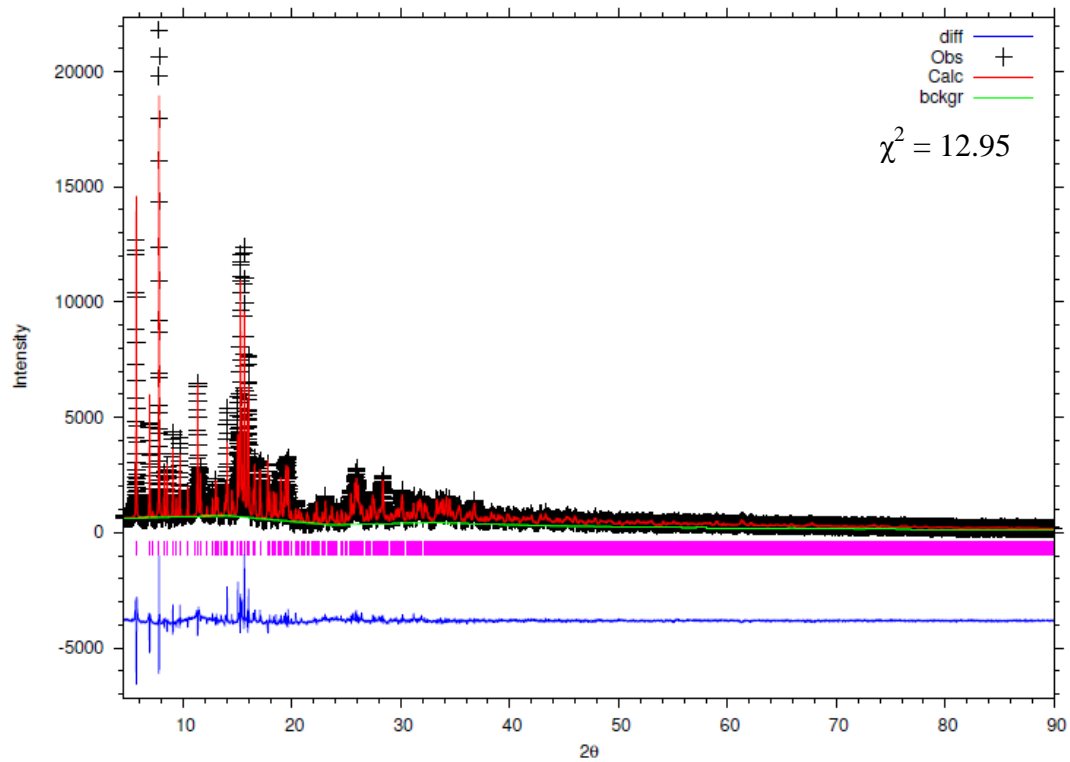


Figure 4.19: Rietveld refinement for $K_{1.8}Zr_{0.8}Sb_{0.2}Ge_3O_9 \cdot H_2O$.

Table 4.17: Lattice parameters, atomic parameters, occupancy and thermal parameters for the refinement of $\text{K}_{1.8}\text{Zr}_{0.8}\text{Sb}_{0.2}\text{Ge}_3\text{O}_9\cdot\text{H}_2\text{O}$. Thermal parameters are grouped by element.

$\lambda/\text{\AA}$	0.82525				
$a/\text{\AA}$	10.4404(2)				
$b/\text{\AA}$	13.6579(2)				
$c/\text{\AA}$	7.4552(1)				
$V/\text{\AA}^3$	1063.08(4)				
<i>Space Group</i>	$P2_12_12_1$				
R_{wp}	0.1019				
R_{exp}	0.0283				
χ^2	12.95				
Site	x	y	z	Occupancy	U_{iso}
Zr1	0.4576(3)	0.2110(2)	0.2632(4)	0.8	0.0056(6)
Ge1	0.1874(3)	0.1724(2)	-0.0076(5)	1	0.0001(4)
Ge2	0.0308(3)	0.0447(2)	0.7259(5)	1	0.0001(4)
Ge3	0.6370(3)	0.3371(2)	0.5912(4)	1	0.0001(4)
O1	0.4238(10)	0.3579(4)	0.2322(24)	1	0.0062(16)
O2	0.3345(10)	0.2232(11)	0.0501(14)	1	0.0062(16)
O3	0.5197(11)	0.0712(4)	0.2649(26)	1	0.0062(16)
O4	0.5605(14)	0.2346(8)	0.4922(14)	1	0.0062(16)
O5	0.6267(9)	0.2217(8)	0.1217(19)	1	0.0062(16)
O6	0.3059(7)	0.1840(13)	0.4335(13)	1	0.0062(16)
O7	0.0978(11)	0.1402(10)	0.1848(9)	1	0.0062(16)
O8	0.0829(14)	0.0520(7)	0.5012(12)	1	0.0062(16)
O9	0.1673(11)	0.0669(8)	0.8629(19)	1	0.0062(16)
K1	0.2231(7)	0.6165(5)	0.1214(10)	0.818(5)	0.0067(13)
K2	0.4424(6)	0.0778(4)	0.7089(9)	0.982(5)	0.0067(13)
O10	0.7055(16)	0.0496(11)	0.8939(22)	1	0.0062(16)
Sb1	0.4576(3)	0.2110(2)	0.2632(4)	0.2	0.0056(6)

Table 4.18: Selected bond lengths from the refinement of $K_{1.8}Zr_{0.8}Sb_{0.2}Ge_3O_9 \cdot H_2O$.

<i>Bond</i>	<i>Distance (Å)</i>		<i>Bond</i>	<i>Distance (Å)</i>
Ge1-O2	1.74(7)		Zr/Sb-O1	2.05(5)
Ge1-O5	1.79(7)		Zr/Sb-O2	2.05(5)
Ge1-O7	1.77(7)		Zr/Sb-O3	2.02(5)
Ge1-O9	1.75(7)		Zr/Sb-O4	2.04(5)
			Zr/Sb-O5	2.06(5)
Ge2-O1	1.77(7)		Zr/Sb-O6	2.06(5)
Ge2-O3	1.69(6)			
Ge2-O8	1.76(7)		Av K1-O	3.16
Ge2-O9	1.78(7)			
			Av K2-O	3.08
Ge3-O4	1.77(7)			
Ge3-O6	1.80(7)			
Ge3-O7	1.75(7)			
Ge3-O8	1.76(7)			

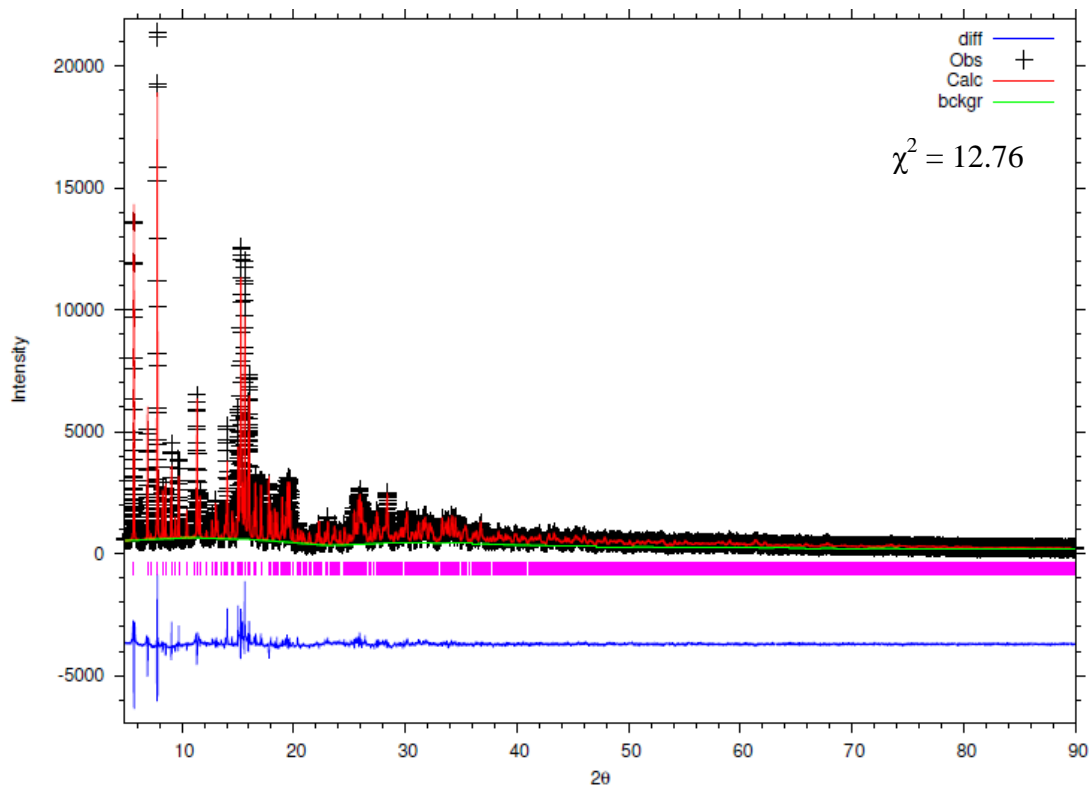


Figure 4.20: Rietveld refinement for $\text{K}_{1.75}\text{Zr}_{0.75}\text{Sb}_{0.25}\text{Ge}_3\text{O}_9 \cdot \text{H}_2\text{O}$.

Table 4.19: Lattice parameters, atomic parameters, occupancy and thermal parameters for the refinement of $\text{K}_{1.75}\text{Zr}_{0.75}\text{Sb}_{0.25}\text{Ge}_3\text{O}_9 \cdot \text{H}_2\text{O}$. Thermal parameters are grouped by element.

$\lambda / \text{\AA}$	0.82525				
$a / \text{\AA}$	10.4387(2)				
$b / \text{\AA}$	13.6509(2)				
$c / \text{\AA}$	7.4534(1)				
$V / \text{\AA}^3$	1062.09(4)				
<i>Space Group</i>	$P2_12_12_1$				
R_{wp}	0.1014				
R_{exp}	0.0284				
χ^2	12.76				
<i>Site</i>	<i>x</i>	<i>y</i>	<i>z</i>	<i>Occupancy</i>	<i>U_{iso}</i>
Zr1	0.4576(2)	0.2111(2)	0.2632(4)	0.75	0.0067(6)
Ge1	0.1863(3)	0.1717(2)	-0.0072(5)	1	0.0001(4)
Ge2	0.0307(3)	0.0442(2)	0.7268(5)	1	0.0001(4)
Ge3	0.6373(3)	0.3369(3)	0.5903(5)	1	0.0001(4)
O1	0.4208(11)	0.3600(5)	0.2326(24)	1	0.0128(17)
O2	0.3374(10)	0.2189(12)	0.0415(15)	1	0.0128(17)
O3	0.5198(11)	0.0703(5)	0.2528(30)	1	0.0128(17)
O4	0.5593(15)	0.2353(8)	0.4955(15)	1	0.0128(17)
O5	0.6277(10)	0.2196(8)	0.1175(19)	1	0.0128(17)
O6	0.3070(8)	0.1841(13)	0.4414(14)	1	0.0128(17)
O7	0.0957(12)	0.1428(10)	0.1865(11)	1	0.0128(17)
O8	0.0855(14)	0.0517(8)	0.5036(14)	1	0.0128(17)
O9	0.1670(12)	0.0649(9)	0.8670(19)	1	0.0128(17)
K1	0.2211(7)	0.6195(5)	0.1233(10)	0.800(5)	0.0055(13)
K2	0.4401(6)	0.0788(4)	0.7103(9)	0.950(5)	0.0055(13)
O10	0.7061(17)	0.0488(11)	0.8924(21)	1	0.0128(17)
Sb1	0.4576(2)	0.2111(2)	0.2632(4)	0.25	0.0067(6)

Table 4.20: Selected bond lengths from the refinement of $K_{1.75}Zr_{0.75}Sb_{0.25}Ge_3O_9 \cdot H_2O$.

<i>Bond</i>	<i>Distance (Å)</i>		<i>Bond</i>	<i>Distance (Å)</i>
Ge1-O2	1.74(8)		Zr/Sb-O1	2.08(6)
Ge1-O5	1.80(8)		Zr/Sb-O2	2.07(6)
Ge1-O7	1.77(8)		Zr/Sb-O3	2.03(6)
Ge1-O9	1.75(8)		Zr/Sb-O4	2.06(6)
			Zr/Sb-O5	2.09(6)
Ge2-O1	1.77(8)		Zr/Sb-O6	2.09(6)
Ge2-O3	1.66(7)			
Ge2-O8	1.76(8)		Av K1-O	3.21
Ge2-O9	1.78(8)			
			Av K2-O	3.08
Ge3-O4	1.76(8)			
Ge3-O6	1.81(8)			
Ge3-O7	1.74(8)			
Ge3-O8	1.76(9)			

Refined occupancies for the two cation sites once again show that the majority of the potassium is removed from cation site one, with a minimal negligible removed from cation site two. This is consistent with niobium doping and confirms that the addition of 5^+ metals to the umbite framework creates vacancies in the channel system. The impact this has on the cation uptake of antimony doped umbite is covered in Section 4.3.7.

4.3.7 Ion exchange of antimony doped umbite

Preliminary ion exchange tests show minimal strontium uptake by the antimony doped material and as result was no longer studied. Preliminary loose powder ion exchange data showed the measured caesium uptake on the first three samples synthesised. The same trend is observed as in Section 4.3.5, as the amount of dopant increases so does the caesium uptake, as shown in Table 4.21.

Table 4.21: XRF analysis of Cs-exchanged Sb doped umbites, samples were prepared as loose powders and molar ratios normalised to germanium.

Element	0.1Sb Cs-exchange Molar ratio	0.2Sb Cs-exchange Molar ratio	0.25Sb Cs-exchange Molar ratio
K	0.40	0.32	0.25
Ge	1	1	1
Zr	0.39	0.39	0.38
Sb (Expected)	0.03 (0.033)	0.06 (0.066)	0.08 (0.083)
Cs	0.30	0.35	0.42

However subsequent attempts to repeat this for the 0.25Sb doped sample resulted in substantially lower measured Cs uptake when compared to the first synthesis attempt, as shown in Table 4.22.

Table 4.22: Variation in XRF data shown for the caesium uptake in the 0.25Sb doped sample repeat syntheses.

Element	0.25Sb Cs-exchange Molar ratio #1	0.25Sb Cs-exchange Molar ratio #2
K	0.25	0.35
Ge	1	1
Zr	0.38	0.40
Sb	0.08	0.08
Cs	0.42	0.33

It is likely that the low solubility of antimony oxide is preventing full incorporation of antimony during synthesis, not perturbing umbite formation like higher Nb doping levels, with some antimony forming an amorphous phase which is not observed in the recorded XRD data. This is reflected in the fused bead data shown in Table 4.23, with the reported Cs uptake being higher for the 0.2Sb compared to the 0.25Sb doped samples, it is likely that 0.2Sb for Zr is the most reliable upper limit for doping using this synthesis method. The observed caesium uptake is similar for both the niobium and antimony doped materials up 0.2 doping levels.

Table 4.23: XRF analysis of Cs-exchanged Sb doped umbites, samples were prepared as fused beads and molar ratios normalised to germanium.

Element	0.1Sb Cs-exchange Molar ratio	0.2Sb Cs-exchange Molar ratio	0.25Sb Cs-exchange Molar ratio
K	0.31	0.26	0.31
Ge	1	1	1
Zr	0.39	0.38	0.38
Sb	0.03	0.06	0.08
Cs	0.16	0.22	0.20

High-resolution powder diffraction data for the exchanged samples once again show similar splitting observed in the niobium doped samples, suggesting that it is something intrinsic to these doped samples, as this behaviour has not been reported for umbite materials in the literature. As shown in Figure 4.21, there is variation between the relative intensities as Sb

content increased. The differences between the fused bead XRF data for the 20% and 25% Sb umbite phases is reflected in the high-resolution powder diffraction data ($\lambda = 0.82525 \text{ \AA}$), with regards to the variation in splitting observed for both samples.

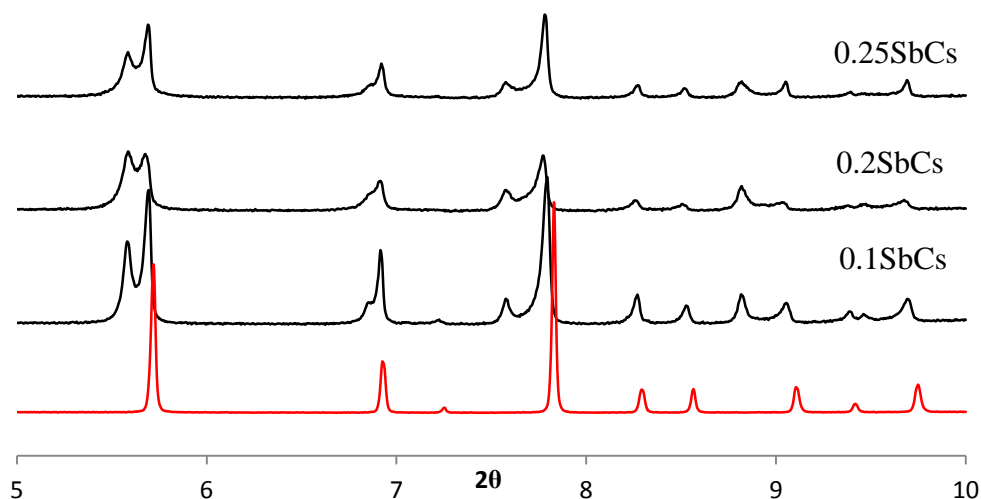


Figure 4.21: Peak splitting observed for the Cs-exchanged Sb doped umbites, parent umbite pattern (Red) added for comparison.

Once again Rietveld refinements used a combination of modified parent umbite models in a two phase refinement, the Caesium rich model derived by Poojary *et al.* did not provide a stable model for refinement.

The Rietveld refinements for $x = 0.1$, 0.2 and 0.25 are shown in Figures 4.22, 4.24 and 4.26. Caesium was added to the two cation sites and occupancies was refined under constraints, with starting cation occupancies at each site dictated by refined values from Tables 4.15, 4.17 and 4.19 respectively. Restraints were applied to Ge-O and Zr-O bonds of 1.74 \AA and 2.07 \AA respectively. The quality of the fit to the peak splitting will also be shown, with the two phase model providing an adequate model this for interesting behaviour.

Refinement of Cs-exchanged 0.1Sb umbite

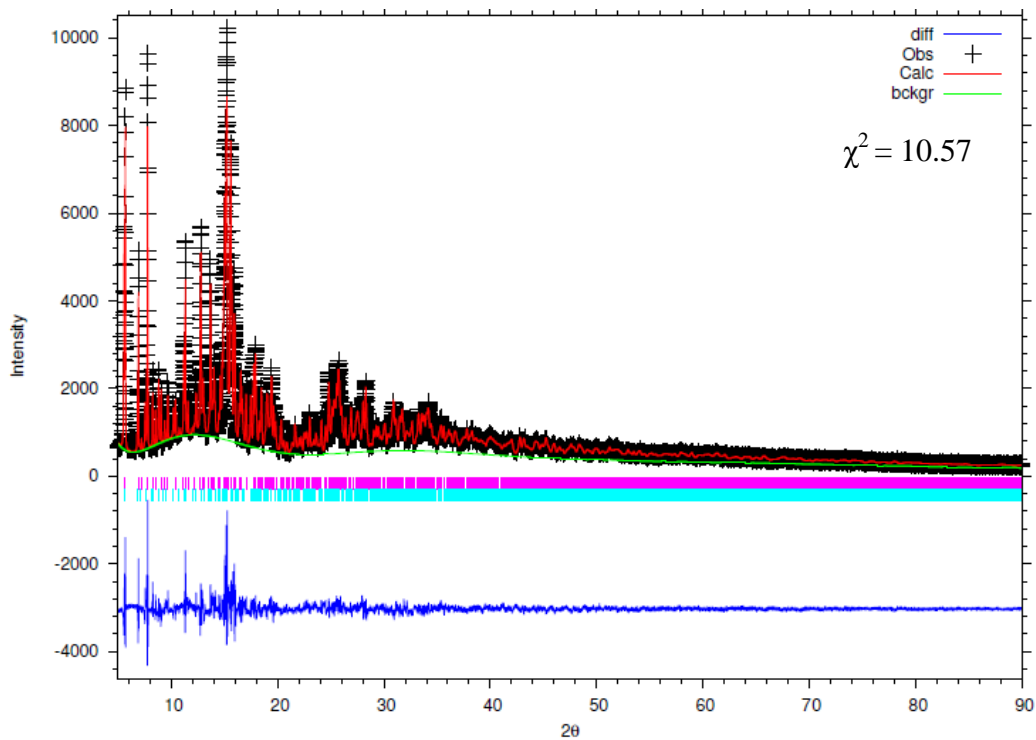


Figure 4.22: Rietveld refinement for Cs-exchanged $K_{1.9}Zr_{0.9}Sb_{0.1}Ge_3O_9 \cdot H_2O$.

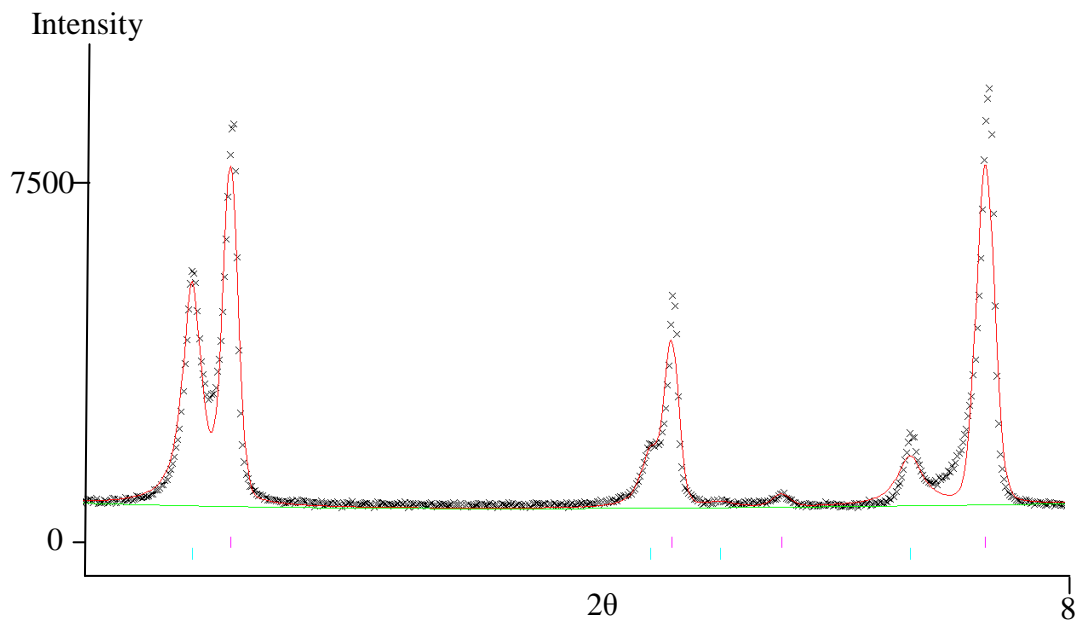


Figure 4.23: Expanded view of figure 4.22 showing fitting to the peak splitting observed.

Table 4.24: Lattice parameters, caesium occupancies and weight fractions from the two phase Rietveld refinement of Cs-exchanged 0.1Sb umbite.

Formula $X=\text{Zr}_{0.9}\text{Sb}_{0.1}\text{Ge}_3\text{O}_9\cdot\text{H}_2\text{O}$	$\text{Cs}_{0.22}\text{K}_{1.68}\text{X}$	$\text{Cs}_{1.29}\text{K}_{0.61}\text{X}$
$a / \text{\AA}$	10.4588(4)	10.7239(3)
$b / \text{\AA}$	13.6772(3)	13.7947(4)
$c / \text{\AA}$	7.4613(2)	7.6754(2)
$V / \text{\AA}^3$	1067.32(4)	1135.45(4)
Weight fraction	0.45	0.55
Cs occupancy site 1	0.131(6)	0.431(8)
Cs occupancy site 2	0.086(5)	0.862(9)

Table 4.24 shows that, as with niobium doping, cation site two is almost fully occupied by caesium and site 1 partially occupied in the caesium rich phase. The potassium rich phase contains only a small amount of caesium, with similar occupancies to that observed previously. Relative weight fractions are also consistent with what has been observed for the 0.1Nb doping, with a relatively even amount of both phases. It is of note that the total caesium exchange is higher for antimony than niobium, with a higher occupancy for cation site one in the exchanged phase.

Refinement of Cs-exchanged 0.2Sb umbite

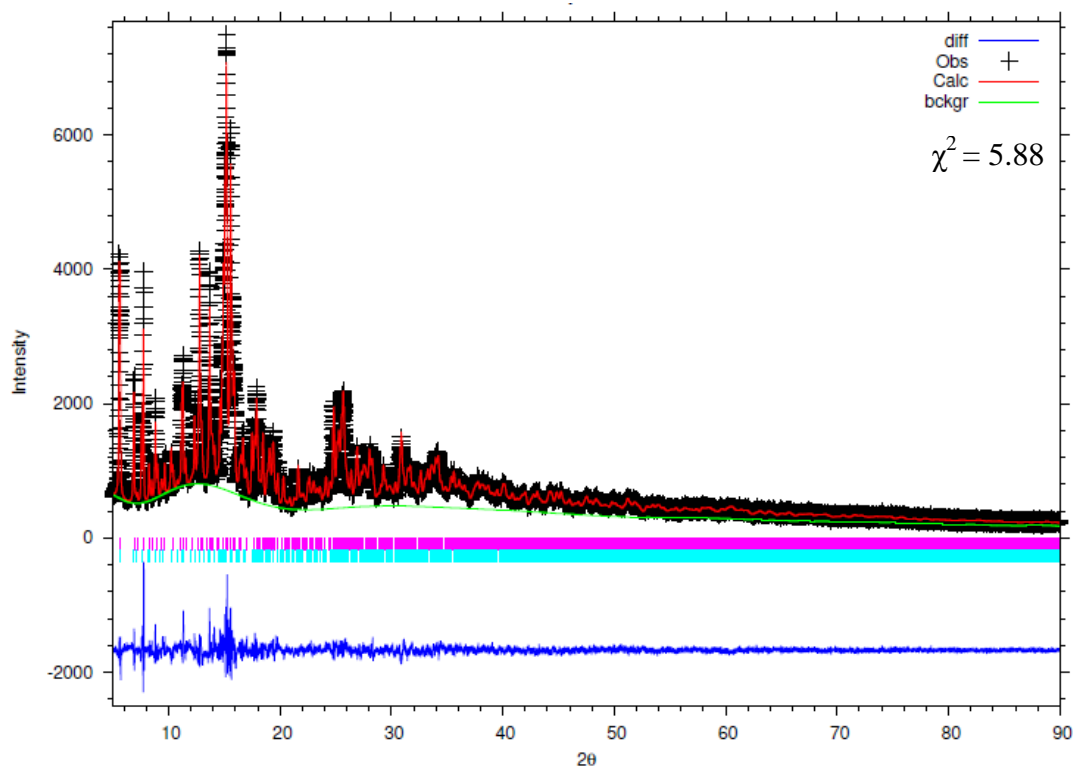


Figure 4.24: Rietveld refinement for Cs-exchanged $K_{1.9}Zr_{0.8}Sb_{0.2}Ge_3O_9 \cdot H_2O$.

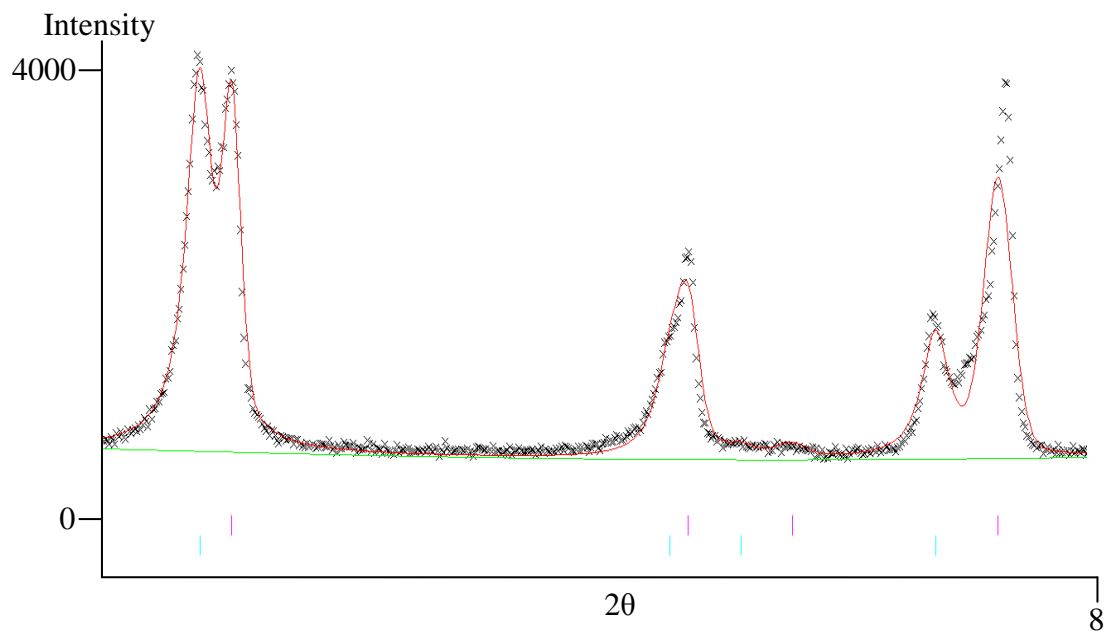


Figure 4.25: Expanded view of figure 4.24 showing fitting to the peak splitting observed.

Table 4.25: Lattice parameters, caesium occupancies and weight fractions from the two phase Rietveld refinement of Cs-exchanged 0.2Sb umbite.

Formula $X=\text{Zr}_{0.8}\text{Sb}_{0.2}\text{Ge}_3\text{O}_9\cdot\text{H}_2\text{O}$	$\text{Cs}_{0.51}\text{K}_{1.29}\text{X}$	$\text{Cs}_{1.25}\text{K}_{0.55}\text{X}$
$a / \text{Å}$	10.5177(9)	10.7336(3)
$b / \text{Å}$	13.7067(9)	13.8054(5)
$c / \text{Å}$	7.5079(6)	7.6820(2)
$V / \text{Å}^3$	1082.37(9)	1138.35(4)
Weight fraction	0.34	0.66
Cs occupancy site 1	0.359(5)	0.394(4)
Cs occupancy site 2	0.150(5)	0.853(4)

Table 4.25 shows that occupancies are in good agreement with those observed before, the calculated occupancies show exchange for the caesium rich phase is lower. However the reduced potassium content in the starting sample means that caesium exchange is equivalent to that of the 0.1Sb exchanged sample. Interestingly the potassium rich phase also contains substantially more caesium than in previous samples, suggesting different exchange characteristics to its niobium doped equivalent. The overall exchange is substantially higher than the equivalent niobium doped sample, this causes some discrepancies with the recorded XRF data which was shown to be very similar for both dopants.

Refinement of Cs-exchanged 0.25Sb umbite

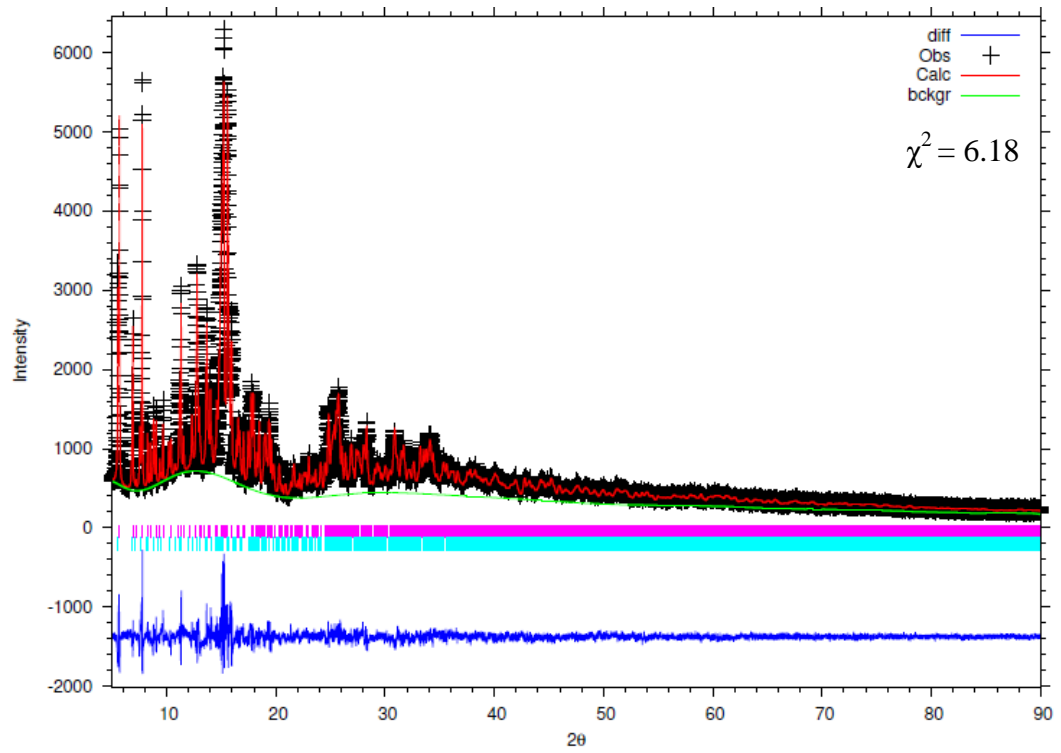


Figure 4.26: Rietveld refinement for Cs-exchanged $K_{1.9}Zr_{0.75}Sb_{0.25}Ge_3O_9 \cdot H_2O$.

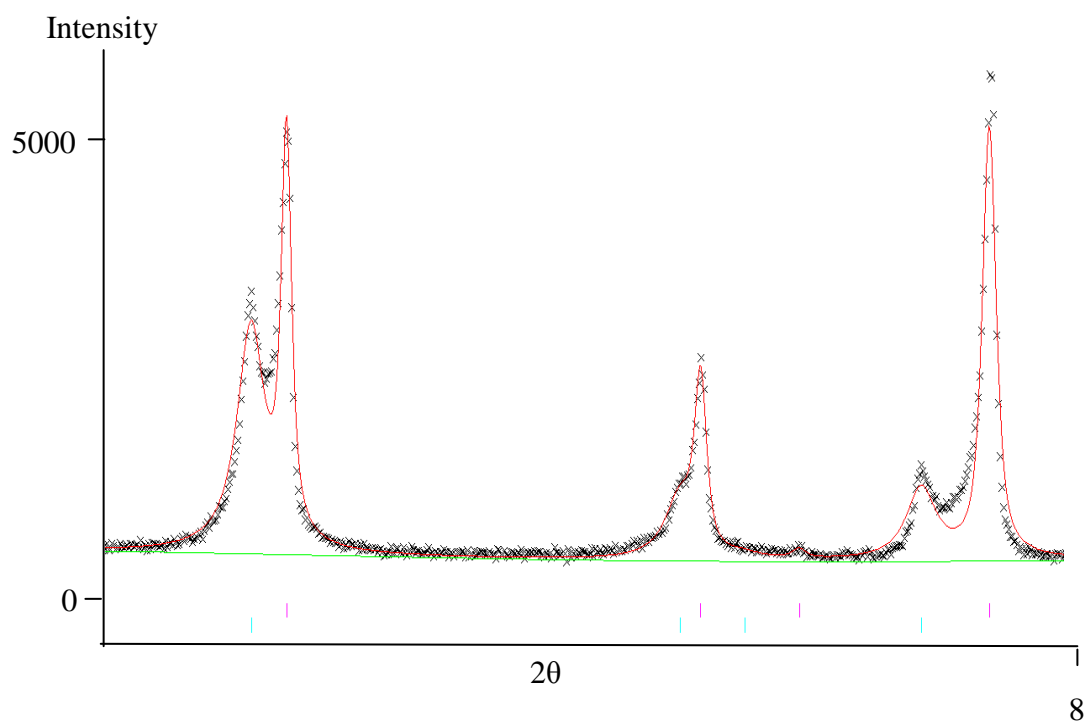


Figure 4.27: Expanded view of figure 4.26 showing fitting to the peak splitting observed.

Table 4.26: Lattice parameters, caesium occupancies and weight fractions from the two phase Rietveld refinement of Cs-exchanged 0.25Sb umbite.

Formula	$\text{Cs}_{0.23}\text{K}_{1.52}\text{X}$	$\text{Cs}_{1.34}\text{K}_{0.41}\text{X}$
$\text{X}=\text{Zr}_{0.75}\text{Sb}_{0.25}\text{Ge}_3\text{O}_9\cdot\text{H}_2\text{O}$		
$a / \text{Å}$	10.4640(4)	10.7261(5)
$b / \text{Å}$	13.6690(4)	13.7869(7)
$c / \text{Å}$	7.4728(3)	7.6780(2)
$V / \text{Å}^3$	1068.84(8)	1135.41(8)
Weight fraction	0.36	0.64
Cs occupancy site 1	0.166(6)	0.482(5)
Cs occupancy site 2	0.067(5)	0.860(6)

Lattice parameters and occupancies for both phases in Table 4.26 are similar to those reported in Table 4.24, with variation being in the relative weight fractions between the two phases. As covered in Section 4.3.6, it is believed that antimony does not fully incorporate due to the poor solubility of the oxide and as a result the 0.25Sb sample is not doped to this level. The observed peak splitting differences in Figure 4.21 and the information in Table 4.26 provide further evidence that this is indeed true. As a result the predicted formulae are not a true representation of the doping level and cation content, due to the unknown doping level. Table 4.27 summarises the weight fraction and Cs occupancies for the Sb doped umbites.

Table 4.27: Summary table for the refinements of Cs-exchanged Sb doped umbites.

	10Sb		20Sb		25Sb	
	Cs _{0.22} K _{1.68}	Cs _{1.29} K _{0.61}	Cs _{0.51} K _{1.29}	Cs _{1.25} K _{0.55}	Cs _{0.23} K _{1.52}	Cs _{1.34} K _{0.41}
Weight fraction (%)	45	55	34	66	36	64
Cation site one - Cs occupancy	0.131(6)	0.431(8)	0.359(5)	0.394(4)	0.166(6)	0.482(5)
Cation site two - Cs occupancy	0.086(5)	0.862(9)	0.150(5)	0.853(4)	0.067(5)	0.860(6)

4.3.8 Critical assessment of the observed ion exchange data

It has been hypothesised that the incorporation of 5^+ species into the umbite framework creates vacancies in the channel system. As the number of vacancies increase, diffusion into the bulk of the material becomes easier hence the increased exchange. The occupancies calculated by the refinements agree with this hypothesis and the suggested mechanism from the literature. However this does not explain the two phase model which appears to best fit the data gathered. The caesium content of the caesium rich phase varies only by small amount with increasing niobium content, the variation observed is the relative fraction of the phase which increases with niobium content. This is reflected by the large increase observed in the XRF data between the 0.2Nb and 0.25Nb. However this does not explain why a portion of the sample does not exchange to the same level, as you would expect the higher diffusion rate to be consistent across the whole sample and for all grains to undergo exchange. Possible explanations for this are outlined below:

- The reduction of symmetry in the system is still a possibility.
- Equilibrium has not been reached in the time frame used during the exchanges.
- Inhomogenous 5^+ distribution.

Attempts to explore other space groups, such as the related monoclinic $P2_1/c$ cell, to better fit the experimental data have yielded no positive results. The two phase model crystallographically appears to fit with the caesium occupancies being consistent regardless of dopant. Variations between the relative dopants appear to be minimal with similar exchange characteristics, from XRD, for both the 0.25Nb and 0.2Sb assumed maximum doping levels.

However this raises a discrepancy in the XRF data collected, with a substantially lower amount of caesium reported for the 0.2Sb compared to the 0.25Nb, which disagrees to that calculated by Rietveld refinement. Treating the XRF data in isolation could suggest an issue with the bead forming process and hence the reduced Cs content. However the reported Cs uptake, in each case, is substantially lower than that calculated from the diffraction patterns. This brings into question the applicability of XRF when requiring accurate quantitative analysis, but it cannot be ruled out that the refinement model used is over estimating occupancies, especially if it does not accurately represent the experimental data.

Suggesting that equilibrium has not been reached would be the simplest answer to the observed peak splitting, it is not uncommon for multiple exchange cycles being required by ion exchange materials when determining maximum uptake. However why some grains exchange to higher Cs content and why it is a function of 5^+ doping is not described by not reaching equilibrium.

Due to the minimal variation in unit cell parameters for the undoped and doped materials, seeing two separate phases in the diffraction data such as that in Figure 4.5 would be incredibly difficult. As Zr^{4+} and Nb^{5+} are isoelectronic occupancies cannot be refined, however attempts to refine Sb occupancies do not yield any positive results, with the occupancies being calculated as negative.

4.3.9 Thermal conversion of doped umbites

In Chapter 3 it was shown that the zircongemanate can be thermally converted to wadeite however, due to the poor ion exchange properties, it was not possible to determine if this phase transition occurs when the material is exchanged. The much improved caesium uptake

observed for both Nb^{5+} and Sb^{5+} allows for the further study of the umbite to wadeite phase transition in regards to the impact of doping and the high caesium content of these materials. Bruker D8 VT diffractometer ($\lambda = 1.5406 \text{ \AA}$) with an Anton Parr heating stage was used to analyse these sample with scans ran at 50 °C intervals from 50-1000 °C.

25NbCs

The thermal conversion of niobium doped umbite behaves very similarly to undoped material, the observed phase transition where the umbite structure breaks down and another crystalline phase forms rapidly in the range of 800 to 850 °C, Figure 4.28. Figure 4.29 shows the room temperature phase assemblage consisting of a major wadeite phase and other minor phases. Due to the lack of wadeite phases in the Bruker database the matched major phase is a tin wadeite $\text{Cs}_2\text{SnGe}_3\text{O}_9$, which is isostructural to the zirconogermanate wadeite. As the doped umbite material was never fully exchanged it could be assumed that a mixed Cs/K wadeite material has formed, as no other potassium containing phases are evident, however this cannot be fully confirmed with the data collected. There are also minor phases in the diffraction pattern, one of which is scheelite, ZrGeO_4 . The peak at $20^\circ 2\theta$ is not present in the 1000 °C scan, which would suggest that it forms on cooling to room temperature, much like that observed in Chapter 3 Section 3.3.10.

No niobium containing phases were matched to the XRD pattern, due to the low levels of incorporation it could be possible that the phases are not XRD visible; however incorporation into the wadeite structure cannot be ruled out. The limitations of the method do not provide a complete story with further work required to fully understand the wadeite phase transition, especially when considering whether niobium incorporation and mixed Cs/K phases are chemically viable. However it can be confirmed that niobium doping does not impact the

expected phase transition for this material and that caesium can be readily incorporated into a denser phase from an open framework material.

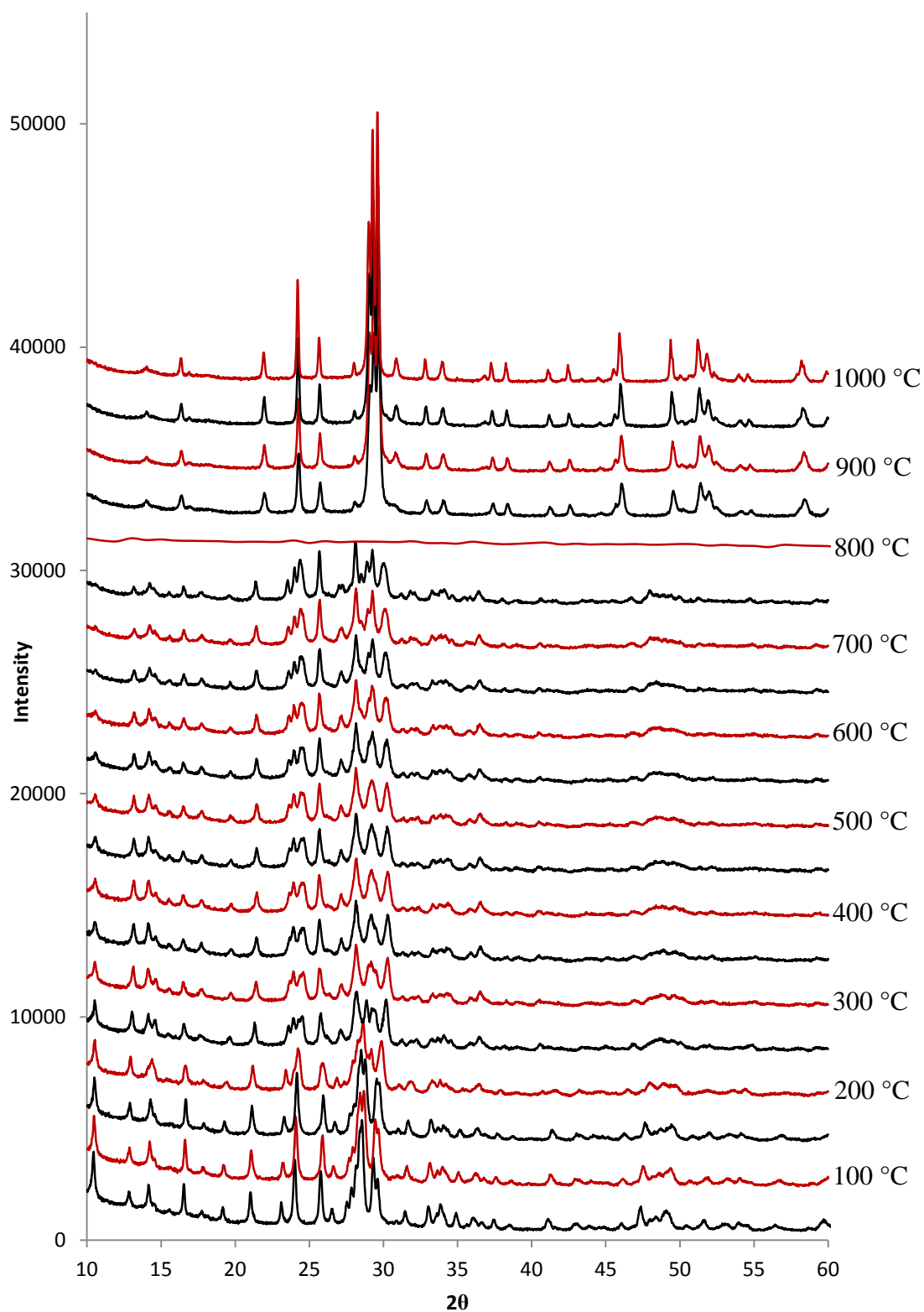


Figure 4.28: VT XRD for the thermal conversion of Cs-exchanged 0.25Nb umbite at 50 °C intervals.

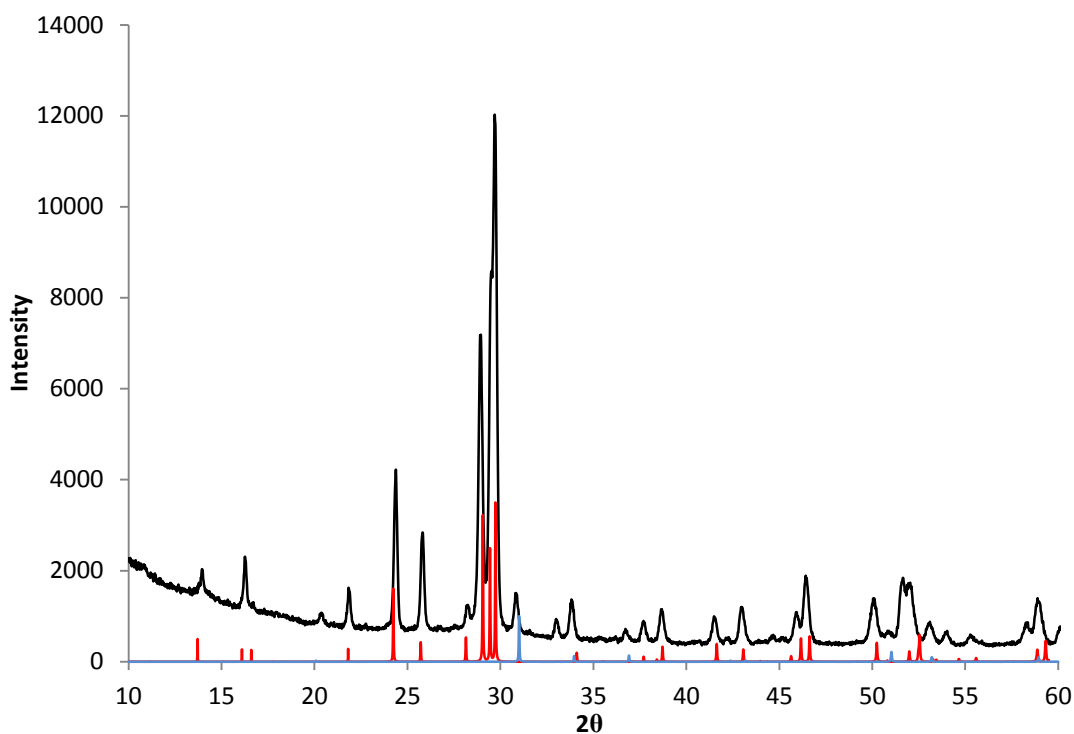


Figure 4.29: X-ray diffraction data ($\lambda = 1.5406 \text{ \AA}$) for the final phase assemblage of heated Cs-exchanged 0.25Nb umbite. Reference patterns have been added for the wadeite phase (Red) and scheelite (Blue). Minor phases are unmarked and form on cooling.

25SbCs

The thermal conversion of the Sb^{5+} material is shown in Figure 4.30 shows a similar phase transition to the niobium doped equivalent, occurring between 800 and 850 °C. The major phase once again matches to $\text{Cs}_2\text{SnGe}_3\text{O}_9$ wadeite phase which is isostructural to the zirconogermanate. This transition occurs much more slowly than the niobium doped material with the resultant wadeite phase fully crystallising at 950 °C and being much less crystalline. The room temperature phase assemblage of the thermal conversion is shown by Figure 4.31. A very minor scheelite phase forms alongside other phases which cannot be identified, as indicated by the extra peaks in the diffraction pattern.

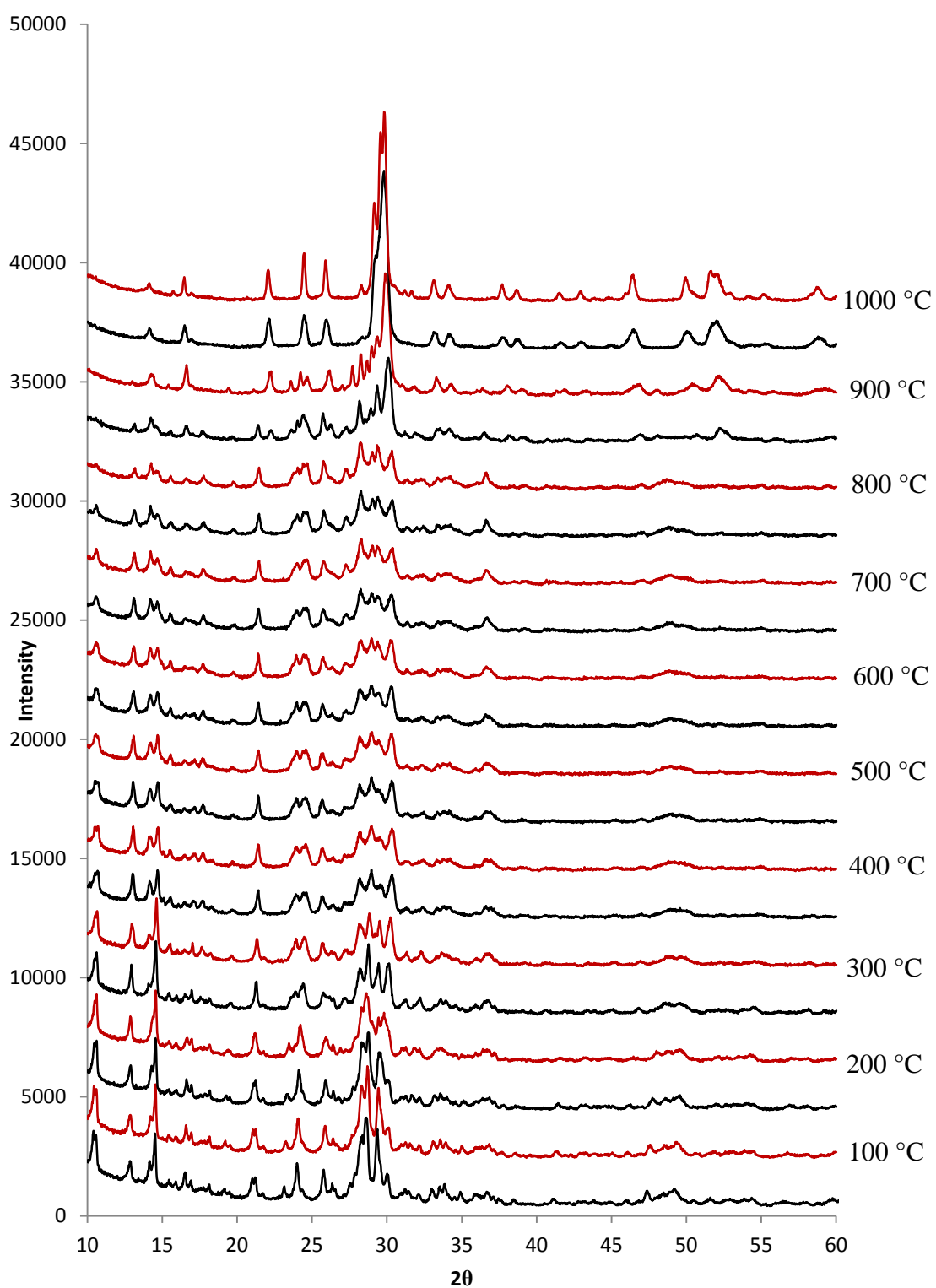


Figure 4.30: VT XRD for the thermal conversion of Cs-exchanged 0.25Sb umbite at 50 °C intervals.

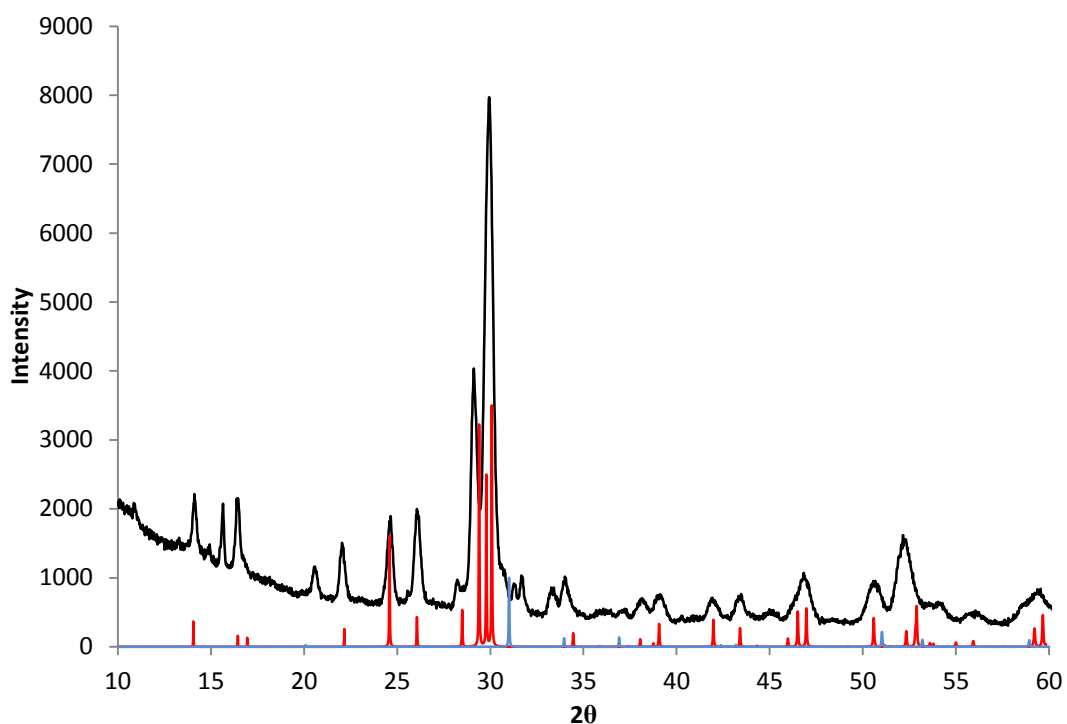


Figure 4.31: X-ray diffraction data ($\lambda = 1.5406 \text{ \AA}$) for the final phase assemblage of heated Cs-exchanged 0.25Sb umbite. Reference patterns have been added for the wadeite phase (Red) and scheelite (Blue). Minor phases are unmarked and form on cooling.

It is of note that there is amorphous Sb_2O_5 in the sample; this is reflected by the variations in ion exchange and diffraction data. Therefore it is possible that there are several side reactions occurring during the heating process, resulting in other minor phases. This is reflected by the complex DTA curve recorded for this sample when compared to the niobium derivative, Figure 4.32. The peak observed in Figure 4.31 at $15^\circ 2\theta$ is of relatively high intensity, however due to the relatively low crystallinity of the sample and subsequent broad peaks no other smaller peaks are evident. Due to the lack of other peaks phase identification cannot be achieved with any confidence and therefore the thermal conversion phase assemblage cannot be fully characterised.

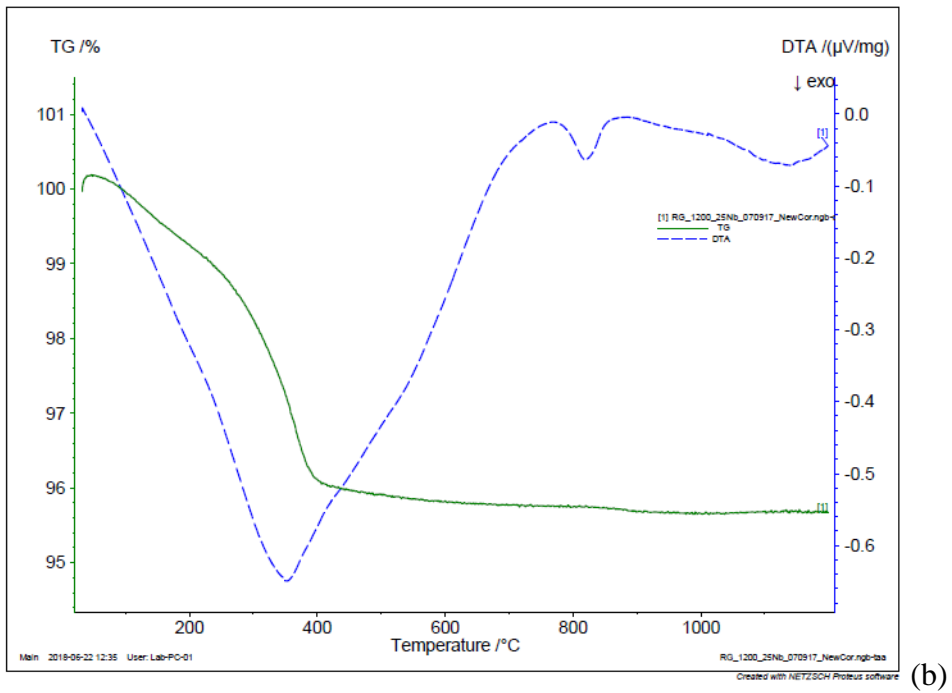
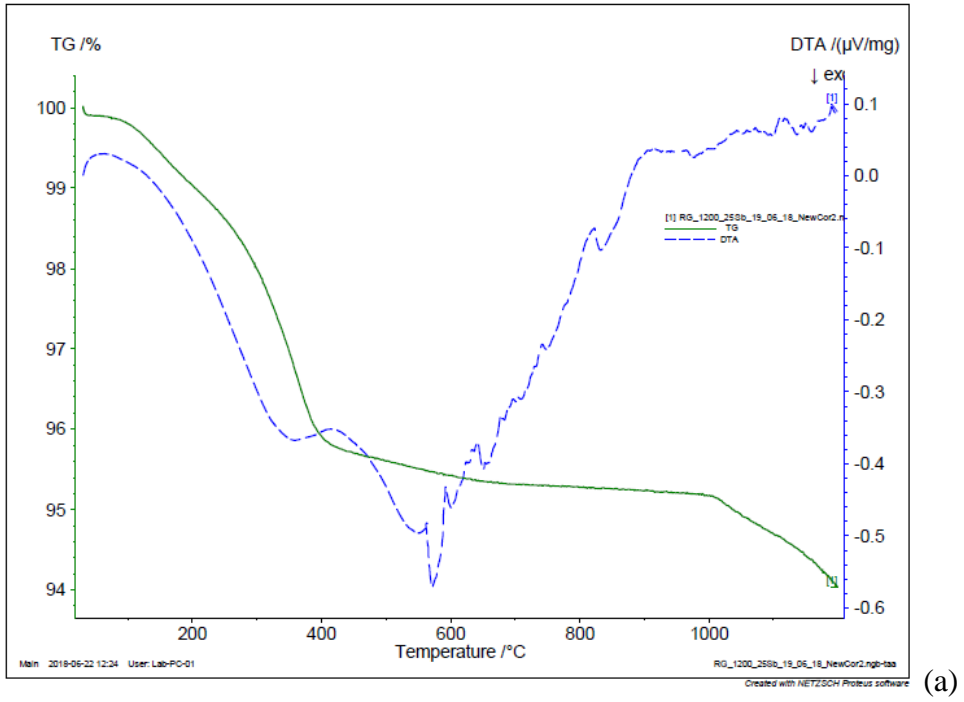


Figure 4.32: TGA and DTA data for the 0.25Sb (a) and Nb (b) doped umbites.

4.4 Conclusions

Due to the ion exchange properties of the parent zirconogermanate umbite being so poor, niobium doping was attempted in order to try and reliably improve cation uptake. Successful doping of up to 25% niobium for zirconium was achieved reproducibly with higher niobium contents perturbing the formation of umbite phases. This resulted in a drastic improvement in ion exchange properties with substantially higher caesium uptake observed in the 25% niobium doped material, this improvement is possibly due to the formation of vacancies in the channel system. High-resolution powder diffraction data shows that the exchange samples are actually multiphase, in each case containing a caesium and potassium rich phase. The phase fraction vary with increasing niobium content with the caesium rich phase being the major phase in the 25% niobium sample. This behaviour is also observed when doping antimony for zirconium, once again a large improvement in ion exchange properties is observed and once again high-resolution powder diffraction data shows that ion exchange products are multiphase. Reasons for why this behaviour occurs are unknown as there appears to be no literature precedent for this type of behaviour. Crystallographically the two phase model appears to best describe the high-resolution powder diffraction data however some questions remain as to the chemical viability of this model.

Chapter 5- Ion Exchange and
Thermal Conversion of
Pharmacosiderites

5.1 Introduction

Natural pharmacosiderite is a ferric arsenate, $\text{KFe}_4(\text{OH})_4(\text{AsO}_4)_3$, however synthetic silicate derivatives have been explored for their potential ion exchange properties since the early 1990's [93-94]. As with the silicate AV materials produced by Rocha and others, pharmacosiderites are mixed octahedral-tetrahedral framework materials with a wide range of compositional variation. However, unlike AV materials, a range of germanium containing materials have been synthesised either being germanium pure, mixed titanium germanium or doped silicate pharmacosiderites.

$\text{M}_3\text{HGe}_7\text{O}_{16}\cdot x\text{H}_2\text{O}$ (where $\text{M} = \text{Li}^+, \text{K}^+, \text{Rb}^+, \text{Cs}^+$ and $x = 4-6$) have been reported, the cubic framework structure of pharmacosiderite consists of clusters of face and edge sharing GeO_6 octahedra which are connected by corner sharing GeO_4 tetrahedra. This forms channels of eight-membered rings, with a pore opening of 4.3 \AA , that lie in the (100) direction. Inside these channels mobile cations and water molecules are located [93], as shown by Figure 5.1.

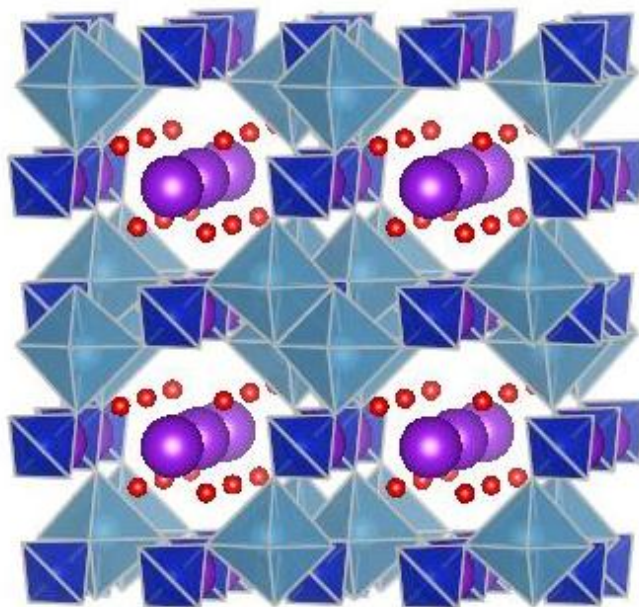


Figure 5.1: Structure of $M_3HGe_7O_{16} \cdot xH_2O$, GeO_4 tetrahedra are shown using dark blue and GeO_6 octahedra shown using light blue. Pore cations are shown using the purple spheres and channel waters shown by smaller red spheres

Feng *et al.* further studied the ion conductivity in $M_3HGe_7O_{16} \cdot xH_2O$, it was shown that the ionic conductivity of this pharmacosiderite phase was substantially higher than that observed in zeolites. Feng *et al.* observed that with increasing cationic radius the activation energy decreased, this was attributed to the decrease of the Coulombic attraction between the cations and the negatively charged framework structure. The electrostatic interaction between the cation and the mixed germanate framework is weaker than that observed in zeolites and hence promotes conductivity [94]. The crystal structure of this material varies depending on the cation size; Fitch *et al.* described the three different structural modifications observed with the majority of pharmacosiderite phases occupying a primitive cubic cell. Larger cations such as K^+ and Cs^+ form a cubic supercell, as shown by Figure 5.2, and exchange for Ag^+ results in a small rhombohedral distortion [95-96].

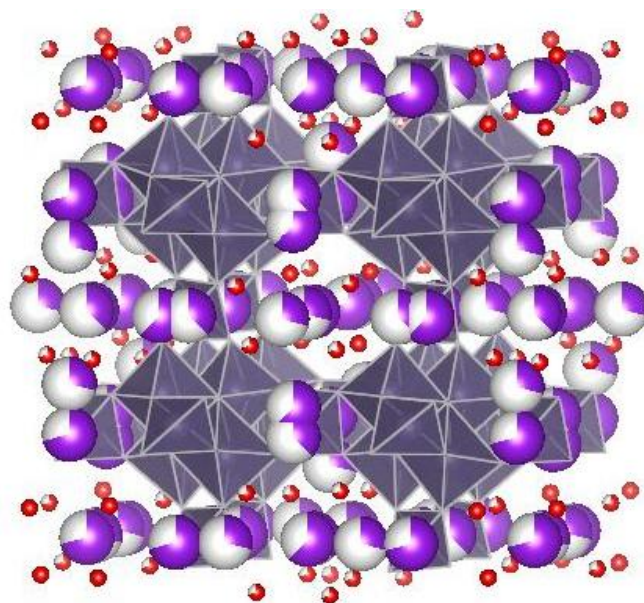


Figure 5.2: Cubic super cell for $K_3HGe_7O_{16}.4H_2O$, potassium occupancies are shown using the multi-coloured spheres (purple indicates potassium and white is hydrogen) and channel waters shown by smaller red spheres.

The rhombohedral distortion was further explored by Nenoff *et al.*, the as synthesised $Na_3H_x(H_2PO_4)_xGe_7O_{16}.4H_2O$ ($x=1.38$) germanium pharmacosiderite has been shown to exhibit both cation and anion exchange properties. The distortion is the result sodium and the anion both occupying space in the cage however upon ion exchange the material will revert to a primitive cubic cell as shown by the incorporation of Cs^+ , Li^+ and Ca^{2+} for Na^+ . Anion exchange was also observed with the dihydrogen phosphate anion being replaced by both nitrate and carbonate; this also causes a reversible change to the primitive cubic cell. It was determined by the authors that both sodium and phosphate are required in the structure to cause the rhombohedral distortion [97].

The previously mentioned examples contain GeO_x units, Behren *et al.* have investigated a range of materials containing TiO_6 and MO_4 ($M=Si$ or Ge) units. They reported the successful synthesis of $M_3HTi_4Si_3O_{16}.4H_2O$ (where $M=K^+$, Cs^+ and H^+), these are isostructural and

crystallise in the primitive cubic space group mentioned previously. The proton located in the structure does not exchange due to a lack of space in the cavity in which it is located, the cavity cannot support a fourth cation on exchange.

Preliminary ion exchange for the proton form, $\text{H}_4\text{Ti}_4\text{Si}_3\text{O}_{16}\cdot 4\text{H}_2\text{O}$, showed high selectivity for Cs^+ over the other alkali metals and a large uptake range of pH 2.75 to 9.5 [98]. If the protons are fully exchangeable then the theoretical capacity is 7.46 meq/g, however the maximum value for caesium uptake is 4.19 meq/g. This is approximately two caesiums per unit cell and 55% of the theoretical capacity,

Behrens *et al.* believe this selectivity could be due to the position in which the cation sits inside the pore; caesium due to its size occupies an off-centre position in the cavity whereas the other alkali metals occupy a central position albeit with longer bonds to the framework. Also due to size constraints species diffuse into the structure unhydrated meaning it is more energetically favourable for caesium to lose its hydration sphere and occupy the pore than smaller cations. Alkali earth uptake was also investigated with the proton form showing selectivity for Ba^{2+} at low pH and Sr^{2+} at high pH.

Behrens *et al.* then expanded upon this by testing the potassium and sodium forms of titanosilicate pharmacosiderite against wastewater simulants. For both materials a constant loading was achieved within 24 hours, the Sr^{2+} and Cs^+ exchange isotherms show capacities of 2.4 meq/g and 3.12 meq/g respectively. This corresponds to approximately 50% of the theoretical limit for strontium and 63% for caesium. Both the sodium and potassium forms have been shown to be highly selective strontium exchangers with 97-98% removal from groundwater waste simulants, with both able to remove ppm levels of Sr^{2+} in the presence of competing ions at neutral and slightly acidic pH [99].

The ion exchange properties of the titanosilicate created interest in the synthesis of germanium analogues, Behrens *et al.* reported the successful synthesis of a series of mixed Si/Ti/Ge pharmacosiderites. Interestingly these materials were synthesised as caesium forms and the potassium forms accessed by the complete exchange of caesium, these are summarised in Table 5.1 [100].

Table 5.1: Composition, space group and lattice parameters for the known germanate pharmacosiderite phases.

Material	Space group	Lattice parameters (Å)
$\text{Cs}_3\text{H}(\text{TiO})_{3.5}(\text{GeO})_{0.5}(\text{GeO}_4)_{2.5}(\text{SiO}_4)_{0.5}\cdot 4\text{H}_2\text{O}$	$P\bar{4}3m$	a = 7.9376
$\text{Cs}_3\text{HTi}_4\text{Ge}_3\text{O}_{16}\cdot 4\text{H}_2\text{O}$	$I23$	a = 15.9606
$\text{K}_3\text{H}(\text{TiO})_{3.5}(\text{GeO})_{0.5}(\text{GeO}_4)_{2.5}(\text{SiO}_4)_{0.5}\cdot 4\text{H}_2\text{O}$	$P\bar{4}b2$	a = 11.1571 c = 7.9165
$\text{K}_3\text{HTi}_4\text{Ge}_3\text{O}_{16}\cdot 4\text{H}_2\text{O}$	$P\bar{4}b2$	a = 11.215 c = 7.9705

Ge substituted compounds have a low affinity for every alkali cations except for caesium and better selectivity than the titanosilicate pharmacosiderite. This trend continues with the alkali earth cations with higher selectivity for both Ba^{2+} and Sr^{2+} compared to the titanosilicate, this would be beneficial for nuclear waste remediation applications [100].

As previously covered in Chapter 4 the substitution of niobium into a structure can result in an improvement of ion exchange properties, this is also shown in the pharmacosiderite system. 20% Nb doping for Ti in the titanosilicate pharmacosiderite resulted in improved uptake of Cs^+ albeit with slightly slower kinetics [101].

The work in this chapter we will explore the direct synthesis and optimisation of the potassium form of the germanogermanate and titanogermanate pharmacosiderites. Ion

exchange forms of these materials will be then thermally converted to examine potential wastefrom phases.

5.2 Experimental

5.2.1 $K_3HGe_7O_{16} \cdot 4H_2O$ synthesis

The pharmacosiderite was prepared by dissolving 0.4468 g of potassium hydroxide (85%, Sigma) in 14.3 ml of deionised water. 0.8336 g of germanium dioxide (Gerald wise and co) was added slowly until fully dissolved, the mixture is then stirred for a further hour to allow it to homogenise.

The resulting mixture was then transferred to a 45 ml Teflon liner and placed in a Parr autoclave at 200 °C for 24 hours. The resulting product was then filtered and washed in deionised water before being dried overnight at 60 °C.

5.2.2 $K_3HTi_4Ge_3O_{16} \cdot 4H_2O$ synthesis

The pharmacosiderite was prepared by dissolving 0.446 g of potassium hydroxide (85%, Sigma) in 14.3 ml of deionised water. 0.5498 g of germanium dioxide (Gerald wise and co) was added slowly until fully dissolved, to which 0.7782 g of titanium isopropoxide (Acros) was added quickly. The mixture is then stirred for a further hour to allow it to homogenise.

The resulting mixture was then transferred to a 45 ml Teflon liner and placed in a Parr autoclave at 200 °C for 48 hours. The resulting product was then filtered and washed in deionised water before being dried overnight at 60 °C.

5.2.3 $K_3HTi_4Si_3O_{16} \cdot 4H_2O$ synthesis

The pharmacosiderite was prepared by dissolving 0.7772 g of potassium hydroxide (85%, Sigma) in 15.4 ml of deionised water. 0.675 g of fumed silica (Sigma) was added slowly until

fully dissolved, to which 3.213 g of titanium isopropoxide (Acros) was added quickly. The mixture is then stirred for a further hour to allow it to homogenise. The resulting mixture was then transferred to a 45ml Teflon liner and placed in a Parr autoclave at 200 °C for 48 hours. The resulting product was then filtered and washed in deionised water before being dried overnight at 60 °C.

All compounds synthesised were analysed using Powder X-ray diffraction (XRD) on a Bruker D8 Advance using a Cu K α source at room temperature. Phase matching was performed using the EVA software from known databases.

5.2.4 Ion exchange studies

0.1 M solutions of strontium nitrate (98%, Alfa Aesar) or caesium nitrate (99.8%, Alfa Aesar) were added to 0.2-0.5 g of sample with an overall w/v ratio of 1:100. This was then shaken for 24 hours before being filtered, washed and dried overnight at 60 °C. Elemental analysis was undertaken using X-ray fluorescence (XRF) on a Bruker S8 Tiger with the samples prepared as either a loose powder, pressed pellet or fused bead.

5.3 Results and Discussion

5.3.1 Synthesis and optimisation of Pharmacosiderites

As covered in Chapter 3, pharmacosiderite phases were accidentally synthesised whilst trying to target different derivatives of the zirconogermante material umbite. It was decided to further explore these materials and compare them to the umbite phases already described in this work. The synthesis of both pharmacosiderite impurity phases that were found in Chapter 3 Section 3.3.7 have been reported in the literature, however they were modified to allow for a simple one step synthesis methodology. The synthesis of the germanogermanate pharmacosiderite, $K_3HGe_7O_{16} \cdot 4H_2O$, is relatively facile and can be easily scaled up for much larger batches with high sample quality, as shown in Figure 5.3.

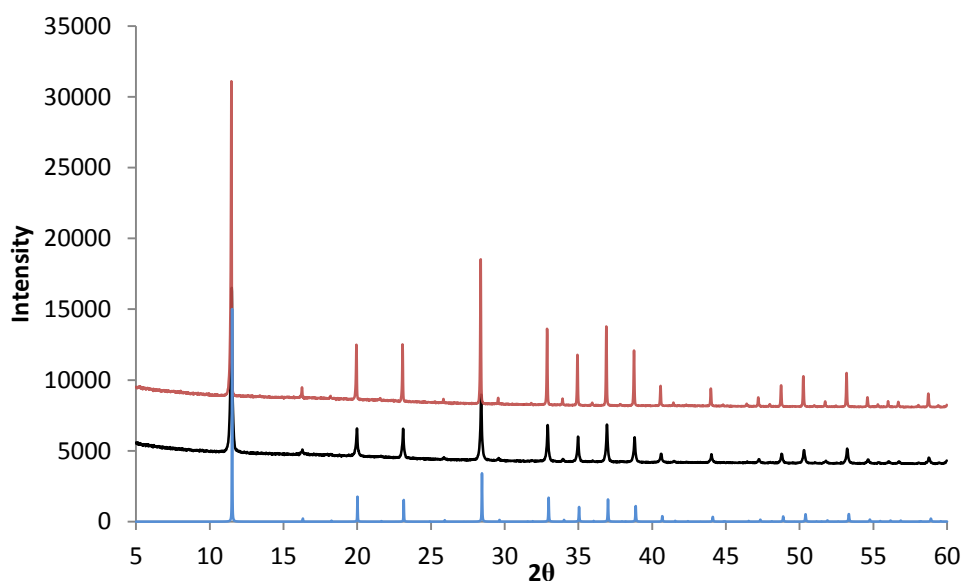


Figure 5.3: X-ray diffraction patterns ($\lambda = 1.5406 \text{ \AA}$) for $K_3HGe_7O_{16} \cdot 4H_2O$, 45 ml synthesis (Black) and 125 ml scale up (Red). Reference pattern (Blue) for $K_3HGe_7O_{16} \cdot 4H_2O$ has been added for comparison.

It is of note that larger batch synthesis is required due to the relatively (sub 1 g) batch produced from a single 45 ml synthesis outlined in Section 5.2.1. Germanium oxide solubility

plays an important role in the successful synthesis of $\text{K}_3\text{HGe}_7\text{O}_{16}\cdot 4\text{H}_2\text{O}$ with adequate time being required to allow for the total dissolution of GeO_2 , incomplete GeO_2 dissolution results in a substantially reduced yield.

High-resolution powder diffraction data collected for this phase was analysed using Rietveld refinement. As stated in Section 5.1, $\text{K}_3\text{HGe}_7\text{O}_{16}\cdot 4\text{H}_2\text{O}$ crystallises in a cubic super cell *I23*. There two distinct variations of this super cell, the first of which describes the archetypal *I23* pharmacosiderite by Fitch *et al.* and the second a potassium deficient phase *F23* pharmacosiderite derived by Gramlich *et al.* [102]. Both models were used for the refinements to see which best represented the experimental data, with the Fitch model providing the better fit overall. Figure 5.4 shows the Rietveld refinement for $\text{K}_3\text{HGe}_7\text{O}_{16}\cdot 4\text{H}_2\text{O}$, an adequate fit has been achieved however there are significant discrepancies between experimental and simulated intensities.

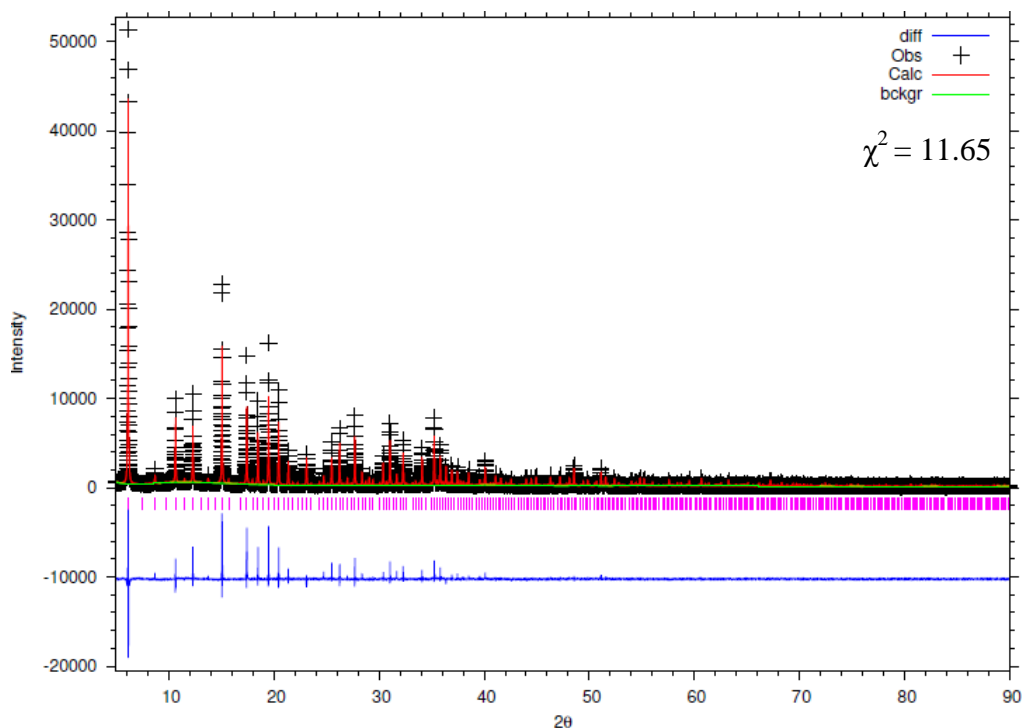


Figure 5.4: Rietveld refinement for $K_3HGe_7O_{16} \cdot 4H_2O$.

The quality of fit can be improved by reducing the refined range and removing the first most intense peak which is the most poorly fit, as shown by Figure 5.5. However there are still large discrepancies in the calculated intensities and a better quality of fit would like to be achieved. For both refinements restraints were applied to Ge-O bonds of 1.74 Å (four-coordinate) and 1.88 Å (six-coordinate).

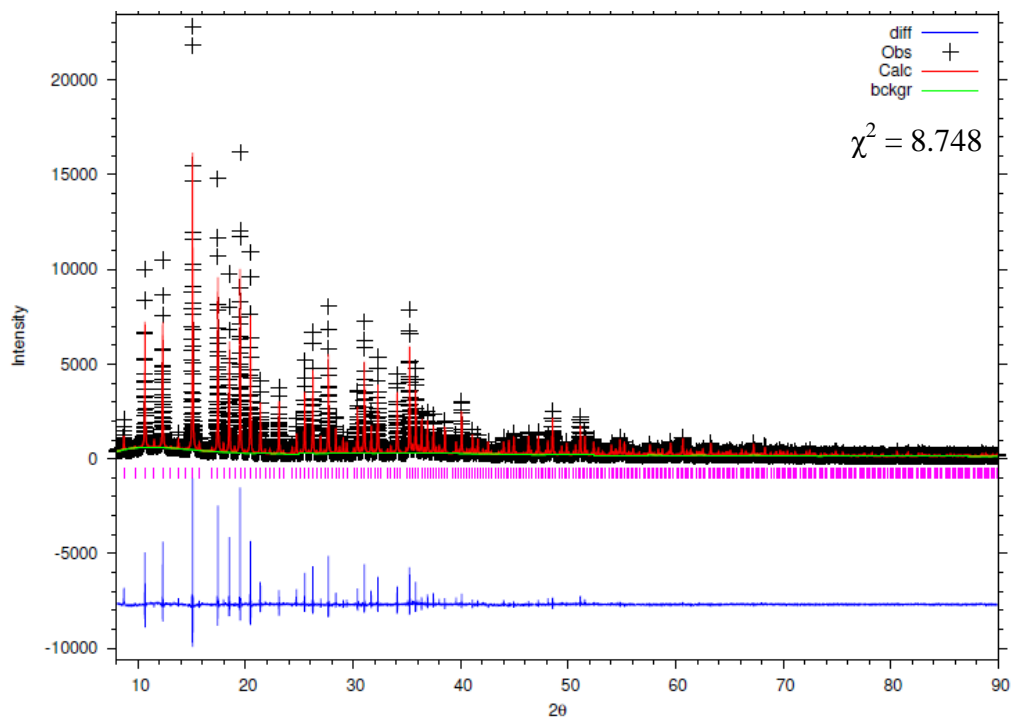


Figure 5.5: Rietveld refinement for $K_3HGe_7O_{16} \cdot 4H_2O$ reduced range.

Table 5.2: Lattice parameters, atomic positions, occupancy and thermal parameters for the reduced range refinement of $\text{K}_3\text{HGe}_7\text{O}_{16}\cdot 4\text{H}_2\text{O}$. Thermal parameters are grouped by element.

$\lambda/\text{\AA}$	0.82525				
$a/\text{\AA}$	15.4176(1)				
$V/\text{\AA}^3$	3664.77(4)				
<i>Space Group</i>	<i>I</i> 23				
R_{wp}	0.1033				
R_{exp}	0.0349				
χ^2	8.748				
<i>Site</i>	<i>x</i>	<i>y</i>	<i>z</i>	<i>Occupancy</i>	<i>U_{iso}</i>
Ge1	0.9996(4)	0.2432(3)	0.2585(2)	1	0.0050(1)
Ge2	0.1812(3)	0.1812(3)	0.1812(3)	1	0.0050(1)
Ge3	0.1846(2)	0.1778(2)	0.6808(4)	1	0.0050(1)
O1	0.1760(10)	0.1949(9)	0.0595(11)	1	0.0047(9)
O2	0.8046(11)	0.8192(13)	0.5652(13)	1	0.0047(9)
O3	0.6755(10)	0.1935(10)	0.0570(8)	1	0.0047(9)
O4	0.1737(12)	0.6801(10)	0.0674(9)	1	0.0047(9)
O5	0.3060(12)	0.3060(12)	0.3060(12)	1	0.0047(9)
O6	0.3029(9)	0.3131(9)	0.8066(10)	1	0.0047(9)
K1	0.2174(9)	0.5	0	0.617	0.0725(2)
K2	0.2845(14)	0.5	0	0.383	0.0725(2)
K3	0.2464(25)	0	0	0.712	0.0725(2)
K4	0.3540(21)	0	0	0.288	0.0725(2)
O7	0.9204(6)	0.9204(6)	0.9204(6)	1	0.0047(9)
O8	0.3857(9)	0.4373(8)	0.9064(10)	0.713	0.0047(9)

Table 5.3: Selected bond lengths from the refinement of $K_3HGe_7O_{16} \cdot 4H_2O$.

<i>Bond</i>	<i>Distance (Å)</i>		<i>Bond</i>	<i>Distance (Å)</i>
Ge1-O1	1.70(2)		Ge3-O2	1.79(2)
Ge1-O2	1.67(2)		Ge3-O3	1.870(1)
Ge1-O3	1.84(1)		Ge3-O4	1.81(1)
Ge1-O4	1.76(1)		Ge3-O5	1.95(2)
			Ge3-O6	1.94(1)
Ge2-O1	1.89(2)		Ge3-O6	2.01(1)
Ge2-O1	1.89(2)			
Ge2-O1	1.89(2)		Av K1-O	3.18
Ge2-O6	1.95(2)		Av K2-O	3.03
Ge2-O6	1.95(2)		Av K3-O	3.17
Ge2-O6	1.95(2)		Av K4-O	2.74

The quality of the refinement is also reduced by observed peak asymmetry, reducing the ability to effectively model the experimental peak shape, as shown by Figure 5.6. This peak asymmetry, which is very subtle, has not been described in the literature and was not observed in the collected lab data. The origins of the asymmetry are unknown however the small shoulders are seen throughout the experimental data and are only observed in very high quality data.

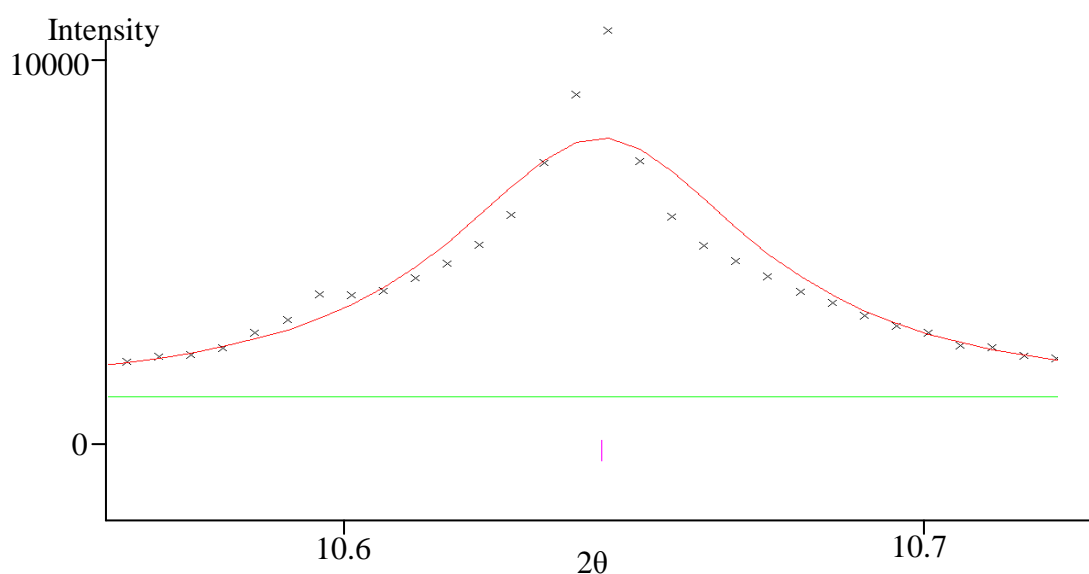


Figure 5.6: Expanded view from the Rietveld refinement for $K_3HGe_7O_{16} \cdot 4H_2O$ showing peak asymmetry.

Titanogermanate pharmacosiderite synthesis in the literature commonly consists of two synthesis steps, the formation of a starting gel and then the addition of an alkali metal hydroxide solution. Commonly the caesium form is synthesised due to the much higher sample quality relative to the potassium derivative. Potassium forms of this material are formed post synthesis using ion exchange to remove the caesium from the framework. In order to compare this material to zirconogermanate umbite, the synthesis of $K_3HTi_4Ge_3O_{16} \cdot 4H_2O$ was attempted using a modified version of the germanogermanate synthesis, Section 5.2.1. The methodology outlined in Section 5.2.2 uses the suggested 1:2 Ti:Ge ratio from the literature [100], interestingly this may explain the synthesis of this phase in Chapter 3 Section 3.3.7, where the Ti:Ge ratio used for the attempted $K_2TiGe_3O_9 \cdot H_2O$ synthesis was 1:3.

The sample quality is substantially lower than the germanogermanate derivative and umbite, as shown in Figure 5.7.

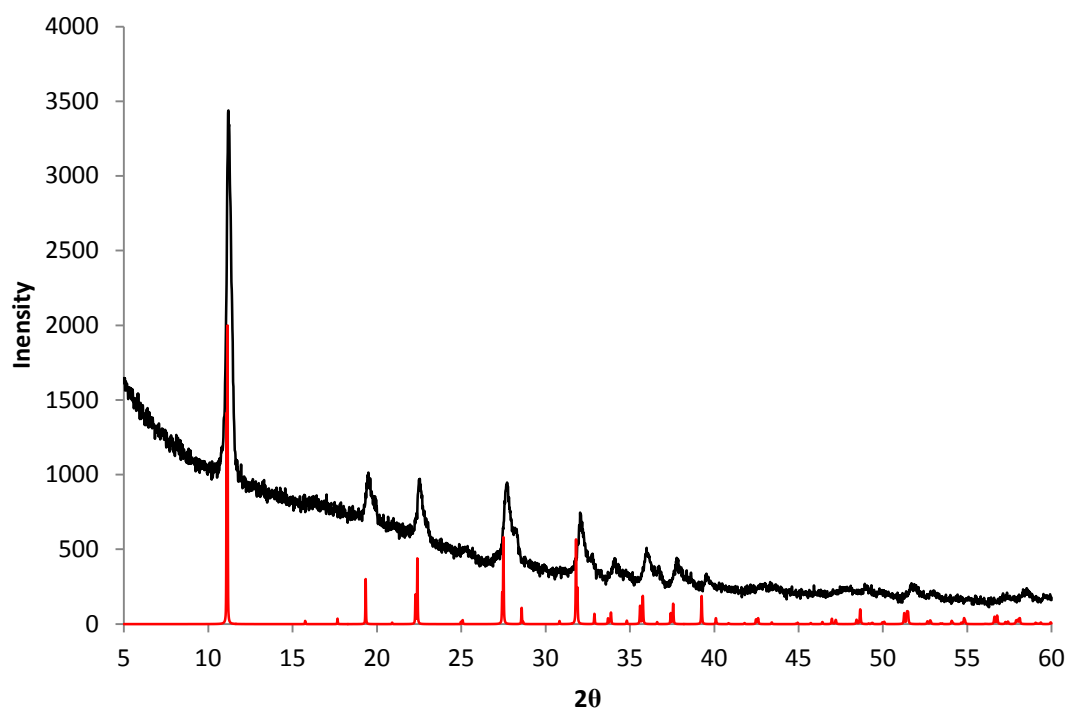


Figure 5.7: X-ray diffraction pattern ($\lambda = 1.5406 \text{ \AA}$) for $\text{K}_3\text{HTi}_4\text{Ge}_3\text{O}_{16}\cdot 4\text{H}_2\text{O}$. Reference pattern (Red) for $\text{K}_3\text{HTi}_4\text{Ge}_3\text{O}_{16}\cdot 4\text{H}_2\text{O}$ added for comparison.

The yield of sample from a typical 45 ml autoclave synthesis is substantially less than 1g however this material does not scale very well when increasing batch size, the result being impure samples. Attempts to improve sample quality by extending synthesis time from two days to ten days, Figure 5.8, also had little impact which supports the literature. Reduction of the synthesis time to one day results in a largely amorphous sample, reflecting the low crystallinity shown by this material when directly synthesised. It is likely the two stage synthesis from the literature introduces some degree of seeding which promote the formation of highly crystalline samples.

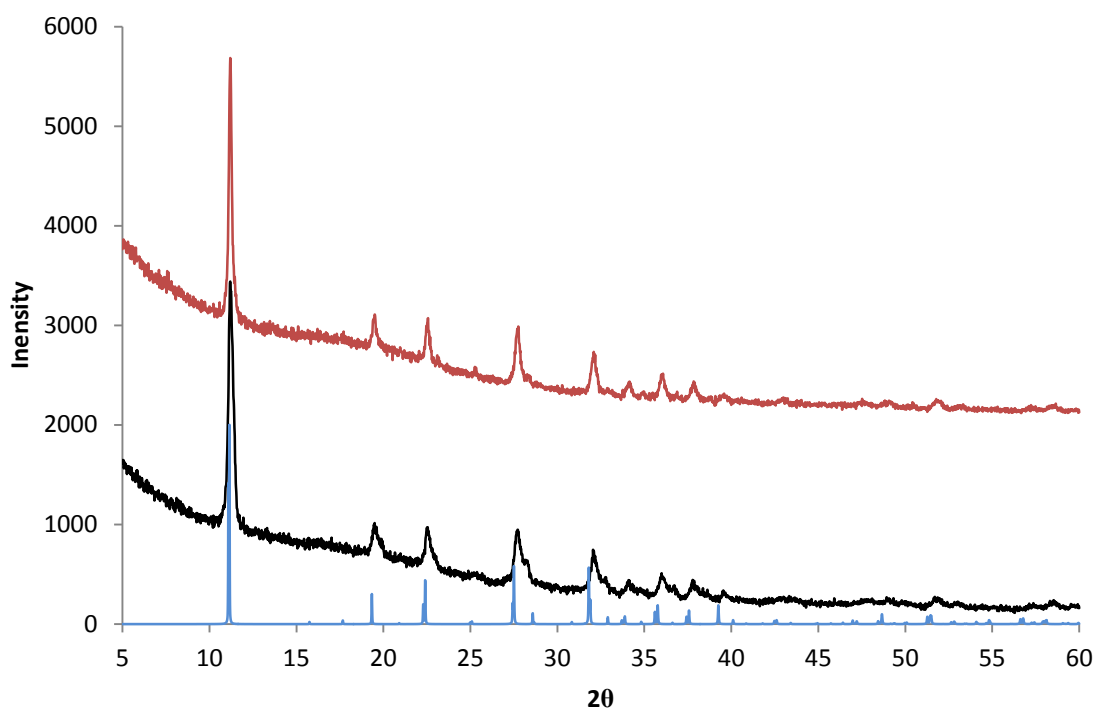


Figure 5.8: X-ray diffraction patterns ($\lambda = 1.5406 \text{ \AA}$) for $\text{K}_3\text{HTi}_4\text{Ge}_3\text{O}_{16}\cdot 4\text{H}_2\text{O}$, two day (Black) and ten day (Red) syntheses. Reference pattern (Blue) for $\text{K}_3\text{HTi}_4\text{Ge}_3\text{O}_{16}\cdot 4\text{H}_2\text{O}$ added for comparison.

High-resolution powder diffraction data collected for this phase was analysed using Rietveld refinement and fit to the tetragonal phase from the literature, Figure 5.9. The resulting refinement was not of the highest quality because of the relatively poor data, with simulated intensity calculated for peaks which are not observable in the experimental data. Bond restraints of 1.74 \AA for Ge-O and 1.955 \AA Ti-O were used, with significant damping required to prevent substantial lengthening of Ti-O bonds, which would result in the refinement diverging. Peak asymmetry is also evident in both high-resolution and lab data, this can be adequately modelled using peak asymmetry and anisotropic crystallite size broadening functions in GSAS. However the observed shoulders for these peaks are not effectively modelled as shown by Figure 5.10.

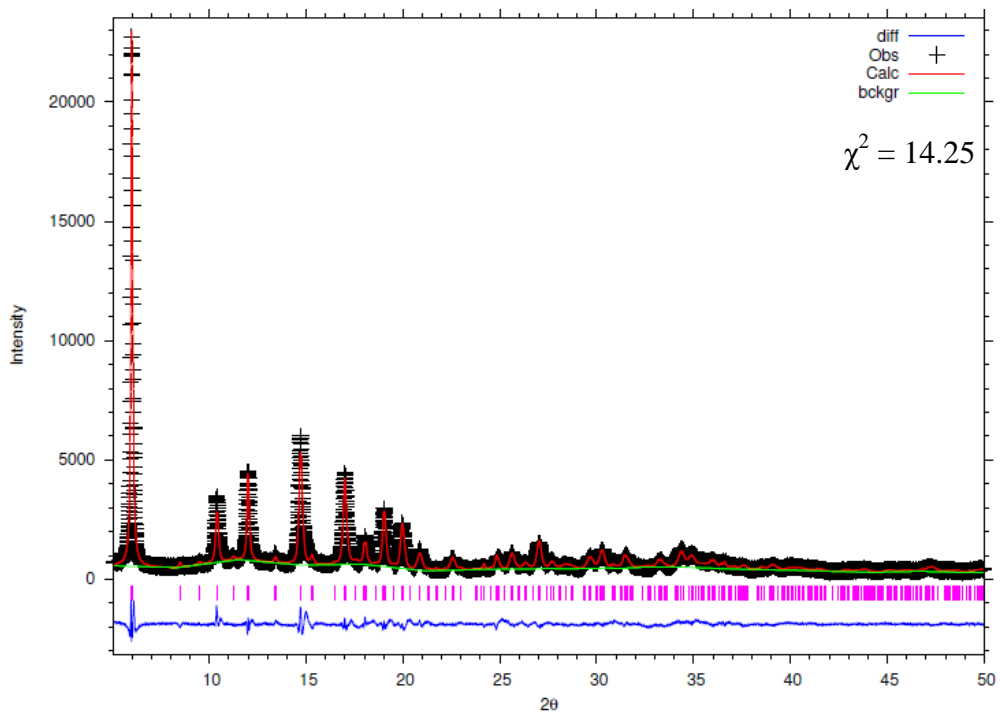


Figure 5.9: Rietveld refinement for $\text{K}_3\text{HTi}_4\text{Ge}_3\text{O}_{16}\cdot 4\text{H}_2\text{O}$

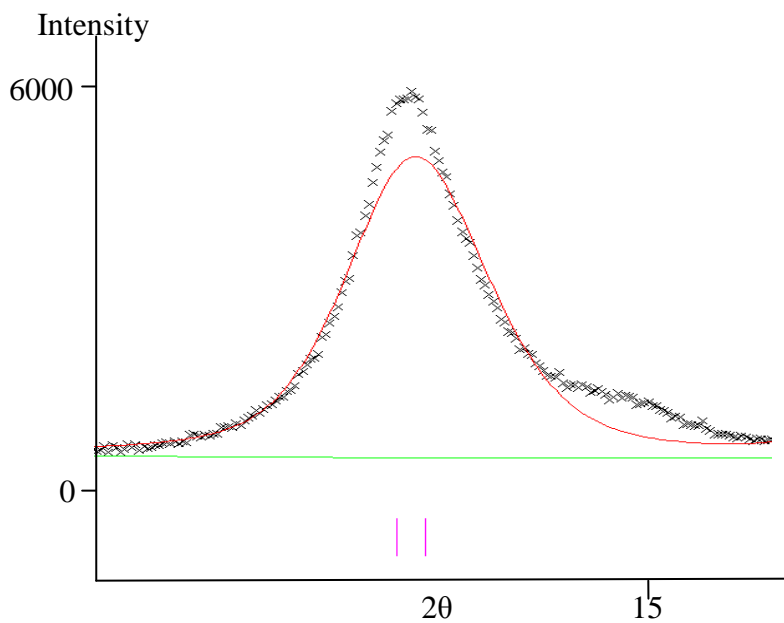


Figure 5.10: An example of the peak shoulders observed in the experimental data for $\text{K}_3\text{HTi}_4\text{Ge}_3\text{O}_{16}\cdot 4\text{H}_2\text{O}$.

Table 5.4: Lattice parameters, atomic positions, occupancy and thermal parameters for the refinement of $\text{K}_3\text{HTi}_4\text{Ge}_3\text{O}_{16}\cdot 4\text{H}_2\text{O}$. Thermal parameters are grouped by element.

$\lambda/\text{\AA}$	0.82525				
$a/\text{\AA}$	11.1503(5)				
$c/\text{\AA}$	7.7927(4)				
$V/\text{\AA}^3$	985.15(7)				
<i>Space Group</i>	<i>P-4b2</i>				
R_{wp}	0.0945				
R_{exp}	0.0250				
χ^2	14.25				
<i>Site</i>	<i>x</i>	<i>y</i>	<i>z</i>	<i>Occupancy</i>	<i>U_{iso}</i>
Ti1	0.1372(4)	-0.0081(7)	0.1429(6)	1	0.0186(16)
Ge1	0.2574(4)	0.2426(4)	0	1	0.0356(10)
Ge2	0	0	0.5	1	0.0356(10)
O1	0.1415(13)	0.2571(17)	0.8668(23)	1	0.0261(29)
O2	0.2447(17)	0.1106(13)	0.1035(23)	1	0.0261(29)
O3	0.1437(10)	-0.0180(15)	-0.0999(15)	1	0.0261(29)
O4	0.8817(10)	0.0178(27)	0.3688(11)	1	0.0261(29)
K1	0.2898(6)	0.2102(6)	0.5	1	0.1060(31)
K2	0.5	0	0	1	0.1060(31)
O5	0.3406(10)	-0.0151(18)	0.7496(13)	1	0.0261(29)

Table 5.5: Selected bond lengths from the refinement of $K_3HTi_4Ge_3O_{16}\cdot 4H_2O$.

<i>Bond</i>	<i>Distance (Å)</i>		<i>Bond</i>	<i>Distance (Å)</i>
Ti1-O1	2.00(1)		Ge2-O4	1.69(1)
Ti1-O2	1.81(1)		Ge2-O4	1.69(1)
Ti1-O3	1.93(1)		Ge2-O4	1.69(1)
Ti1-O3	2.32(2)		Ge2-O4	1.69(1)
Ti1-O3	2.18(2)			
Ti1-O4	1.81(1)			
Ge1-O1	1.68(1)		Av K1-O	3.34
Ge1-O1	1.68(1)		Av K2-O	3.06
Ge1-O2	1.69(1)			
Ge1-O2	1.69(1)			

The origins of the asymmetry cannot be explained with confidence from the refinement data and more information is required. However from practical observations, the synthesis of pharmacosiderites likely results in a range of crystallite size. A portion of the sample is lost during the filtration step to isolate the product, suggesting small particles sizes. This occurs for both the titanium and germanogermanate pharmacosiderite materials regardless of synthesis time and batch size.

Attempts to synthesise tin and zirconium containing pharmacosiderites by replacing titanium isopropoxide with tin chloride pentahydrate and zirconyl chloride respectively failed. The addition of a tin source to the reaction mixture resulted in the formation of non-pharmacosiderite phases. Further attempts to synthesise tin containing pharmacosiderite derivatives by increasing the pH of the starting solution resulted in a mixed umbite and pharmacosiderite phases, Figure 5.11, similar to that observed in Chapter 3.

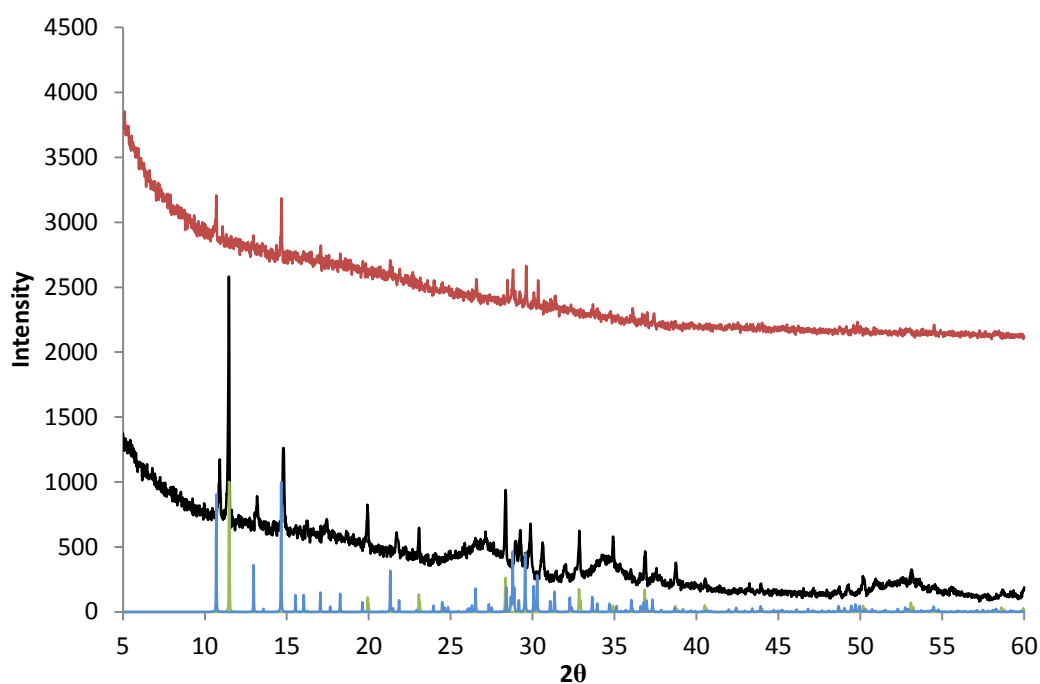


Figure 5.11: X-ray diffraction patterns ($\lambda = 1.5406 \text{ \AA}$) for $\text{K}_3\text{HX}_4\text{Ge}_3\text{O}_{16}\cdot 4\text{H}_2\text{O}$, where X= Sn (Black) and Zr (Red). Reference pattern for umbite (Blue) and pharmacosiderite (Green) added for comparison.

The addition of a zirconium source resulted in a mainly amorphous product however the observed peaks correspond to the most intense peaks observed for the zirconogermanate umbite phase, Figure 5.11. This highlights the synthetically close relationship between the two different materials.

5.3.2 $\text{K}_3\text{HGe}_7\text{O}_{16}\cdot 4\text{H}_2\text{O}$ ion exchange

Ion exchange properties for the germanogermanium pharmacosiderite have been briefly explored in the literature. Tripathi *et al.* describe a negligible K_d value for this material with relatively slow uptake when compared to other pharmacosiderite phases. The literature also reports a reduction in symmetry on partial ion exchange of caesium from the cubic to a tetragonal cell. However there is no mention of alkali earth uptake and due to the close

relationship to uptake, it was decided to further study uptake in order to compare the different phases. XRF analysis, Table 5.6 on pressed pellets shows relatively high caesium uptake with just over 50% of potassium replaced in 24 hours. Strontium uptake, like all germanates studied previously, is minimal with only a small proportion of potassium removed from the structure.

Table 5.6: XRF data of pressed pellets for $K_3HGe_7O_{16} \cdot 4H_2O$, all molar ratios are normalised to germanium.

Element	Unexchanged	Cs-exchange	Sr-exchange
K	0.51	0.20	0.44
Ge	1	1	1
Sr	-	-	0.03
Cs	-	0.28	-

There is also good agreement between the pressed pellet and fused bead XRF data collected for this material, as shown in Table 5.7.

Table 5.7: XRF data of fused beads for $K_3HGe_7O_{16} \cdot 4H_2O$, all molar ratios are normalised to germanium.

Element	Unexchanged	Cs-exchange
K	0.48	0.18
Ge	1	1
Cs	-	0.30

The fused bead data reports slightly higher caesium content than that from Table 5.7, this could be due to the differences in preparation methods but also batch variations cannot be discounted. The caesium uptake reported is substantially better than the parent zirconogermanate phase and is comparable to the doped materials from Chapter 4. It is also noticeable that the total cation content relative to germanium, roughly 0.5:1, is higher than that expected from the formula.

High-resolution powder diffraction data collected for the caesium exchange of $K_3HGe_7O_{16} \cdot 4H_2O$, Figure 5.12, allows for the calculation of caesium uptake from the diffraction data and how it subsequently compares to the XRF data. Restraints were applied to Ge-O bonds of 1.74 Å (four coordinate) and 1.88 Å (six coordinate). Cation site occupancies were refined under constraints; caesium was added to each cation site and constrained to a maximum occupancy of 1.

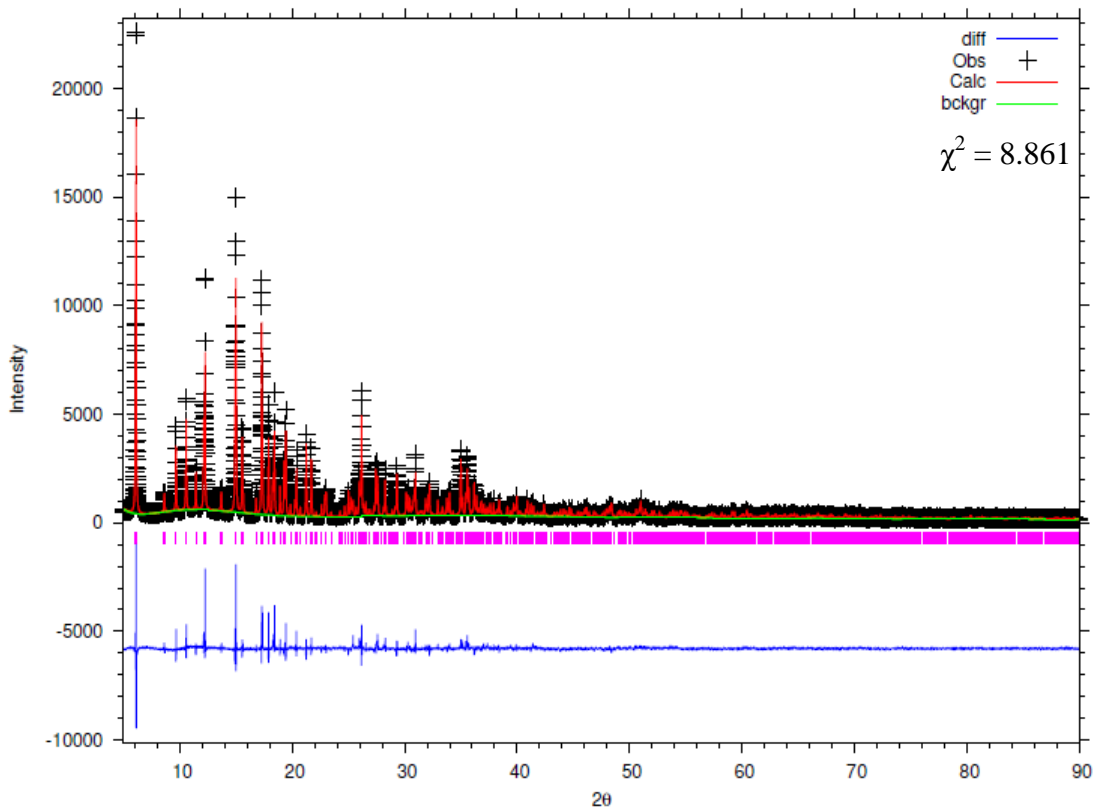


Figure 5.12: Rietveld refinement for the Cs-exchanged $K_3HGe_7O_{16} \cdot 4H_2O$

Table 5.8: Lattice parameters, atomic positions, occupancy and thermal parameters for the refinement of Cs-exchanged $\text{K}_3\text{HGe}_7\text{O}_{16}\cdot 4\text{H}_2\text{O}$. Thermal parameters are grouped by element and cation site.

$\lambda/\text{\AA}$	0.82525				
$a/\text{\AA}$	10.9281(1)				
$c/\text{\AA}$	7.7960(1)				
$V/\text{\AA}^3$	931.03(2)				
<i>Space Group</i>	<i>P-4b2</i>				
R_{wp}	0.0952				
R_{exp}	0.0320				
χ^2	8.861				
<i>Site</i>	<i>X</i>	<i>y</i>	<i>z</i>	<i>Occupancy</i>	<i>U_{iso}</i>
Ge1	0.1380(1)	-0.0080(1)	0.1390(2)	1	0.0023(2)
Ge2	0.2662(1)	0.2337(1)	0	1	0.0023(2)
Ge3	0	0	0.5	1	0.0023(2)
O1	0.1413(6)	0.2523(7)	0.8616(10)	1	0.0139(10)
O2	0.2708(7)	0.1037(6)	0.1265(10)	1	0.0139(10)
O3	0.1186(6)	-0.0217(8)	0.8926(9)	1	0.0139(10)
O4	0.8675(6)	0.0090(10)	0.3777(8)	1	0.0139(10)
Cs1	0.2953(1)	0.2047(1)	0.5	0.897(4)	0.0316(5)
K1	0.2953(1)	0.2047(1)	0.5	0.103(4)	0.0316(5)
K2	0.5	0	0	1	0.0218(15)
O5	0.3547(7)	-0.0423(6)	0.7039(10)	1	0.0139(10)

Table 5.9: Selected bond lengths from the refinement of Cs-exchanged $K_3HGe_7O_{16} \cdot 4H_2O$.

<i>Bond</i>	<i>Distance (Å)</i>		<i>Bond</i>	<i>Distance (Å)</i>
Ge1-O1	1.92(1)		Ge3-O4	1.74(1)
Ge1-O2	1.90(1)		Ge3-O4	1.74(1)
Ge1-O3	1.94(1)		Ge3-O4	1.74(1)
Ge1-O3	2.14(1)		Ge3-O4	1.74(1)
Ge1-O3	1.89(1)			
Ge1-O4	1.86(1)			
Ge2-O1	1.75(1)		Av M1-O	3.28
Ge2-O1	1.75(1)		Av K2-O	3.02
Ge2-O2	1.73(1)			
Ge2-O2	1.73(1)			

Fitting to the tetragonal cell derived by Clearfield *et al.* provided an adequate fit, however intensity discrepancies are observed once again. Clearly this is intrinsic to this material and further work must be done to understand the origin of the discrepancy as peak profile fitting does not effectively model the experimental peak shape and intensity.

However occupancies from table 5.8 allow for the approximation of caesium uptake in this material. The caesium occupancy is in good agreement with that derived by Trpiathi *et al.* and is equivalent to a formula of $K_{1.21}Cs_{1.79}HGe_7O_{16} \cdot 4H_2O$. This is lower than the reported XRF data however, as previously discussed, XRF analysis on these materials over estimates the total cation content.

5.3.3 K₃HTi₄Ge₃O₁₆·4H₂O ion exchange

The titanopharmacosiderites have been studied in much greater detail and have been shown to be incredibly good exchange materials, as outlined in Section 5.1. In order to compare all the materials in this work, XRF was used to study both the caesium and strontium uptake. It is of note that the concentration used in the literature is significantly lower than that described in Section 5.2.4; a 0.1 M exchange should give a good idea of the maximum uptake after a single exchange cycle. Table 5.10 shows the XRF data for pressed pellets of K₃HTi₄Ge₃O₁₆·4H₂O for both caesium and strontium exchange.

Table 5.10: XRF data of pressed pellets for K₃HTi₄Ge₃O₁₆·4H₂O, all molar ratios are normalised to germanium.

Element	Unexchanged	Cs-exchange	Sr-exchange
K	0.86	0.23	0.29
Ti	1.12	1.15	1.13
Ge	1	1	1
Sr	-	-	0.28
Cs	-	0.74	-

The reported exchange data confirms exchange properties in the literature, with both high caesium and strontium uptake observed. Rough approximation by scaling the above data would indicate approximately 70% of the potassium replaced by caesium and 55% strontium. This is in agreement with the loading values for the titanosilicate pharmacosiderite, discussed in Section 5.1, after 24 hours. However this is only a rough approximation as there are some

discrepancies in the XRF data that need to be considered. The titanium germanium ratio is lower than the 1.33:1 expected from the chemical formula and the overall cation content is slightly lower than expected for both the unexchanged and strontium exchanged data.

In order to reduce the errors from sample preparation, fused beads for the titanogermanate were synthesised with regards to generating more chemically sensible values. Fused bead data for the titanogermanates is shown in Table 5.11; fused beads were made using the methodology outlined in the experimental section.

Table 5.11: XRF data of fused beads for $K_3HTi_4Ge_3O_{16} \cdot 4H_2O$, all molar ratios are normalised to germanium.

Element	Unexchanged	Cs-exchange	Sr-exchange
K	0.79	0.18	0.23
Ti	0.85	0.85	0.77
Ge	1	1	1
Sr	-	-	0.24
Cs	-	0.57	-

Unfortunately XRF analysis on fused beads resulted in less chemically sensible data, with the reported titanium content much lower than was expected. The ability to fuse titanium could provide a reason for the lower values; if titanium incorporates poorly in the flux of choice then the reported titanium content will be lower. This is not uncommon when making fused beads and as a result care must be taken to ensure all elements can be incorporated into the bead. Flux choices and dilution factors play a vital role in acquiring sensible XRF data; elements such as tin require a much higher dilution in lithium borate fluxes than zirconium for example. This also highlights that the choice of preparation in order to gain better data can vary sample to sample. Pressed pellet data, in this case, is more chemically sensible than the equivalent fused bead data despite fused beads being considered a better preparation method. Each sample must be treated independently, with different preparation methods compared, to increase confidence in the XRF analysis.

Despite the relative depth of the literature on these titanium containing pharmacosidrite phases, all synthesised phases except the exchanged titanogermanate pharmacosiderite have been studied structurally. In order to analyse the caesium uptake by Rietveld refinement a model would need to be derived. The tetragonal unit cell used to refine the unexchanged phase was modified with caesium occupying the same positions as potassium. Cation occupancies were refined under constraints; each site was constrained to a maximum occupancy of 1. Restraints were applied to Ge-O and Ti-O bonds of 1.74 Å and 1.955 Å respectively, with heavy dampening required to achieve a stable fit. The resultant Rietveld refinement is shown by Figure 5.13.

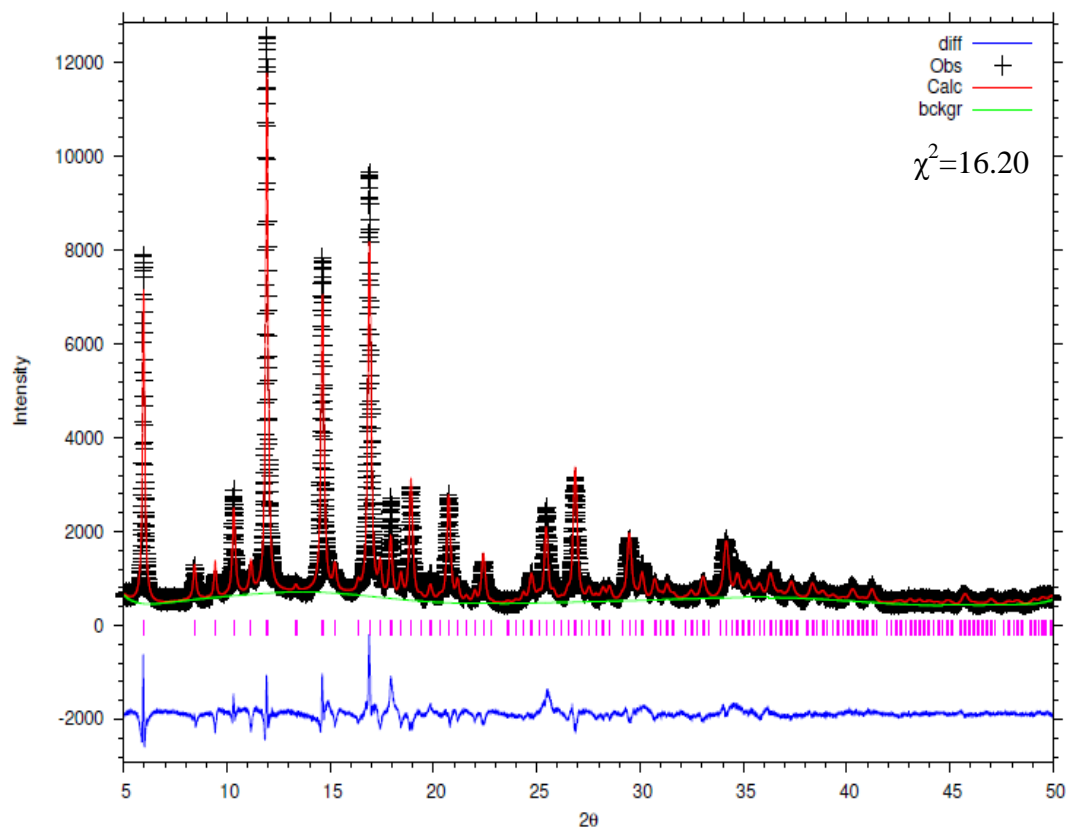


Figure 5.13: Rietveld refinement for Cs-exchanged $K_3HTi_4Ge_3O_{16} \cdot 4H_2O$

Table 5.12: Lattice parameters, atomic positions, occupancy and thermal parameters for the refinement of Cs-exchanged $\text{K}_3\text{HTi}_4\text{Ge}_3\text{O}_{16}\cdot 4\text{H}_2\text{O}$. Thermal parameters are grouped by element and cation sites.

$\lambda/\text{\AA}$	0.82525				
$a/\text{\AA}$	11.2473(7)				
$c/\text{\AA}$	7.9386(8)				
$V/\text{\AA}^3$	1004.26(11)				
<i>Space Group</i>	<i>P-4b2</i>				
R_{wp}	0.0954				
R_{exp}	0.0237				
χ^2	16.20				
<i>Site</i>	<i>x</i>	<i>y</i>	<i>z</i>	<i>Occupancy</i>	<i>U_{iso}</i>
Ti1	0.1408(6)	0.0005(9)	0.1416(13)	1	0.025 (fixed)
Ge1	0.2515(2)	0.2485(2)	0	1	0.0267(11)
Ge2	0	0	0.5	1	0.0267(11)
O1	0.1229(12)	0.2328(13)	0.8504(23)	1	0.0049(26)
O2	0.2421(14)	0.1324(13)	0.1466(23)	1	0.0049(26)
O3	0.1068(11)	-0.0091(16)	-0.0944(20)	1	0.0049(26)
O4	0.8676(9)	0.0040(20)	0.3833(15)	1	0.0049(26)
K1	0.2807(2)	0.2193(2)	0.5	0.258(11)	0.0658(26)
Cs1	0.2807(2)	0.2193(2)	0.5	0.260(20)	0.0658(26)
K2	0.5	0	0	0.742(11)	0.0477(27)
Cs2	0.5	0	0	0.740(20)	0.0477(27)
O5	0.3867(12)	-0.0119(13)	0.7311(18)	1	0.0049(26)

Table 5.13: Selected bond lengths from the refinement of Cs-exchanged $K_3HTi_4Ge_3O_{16} \cdot 4H_2O$.

<i>Bond</i>	<i>Distance (Å)</i>		<i>Bond</i>	<i>Distance (Å)</i>
Ti1-O1	1.73(1)		Ge2-O4	1.75(1)
Ti1-O2	1.87(1)		Ge2-O4	1.75(1)
Ti1-O3	1.92(2)		Ge2-O4	1.75(1)
Ti1-O3	2.11(2)		Ge2-O4	1.75(1)
Ti1-O3	1.94(2)			
Ti1-O4	1.92(1)			
Ge1-O1	1.88(1)		Av K1-O	3.24
Ge1-O1	1.88(1)		Av K2-O	3.16
Ge1-O2	1.75(1)			
Ge1-O2	1.75(1)			

The low data quality limits the ability to reliably fit the experimental data with heavy restraints and damping required to obtain a stable refinement. As with previous iterations peak asymmetry had a large impact on overall quality of fit, however in this case peak asymmetry terms do not accurately describe the peak shape. Attempts to refine the strontium exchange data were not stable using the tetragonal cell which describes the other titanium containing pharmacosiderites. There is also no precedent in the literature for strontium exchange structural variation in pharmacosiderites, as the focus was primarily on caesium exchange. As a result further work and better data would be required to study strontium uptake in these materials.

5.3.4 Titanosilicate pharmacosiderite thermal conversion

Following the successful ion exchange of both of the pharmacosiderites, the thermal conversion products were explored for any potential ceramic wastefrom phases. This could

provide potential candidates for long term storage and to provide a greater understanding of thermal stability of these phases.

There is very little literature which explores the thermal decomposition of these phases, with only the titanosilicate pharmacosiderite explored in detail. Xu *et al.* report that the $K_3HTi_4Si_3O_{16} \cdot 4H_2O$ framework breaks down at 657 °C, with a new phase isostructural to the mineral Jeppeite recrystallising at approximately 680 °C [103]. Jeppeite ($K_2Ti_6O_{13}$) is stable up to 1370 °C but it has never been suggested as a potential wasteform for radionuclides [104], however Ilyushin *et al.* report the phase relationship between jeppeite and the titanium analogue of zirconium wadeite ($K_2ZrSi_3O_9$) [105].

Variable temperature XRD ($\lambda = 1.5406 \text{ \AA}$), recorded by Joseph Davies, has been used to examine the phase assembly of the converted products for both the titanosilicate and titanogermanate. Figure 5.14 shows the VT XRD data for $K_3HTi_4Si_3O_{16} \cdot 4H_2O$, the material rapidly decreases in crystallinity before becoming largely amorphous at 400 °C. At approximately 700 °C recrystallisation is observed with the resultant phase being initially identified as a mixture of anatase and rutile. The high intensity marked peaks are from the corundum sample holder due to substantial amount of sample contraction observed, which was expected due to the water content of pharmacosiderites.

Analysis of the room temperature phase assemblage after the heating cycle confirms the presence of two TiO_2 polymorphs and no jeppeite phase. No silicon containing phases were observed and it is assumed that it occupies an amorphous phase, as shown by Figure 5.15. This would suggest that the titanosilicate pharmacosiderite has undergone complete framework breakdown and no stable ceramic phases were formed, contrary to what was reported by Xu *et al.*

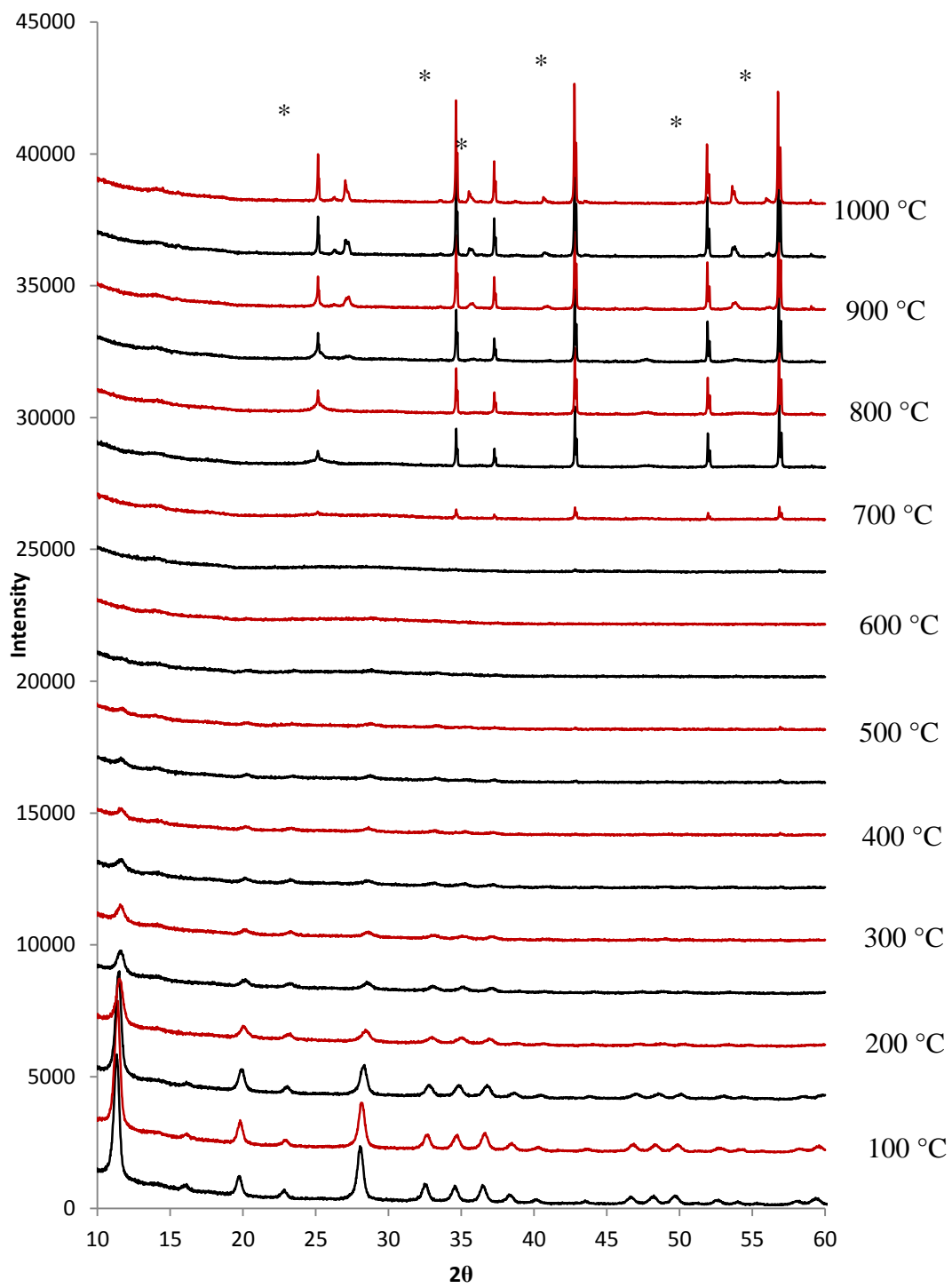


Figure 5.14: VT XRD data for $K_3HTi_4Si_3O_{16} \cdot 4H_2O$, peaks marked with asterisk are from the sample holder.

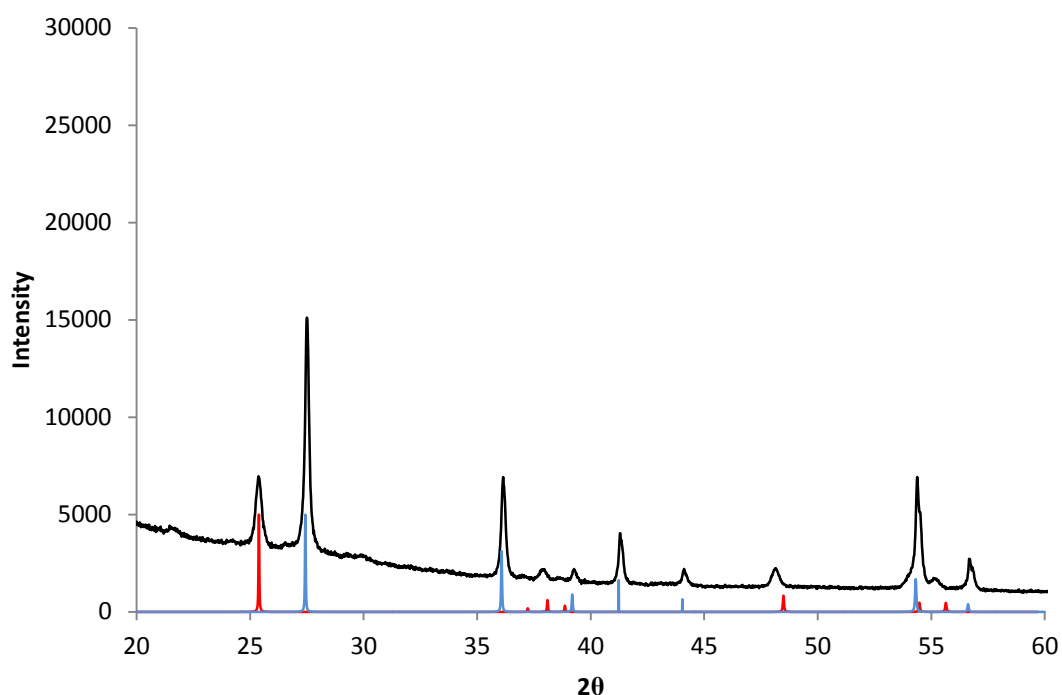


Figure 5.15: X-ray diffraction pattern ($\lambda = 1.5406 \text{ \AA}$) for the final phase assemblage of heated $\text{K}_3\text{HTi}_4\text{Si}_3\text{O}_{16}\cdot 4\text{H}_2\text{O}$. Reference patterns for rutile (Blue) and anatase (Red) have been added for comparison.

The titanosilicate pharmacosiderite is able to fully exchange potassium for caesium, VT XRD shows that caesium may potentially stabilise the formation denser ceramic type phases and this is supported by Xu *et al.* [103]. Figure 5.16 shows that the caesium exchanged titanosilicate becomes amorphous at a higher temperature, approximately $650 \text{ }^\circ\text{C}$, than the potassium form of the material. Recrystallisation then occurs at $700 \text{ }^\circ\text{C}$ with the formation of three different caesium containing phases. Figure 5.17 shows the phase assemblage at room temperature, the three caesium phases are $\text{CsTiSi}_2\text{O}_{6.5}$ and two polymorphs of $\text{Cs}_2\text{TiSi}_6\text{O}_{15}$, alongside rutile. $\text{CsTiSi}_2\text{O}_{6.5}$ is a pollucite analogue in which Al^{3+} is replaced by Ti^{4+} , Balmer *et al.* report the synthesis of this material at $700 \text{ }^\circ\text{C}$ to $800 \text{ }^\circ\text{C}$ which agrees with the reported XRD data in Figure 5.16 [106].

Leach rates for caesium have been studied for the pollucite analogue, Balmer *et al.* report that the material has leach rates several times better than loaded silicate glasses. The second caesium containing phase $\text{Cs}_2\text{TiSi}_6\text{O}_{15}$ has two polymorphs both of which are present in the thermal conversion products. Nyman *et al.* report the synthesis of the $\text{Cs}_2\text{TiSi}_6\text{O}_{15}$ Cc polymorph hydrothermally with the second C2/c polymorph attained through a high temperature route [107-108]. This expands on the Cs-Si-Ti phase mapping of Balmer *et al.*, in which the pollucite phase was discovered. Both polymorphs are stable up to 1150 °C after which a glass like material is formed, with the Cc polymorph showing both high radiation and chemical stability. Due to the stability of the material the reported Cs leach rate is very low and hence the material is suggested as a potential ceramic wasteform.

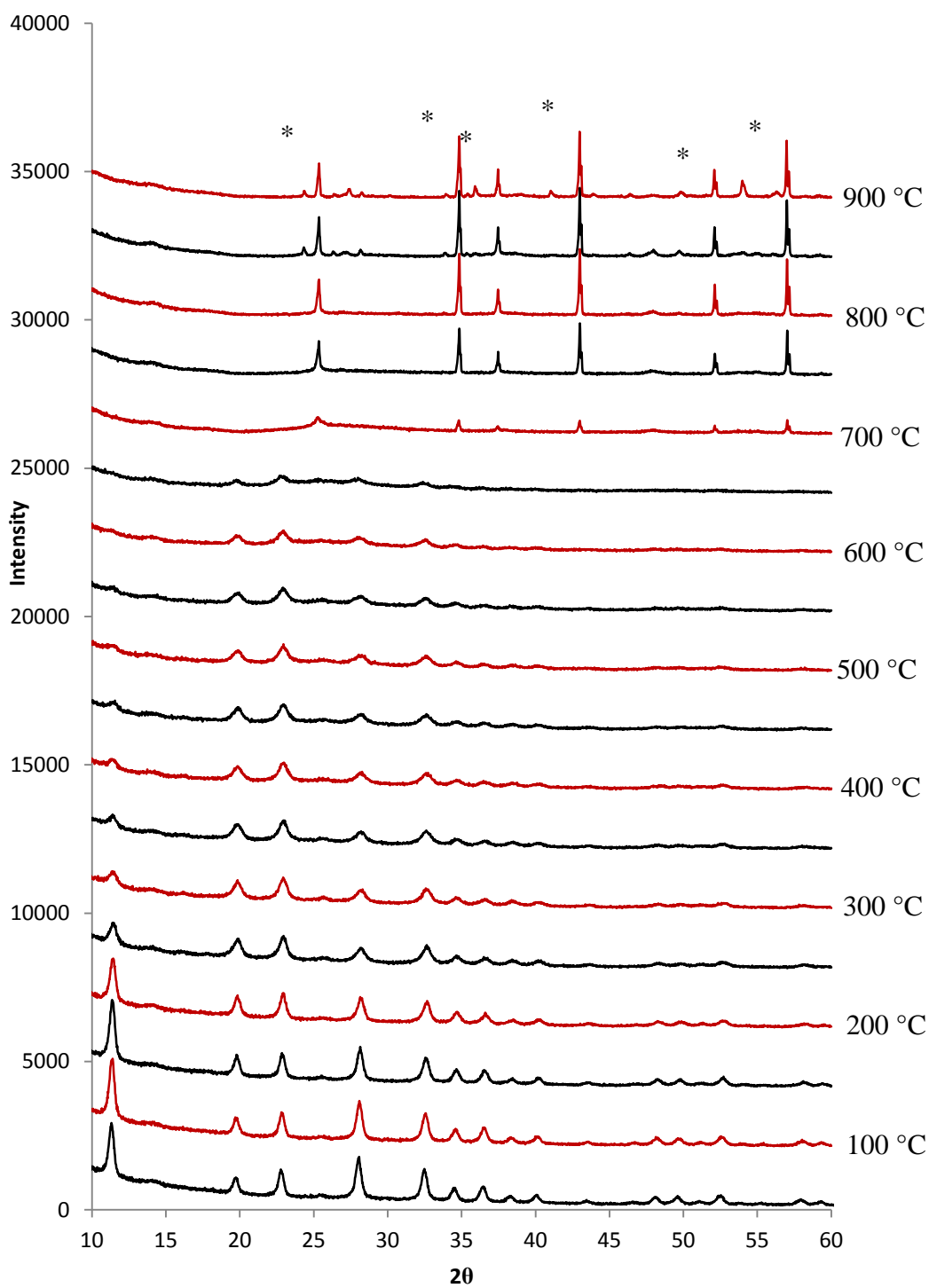


Figure 5.16: VT XRD pattern for Cs-exchanged $\text{K}_3\text{HTi}_4\text{Si}_3\text{O}_{16} \cdot 4\text{H}_2\text{O}$; peaks marked with asterisk are from the sample holder.

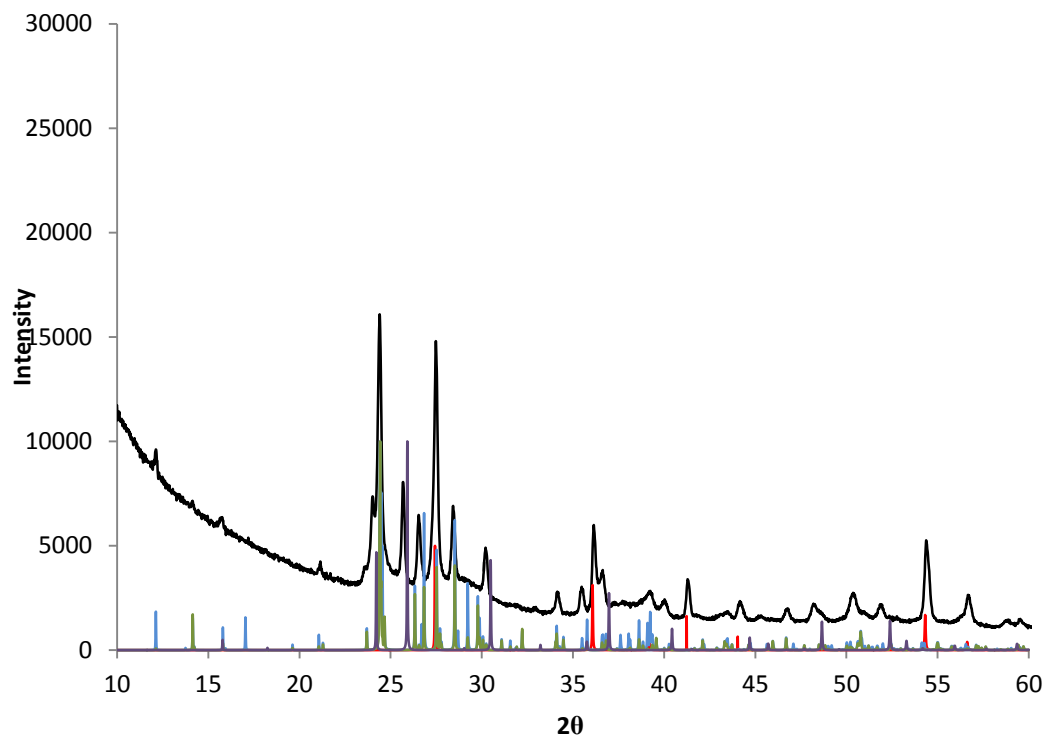


Figure 5.17: X-ray diffraction pattern ($\lambda = 1.5406 \text{ \AA}$) for the final phase assemblage of heated Cs-exchanged $\text{K}_3\text{HTi}_4\text{Si}_3\text{O}_{16}\cdot 4\text{H}_2\text{O}$. Reference patterns for the $\text{Cs}_2\text{TiSi}_6\text{O}_{15}$ phases (Green and Blue), pollucite (Purple) and circles rutile (Red) have been added for comparison.

5.3.5 Thermal conversion of germanogermanium pharmacosiderites

The thermal conversion products for the sodium form of the germanogermanium pharmacosiderite have been studied by Feng *et al.* Dehydration occurs at approximately 160-220 °C before thermal conversion to $\text{Na}_4\text{Ge}_9\text{O}_{20}$ at approximately 560 °C [93], however no maximum temperature was reported. In order to fully study the thermal conversion products of the potassium form of the germanogermanium pharmacosiderite and hence the suitability of the converted phases as wasteforms the high temperature stability needs to be considered. Initial attempts to heat the sample to 1000 °C resulted in the material completely melting into a glass like material, reduction of the temperature to 900 °C yielded the same result. Due to the low temperature stability of this material VT XRD was not considered suitable, however

XRD analysis for the material pre-treated at 700 °C for fused beads gives some insight into the phase assemblage. Interestingly at 700 °C some of the pharmacosiderite still remains alongside two potassium germanium oxide phases, Figure 5.18.

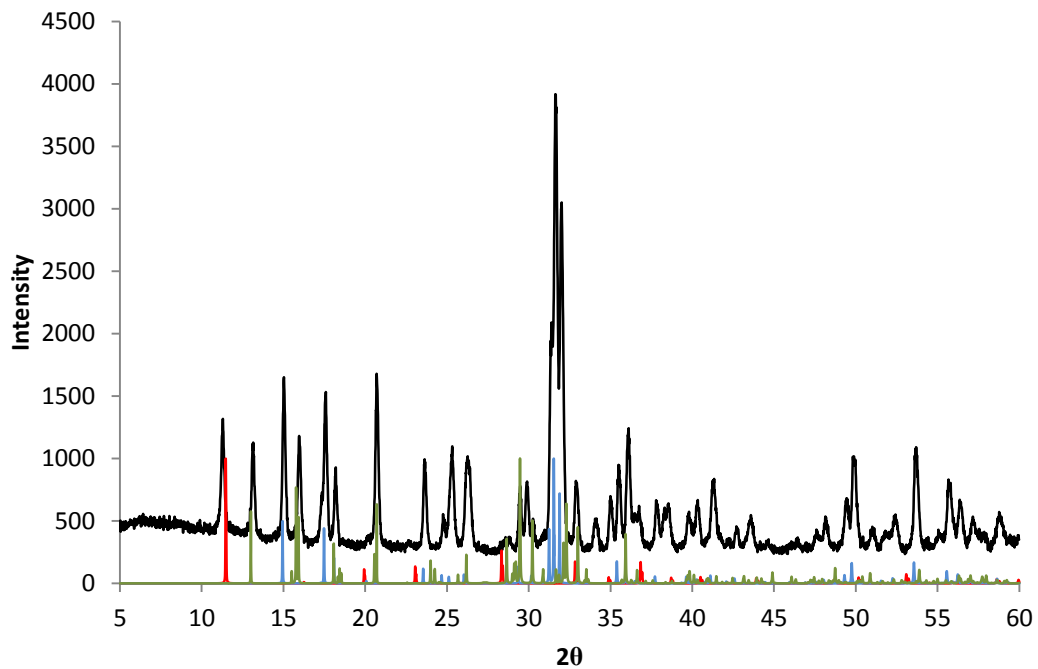


Figure 5.18: X-ray diffraction pattern ($\lambda = 1.5406 \text{ \AA}$) for the final phase assemblage of heated $\text{K}_3\text{HGe}_7\text{O}_{16.4}\text{H}_2\text{O}$. Reference patterns have been added showing $\text{K}_2\text{Ge}_4\text{O}_9$ (Blue), $\text{K}_6\text{Ge}_2\text{O}_7$ (Green) and $\text{K}_3\text{HGe}_7\text{O}_{16.4}\text{H}_2\text{O}$ (Red) for comparison.

This phase transition is different to that reported for the sodium form and occurs at much higher temperature; however this is not fully complete by 700 °C. The two potassium germanium oxide phases, $\text{K}_2\text{Ge}_4\text{O}_9$ and $\text{K}_6\text{Ge}_2\text{O}_7$ [109-110], have been well characterised in the literature but are not considered as potential ceramic wastefoms due to limited thermal stability and as a result melting at approximately 900 °C.

As shown by the titanosilicate pharmacosiderites, caesium can allow for the formation of stable wastefom phases relative the potassium analogue. However the thermal stability of the

ion exchanged material is limited with the sample completely melting by 900 °C, much like the potassium form. XRD patterns for the materials at 700 °C, shows a different phase transition than the potassium form shown in Figure 5.19.

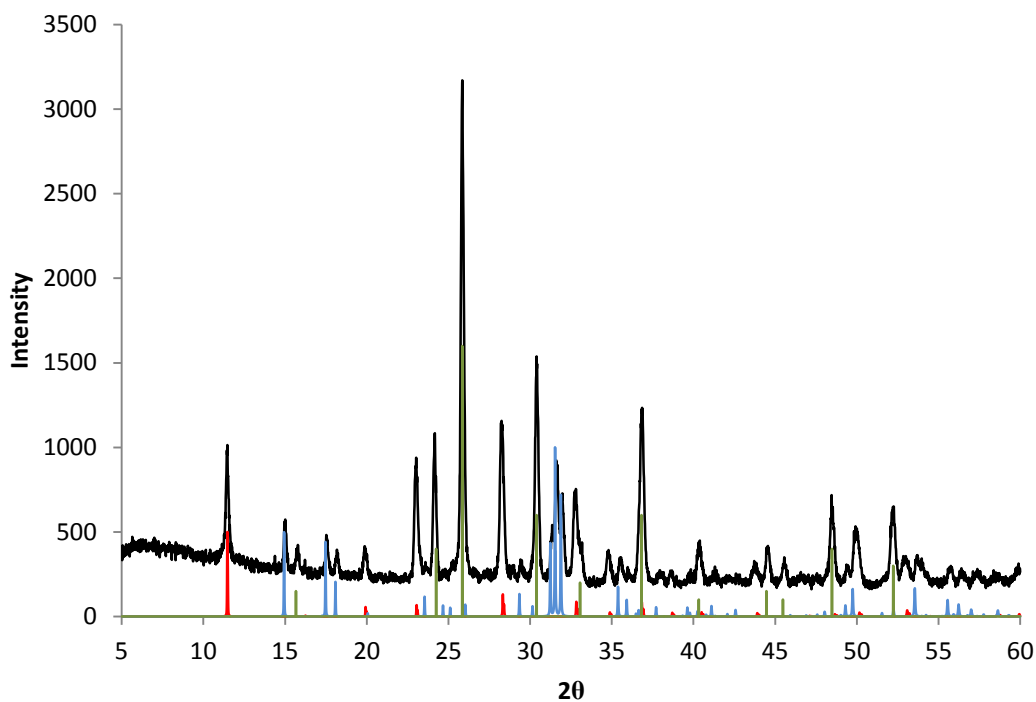


Figure 5.19: X-ray diffraction data ($\lambda = 1.5406 \text{ \AA}$) for the final phase assemblage of heated Cs-exchanged $\text{K}_3\text{HGe}_7\text{O}_{16}\cdot 4\text{H}_2\text{O}$. Reference patterns have been added showing $\text{Cs}_2\text{Ge}_6\text{O}_{13}$ (Green), $\text{K}_2\text{Ge}_4\text{O}_9$ (Blue) and $\text{K}_3\text{HGe}_7\text{O}_{16}\cdot 4\text{H}_2\text{O}$ (Red) for comparison.

The resultant phase assemblage once again consists of some remaining pharamacosiderite, caesium germanium oxide ($\text{Cs}_2\text{Ge}_6\text{O}_{13}$) and potassium germanium oxide ($\text{K}_2\text{Ge}_4\text{O}_9$). The caesium containing phase identified has been very poorly characterised with very little reported in the literature and as a result the reliability of the pattern on the PDF database can be called into question. However as with the unexchanged material, the low thermal stability reduces the viability of the reported thermal conversion products as wastefoms.

The analysis of the thermal conversion products for the germanogermanium system resulted in no phases of interest. What this would suggest is that a transition metal being located at the octahedral site is critical to the formation of stable ceramic phase when thermally converting OT materials, as shown for both umbite and titanosilicate pharamacosiderite.

5.3.6 Thermal conversion of titanogermanate pharamacosiderites

Unlike the titanosilicate pharamacosiderite, the thermal conversion products for the germanium system have not been reported in the literature. In order to gain a greater understanding of the thermal stability of these materials both the unexchanged and Cs/Sr exchanged materials were analysed by VT XRD ($\lambda = 1.5406 \text{ \AA}$).

Figure 5.20 shows the variable temperature XRD at 50 °C intervals up to 900 °C, above this temperature the thermal conversion products melt showing substantially lower thermal stability than the umbite materials. The unexchanged titanogermanate pharamacosiderite undergoes a phase transition between 600 °C and 650 °C, with the sample being completely amorphous at 600 °C before recrystallising to a $\text{K}_2\text{TiGe}_3\text{O}_9$ phase. Despite formulaically being similar to the previous mentioned wadeite phases, $\text{K}_2\text{TiGe}_3\text{O}_9$ belongs to a family of tetragermanates with general formula $\text{M}_2\text{Ge}_4\text{O}_9$, where titanium has substituted for a germanium. Tetragermanates crystallise in a trigonal space group ($P-3c1$) as opposed to the hexagonal crystal structure of wadeite[111].

Figure 5.21 shows the room temperature phase assemblage after the heating cycle, with the tetragermanate phase forming alongside anatase and rutile.

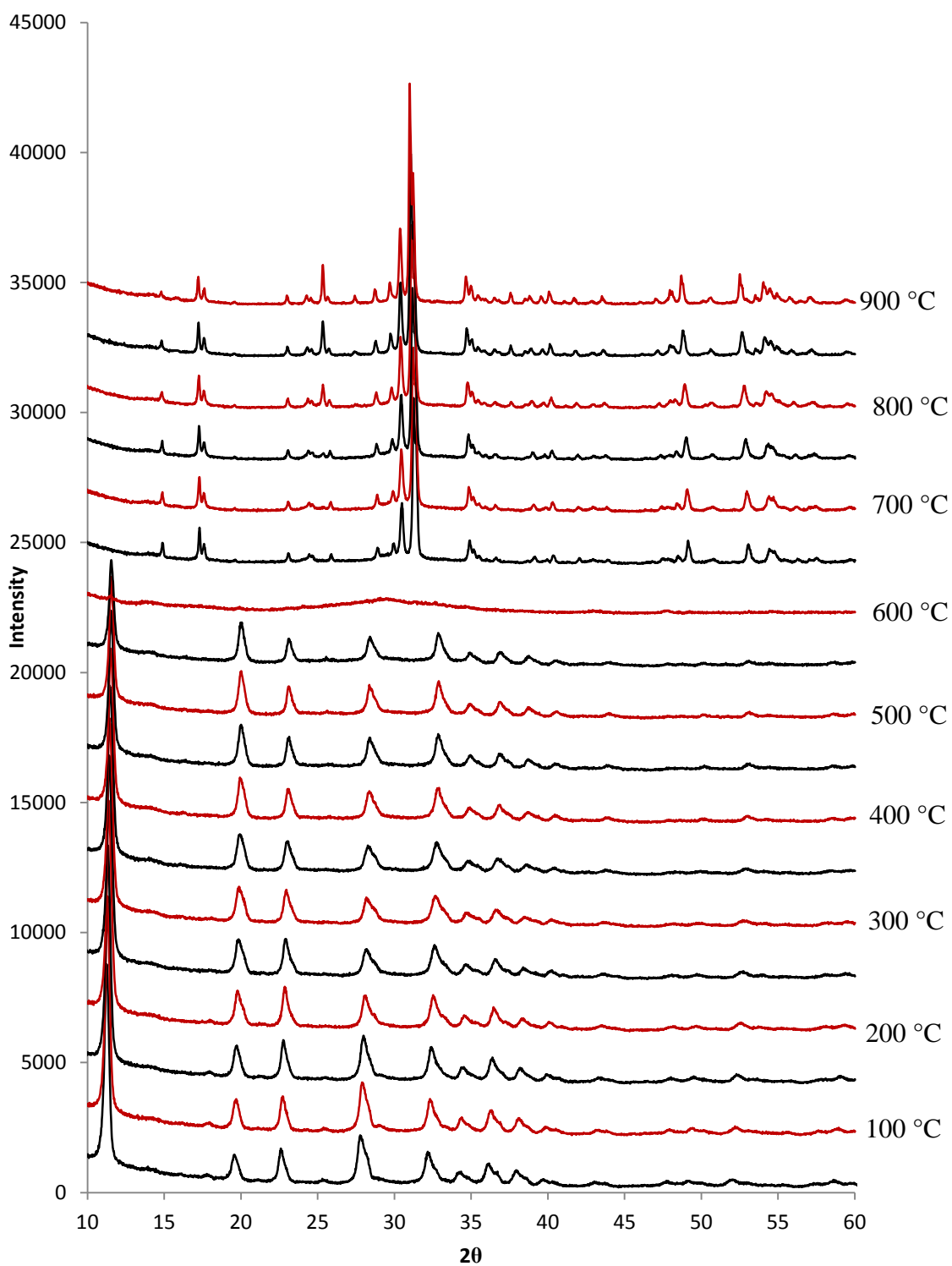


Figure 5.20: VT XRD data for $K_3HTi_4Ge_3O_{16} \cdot 4H_2O$.

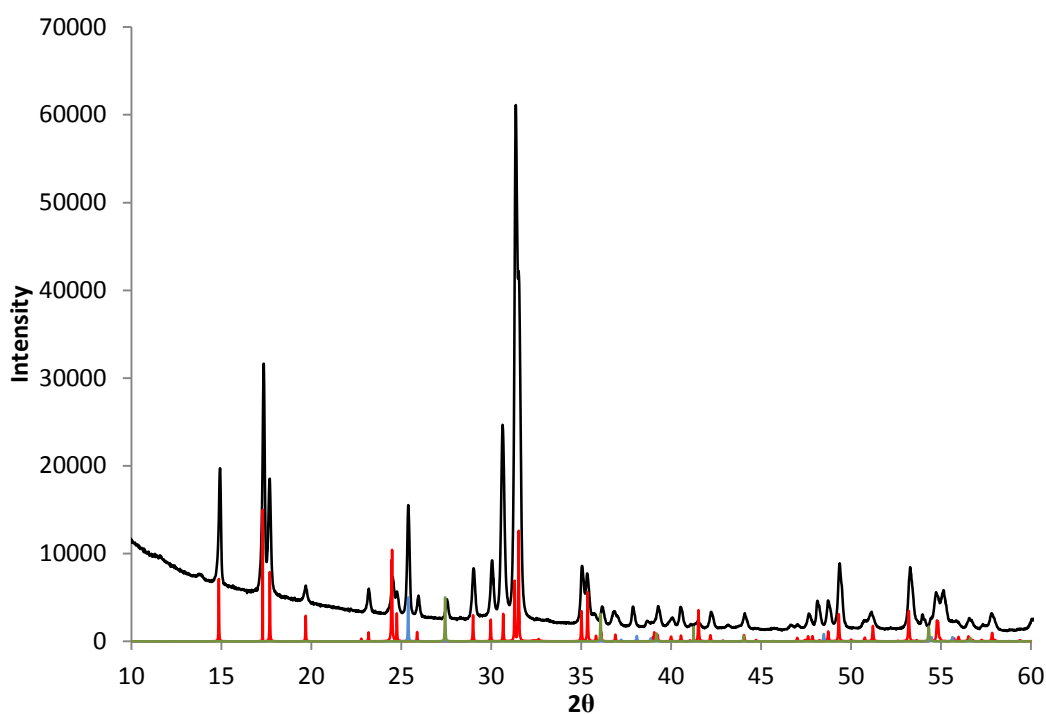


Figure 5.21: X-ray diffraction data ($\lambda = 1.5406 \text{ \AA}$) for the final phase assemblage of heated $\text{K}_3\text{HTi}_4\text{Ge}_3\text{O}_{16}\cdot 4\text{H}_2\text{O}$. Reference patterns have been added showing $\text{K}_2\text{TiGe}_3\text{O}_9$ (Red), anatase (Blue) and rutile (Green) for comparison.

Caesium-exchanged titanogermanate pharamcosiderites

Thermal conversion of the partially caesium exchanged titanogermanate pharamcosiderite shows a quite different conversion pathway, as shown by Figure 5.22. The pharamcosiderite framework is stable to approximately 650 °C before recrystallising rapidly to a wadeite type phase at 700 °C. Caesium has promoted the formation of a wadeite phase and increased the thermal stability of the pharamcosiderite framework, as shown by the higher transition temperature relative to the unexchanged phase. However this wadeite phase, identified by Bruker phase match software as $\text{Cs}_2\text{TiGe}_3\text{O}_9$ [111], melts at approximately 900 °C.

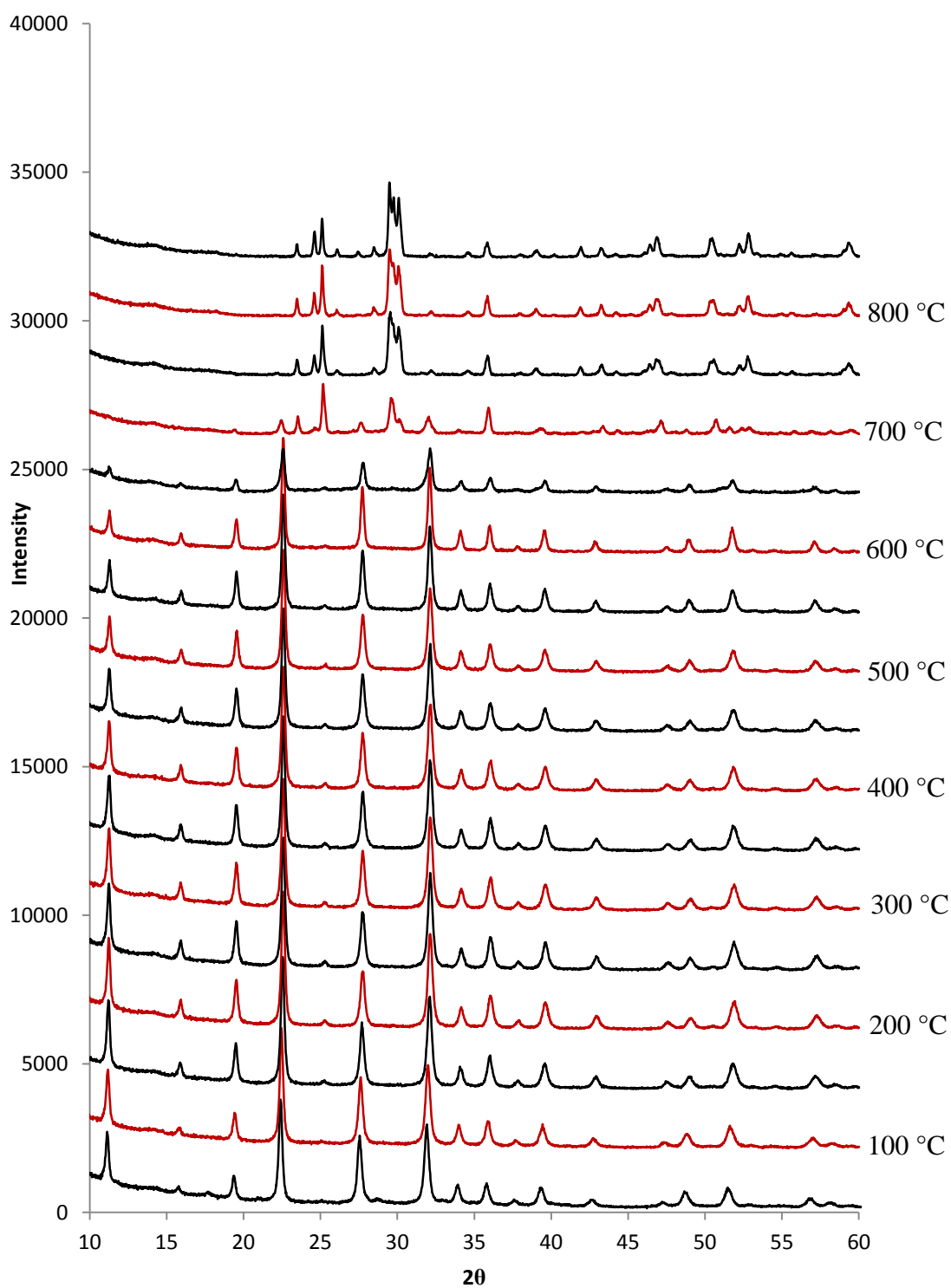


Figure 5.22: VT XRD data for Cs-exchanged $K_3HTi_4Ge_3O_{16} \cdot 4H_2O$.

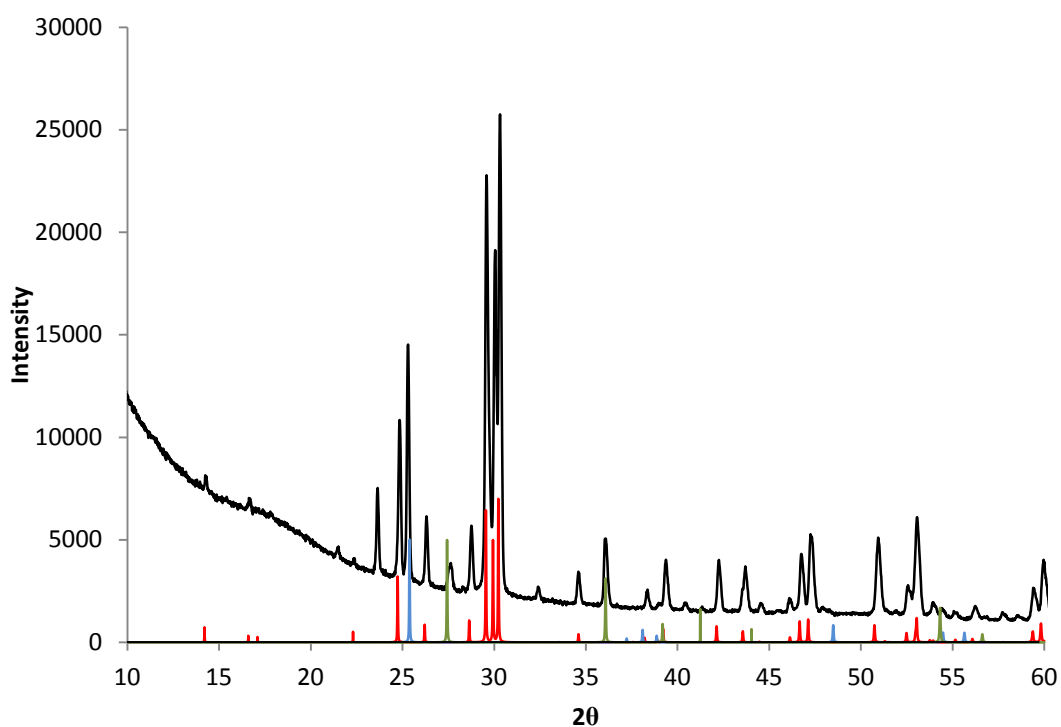


Figure 5.23 X-ray diffraction data ($\lambda = 1.5406 \text{ \AA}$) for the final phase assemblage of heated Cs-exchanged $\text{K}_3\text{HTi}_4\text{Ge}_3\text{O}_{16}\cdot 4\text{H}_2\text{O}$. Reference patterns have been added showing $\text{Cs}_2\text{TiGe}_3\text{O}_9$ (Red), anatase (Blue) and rutile (Green) for comparison.

This reduced thermal stability is substantially worse than the archetypal zirconium wadeites, which are stable to much higher temperatures. The room temperature phase assemblage after heating is shown by Figure 5.23, with minor anatase and rutile phases present alongside an unidentified phase. No potassium containing phases are identified using phase match software however it is possible that there is some incorporation into the wadeite phase, which may explain the low melting temperature.

Strontium-exchanged titanogermanate pharamcosiderites

The incorporation of strontium into the pharamcosiderite structure has a drastic impact on the thermal stability of the material. Figure 5.24 shows the variable temperature XRD at 50 °C intervals up to 900 °C. The pharamcosiderite framework has broken down by 300 °C and remains largely amorphous to approximately 700 °C. Recrystallisation above this temperature results in a complex phase assemblage as shown by Figure 5.25.

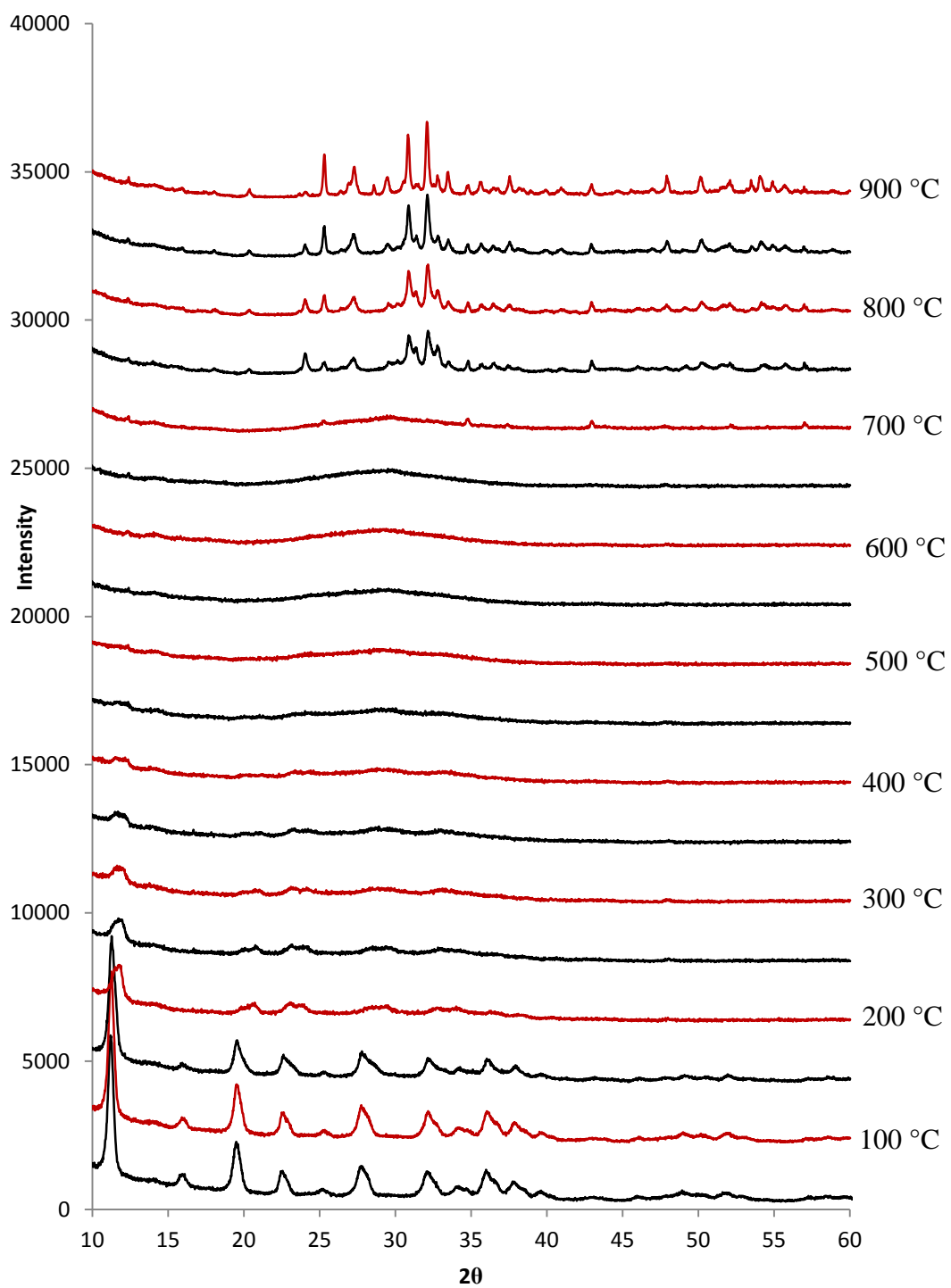


Figure 5.24: VT XRD data for Sr-exchanged $\text{K}_3\text{HTi}_4\text{Ge}_3\text{O}_{16}\cdot 4\text{H}_2\text{O}$.

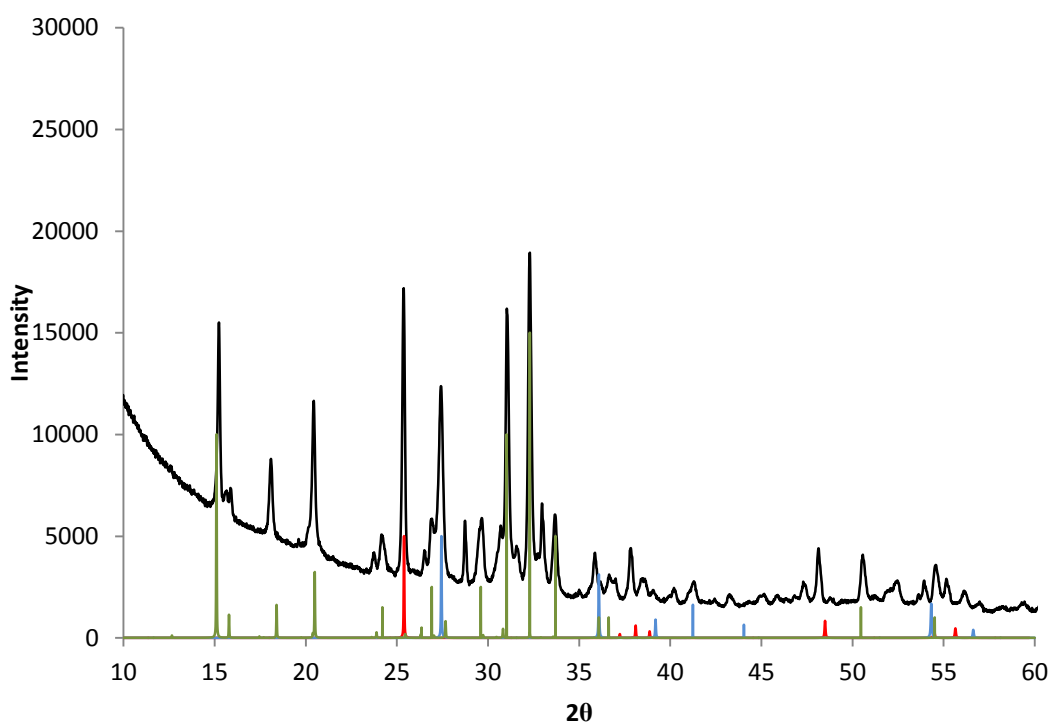


Figure 5.25: X-ray diffraction data ($\lambda = 1.5406 \text{ \AA}$) for the final phase assemblage of heated Sr-exchanged $\text{K}_3\text{HTi}_4\text{Ge}_3\text{O}_{16}\cdot 4\text{H}_2\text{O}$. Reference patterns have been added showing $\text{K}_2\text{Sr}(\text{Ge}_4\text{O}_9)_2$ (Green), anatase (Red) and rutile (Blue) for comparison.

As the strontium loading is approximately 50% a different tetragermanate phase $\text{K}_2\text{Sr}(\text{Ge}_4\text{O}_9)_2$ forms [112]. A strontium containing germanate with the perovskite structure, SrGeO_3 [113], and another tetragermanate, SrGe_4O_9 , form minor phases which have been excluded for clarity in the figure. This would suggest a very different thermal conversion pathway relative to the other titanogermanate pharmacosiderites studied.

The purpose of exploring the ion exchange and thermal conversion products of pharmacosiderite materials was to compare them to the previous work on umbite. It has been shown that the doped umbites and pharmacosiderites have similar Cs^+ uptake, with $\text{K}_3\text{HTi}_4\text{Ge}_3\text{O}_{16}\cdot 4\text{H}_2\text{O}$ showing much better Sr^{2+} uptake. The thermal conversion of pharmacosiderites, despite forming a potential wastefrom phase when caesium exchanged,

does not show the same thermal stability as zirconium containing wadeites. As strontium uptake in umbite is very poor, exploring the conversion products was not possible and therefore any potential wasteform transition cannot be commented on. However from what was observed in the pharmacosiderite system it would be likely that wadeite could not accommodate strontium and hence is not a viable strontium wasteform.

5.4 Conclusions

The relationship between germanium containing umbite and pharmacosiderites has been explored, with the pharmacosiderites being impurities during the attempted synthesis of Ti/Sn containing umbites. The ion exchange properties have been explored in the literature however the thermal conversion products were of the most interest due to potential wasteform phases. Successful optimisation of the synthesis of the pharmacosiderites and subsequent ion exchange confirms the excellent cation exchange properties reported in the literature for this family of materials. These materials are not as thermally robust as zirconogermante umbite however the formation of a wasteform phase was observed for the caesium exchanged titanogermanate pharmacosiderite. This wasteform phase is analogous to wadeite and its formation is stabilised by the presence of caesium in the precursor pharmacosiderite phase, however exhibits substantially poorer thermal stability.

Chapter 6-Conclusions and Further

work

6.1 Conclusions

The purpose of this work was to increase understanding of the umbite system, with regards to understanding ion exchange properties and potential nuclear industry applications. The ion exchange properties of the various forms of umbite have been explored both in the literature and internally, focusing on the metal octahedra containing silicates. The germanate derivatives of umbite have not been previously studied in any real depth, with only a single reference in the literature and very limited information with regards to ion exchange properties. The hydrothermal synthesis of germanium containing umbites were investigated, the optimisation and scale up of the fully germanium containing umbite was also undertaken. Ion exchange properties were explored for the germanate umbite, with work done to try and improve the ion exchange properties of the material. Successful niobium doping allowed for a drastic improvement of caesium uptake relative to the undoped phase, however interesting ion exchange behaviour was observed which required further investigation. Other octahedral-tetrahedral framework material were synthesised whilst studying the umbite system, with ion exchange and thermal properties were explored for comparison.

6.1.1 Germanoumbites

Isomorphous substitution at the octahedral site in the umbite structure has been shown to be possible in the literature. However very little work focused on substitution at the tetrahedral site, the elements that can be substituted for silicon are limited and germanium was chosen as it is the most chemically similar. Attempts to partially dope germanium into the silicate umbite structure were unsuccessful, with impurity phases formed on germanium dioxide addition to the silicate umbite synthesis. Further focus was given to the optimisation of the

synthesis of the zirconogermanate umbite, with the optimised synthesis methodology capable of producing multigram quantities with reduced synthesis time, when compared to the literature. The ion exchange properties of the zirconogermanate were explored with respect to caesium and strontium uptake; however the material showed minimal uptake of both target cations. The inherently poor ion exchange of the zirconogermanate was further shown with no observed sodium, magnesium and calcium uptake by XRF. These ion exchange properties are substantially worse than those shown in the literature for the zirconosilicate umbite, which would readily exchange potassium for both caesium and sodium. Attempts to improve the ion exchange properties of the germanoumbite by synthesising a sodium derivative of the zirconogermanate failed. Using reflux conditions and a high concentration sodium chloride solution to try and force sodium into the framework resulted in unusual ion exchange behaviour. XRF analysis showed a decrease of potassium in the sample but no sodium uptake, XRD analysis showed a variation in diffraction pattern relative to the zirconogermanate parent material. Interestingly this behaviour can be reversed using a potassium chloride reflux, with XRF data and the diffraction pattern showing a regeneration of the parent phase. Despite the interesting pore chemistry observed when refluxing this material, with the variation of the pore species inducing a structural change, the formation of a sodium form by exchange is not possible.

Synthesis of the proton form was investigated, with an apparent improvement in exchange properties observed relative to the parent material. However due to the acid solubility of germanium, sample quality and yield is considerably reduced after acetic acid treatment. Despite the improvement of ion exchange properties, synthesis of the proton form was not a reliable method of improving exchange characteristics of the zirconogermanate umbite.

Attempts to synthesise germanoumbite with different octahedral components besides zirconium were not successful, with pharmacosiderite phases formed instead. This suggests a very narrow phase boundary for umbite formation with minimal variation in synthesis methodology resulting in other octahedral-tetrahedral materials. Thermal conversion of the umbite phase confirms the expected phase transition to wadeite which could act as a final wasteform. However due to poor uptake characteristics caesium incorporation into this phase, could not be confirmed.

6.1.2 Doped Germanoumbites

Improving the ion exchange properties by doping was investigated in the zirconogermanate umbite system. The successful doping of niobium up to 25% was shown to be possible, doping levels above 25% were not reproducible and resulted in pharmacosiderite impurity phases. High-resolution powder diffraction data showed the material was single phase with minimal reduction in sample quality relative to the parent phase. The successful incorporation of antimony has also been shown to be possible however due to the solubility of antimony oxide the maximum doping level is 20%. Ion exchange studies for the doped species showed a substantial improvement in caesium uptake relative to the parent material. Strontium exchange was still minimal however caesium uptake increased proportionally to niobium and antimony content. This could be due to the creation of vacancies in the pore system, as the number of vacancies increases the diffusion into the bulk also increases. However high-resolution powder diffraction data showed some interesting crystallographic characteristics with respects to caesium uptake in the doped materials. Peak splitting was observed in the high-resolution data which could be attributed to either a reduction in symmetry or multiple

phases. By using various different models to try to best fit the recorded data by Rietveld, it was shown that the exchanged samples could consist of two different exchanged phases. One phase is potassium rich and the second is much more caesium rich, by increasing the niobium content the relative weight percentages between the two different phases also varies.

Increasing the niobium content in the sample results in a higher calculated weight percentage for the caesium rich phase in the sample. Crystallographically the two phase models fits the data quite well however chemically there are still issues that need to be addressed which will be covered in the further work section. This strange ion exchange behaviour is also shown when antimony doping with similar trends observed in the refinement data. Analysis of the thermal conversion of the doped exchanged samples for potential wastefrom phases showed promising results. For both antimony and niobium the major phase was a wadeite type phase suggesting that dopants do not perturb the expected phase transition and secondly wadeite can accommodate caesium. A range of unidentifiable impurity phases are present suggesting quite a complex thermal conversion pathway for the doped species.

6.1.3 Pharmacosiderites

The relationship between germanium containing umbite and pharmacosiderites has been explored, with the pharmacosiderites being synthesised as impurities during the attempted synthesis of Ti/Sn containing umbites. The ion exchange properties have been explored in the literature however the thermal conversion products were of the most interest due to potential wastefrom phases. This would allow for the comparison between the umbite structure and other related OT materials, especially as they are closely related synthetically. Successful optimisation of the synthesis of the pharmacosiderites and subsequent ion exchange confirms

the excellent cation exchange properties reported in the literature for this family of materials. These materials are not as thermally robust as zirconogermanate umbite however the formation of a potential wasteform phase was observed for the caesium exchange titanogermanate pharmacosiderite. This wasteform phase is analogous to wadeite and its formation is stabilised by the presence of caesium in the precursor pharmacosiderite phase. The importance of the octahedral metal is shown by the thermal conversion of the germanogermanium pharmacosiderite which has low thermal stability. High temperature treatment of this material resulted in the formation of a glass like material and complete sample melting at relative low temperatures relative to other phases mentioned in this work.

To conclude this work provides a study into the germanium umbite system and the related phases for potential ion exchange applications. It is difficult to compare the phases reported in this work against already established exchange materials as we have no kinetic information as of yet, as a result the rate of uptake could be too slow for nuclear applications. However it has been shown that doped umbites are able to incorporate caesium, with a higher caesium uptake in a single cycle (63% vs 50%) when compared to silicate umbite. The inability to take up sodium and magnesium could also suggest good caesium selectivity; however this is cannot be confirmed. However the requirement for both caesium and strontium uptake would mean the phases reported in this work does not outperform clinoptilolite used on SIXEP, which successfully uptakes both radionuclides. The initial hypothesis of synthesising an open framework material, exchanging with cations and then thermally converting has been shown to be possible with the materials covered in this work. It has been shown that despite initial poor ion exchange synthetic modification caused a drastic improvement in uptake and could provide a methodology of improving any other poor exchange materials such as AV-7 and AV-13. Thermal properties of both umbite and pharmacosiderites show the conversion to

wadeite wastefrom phases. This work provides the foundations for further work on these materials and a greater understanding of OT germanate materials.

6.2 Further work

6.2.1 Chapter 3

The ability to synthesise umbite materials related to the parent zirconogermanate proved to be a challenge, however despite the lack of success reported in this work optimisation of synthesis conditions for both Ti and Sn containing umbite could allow for access of these phases. In general the hydrothermal synthesis approach used focused on maintaining similar batch compositions and conditions however a more systematic approach may yield more materials of interest. This could be incorporated into phase mapping in which the relationship between umbite, pharmacosiderites and the possible synthesis of other phases could be probed. However due to the number of potential variables, very specific experiments would be required to minimise the time required to do such work.

A greater crystallographic understanding of the umbite system is required especially deriving a model which best describes the peak splitting and potential reduction in symmetry observed in the high-resolution powder diffraction data. This will provide a more robust model which could then be applied to the exchanged materials which would improve the reliability of the analysis. Further structural analysis is required for the potential caesium and ammonium forms of umbite; unfortunately the lab data collected was not of high enough quality. As a result synchrotron data would be required to improve the analysis for these novel germanate phases.

6.2.2 Chapter 4

There are multiple areas in which this work could be expanded upon; especially considering all exchange work reported was done in bulk to determine maximum uptake levels of cation of interest. Further work would focus on developing a better understanding of the ion exchange properties using more representative conditions. This could be done using waste stream stimulants from which we could determine the selectivity when other elements are present in the exchange solutions and calculate K_d values for both caesium and strontium. This could be further developed by considering exchange properties across a wide pH range and any pH dependent variations in cation uptake. This will allow for greater insight into any trends due to the increased amount of data points which in turn will improve confidence in the capabilities of the material covered in this work. The exchange work could be supported by in-situ XRD ion exchange experiments; this would allow for the exchange mechanism for the doped materials to be determined and may provide an explanation for some of the exchange characteristics observed.

To fully understand the industrial applications of these materials, there would need to be some degree material processing and functionalisation. This could be combined with column tests which would provide a more representative understanding of the materials capabilities from an industrial standpoint. This would also provide some insight into the kinetic aspects of the exchange process over varying time lengths other than the 24 hour exchange used in this work.

The thermal conversion of these materials has been reported for potential ceramic wastefrom phases, however some question remain as to the nature of the thermal conversion products. Exploring this could be done through traditional solid state routes, firstly to confirm if the

dopant is incorporated into the structure by replacing zirconium in wadeite, and secondly are mixed Cs/K wadeite phase chemically viable. The leachability and physical properties of the phases were not explored within this work, this was due to the time lengths required to investigate wastefrom properties thoroughly however the next logical step is to test the viability of the wastefrom phases observed. It would be of interest to see how a pure wadeite synthesised via solid state compares to the thermal conversion products with the minor phases present, to see if these other phase impact leaching rates.

6.2.3 Chapter 5

The ion exchange properties of pharmacosiderite phases have been already well studied in the literature, this work gives further insight into the thermal properties related to the open-framework to wastefrom hypothesis. Further work could focus on post processing of these material and more industrial applicable studies such as column testing. Functionalisation of these materials would be the next obvious step especially if commercialisation is being considered and the impact this will have on the materials chemical behaviour. The germanogermanium pharmacosiderite phase does not convert to a ceramic wastefrom and the ion exchange properties are worse than the titanogermanate derivative. However the literature for the phase is relatively old and the diffraction data shown in this work showed features not reported in the literature. Crystallographically it would be interesting to better understand these features from a completion point of view. However industrial practicality is limited for this material and hence it would not be beneficial to further probe the ion exchange beyond that shown in the literature.

References

- [1] J.Price, M.Zeyringer, D.Konadu, Z.S.Mourão, A.Moore and E.Sharp, *Appl. Energ.*, 2018, **228**, 928-941
- [2] E.A.Byers, J.W.Hall and J.M.Amezaga, *Global Environmental Change*, 2014, **25**, 16-30
- [3] S.H.Roberts, B.D.Foran, C.J.Axon, B.S.Warr and N.H.Goddard, *Appl. Energ.*, 2018, **228**, 409-425.
- [4] M.Kotak and M.Kirchel, *Energy*, 2017, **170**, 47-50.
- [5] M.Grimston, W.J.Nuttall and G.Vaughan, *J. Radiol. Prot.*, 2014, **34**, R1-R24.
- [6] S.F.Ashley, G.J.Vaughan, W.J.Nuttall and P.J.Thomas, *Process. Saf. Environ.*, 2017, **112**, 77-95.
- [7] H.Smyth, L.Lecoeuvre and P.Vaesken, *Int. J. Proj. Manag.*, 2018, **36**, 170-183.
- [8] S.Wallbridge, A.Banford and A.Azapagic, *Int. J. life. Cycle. Assess.*, 2013, **18**, 990-1008.
- [9] I.W.Donald, B.L.Metcalf and R.N.J.Taylor, *J Mater Sci.*, 1997, **32**, 5851-5887.
- [10] E.R.Vance and D.S.Perera, *Handbook of advanced radioactive waste conditioning technologies*, Woodhead Publishing, 2011, 207-229.
- [11] L.L.Hench, D.E.Clark and J.Campbell, *Nucl. Chem. Waste. Man.*, 1984, **5**, 149-173.
- [12] S.Gin, P.Jollivet, M.Tribet, S.Peuget and S.Schuller, *Radiochim. Acta.*, 2017, **105**, 927-959.
- [13] M.I.Ojovan and W.E.Lee, *Metall. Mater. Trans. A*, 2011, **42**, 837-851.
- [14] C.Lopez, X.Deschanel, J.M.Bart, J.M.Boubals, C. Den Auwer and E.Simoni, *J. Nucl. Mater.*, 2003, **312** 76-80.
- [15] X.Deschanel, S.Peuget, J.N.Cachia and T.Charpentier, *Prog. Nucl. Energ.*, 2007, **49**, 623-634.
- [16] F.H.Elbatat, Y.M.Hamdy and S.Y.Marzouk, *J. Non-Cryst. Solids*, 2009, **355**, 2439-2447.
- [17] B.C.Sales and L.A.Boatner, *Science*, 1984, **226**, 45-48.
- [18] E.M.Pierce, B.P.McGrail, P.F.Martin, J.Marra, B.W.Arey and K.N.Geiszler, *Appl. Geochem.*, 2007, **22**, 1841-1859.
- [19] W.L.Gong, W.Lutze and R.C.Ewing, *J. Nucl. Mater.*, 2000, **278**, 73-84.

- [20] A.E.Ringwood, S.E.Kesson, N.G.Ware, W.Hibberson and A.Major, *Nature*, 1979, **278**, 219-223.
- [21] A.E.Ringwood, S.E.Kesson, N.G.Ware, W.Hibberson and A.Major, *Geochem. J.*, 1979, **13**, 141-165.
- [22] E.R.Vance, *MRS. Bull.*, 1994, **333**, 28-32.
- [23] E.R.Vance, D.T.Chavara and D.J.Gregg, *MRS Energy and Sustainability*, 2017, **4**, 1-8.
- [24] S.Gupta, N.Pathak, R.Gupta, S.K.Thulasidas and V.Natarajan, *J. Mol. Struct.*, 2014, **1068**, 204-209.
- [25] M.Jafar, S.Phapale, S.N.Achary, R.Mishra and A.K.Tyagi, *J. Therm. Anal. Calorim.*, 2018, **131**, 2709-2718.
- [26] K.Zhang, G.Wen, H.Zhang and Y.Teng, *J. Eur. Ceram. Soc.*, 2015, **35**, 3085-3093.
- [27] Y.Xu, M.Feyngenson, K.Page, L.Shuller Nickles and K.S.Brinkman, *J. Am. Ceram. Soc.*, 2016, **99**, 4100-4106.
- [28] P.Tumurugoti, S.K.Sundaram and S.T.Misture, *J. Solid. State. Chem.*, 2018, **258** 72-78.
- [29] J.Amoroso, J.Marra, S.D.Conradson, M.Tang and K.Brinkman, *J. Alloy. Compd.*, 2014, **584**, 590-599.
- [30] D.M.Roy, *Science*, 1987, **235**, 651-658.
- [31] N.Chapman and A.Hooper, *P. Geologist. Assoc.*, 2012, **123**, 46-63.
- [32] M.M.Abu-Khader, *Prog. Nucl. Energ.*, 2009, **51**, 225-235.
- [33] N.Evangelidou, Y.Balkanski, A.Cozić and A.P.Møller, *Environ. Int.*, 2014, **64**, 17-27.
- [34] M.Inoue, H.Kofuji, K.Fujimoto, Y.Furusawa, K.Yoshida, S.Nagao, M.Yamamoto, Y.Hamajima and M.Minakawa, *J. Environ. Radioactiv.*, 2014, **137**, 113-118.
- [35] S.Wang and Y.Peng, *Chem. Eng. J.*, 2010, **156**, 11-24.
- [36] A.Dyer, A.Chimedtsogzol, L.Campbell and C.Williams, *Micropor. Mesopor. Mat.*, 2006, **95**, 172-175.
- [37] A.Dyer, J.Hriljac, N.Evans, I.Stokes, P.Rand, S.Kellet, R.Harjula, .Moller, Z.Maher, R.Heathlie-Branson, J.Austin, S.Williamson-Owens, M.Higgins-Bos, K.Smith, L.O'Brien, N.Smith and N.Bryan, *J. Radioanal. Nucl. Ch.*, 2018, **318**, 2473-2491.
- [38] E.H.Borai, R.Harjula, L.Malinen and A.Paajanen, *J. Hazard. Mater.*, 2009, **172**, 416-422.
- [39] H.Buchwald and W.P.Thistlethwaite, *J. Inorg. Nucl. Chem.*, 1958, **5**, 341.

- [40] J.V.R.Smit, *Nature*, 1958, **181**, 1530-1531.
- [41] F.Sebesta and V.Stefula, *J. Radioanal. Nucl. Ch.*, 1990, **140**, 5-21.
- [42] Y.Park, Y.C.Lee, W.S.Shin and S.J.Choi, *Chem. Eng. J.*, 2010, **162**, 685-695.
- [43] X.Zhang, Y.Wu, B.Chen, and Y.Weii, *J. Radioana. Nuc. Chem.*, 2016, **310**, 905-910.
- [44] Y.Wu, X.X.Zhang, Y.Z.Weii and H.Mimura, *Sep. Purif. Technol.*, 2017, **181**, 76-84.
- [45] D.F.Thompson and C.O.Church, *Pharmacotherapy*, 2001, **21**, 1364-1367.
- [46] G.R.Chen, Y.R.Chang, X.Liu, T.Kawamoto, H.Tanaka, D.Parajuli, T.Kawasaki, Y.Kawatsu, T.Kobayashi, M.L.Chen, Y.K.Lo, Z.Lei and D.J.lee, *Sep. Purif. Technol.*, 2017, **172**, 147-151.
- [47] H.Zhang, X.Zhao, J.Weii and F.Li, *Chem. Eng. J.*, 2015, **275**, 262-270.
- [48] S.K.Samantha, M.K.Thomas and T.K.Theyyunni, *J. Radioanal. Nucl. Chem.*, 1995, 199, 183-190.
- [49] D.M.Poojary, R.A.Chill and A.Clearfield, *Chem. Mater.*, 1994, **6**, 2364-2368.
- [50] A.J.Celestian and A.Clearfield, *J. Mater. Chem.*, 2007, **17**, 4839-4842.
- [51] A.Clearfield, L.N.Burton and A.I.Burton, *React. Funct. Polym.*, 2000, **43**, 85-95.
- [52] V.Luca, J.V.Hanna, M.E.Smith, M.James, D.R.G.Mitchell and J.R.Bartlett, *Micropor. Mesopor. Mat.*, 2002, **55**, 1-13.
- [53] A.Clearfield, D.M.Medvedev, S.Kerlegon, T.Bosser, J.D.Buns and M.Jackson, *Solvent. Extr. Ion. Exc.*, 2012, **30**, 229-243.
- [54] J.E.Crooks, H.El-Daly, M.Y.El-Sheikh, A.F.M.Habib and A.B.Zaki, *Int. J. Chem. Kinet.*, 1993, **25**, 161-168.
- [55] P.Srivastava, B.Singh and M.Angove, *J. Colloid. Interf. Sci.*, 2005, **290**, 28-38.
- [56] D.W.Oscarson, H.B.Hume and F.King, *Clay. Clay. Miner.*, 1994, **42**, 731-736.
- [57] S.A.Khan, R.U.Rehman and M.A.Khan, *Waste. Manage.*, **15**, 1995, 641-650.
- [58] S.Babel and T.A.Kurniawan, *J. Hazard. Mater.*, 2003, **B97**, 219-243.
- [59] Z.Lin, J.Rocha, P.Ferreira, A.Thursfield, J.R.Agger and M.W.Anderson, *J. Phys. Chem. B*, 1999, **103**, 957-963.
- [60] Z.Lin, J.Rocha, J.D.Pedrosa de Jesus and A.Ferreira, *J. Mater. Chem.*, 2000, **10**, 1353-1356.
- [61] J.Hriljac, Unpublished work.
- [62] J.Rocha, P.Ferreira, Z.Lin, J.R.Agger and M.W.Anderson, *Chem. Commun.*, 1998, **12**, 1267-1270.

- [63] A.Ferreira, Z.Lin, M.R.Soaes and J.Rocha, *Inorganica. Chimica. Acta.*, 2003, **356** 19-26.
- [64] E.W.Corcoran and D.E.W. Vaughan, *Solid State ionics*, 1989, **32/33**, 423-429.
- [65] J.Rocha, P.Ferreira, Z.Lin, P.Brandaõ, A.Ferreira and J.D.Pedrosa de Jesus, *Chem. Commun.*, 1997, **21**, 2103-2104.
- [66] J.Rocha, P.Ferreira, L.D.Carlos and A.Ferreira, *Angew. Chem. Int. Ed.*, 2000, **39**, 3277-3279.
- [67] B.R.Figueiredo, D.Ananias, I.Portugal, J.Rocha and C.M.Silva, *Chem. Eng. J.*, 2016, **286**, 679-688.
- [68] C.Giacovazzo, H.L. Monaco, G.Artioli, D.Viterbo, M.Milanesio, G.Gilli, P.Gilli, G.Zanotti, G.Ferraris, and Michele Catti, *Fundamentals of Crystallography*, Oxford University Press, 2011.
- [69] W. L. Bragg, *Proc. Cambridge Phil.Soc.*, 1913, **17**, 43-57.
- [70] R. E. Dinnebier, A. Fitch, S. J. L. Billinge, , A. Le Bail, , I.Madsen, , L. M.D. Cranswick, , J.K.Cockcroft, , P.Norby and A.D. Zuev, *Powder Diffraction Theory and Practice*, Royal Society of Chemistry, 2008.
- [71] N.Sahu and S.Panigrahi, *Bull. Mater. Sci.*, 2011, **34**, 1495-1500.
- [72] L.B.McCusker, R.B.von Dreele, D.E.Cox, D.louer and P.Scardi, *J. Appl. Cryst.*, 1999, **32**, 36-50.
- [73] A.C. Larson and R.B. Von Dreele, "*General Structure Analysis System (GSAS)*", Los Alamos National Laboratory Report LAUR, 2000, 86-748.
- [74] B.H. Toby, *J. Appl. Cryst.*, 2001, **34**, 210-213.
- [75] P.Brouwer, *Theory of XRF*, PANalytical, 2010.
- [76] Y.Yamada, *The Rigaku Journal*, 2010, **26**, 15-23.
- [77] M.Watanabe, *The Rigaku Journal*, 2015, **31**, 12-16.
- [78] Z.Lin, J.Rocha, P.Brandao A.Ferreira, A.P.Esculcas, J.D.Pedrosa de Jesus, A.Philippou and M.W.Anderson, *J. Phys. Chem. B*, 1997, **101**, 7114-7120.
- [79] D.M.Poojary, A.I.Bortun, L.N.Bortun and A.Clearfield, *Inorg. Chem.*, 1997, **36**, 3072-3079.
- [80] Z.Lin, J.Rocha and A.Valente, *Chem. Commun.*, 1999, 2489-2490.
- [81] V.Sebastian, J.Bosque, I.Kumakiri, R.Bredesen, A.Anson, J.A.Macia-Agullo, A.Linares-Solano, C.Tellez and J.Coronas, *Micropor. Mesopor. Mat.*, 2011, **142**, 649-654.
- [82] C.S. Fewox, A. Clearfield and A.J. Celestian, *Inorg. Chem.*, 2011, **50**, 3596-3604.

- [83] B.Wu, R.C.Wang, J.H.Yang, F.Y.Wu, W.L.Zhang, X.P.Gu and A.C.Zhang, *Lithos*, 2015, **224–225**, 126-142.
- [84] H.Xu, A.Navrotsky, M.L.Balmer and Y.Su, *Phys.Chem.Miner.*, 2005, **32**, 426-435.
- [85] M.L.Balmer, Y.Su, H.Xu, E.Bitten, D.McCready and A.Navrotsky, *J. Am. Ceram. Soc.*, 2001, **84**, 153-60.
- [86] J. Plevert, R. Sanchez-Smith, T.M. Gentz, H. Li, T.L. Groy, O.M. Yaghi and M. O’Keeffe, *Inorg. Chem.*, 2003, **42**, 5954-5959.
- [87] G.D.Ilyushin, *Crystallogr. Rep+.*, 2005, **50**, 504-512.
- [88] P.Pertierra, M.A.Salvado, S.Garcia-Granda, C.Trabajo, J.R.Garcia, A.I.Bortun and A.Clearfield, *J. Solid. State. Chem.*, 1999,**148**, 41-49.
- [89] Z.Liu, L.Weng, Z.Chen and D.Zhao, *Acta. Cryst.*, 2003, **C59**, i29-i31.
- [90] A.Tripathi, D.G.Medvedev, M.Nyman and A.Clearfield, *J. Solid. State. Chem.*, 2003, **175**, 72-83.
- [91] A.Tripathi, D.G.Medvedev and A.Clearfield, *J. Solid. State. Chem.*, 2005, **178**, 253-261.
- [92] A.J.Celestian, J.B.Parise, R.L.Smith, B.H.Toby and A.Cleafield, *Inorg. Chem.*, 2007, **46**, 1081-1089.
- [93] S.Feng, M.Tsai and M.Greenblatt, *Chem. Mater.*, 1992, **4**, 388-393.
- [94] S.Feng and M.Greenblatt, *Chem. Mater.*, 1992, **4**, 462-468.
- [95] M.R.Roberts and A.N.Fitch, *J. Phys. Chem. Solids*, 1991, **52**, 1209-1218.
- [96] M.R.Roberts, A.N.Fitch and A.V.Chadwick, *J. Phys. Chem. Solids*, 1995, **56**, 1353-1358.
- [97] T.M.Nenoff, W.T.A.Harrison and G.D.Stucky, *Chem. Mater.*, 1994, **6**, 525-530.
- [98] E.A.Behrens, D.M.Poojary and A.Clearfield, *Chem. Mater.*, 1996, **8**, 1236-1244.
- [99] E.A.Behrens and A.Clearfield, *Microporous. Mater.*, 1997, **11**, 65-75.
- [100] E.A.Behrens, D.M.Poojary and A.Clearfield, *Chem. Mater.*, 1998, **10**, 959-967.
- [101] A.Tripathi, D.G.Medvedev, J.Delgado and A.Clearfield, *J. Solid. State. Chem.*, 2004, **177**, 2903-2915.
- [102] R.Bialek and V.Gramlich, *Z. Kristallogr.*, 1992, **198**, 67-77.
- [103] H.Xu, A.Navrotsky, M.Nyman and T.M.Nenoff, *Micropor. Mesopor. Mat.*, 2004, **72**, 209-218.

- [104] G.D.Ilyushin, *Inorg. Mater.*, 2003, **39**, 1067-1073.
- [105] T.Mitsubishi, H.Tanaka and Y.Fujiki, *Yogyo-Kyokai-Shi*, 1982, **90**, 58-60.
- [106] M.L.Balmer and B.C.Bunker, PNNL, 1995.
- [107] M.Nyman, F.Bonhomme, D.M.Teter, R.S.Maxwell, B.X.Gu, L.M.Wang, R.C.Ewing and T.M.Nenoff, *Chem. Mater.*, 2000, **12**, 3449-3458.
- [108] I.E.Grey, R.S.Roth and M.L.Balmer, *J. Solid. State. Chem.*, 1997, **131**, 38-42.
- [109] G.J.Redhammer and G.Tippelt, *Acta. Cryst.*, 2013, **C69**, 995-1001.
- [110] M.Monz, D.Ostermann and H.Jacobs, *J. Alloy. Compd.*, 1993, **200**, 211-215.
- [111] J.Choisnet, A.Deschanvres and B.Raveau, *J. Solid. State. Chem.*, 1973, **7**, 408-417.
- [112] O.Baumgartner and H.Vollenkle, *Monatsh. Chemie*, 1978, **109**, 1145-1153.
- [113] A.Nakatsuka, K.Sugiyama, M.Ohkawa, O.Ohtaka, K.Fujiwara and A.Yoshiasa, *Acta. Cryst.*, 2016, **C72**, 716-719.

Appendices

(See attached CD for appendices)

Appendices

Appendix 1: Full CIF information for the refinement of the parent zirconogermanate umbite, figure 3.9.

_cell_length_a	10.38984(10)
_cell_length_b	13.64791(12)
_cell_length_c	7.42539(6)
_cell_angle_alpha	90.0
_cell_angle_beta	90.0
_cell_angle_gamma	90.0
_cell_volume	1052.918(19)
_symmetry_cell_setting	orthorhombic
_symmetry_space_group_name_H-M	"P 21 21 21"

loop_ _symmetry_equiv_pos_site_id _symmetry_equiv_pos_as_xyz

1	+x,+y,+z
2	+x+1/2,-y+1/2,-z
3	-x,+y+1/2,-z+1/2
4	-x+1/2,-y,+z+1/2

ATOMIC COORDINATES AND DISPLACEMENT PARAMETERS

Zr

Zr1 0.45643(19) 0.20949(12) 0.26489(29) 1.0 Uiso 0.0070(5) 4

Ge

Ge1 0.18777(22) 0.17148(17) -0.00994(34) 1.0 Uiso 0.00189(29) 4

Ge

Ge2 0.03146(22) 0.04504(14) 0.72557(33) 1.0 Uiso 0.00189(29) 4

Ge

Ge3 0.63645(21) 0.33802(19) 0.59727(32) 1.0 Uiso 0.00189(29) 4

O

O1 0.4179(10) 0.3637(6) 0.2379(18) 1.0 Uiso 0.0108(13) 4

O

O2 0.3397(9) 0.1868(10) 0.0348(14) 1.0 Uiso 0.0108(13) 4

O

O3 0.5285(10) 0.0674(6) 0.2835(17) 1.0 Uiso 0.0108(13) 4

O

O4 0.5513(12) 0.2398(8) 0.5039(15) 1.0 Uiso 0.0108(13) 4

O

O5 0.6315(10) 0.2231(8) 0.1139(15) 1.0 Uiso 0.0108(13) 4

O

O6 0.3000(10) 0.1849(10) 0.4359(13) 1.0 Uiso 0.0108(13) 4

O

O7 0.0867(10) 0.1438(8) 0.1769(13) 1.0 Uiso 0.0108(13) 4

O

O8 0.0812(11) 0.0544(8) 0.4993(14) 1.0 Uiso 0.0108(13) 4

O

O9 0.1732(10) 0.0696(8) 0.8465(15) 1.0 Uiso 0.0108(13) 4

K

K1 0.2166(5) 0.62703(32) 0.1232(6) 1.0 Uiso 0.0201(11) 4

K

K2 0.4403(4) 0.08120(32) 0.7087(7) 1.0 Uiso 0.0201(11) 4

O

O10 0.6915(12) 0.0642(8) 0.8764(16) 1.0 Uiso 0.0108(13) 4

If you change Z, be sure to change all 3 of the following

_chemical_formula_sum "Ge3 K2 O10 Zr"

_chemical_formula_weight 547.18

_cell_formula_units_Z 4

MOLECULAR GEOMETRY

Bond	Distance Å
Zr1 O1	2.151(9)
Zr1 O2	2.118(9)
Zr1 O3	2.084(9)
Zr1 O4	2.072(10)
Zr1 O5	2.145(9)
Zr1 O6	2.090(9)
Zr1 K1	3.674(5)
Zr1 K1	3.910(5)
Zr1 K2	3.736(5)
Ge1 Ge2	3.0778(31)
Ge1 Ge3	3.1130(33)
Ge1 O2	1.626(9)
Ge1 O5	1.734(10)
Ge1 O7	1.781(9)
Ge1 O9	1.758(10)
Ge1 K1	3.996(5)
Ge1 K2	3.573(6)
Ge1 K2	4.037(5)

Ge2	Ge1	3.0778(31)
Ge2	Ge3	3.0796(33)
Ge2	O1	1.737(9)
Ge2	O3	1.711(9)
Ge2	O8	1.763(10)
Ge2	O9	1.757(9)
Ge2	K1	3.821(5)
Ge2	K2	3.991(6)
Ge3	Ge1	3.1130(33)
Ge3	Ge2	3.0796(33)
Ge3	O4	1.749(10)
Ge3	O6	1.746(10)
Ge3	O7	1.772(9)
Ge3	O8	1.732(10)
Ge3	K1	3.648(5)
Ge3	K1	3.704(5)
Ge3	K2	4.138(5)
Ge3	K2	4.043(5)
Ge3	K2	3.705(5)
O1	Zr1	2.151(9)
O1	Ge2	1.737(9)
O1	K1	3.187(14)
O2	Zr1	2.118(9)
O2	Ge1	1.626(9)
O2	K2	3.005(12)
O3	Zr1	2.084(9)
O3	Ge2	1.711(9)
O3	K1	2.856(11)
O3	K2	3.293(14)
O4	Zr1	2.072(10)
O4	Ge3	1.749(10)
O4	K1	3.013(13)
O4	K1	3.440(13)
O4	K2	2.886(12)
O5	Zr1	2.145(9)
O5	Ge1	1.734(10)
O5	K1	2.832(11)
O6	Zr1	2.090(9)
O6	Ge3	1.746(10)
O6	K1	2.924(13)
O6	K2	2.869(12)
O7	Ge1	1.781(9)
O7	Ge3	1.772(9)
O7	K1	3.490(11)
O7	K2	3.093(12)
O8	Ge2	1.763(10)

O8	Ge3	1.732(10)
O8	K1	3.374(12)
O8	K2	2.851(12)
O9	Ge1	1.758(10)
O9	Ge2	1.757(9)
O9	K2	2.962(12)
O9	K2	3.587(13)
K1	Zr1	3.674(5)
K1	Zr1	3.910(5)
K1	Ge1	3.996(5)
K1	Ge2	3.821(5)
K1	Ge3	3.648(5)
K1	Ge3	3.704(5)
K1	O1	3.187(14)
K1	O3	2.856(11)
K1	O4	3.013(13)
K1	O4	3.440(13)
K1	O5	2.832(11)
K1	O6	2.924(13)
K1	O7	3.490(11)
K1	O8	3.374(12)
K1	K1	5.127(6)
K1	K1	5.127(6)
K1	K2	4.228(6)
K1	K2	4.379(7)
K1	K2	4.349(6)
K1	O10	2.623(11)
K2	Zr1	3.736(5)
K2	Ge1	3.573(6)
K2	Ge1	4.037(5)
K2	Ge2	3.991(6)
K2	Ge3	4.138(5)
K2	Ge3	4.043(5)
K2	Ge3	3.705(5)
K2	O2	3.005(12)
K2	O3	3.293(14)
K2	O4	2.886(12)
K2	O6	2.869(12)
K2	O7	3.093(12)
K2	O8	2.851(12)
K2	O9	2.962(12)
K2	O9	3.587(13)
K2	K1	4.228(6)
K2	K1	4.379(7)
K2	K1	4.349(6)
K2	O10	2.901(12)

O10	K1	2.623(11)
O10	K2	2.901(12)

Appendix 2: Full CIF information for the refinement of the caesium exchanged zirconogermanate umbite, figure 3.12.

_cell_length_a	10.40075(8)
_cell_length_b	13.65169(10)
_cell_length_c	7.43021(5)
_cell_angle_alpha	90.0
_cell_angle_beta	90.0
_cell_angle_gamma	90.0
_cell_volume	1055.000(16)
_symmetry_cell_setting	orthorhombic
_symmetry_space_group_name_H-M	"P 21 21 21"

loop_ _symmetry_equiv_pos_site_id _symmetry_equiv_pos_as_xyz

- 1 +x,+y,+z
- 2 +x+1/2,-y+1/2,-z
- 3 -x,+y+1/2,-z+1/2
- 4 -x+1/2,-y,+z+1/2

ATOMIC COORDINATES AND DISPLACEMENT PARAMETERS

Zr

Zr1 0.45647 0.20949 0.26523 1.0 Uiso 0.0059(4) 4

Ge

Ge1 0.18716 0.17181 -0.00796 1.0 Uiso 0.00218(24) 4

Ge

Ge2 0.03149 0.04547 0.72544 1.0 Uiso 0.00218(24) 4

Ge

Ge3 0.63569 0.33766 0.59693 1.0 Uiso 0.00218(24) 4

O

O1 0.41969 0.3645 0.23557 1.0 Uiso 0.0080(11) 4

O

O2 0.34077 0.18365 0.03506 1.0 Uiso 0.0080(11) 4

O

O3 0.53411 0.06416 0.27673 1.0 Uiso 0.0080(11) 4

O

O4 0.55003 0.24212 0.50225 1.0 Uiso 0.0080(11) 4

O

O5 0.62806 0.22427 0.11082 1.0 Uiso 0.0080(11) 4

O

O6 0.29639 0.18334 0.43844 1.0 Uiso 0.0080(11) 4

O

O7 0.08403 0.14224 0.17945 1.0 Uiso 0.0080(11) 4

O

O8 0.07699 0.05257 0.49668 1.0 Uiso 0.0080(11) 4

O

O9 0.17361 0.06813 0.84707 1.0 Uiso 0.0080(11) 4

K

K1	0.21641	0.62619	0.12124	0.94184	Uiso	0.0559(17)	4
----	---------	---------	---------	---------	------	------------	---

K

K2	0.43916	0.08016	0.70946	0.9686(23)	Uiso	0.0262(15)	4
----	---------	---------	---------	------------	------	------------	---

O

O10	0.69553	0.07049	0.88175	1.0	Uiso	0.038(4)	4
-----	---------	---------	---------	-----	------	----------	---

Cs

Cs1	0.21641	0.62619	0.12124	0.05816	Uiso	0.0559(17)	4
-----	---------	---------	---------	---------	------	------------	---

Cs

Cs2	0.43916	0.08016	0.70946	0.0314(23)	Uiso	0.0262(15)	4
-----	---------	---------	---------	------------	------	------------	---

If you change Z, be sure to change all 3 of the following

_chemical_formula_sum "Cs0.09 Ge3 K1.91 O10 Zr"

_chemical_formula_weight 555.58

_cell_formula_units_Z 4

MOLECULAR GEOMETRY

Bond	Distance Å
Zr1 O1	2.161800(10)
Zr1 O2	2.120690(10)
Zr1 O3	2.143650(10)
Zr1 O4	2.060820(10)
Zr1 O5	2.131230(10)
Zr1 O6	2.134390(10)
Zr1 K1	3.685200(20)
Zr1 K1	3.906750(20)
Zr1 K2	3.747520(20)
Zr1 Cs1	3.685200(20)
Zr1 Cs1	3.906750(20)

Zr1	Cs2	4.494730(30)
Zr1	Cs2	3.747520(20)
Ge1	Ge2	3.085440(10)
Ge1	Ge3	3.103310(20)
Ge1	O2	1.637250(10)
Ge1	O5	1.724670(10)
Ge1	O7	1.803520(10)
Ge1	O9	1.784250(10)
Ge1	K1	4.025040(20)
Ge1	K2	3.583760(20)
Ge1	K2	4.021000(20)
Ge1	Cs1	4.025040(20)
Ge1	Cs2	3.583760(20)
Ge1	Cs2	4.021000(20)
Ge2	Ge1	3.085440(10)
Ge2	Ge3	3.075280(10)
Ge2	O1	1.716510(10)
Ge2	O3	1.688470(10)
Ge2	O8	1.767040(10)
Ge2	O9	1.759860(10)
Ge2	K1	3.807580(20)
Ge2	K2	3.996020(20)
Ge2	Cs1	4.186760(20)
Ge2	Cs1	3.807580(20)
Ge2	Cs2	4.268030(30)
Ge2	Cs2	4.211130(20)
Ge2	Cs2	3.996020(20)
Ge3	Ge1	3.103310(20)
Ge3	Ge2	3.075280(10)
Ge3	O4	1.729110(10)
Ge3	O6	1.716050(10)
Ge3	O7	1.767670(10)
Ge3	O8	1.761250(10)
Ge3	K1	3.650890(20)
Ge3	K1	3.699600(30)
Ge3	K2	4.050090(20)
Ge3	K2	3.692560(20)
Ge3	Cs1	3.650890(20)
Ge3	Cs1	3.699600(30)
Ge3	Cs2	4.151500(20)
Ge3	Cs2	4.050090(20)
Ge3	Cs2	3.692560(20)
O1	Zr1	2.161800(10)
O1	Ge2	1.716510(10)
O1	K1	3.198700(20)
O1	Cs1	3.198700(20)

O2	Zr1	2.120690(10)
O2	Ge1	1.637250(10)
O2	K2	2.982690(10)
O2	Cs2	2.982690(10)
O3	Zr1	2.143650(10)
O3	Ge2	1.688470(10)
O3	K1	2.832810(20)
O3	K2	3.370570(20)
O3	Cs1	2.832810(20)
O3	Cs2	3.370570(20)
O4	Zr1	2.060820(10)
O4	Ge3	1.729110(10)
O4	K1	3.041070(20)
O4	K1	3.419510(20)
O4	K2	2.930670(10)
O4	Cs1	3.041070(20)
O4	Cs1	3.419510(20)
O4	Cs2	2.930670(10)
O5	Zr1	2.131230(10)
O5	Ge1	1.724670(10)
O5	K1	2.893680(10)
O5	Cs1	2.893680(10)
O6	Zr1	2.134390(10)
O6	Ge3	1.716050(10)
O6	K1	2.936630(20)
O6	K2	2.871280(10)
O6	Cs1	2.936630(20)
O6	Cs2	2.871280(10)
O7	Ge1	1.803520(10)
O7	Ge3	1.767670(10)
O7	K1	3.464840(20)
O7	K2	3.053910(20)
O7	Cs1	3.464840(20)
O7	Cs2	3.053910(20)
O8	Ge2	1.767040(10)
O8	Ge3	1.761250(10)
O8	K1	3.330080(20)
O8	K2	2.804700(10)
O8	Cs1	3.330080(20)
O8	Cs2	2.804700(10)
O9	Ge1	1.784250(10)
O9	Ge2	1.759860(10)
O9	K2	2.949710(20)
O9	K2	3.567050(20)
O9	Cs2	2.949710(20)
O9	Cs2	3.567050(20)

K1	Zr1	3.685200(20)
K1	Zr1	3.906750(20)
K1	Ge1	4.025040(20)
K1	Ge2	3.807580(20)
K1	Ge3	3.650890(20)
K1	Ge3	3.699600(30)
K1	O1	3.198700(20)
K1	O3	2.832810(20)
K1	O4	3.041070(20)
K1	O4	3.419510(20)
K1	O5	2.893680(10)
K1	O6	2.936630(20)
K1	O7	3.464840(20)
K1	O8	3.330080(20)
K1	K1	5.114750(20)
K1	K1	5.114750(20)
K1	K2	4.222910(20)
K1	K2	4.389310(20)
K1	K2	4.372460(30)
K1	O10	2.693770(20)
K1	Cs1	5.114750(20)
K1	Cs1	5.114750(20)
K1	Cs2	4.222910(20)
K1	Cs2	4.389310(20)
K1	Cs2	4.372460(30)
K2	Zr1	3.747520(20)
K2	Ge1	3.583760(20)
K2	Ge1	4.021000(20)
K2	Ge2	3.996020(20)
K2	Ge3	4.050090(20)
K2	Ge3	3.692560(20)
K2	O2	2.982690(10)
K2	O3	3.370570(20)
K2	O4	2.930670(10)
K2	O6	2.871280(10)
K2	O7	3.053910(20)
K2	O8	2.804700(10)
K2	O9	2.949710(20)
K2	O9	3.567050(20)
K2	K1	4.222910(20)
K2	K1	4.389310(20)
K2	K1	4.372460(30)
K2	O10	2.960830(20)
K2	Cs1	4.222910(20)
K2	Cs1	4.389310(20)
K2	Cs1	4.372460(30)

O10	K1	2.693770(20)
O10	K2	2.960830(20)
O10	Cs1	2.693770(20)
O10	Cs1	3.922370(20)
O10	Cs1	3.879980(20)
O10	Cs2	2.960830(20)
Cs1	Zr1	3.685200(20)
Cs1	Zr1	3.906750(20)
Cs1	Ge1	4.025040(20)
Cs1	Ge2	4.186760(20)
Cs1	Ge2	3.807580(20)
Cs1	Ge3	3.650890(20)
Cs1	Ge3	3.699600(30)
Cs1	O1	3.198700(20)
Cs1	O3	2.832810(20)
Cs1	O4	3.041070(20)
Cs1	O4	3.419510(20)
Cs1	O5	2.893680(10)
Cs1	O6	2.936630(20)
Cs1	O7	3.464840(20)
Cs1	O8	3.330080(20)
Cs1	K1	5.114750(20)
Cs1	K1	5.114750(20)
Cs1	K2	4.222910(20)
Cs1	K2	4.389310(20)
Cs1	K2	4.372460(30)
Cs1	O10	2.693770(20)
Cs1	O10	3.922370(20)
Cs1	O10	3.879980(20)
Cs1	Cs1	5.114750(20)
Cs1	Cs1	5.114750(20)
Cs1	Cs2	4.222910(20)
Cs1	Cs2	4.389310(20)
Cs1	Cs2	4.372460(30)
Cs2	Zr1	3.747520(20)
Cs2	Zr1	4.494730(30)
Cs2	Ge1	3.583760(20)
Cs2	Ge1	4.021000(20)
Cs2	Ge2	4.268030(30)
Cs2	Ge2	3.996020(20)
Cs2	Ge2	4.211130(20)
Cs2	Ge3	4.151500(20)
Cs2	Ge3	4.050090(20)
Cs2	Ge3	3.692560(20)
Cs2	O2	2.982690(10)
Cs2	O3	3.370570(20)

Cs2	O4	2.930670(10)
Cs2	O6	2.871280(10)
Cs2	O7	3.053910(20)
Cs2	O8	2.804700(10)
Cs2	O9	2.949710(20)
Cs2	O9	3.567050(20)
Cs2	K1	4.222910(20)
Cs2	K1	4.389310(20)
Cs2	K1	4.372460(30)
Cs2	O10	2.960830(20)
Cs2	Cs1	4.222910(20)
Cs2	Cs1	4.389310(20)
Cs2	Cs1	4.372460(30)
Cs2	Cs2	5.837330(30)
Cs2	Cs2	5.837330(30)

Appendix 3: Full CIF information for the refinement of the 10Nb zirconogermanate umbite, figure 4.5.

_cell_length_a	10.39787(10)
_cell_length_b	13.64671(12)
_cell_length_c	7.43369(6)
_cell_angle_alpha	90.0
_cell_angle_beta	90.0
_cell_angle_gamma	90.0
_cell_volume	1054.815(19)
_symmetry_cell_setting	orthorhombic
_symmetry_space_group_name_H-M	"P 21 21 21"

loop_ _symmetry_equiv_pos_site_id _symmetry_equiv_pos_as_xyz

1	+x,+y,+z
2	+x+1/2,-y+1/2,-z
3	-x,+y+1/2,-z+1/2
4	-x+1/2,-y,+z+1/2

ATOMIC COORDINATES AND DISPLACEMENT PARAMETERS

Zr

Zr1 0.45620(18) 0.20957(12) 0.26484(28) 0.9 Uiso 0.0052(5) 4

Ge

Ge1 0.18754(22) 0.17228(17) -0.00979(33) 1.0 Uiso 0.00120(28) 4

Ge

Ge2 0.03131(22) 0.04505(14) 0.72527(33) 1.0 Uiso 0.00120(28) 4

Ge

Ge3 0.63595(21) 0.33770(18) 0.59569(31) 1.0 Uiso 0.00120(28) 4

O

O1 0.4238(7) 0.35704(29) 0.2392(16) 1.0 Uiso 0.0006(10) 4

O

O2 0.3470(6) 0.1931(9) 0.0394(9) 1.0 Uiso 0.0006(10) 4

O

O3 0.5246(8) 0.07014(29) 0.2819(15) 1.0 Uiso 0.0006(10) 4

O

O4 0.5529(10) 0.2374(6) 0.4992(10) 1.0 Uiso 0.0006(10) 4

O

O5 0.6233(7) 0.2241(6) 0.1191(13) 1.0 Uiso 0.0006(10) 4

O

O6 0.3018(5) 0.1834(9) 0.4288(9) 1.0 Uiso 0.0006(10) 4

O

O7 0.0944(8) 0.1418(7) 0.1796(7) 1.0 Uiso 0.0006(10) 4

O

O8 0.0782(10) 0.0535(5) 0.4981(9) 1.0 Uiso 0.0006(10) 4

O

O9 0.1682(7) 0.0698(6) 0.8534(13) 1.0 Uiso 0.0006(10) 4

K

K1 0.2186(5) 0.62302(33) 0.1242(7) 0.9200(33) Uiso 0.0117(10) 4

K

K2 0.4411(4) 0.08007(31) 0.7076(7) 0.9800(33) Uiso 0.0117(10) 4

O

O10 0.6963(11) 0.0622(8) 0.8797(15) 1.0 Uiso 0.0006(10) 4

Nb

Nb1 0.45620(18) 0.20957(12) 0.26484(28) 0.1 Uiso 0.0052(5) 4

If you change Z, be sure to change all 3 of the following

_chemical_formula_sum "Ge3 K1.90 Nb0.10 O10 Zr0.90"

_chemical_formula_weight 543.43

_cell_formula_units_Z 4

MOLECULAR GEOMETRY

Bond	Distance Å
Zr1 O1	2.049(4)
Zr1 O2	2.037(4)
Zr1 O3	2.035(4)
Zr1 O4	2.047(4)
Zr1 O5	2.057(4)
Zr1 O6	2.047(4)
Zr1 K1	3.676(5)
Zr1 K1	3.957(5)
Zr1 K2	3.739(5)
Ge1 Ge2	3.0875(31)
Ge1 Ge3	3.1277(32)
Ge1 O2	1.721(5)
Ge1 O5	1.762(5)
Ge1 O7	1.759(5)
Ge1 O9	1.741(5)
Ge1 K1	4.020(5)

Ge1	K2	3.598(5)
Ge1	K2	4.032(5)
Ge2	Ge1	3.0875(31)
Ge2	Ge3	3.0719(32)
Ge2	O1	1.762(5)
Ge2	O3	1.728(5)
Ge2	O8	1.761(5)
Ge2	O9	1.746(5)
Ge2	K1	4.134(5)
Ge2	K1	3.825(5)
Ge2	K2	3.982(6)
Ge3	Ge1	3.1277(32)
Ge3	Ge2	3.0719(32)
Ge3	O4	1.770(5)
Ge3	O6	1.758(5)
Ge3	O7	1.748(5)
Ge3	O8	1.747(5)
Ge3	K1	3.680(5)
Ge3	K1	3.731(5)
Ge3	K2	4.142(5)
Ge3	K2	4.051(5)
Ge3	K2	3.704(5)
O1	Zr1	2.049(4)
O1	Ge2	1.762(5)
O1	K1	3.234(13)
O1	Nb1	2.049(4)
O2	Zr1	2.037(4)
O2	Ge1	1.721(5)
O2	K2	3.068(10)
O2	Nb1	2.037(4)
O3	Zr1	2.035(4)
O3	Ge2	1.728(5)
O3	K1	2.852(9)
O3	K2	3.285(13)
O3	Nb1	2.035(4)
O4	Zr1	2.047(4)
O4	Ge3	1.770(5)
O4	K1	2.987(12)
O4	K1	3.530(13)
O4	K2	2.892(9)
O4	Nb1	2.047(4)
O5	Zr1	2.057(4)
O5	Ge1	1.762(5)
O5	K1	2.872(10)
O5	Nb1	2.057(4)
O6	Zr1	2.047(4)

O6	Ge3	1.758(5)
O6	K1	3.022(12)
O6	K2	2.895(10)
O6	Nb1	2.047(4)
O7	Ge1	1.759(5)
O7	Ge3	1.748(5)
O7	K1	3.575(8)
O7	K2	3.057(11)
O8	Ge2	1.761(5)
O8	Ge3	1.747(5)
O8	K1	3.355(12)
O8	K2	2.833(9)
O9	Ge1	1.741(5)
O9	Ge2	1.746(5)
O9	K2	3.041(10)
O9	K2	3.522(12)
K1	Zr1	3.676(5)
K1	Zr1	3.957(5)
K1	Ge1	4.020(5)
K1	Ge2	4.134(5)
K1	Ge2	3.825(5)
K1	Ge3	3.680(5)
K1	Ge3	3.731(5)
K1	O1	3.234(13)
K1	O3	2.852(9)
K1	O4	2.987(12)
K1	O4	3.530(13)
K1	O5	2.872(10)
K1	O6	3.022(12)
K1	O7	3.575(8)
K1	O8	3.355(12)
K1	K1	5.051(6)
K1	K1	5.051(6)
K1	K2	4.192(6)
K1	K2	4.353(7)
K1	K2	4.422(6)
K1	O10	2.538(11)
K1	Nb1	3.676(5)
K1	Nb1	3.957(5)
K2	Zr1	3.739(5)
K2	Ge1	3.598(5)
K2	Ge1	4.032(5)
K2	Ge2	3.982(6)
K2	Ge3	4.142(5)
K2	Ge3	4.051(5)
K2	Ge3	3.704(5)

K2	O2	3.068(10)
K2	O3	3.285(13)
K2	O4	2.892(9)
K2	O6	2.895(10)
K2	O7	3.057(11)
K2	O8	2.833(9)
K2	O9	3.041(10)
K2	O9	3.522(12)
K2	K1	4.192(6)
K2	K1	4.353(7)
K2	K1	4.422(6)
K2	O10	2.956(12)
K2	Nb1	3.739(5)
O10	K1	2.538(11)
O10	K2	2.956(12)
Nb1	O1	2.049(4)
Nb1	O2	2.037(4)
Nb1	O3	2.035(4)
Nb1	O4	2.047(4)
Nb1	O5	2.057(4)
Nb1	O6	2.047(4)
Nb1	K1	3.676(5)
Nb1	K1	3.957(5)
Nb1	K2	3.739(5)

Appendix 4: Full CIF information for the refinement of the 20Nb zirconogermanate umbite,

figure 4.6

_cell_length_a	10.39413(16)
_cell_length_b	13.63214(18)
_cell_length_c	7.43522(10)
_cell_angle_alpha	90.0
_cell_angle_beta	90.0
_cell_angle_gamma	90.0
_cell_volume	1053.528(30)
_symmetry_cell_setting	orthorhombic
_symmetry_space_group_name_H-M	"P 21 21 21"

loop_ _symmetry_equiv_pos_site_id _symmetry_equiv_pos_as_xyz

- 1 +x,+y,+z
- 2 +x+1/2,-y+1/2,-z
- 3 -x,+y+1/2,-z+1/2
- 4 -x+1/2,-y,+z+1/2

ATOMIC COORDINATES AND DISPLACEMENT PARAMETERS

Zr

Zr1 0.45671(24) 0.20971(16) 0.2649(4) 0.8 Uiso 0.0059(6) 4

Ge

Ge1 0.18776(28) 0.17178(22) -0.0099(4) 1.0 Uiso 0.0017(4) 4

Ge

Ge2 0.03115(28) 0.04423(17) 0.7253(4) 1.0 Uiso 0.0017(4) 4

Ge

Ge3 0.63588(27) 0.33755(23) 0.5946(4) 1.0 Uiso 0.0017(4) 4

O

O1 0.4230(9) 0.35729(32) 0.2395(22) 1.0 Uiso 0.0059(14) 4

O

O2 0.3477(7) 0.1974(12) 0.0377(10) 1.0 Uiso 0.0059(14) 4

O

O3 0.5257(10) 0.07052(32) 0.2789(20) 1.0 Uiso 0.0059(14) 4

O

O4 0.5546(14) 0.2356(7) 0.4999(12) 1.0 Uiso 0.0059(14) 4

O

O5 0.6240(9) 0.2237(7) 0.1185(17) 1.0 Uiso 0.0059(14) 4

O

O6 0.3023(6) 0.1854(12) 0.4310(11) 1.0 Uiso 0.0059(14) 4

O

O7 0.0967(10) 0.1412(10) 0.1807(8) 1.0 Uiso 0.0059(14) 4

O

O8 0.0802(13) 0.0524(6) 0.4984(10) 1.0 Uiso 0.0059(14) 4

O

O9 0.1666(9) 0.0671(7) 0.8600(17) 1.0 Uiso 0.0059(14) 4
K
K1 0.2187(6) 0.6223(4) 0.1259(9) 0.862(4) Uiso 0.0060(12) 4
K
K2 0.4424(5) 0.0805(4) 0.7080(8) 0.938(4) Uiso 0.0060(12) 4
O
O10 0.6960(14) 0.0581(10) 0.8756(19) 1.0 Uiso 0.0059(14) 4
Nb
Nb1 0.45671(24) 0.20971(16) 0.2649(4) 0.2 Uiso 0.0059(6) 4

If you change Z, be sure to change all 3 of the following

_chemical_formula_sum "Ge3 K1.80 Nb0.20 O10 Zr0.80"

_chemical_formula_weight 539.69

_cell_formula_units_Z 4

MOLECULAR GEOMETRY

Bond	Distance Å
Zr1 O1	2.051(4)
Zr1 O2	2.041(4)
Zr1 O3	2.031(4)
Zr1 O4	2.053(4)
Zr1 O5	2.060(4)
Zr1 O6	2.052(4)
Zr1 K1	3.669(7)
Zr1 K1	3.972(6)
Zr1 K2	3.739(7)
Ge1 Ge2	3.090(4)
Ge1 Ge3	3.137(4)
Ge1 O2	1.735(5)
Ge1 O5	1.767(6)

Ge1	O7	1.754(6)
Ge1	O9	1.738(6)
Ge1	K1	4.020(7)
Ge1	K2	3.599(7)
Ge1	K2	4.035(6)
Ge2	Ge1	3.090(4)
Ge2	Ge3	3.073(4)
Ge2	O1	1.770(6)
Ge2	O3	1.719(5)
Ge2	O8	1.766(6)
Ge2	O9	1.755(6)
Ge2	K1	4.114(7)
Ge2	K1	3.834(7)
Ge2	K2	3.981(7)
Ge3	Ge1	3.137(4)
Ge3	Ge2	3.073(4)
Ge3	O4	1.772(6)
Ge3	O6	1.769(5)
Ge3	O7	1.744(6)
Ge3	O8	1.751(6)
Ge3	K1	3.686(7)
Ge3	K1	3.733(7)
Ge3	K2	4.127(6)
Ge3	K2	4.058(6)
Ge3	K2	3.713(6)
O1	Zr1	2.051(4)
O1	Ge2	1.770(6)
O1	K1	3.241(17)
O1	Nb1	2.051(4)
O2	Zr1	2.041(4)
O2	Ge1	1.735(5)
O2	K2	3.085(14)
O2	Nb1	2.041(4)
O3	Zr1	2.031(4)
O3	Ge2	1.719(5)
O3	K1	2.839(11)
O3	K2	3.309(17)
O3	Nb1	2.031(4)
O4	Zr1	2.053(4)
O4	Ge3	1.772(6)
O4	K1	2.969(16)
O4	K1	3.564(17)
O4	K2	2.868(12)
O4	Nb1	2.053(4)
O5	Zr1	2.060(4)
O5	Ge1	1.767(6)

O5	K1	2.863(13)
O5	Nb1	2.060(4)
O6	Zr1	2.052(4)
O6	Ge3	1.769(5)
O6	K1	3.003(16)
O6	K2	2.900(13)
O6	Nb1	2.052(4)
O7	Ge1	1.754(6)
O7	Ge3	1.744(6)
O7	K1	3.589(10)
O7	K2	3.056(14)
O8	Ge2	1.766(6)
O8	Ge3	1.751(6)
O8	K1	3.379(15)
O8	K2	2.828(10)
O9	Ge1	1.738(6)
O9	Ge2	1.755(6)
O9	K2	3.088(13)
O9	K2	3.468(16)
K1	Zr1	3.669(7)
K1	Zr1	3.972(6)
K1	Ge1	4.020(7)
K1	Ge2	4.114(7)
K1	Ge2	3.834(7)
K1	Ge3	3.686(7)
K1	Ge3	3.733(7)
K1	O1	3.241(17)
K1	O3	2.839(11)
K1	O4	2.969(16)
K1	O4	3.564(17)
K1	O5	2.863(13)
K1	O6	3.003(16)
K1	O7	3.589(10)
K1	O8	3.379(15)
K1	K1	5.036(8)
K1	K1	5.036(8)
K1	K2	4.173(8)
K1	K2	4.347(9)
K1	K2	4.426(8)
K1	O10	2.471(14)
K1	Nb1	3.669(7)
K1	Nb1	3.972(6)
K2	Zr1	3.739(7)
K2	Ge1	3.599(7)
K2	Ge1	4.035(6)
K2	Ge2	3.981(7)

K2	Ge3	4.127(6)
K2	Ge3	4.058(6)
K2	Ge3	3.713(6)
K2	O2	3.085(14)
K2	O3	3.309(17)
K2	O4	2.868(12)
K2	O6	2.900(13)
K2	O7	3.056(14)
K2	O8	2.828(10)
K2	O9	3.088(13)
K2	O9	3.468(16)
K2	K1	4.173(8)
K2	K1	4.347(9)
K2	K1	4.426(8)
K2	O10	2.931(16)
K2	Nb1	3.739(7)
O10	K1	2.471(14)
O10	K2	2.931(16)
Nb1	O1	2.051(4)
Nb1	O2	2.041(4)
Nb1	O3	2.031(4)
Nb1	O4	2.053(4)
Nb1	O5	2.060(4)
Nb1	O6	2.052(4)
Nb1	K1	3.669(7)
Nb1	K1	3.972(6)
Nb1	K2	3.739(7)

Appendix 5: Full CIF information for the refinement of the 25Nb zirconogermanate umbite,

figure 4.7

_cell_length_a	10.40064(20)
_cell_length_b	13.62446(27)
_cell_length_c	7.44143(13)
_cell_angle_alpha	90.0
_cell_angle_beta	90.0
_cell_angle_gamma	90.0
_cell_volume	1054.47(4)
_symmetry_cell_setting	orthorhombic
_symmetry_space_group_name_H-M	"P 21 21 21"

loop_ _symmetry_equiv_pos_site_id _symmetry_equiv_pos_as_xyz

- 1 +x,+y,+z
- 2 +x+1/2,-y+1/2,-z
- 3 -x,+y+1/2,-z+1/2
- 4 -x+1/2,-y,+z+1/2

ATOMIC COORDINATES AND DISPLACEMENT PARAMETERS

Zr

Zr1 0.45708(25) 0.21000(17) 0.2647(4) 0.75 Uiso 0.0049(6) 4

Ge

Ge1 0.18857(29) 0.17204(24) -0.0091(4) 1.0 Uiso 0.0024(4) 4

Ge

Ge2 0.03157(30) 0.04420(19) 0.7257(4) 1.0 Uiso 0.0024(4) 4

Ge

Ge3 0.63646(28) 0.33737(25) 0.5946(4) 1.0 Uiso 0.0024(4) 4

O

O1 0.4255(9) 0.35731(32) 0.2346(22) 1.0 Uiso 0.0042(14) 4

O

O2 0.3456(8) 0.2056(13) 0.0393(11) 1.0 Uiso 0.0042(14) 4

O

O3 0.5264(9) 0.07099(32) 0.2747(22) 1.0 Uiso 0.0042(14) 4

O

O4 0.5538(14) 0.2359(7) 0.5001(13) 1.0 Uiso 0.0042(14) 4

O

O5 0.6230(9) 0.2244(7) 0.1178(18) 1.0 Uiso 0.0042(14) 4

O

O6 0.3036(6) 0.1851(13) 0.4321(11) 1.0 Uiso 0.0042(14) 4

O

O7 0.0964(10) 0.1434(10) 0.1816(7) 1.0 Uiso 0.0042(14) 4

O

O8 0.0857(13) 0.0521(6) 0.5016(11) 1.0 Uiso 0.0042(14) 4

O

O9 0.1662(10) 0.0672(7) 0.8614(17) 1.0 Uiso 0.0042(14) 4

K

K1 0.2205(7) 0.6197(5) 0.1233(9) 0.823(4) Uiso 0.0040(12) 4
 K
 K2 0.4424(6) 0.0800(5) 0.7089(9) 0.927(4) Uiso 0.0040(12) 4
 O
 O10 0.6973(15) 0.0533(11) 0.8802(20) 1.0 Uiso 0.0042(14) 4
 Nb
 Nb1 0.45708(25) 0.21000(17) 0.2647(4) 0.25 Uiso 0.0049(6) 4

If you change Z, be sure to change all 3 of the following

_chemical_formula_sum "Ge3 K1.75 Nb0.25 O10 Zr0.75"

_chemical_formula_weight 537.82

_cell_formula_units_Z 4

MOLECULAR GEOMETRY

Bond	Distance Å
Zr1 O1	2.046(4)
Zr1 O2	2.040(4)
Zr1 O3	2.028(4)
Zr1 O4	2.050(4)
Zr1 O5	2.052(4)
Zr1 O6	2.053(4)
Zr1 K1	3.668(7)
Zr1 K1	3.989(7)
Zr1 K2	3.753(7)
Ge1 Ge2	3.098(4)
Ge1 Ge3	3.134(4)
Ge1 O2	1.734(5)
Ge1 O5	1.763(5)
Ge1 O7	1.757(5)
Ge1 O9	1.739(5)

Ge1	K1	4.053(8)
Ge1	K2	3.599(7)
Ge1	K2	4.035(7)
Ge2	Ge1	3.098(4)
Ge2	Ge3	3.078(4)
Ge2	O1	1.762(5)
Ge2	O3	1.720(5)
Ge2	O8	1.763(6)
Ge2	O9	1.755(5)
Ge2	K1	4.089(7)
Ge2	K1	3.831(7)
Ge2	K2	3.983(8)
Ge3	Ge1	3.134(4)
Ge3	Ge2	3.078(4)
Ge3	O4	1.774(5)
Ge3	O6	1.777(5)
Ge3	O7	1.736(5)
Ge3	O8	1.749(6)
Ge3	K1	3.693(7)
Ge3	K1	3.764(7)
Ge3	K2	4.134(7)
Ge3	K2	4.061(6)
Ge3	K2	3.707(7)
O1	Zr1	2.046(4)
O1	Ge2	1.762(5)
O1	K1	3.282(17)
O1	Nb1	2.046(4)
O2	Zr1	2.040(4)
O2	Ge1	1.734(5)
O2	K2	3.161(16)
O2	Nb1	2.040(4)
O3	Zr1	2.028(4)
O3	Ge2	1.720(5)
O3	K1	2.820(11)
O3	K2	3.349(19)
O3	Nb1	2.028(4)
O4	Zr1	2.050(4)
O4	Ge3	1.774(5)
O4	K1	2.977(17)
O4	K1	3.584(18)
O4	K2	2.874(12)
O4	Nb1	2.050(4)
O5	Zr1	2.052(4)
O5	Ge1	1.763(5)
O5	K1	2.898(14)
O5	Nb1	2.052(4)

O6	Zr1	2.053(4)
O6	Ge3	1.777(5)
O6	K1	3.027(17)
O6	K2	2.894(13)
O6	Nb1	2.053(4)
O7	Ge1	1.757(5)
O7	Ge3	1.736(5)
O7	K1	3.615(10)
O7	K2	3.077(15)
O8	Ge2	1.763(6)
O8	Ge3	1.749(6)
O8	K1	3.442(16)
O8	K2	2.841(11)
O9	Ge1	1.739(5)
O9	Ge2	1.755(5)
O9	K2	3.094(14)
O9	K2	3.462(17)
K1	Zr1	3.668(7)
K1	Zr1	3.989(7)
K1	Ge1	4.053(8)
K1	Ge2	4.089(7)
K1	Ge2	3.831(7)
K1	Ge3	3.693(7)
K1	Ge3	3.764(7)
K1	O1	3.282(17)
K1	O3	2.820(11)
K1	O4	2.977(17)
K1	O4	3.584(18)
K1	O5	2.898(14)
K1	O6	3.027(17)
K1	O7	3.615(10)
K1	O8	3.442(16)
K1	K1	4.987(9)
K1	K1	4.987(9)
K1	K2	4.163(9)
K1	K2	4.324(9)
K1	K2	4.473(9)
K1	O10	2.370(15)
K1	Nb1	3.668(7)
K1	Nb1	3.989(7)
K2	Zr1	3.753(7)
K2	Ge1	3.599(7)
K2	Ge1	4.035(7)
K2	Ge2	3.983(8)
K2	Ge3	4.134(7)
K2	Ge3	4.061(6)

K2	Ge3	3.707(7)
K2	O2	3.161(16)
K2	O3	3.349(19)
K2	O4	2.874(12)
K2	O6	2.894(13)
K2	O7	3.077(15)
K2	O8	2.841(11)
K2	O9	3.094(14)
K2	O9	3.462(17)
K2	K1	4.163(9)
K2	K1	4.324(9)
K2	K1	4.473(9)
K2	O10	2.963(16)
K2	Nb1	3.753(7)
O10	K1	2.370(15)
O10	K2	2.963(16)
Nb1	O1	2.046(4)
Nb1	O2	2.040(4)
Nb1	O3	2.028(4)
Nb1	O4	2.050(4)
Nb1	O5	2.052(4)
Nb1	O6	2.053(4)
Nb1	K1	3.668(7)
Nb1	K1	3.989(7)
Nb1	K2	3.753(7)

Appendix 6: Full CIF information for the refinement of the 10Sb zirconogermanate umbite,

figure 4.18

_cell_length_a	10.41660(11)
_cell_length_b	13.65654(13)
_cell_length_c	7.43939(7)
_cell_angle_alpha	90.0
_cell_angle_beta	90.0
_cell_angle_gamma	90.0
_cell_volume	1058.288(21)
_symmetry_cell_setting	orthorhombic
_symmetry_space_group_name_H-M	"P 21 21 21"

loop_ _symmetry_equiv_pos_site_id _symmetry_equiv_pos_as_xyz

- 1 +x,+y,+z
- 2 +x+1/2,-y+1/2,-z
- 3 -x,+y+1/2,-z+1/2
- 4 -x+1/2,-y,+z+1/2

ATOMIC COORDINATES AND DISPLACEMENT PARAMETERS

Zr

Zr1 0.45670(17) 0.21013(12) 0.26443(27) 0.9 Uiso 0.0057(5) 4

Ge

Ge1 0.18768(21) 0.17181(16) -0.00895(32) 1.0 Uiso 0.00029(27) 4

Ge

Ge2 0.03096(21) 0.04510(13) 0.72483(31) 1.0 Uiso 0.00029(27) 4

Ge

Ge3 0.63665(20) 0.33765(18) 0.59430(30) 1.0 Uiso 0.00029(27) 4

O

O1 0.4248(7) 0.35696(26) 0.2365(17) 1.0 Uiso 0.0110(12) 4

O

O2 0.3456(6) 0.1951(10) 0.0425(8) 1.0 Uiso 0.0110(12) 4

O

O3 0.5246(7) 0.07118(26) 0.2772(16) 1.0 Uiso 0.0110(12) 4

O

O4 0.5551(10) 0.2381(5) 0.4949(10) 1.0 Uiso 0.0110(12) 4

O

O5 0.6219(7) 0.2254(5) 0.1194(13) 1.0 Uiso 0.0110(12) 4

O

O6 0.3030(5) 0.1842(10) 0.4279(9) 1.0 Uiso 0.0110(12) 4

O

O7 0.0944(7) 0.1426(8) 0.1812(6) 1.0 Uiso 0.0110(12) 4

O

O8 0.0820(10) 0.0528(5) 0.4998(8) 1.0 Uiso 0.0110(12) 4

O

O9 0.1688(7) 0.0697(6) 0.8519(13) 1.0 Uiso 0.0110(12) 4

K

K1 0.2195(5) 0.62264(32) 0.1260(6) 0.9087(32) Uiso 0.0121(10) 4

K

K2 0.4408(4) 0.07968(30) 0.7077(6) 0.9913(32) Uiso 0.0121(10) 4

O

O10 0.7023(11) 0.0625(8) 0.8784(15) 1.0 Uiso 0.0110(12) 4

Sb

Sb1 0.45670(17) 0.21013(12) 0.26443(27) 0.1 Uiso 0.0057(5) 4

If you change Z, be sure to change all 3 of the following

_chemical_formula_sum "Ge3 K1.90 O10 Sb0.10 Zr0.90"

_chemical_formula_weight 546.32

_cell_formula_units_Z 4

MOLECULAR GEOMETRY

Bond	Distance Å
Zr1 O1	2.0432(33)
Zr1 O2	2.0267(33)
Zr1 O3	2.0272(33)
Zr1 O4	2.0333(33)
Zr1 O5	2.0417(33)
Zr1 O6	2.0417(33)
Zr1 K1	3.670(5)
Zr1 K1	3.977(5)
Zr1 K2	3.752(5)
Ge1 Ge2	3.0954(30)
Ge1 Ge3	3.1329(31)
Ge1 O2	1.719(4)
Ge1 O5	1.765(4)
Ge1 O7	1.762(4)

Ge1	O9	1.748(5)
Ge1	K1	4.024(5)
Ge1	K2	3.602(5)
Ge1	K2	4.023(5)
Ge2	Ge1	3.0954(30)
Ge2	Ge3	3.0679(31)
Ge2	O1	1.759(4)
Ge2	O3	1.734(4)
Ge2	O8	1.759(5)
Ge2	O9	1.752(4)
Ge2	K1	4.124(5)
Ge2	K1	3.839(5)
Ge2	K2	3.987(6)
Ge3	Ge1	3.1329(31)
Ge3	Ge2	3.0679(31)
Ge3	O4	1.766(4)
Ge3	O6	1.766(4)
Ge3	O7	1.748(4)
Ge3	O8	1.747(5)
Ge3	K1	3.682(5)
Ge3	K1	3.756(5)
Ge3	K2	4.045(4)
Ge3	K2	3.707(5)
O1	Zr1	2.0432(33)
O1	Ge2	1.759(4)
O1	K1	3.276(13)
O1	Sb1	2.0432(33)
O2	Zr1	2.0267(33)
O2	Ge1	1.719(4)
O2	K2	3.109(11)
O2	Sb1	2.0267(33)
O3	Zr1	2.0272(33)
O3	Ge2	1.734(4)
O3	K1	2.850(8)
O3	K2	3.322(14)
O3	Sb1	2.0272(33)
O4	Zr1	2.0333(33)
O4	Ge3	1.766(4)
O4	K1	2.968(13)
O4	K1	3.570(13)
O4	K2	2.933(9)
O4	Sb1	2.0333(33)
O5	Zr1	2.0417(33)
O5	Ge1	1.765(4)
O5	K1	2.879(10)
O5	Sb1	2.0417(33)

O6	Zr1	2.0417(33)
O6	Ge3	1.766(4)
O6	K1	3.031(13)
O6	K2	2.904(10)
O6	Sb1	2.0417(33)
O7	Ge1	1.762(4)
O7	Ge3	1.748(4)
O7	K1	3.580(8)
O7	K2	3.064(11)
O8	Ge2	1.759(5)
O8	Ge3	1.747(5)
O8	K1	3.413(12)
O8	K2	2.837(8)
O9	Ge1	1.748(5)
O9	Ge2	1.752(4)
O9	K2	3.033(10)
O9	K2	3.531(13)
K1	Zr1	3.670(5)
K1	Zr1	3.977(5)
K1	Ge1	4.024(5)
K1	Ge2	4.124(5)
K1	Ge2	3.839(5)
K1	Ge3	3.682(5)
K1	Ge3	3.756(5)
K1	O1	3.276(13)
K1	O3	2.850(8)
K1	O4	2.968(13)
K1	O4	3.570(13)
K1	O5	2.879(10)
K1	O6	3.031(13)
K1	O7	3.580(8)
K1	O8	3.413(12)
K1	K1	5.046(6)
K1	K1	5.046(6)
K1	K2	4.194(6)
K1	K2	4.363(7)
K1	K2	4.436(6)
K1	O10	2.535(11)
K1	Sb1	3.670(5)
K1	Sb1	3.977(5)
K2	Zr1	3.752(5)
K2	Ge1	3.602(5)
K2	Ge1	4.023(5)
K2	Ge2	3.987(6)
K2	Ge3	4.045(4)
K2	Ge3	3.707(5)

K2	O2	3.109(11)
K2	O3	3.322(14)
K2	O4	2.933(9)
K2	O6	2.904(10)
K2	O7	3.064(11)
K2	O8	2.837(8)
K2	O9	3.033(10)
K2	O9	3.531(13)
K2	K1	4.194(6)
K2	K1	4.363(7)
K2	K1	4.436(6)
K2	O10	3.014(12)
K2	Sb1	3.752(5)
O10	K1	2.535(11)
O10	K2	3.014(12)
Sb1	O1	2.0432(33)
Sb1	O2	2.0267(33)
Sb1	O3	2.0272(33)
Sb1	O4	2.0333(33)
Sb1	O5	2.0417(33)
Sb1	O6	2.0417(33)
Sb1	K1	3.670(5)
Sb1	K1	3.977(5)
Sb1	K2	3.752(5)

Appendix 7: Full CIF information for the refinement of the 20Sb zirconogermanate umbite,

figure 4.19

_cell_length_a	10.44043(20)
_cell_length_b	13.65789(22)
_cell_length_c	7.45525(13)
_cell_angle_alpha	90.0
_cell_angle_beta	90.0
_cell_angle_gamma	90.0
_cell_volume	1063.08(4)
_symmetry_cell_setting	orthorhombic
_symmetry_space_group_name_H-M	"P 21 21 21"

loop_ _symmetry_equiv_pos_site_id _symmetry_equiv_pos_as_xyz

- 1 +x,+y,+z
- 2 +x+1/2,-y+1/2,-z
- 3 -x,+y+1/2,-z+1/2
- 4 -x+1/2,-y,+z+1/2

ATOMIC COORDINATES AND DISPLACEMENT PARAMETERS

Zr

Zr1 0.45762(25) 0.21096(16) 0.2632(4) 0.8 Uiso 0.0056(6) 4

Ge

Ge1 0.18736(29) 0.17249(24) -0.0076(5) 1.0 Uiso 0.0001(4) 4

Ge

Ge2 0.03084(30) 0.04469(18) 0.7259(5) 1.0 Uiso 0.0001(4) 4

Ge

Ge3 0.63696(29) 0.33710(25) 0.5912(4) 1.0 Uiso 0.0001(4) 4

O

O1 0.4238(10) 0.3579(4) 0.2322(24) 1.0 Uiso 0.0060(16) 4

O

O2 0.3345(10) 0.2232(11) 0.0501(14) 1.0 Uiso 0.0060(16) 4

O

O3 0.5197(11) 0.0712(4) 0.2649(26) 1.0 Uiso 0.0060(16) 4

O

O4 0.5605(14) 0.2346(8) 0.4922(14) 1.0 Uiso 0.0060(16) 4

O

O5 0.6267(9) 0.2217(8) 0.1217(19) 1.0 Uiso 0.0060(16) 4

O

O6 0.3059(7) 0.1840(13) 0.4335(13) 1.0 Uiso 0.0060(16) 4

O

O7 0.0978(11) 0.1402(10) 0.1848(9) 1.0 Uiso 0.0060(16) 4

O

O8 0.0829(14) 0.0520(7) 0.5012(12) 1.0 Uiso 0.0060(16) 4

O

O9 0.1673(11) 0.0669(8) 0.8629(19) 1.0 Uiso 0.0060(16) 4

K

K1 0.2231(7) 0.6165(5) 0.1214(10) 0.818(5) Uiso 0.0067(13) 4

K

K2 0.4424(6) 0.0778(4) 0.7089(9) 0.982(5) Uiso 0.0067(13) 4

O

O10 0.7055(16) 0.0496(11) 0.8939(22) 1.0 Uiso 0.0060(16) 4

Sb

Sb1 0.45762(25) 0.21096(16) 0.2632(4) 0.2 Uiso 0.0056(6) 4

If you change Z, be sure to change all 3 of the following

_chemical_formula_sum "Ge3 K1.80 O10 Sb0.20 Zr0.80"

_chemical_formula_weight 545.46

_cell_formula_units_Z 4

MOLECULAR GEOMETRY

Bond	Distance Å
Zr1 O1	2.050(5)
Zr1 O2	2.050(5)
Zr1 O3	2.016(5)
Zr1 O4	2.043(5)
Zr1 O5	2.062(5)
Zr1 O6	2.063(5)
Zr1 K1	3.676(8)
Zr1 K1	4.030(7)
Zr1 K2	3.792(7)
Ge1 Ge2	3.108(4)
Ge1 O2	1.740(7)
Ge1 O5	1.792(7)
Ge1 O7	1.768(7)
Ge1 O9	1.748(7)
Ge1 K1	4.102(8)
Ge1 K2	3.637(8)

Ge1	K2	4.015(6)
Ge2	Ge1	3.108(4)
Ge2	Ge3	3.070(4)
Ge2	O1	1.766(7)
Ge2	O3	1.693(6)
Ge2	O8	1.764(7)
Ge2	O9	1.779(7)
Ge2	K1	4.058(8)
Ge2	K1	3.834(8)
Ge2	K2	3.980(8)
Ge3	Ge2	3.070(4)
Ge3	O4	1.772(7)
Ge3	O6	1.797(7)
Ge3	O7	1.747(7)
Ge3	O8	1.757(7)
Ge3	K1	3.704(8)
Ge3	K1	3.819(8)
Ge3	K2	4.065(6)
Ge3	K2	3.703(6)
O1	Zr1	2.050(5)
O1	Ge2	1.766(7)
O1	K1	3.301(19)
O1	Sb1	2.050(5)
O2	Zr1	2.050(5)
O2	Ge1	1.740(7)
O2	K2	3.418(18)
O2	Sb1	2.050(5)
O3	Zr1	2.016(5)
O3	Ge2	1.693(6)
O3	K1	2.883(13)
O3	K2	3.409(22)
O3	Sb1	2.016(5)
O4	Zr1	2.043(5)
O4	Ge3	1.772(7)
O4	K1	2.902(17)
O4	K2	2.953(14)
O4	Sb1	2.043(5)
O5	Zr1	2.062(5)
O5	Ge1	1.792(7)
O5	K1	2.862(15)
O5	Sb1	2.062(5)
O6	Zr1	2.063(5)
O6	Ge3	1.797(7)
O6	K1	3.078(18)
O6	K2	2.890(14)
O6	Sb1	2.063(5)

O7	Ge1	1.768(7)
O7	Ge3	1.747(7)
O7	K1	3.663(12)
O7	K2	3.012(14)
O8	Ge2	1.764(7)
O8	Ge3	1.757(7)
O8	K1	3.439(17)
O8	K2	2.821(12)
O9	Ge1	1.748(7)
O9	Ge2	1.779(7)
O9	K2	3.096(15)
O9	K2	3.446(18)
K1	Zr1	3.676(8)
K1	Zr1	4.030(7)
K1	Ge1	4.102(8)
K1	Ge2	4.058(8)
K1	Ge2	3.834(8)
K1	Ge3	3.704(8)
K1	Ge3	3.819(8)
K1	O1	3.301(19)
K1	O3	2.883(13)
K1	O4	2.902(17)
K1	O5	2.862(15)
K1	O6	3.078(18)
K1	O7	3.663(12)
K1	O8	3.439(17)
K1	K1	4.934(9)
K1	K1	4.934(9)
K1	K2	4.151(9)
K1	K2	4.306(10)
K1	K2	4.565(9)
K1	O10	2.279(15)
K1	Sb1	3.676(8)
K1	Sb1	4.030(7)
K2	Zr1	3.792(7)
K2	Ge1	3.637(8)
K2	Ge1	4.015(6)
K2	Ge2	3.980(8)
K2	Ge3	4.065(6)
K2	Ge3	3.703(6)
K2	O2	3.418(18)
K2	O3	3.409(22)
K2	O4	2.953(14)
K2	O6	2.890(14)
K2	O7	3.012(14)
K2	O8	2.821(12)

K2	O9	3.096(15)
K2	O9	3.446(18)
K2	K1	4.151(9)
K2	K1	4.306(10)
K2	K1	4.565(9)
K2	O10	3.098(18)
K2	Sb1	3.792(7)
O10	K1	2.279(15)
O10	K2	3.098(18)
Sb1	O1	2.050(5)
Sb1	O2	2.050(5)
Sb1	O3	2.016(5)
Sb1	O4	2.043(5)
Sb1	O5	2.062(5)
Sb1	O6	2.063(5)
Sb1	K1	3.676(8)
Sb1	K1	4.030(7)
Sb1	K2	3.792(7)

Appendix 8: Full CIF information for the refinement of the 25Sb zirconogermanate umbite,
figure 4.20

_cell_length_a	10.43870(18)
_cell_length_b	13.65089(21)
_cell_length_c	7.45339(12)
_cell_angle_alpha	90.0
_cell_angle_beta	90.0
_cell_angle_gamma	90.0
_cell_volume	1062.089(35)
_symmetry_cell_setting	orthorhombic
_symmetry_space_group_name_H-M	"P 21 21 21"

loop_ _symmetry_equiv_pos_site_id _symmetry_equiv_pos_as_xyz

- 1 +x,+y,+z
- 2 +x+1/2,-y+1/2,-z
- 3 -x,+y+1/2,-z+1/2
- 4 -x+1/2,-y,+z+1/2

ATOMIC COORDINATES AND DISPLACEMENT PARAMETERS

Zr

Zr1 0.45755(24) 0.21107(16) 0.2632(4) 0.75 Uiso 0.0067(6) 4

Ge

Ge1 0.18632(29) 0.17170(24) -0.0072(5) 1.0 Uiso 0.0000(4) 4

Ge

Ge2 0.03072(29) 0.04419(18) 0.7268(5) 1.0 Uiso 0.0000(4) 4

Ge

Ge3 0.63727(29) 0.33689(25) 0.5903(4) 1.0 Uiso 0.0000(4) 4

O

O1 0.4208(11) 0.3600(5) 0.2326(24) 1.0 Uiso 0.0127(17) 4

O

O2 0.3374(10) 0.2189(12) 0.0415(15) 1.0 Uiso 0.0127(17) 4

O

O3 0.5198(11) 0.0703(5) 0.2528(30) 1.0 Uiso 0.0127(17) 4

O

O4 0.5593(15) 0.2353(8) 0.4955(15) 1.0 Uiso 0.0127(17) 4

O

O5 0.6277(10) 0.2196(8) 0.1175(19) 1.0 Uiso 0.0127(17) 4

O

O6 0.3070(8) 0.1841(13) 0.4414(14) 1.0 Uiso 0.0127(17) 4

O

O7 0.0957(12) 0.1428(10) 0.1865(11) 1.0 Uiso 0.0127(17) 4

O

O8 0.0855(14) 0.0517(8) 0.5036(14) 1.0 Uiso 0.0127(17) 4

O

O9 0.1670(12) 0.0649(9) 0.8670(19) 1.0 Uiso 0.0127(17) 4

K

K1 0.2211(7) 0.6195(5) 0.1233(10) 0.800(5) Uiso 0.0055(13) 4

K

K2 0.4401(6) 0.0788(4) 0.7103(9) 0.950(5) Uiso 0.0055(13) 4

O

O10 0.7061(17) 0.0488(11) 0.8924(21) 1.0 Uiso 0.0127(17) 4

Sb

Sb1 0.45755(24) 0.21107(16) 0.2632(4) 0.25 Uiso 0.0067(6) 4

If you change Z, be sure to change all 3 of the following

_chemical_formula_sum "Ge3 K1.75 O10 Sb0.25 Zr0.75"

_chemical_formula_weight 545.03

_cell_formula_units_Z 4

MOLECULAR GEOMETRY

Bond	Distance Å
Zr1 O1	2.081(6)
Zr1 O2	2.077(6)
Zr1 O3	2.030(6)
Zr1 O4	2.058(6)
Zr1 O5	2.085(6)
Zr1 O6	2.090(6)
Zr1 K1	3.679(8)
Zr1 K1	4.004(7)
Zr1 K2	3.794(7)
Ge1 Ge2	3.098(4)
Ge1 O2	1.742(8)
Ge1 O5	1.803(8)
Ge1 O7	1.770(8)
Ge1 O9	1.745(8)

Ge1	K1	4.080(8)
Ge1	K2	3.614(7)
Ge1	K2	4.008(6)
Ge2	Ge1	3.098(4)
Ge2	Ge3	3.075(4)
Ge2	O1	1.766(8)
Ge2	O3	1.661(7)
Ge2	O8	1.762(8)
Ge2	O9	1.788(8)
Ge2	K1	4.085(8)
Ge2	K1	3.844(8)
Ge2	K2	3.988(8)
Ge3	Ge2	3.075(4)
Ge3	O4	1.756(8)
Ge3	O6	1.810(8)
Ge3	O7	1.741(8)
Ge3	O8	1.759(9)
Ge3	K1	3.678(7)
Ge3	K1	3.796(8)
Ge3	K2	4.042(6)
Ge3	K2	3.711(6)
O1	Zr1	2.081(6)
O1	Ge2	1.766(8)
O1	K1	3.279(19)
O1	Sb1	2.081(6)
O2	Zr1	2.077(6)
O2	Ge1	1.742(8)
O2	K2	3.302(18)
O2	Sb1	2.077(6)
O3	Zr1	2.030(6)
O3	Ge2	1.661(7)
O3	K1	2.936(15)
O3	K2	3.511(24)
O3	Sb1	2.030(6)
O4	Zr1	2.058(6)
O4	Ge3	1.756(8)
O4	K1	2.922(18)
O4	K1	3.661(18)
O4	K2	2.946(14)
O4	Sb1	2.058(6)
O5	Zr1	2.085(6)
O5	Ge1	1.803(8)
O5	K1	2.845(15)
O5	Sb1	2.085(6)
O6	Zr1	2.090(6)
O6	Ge3	1.810(8)

O6	K1	3.019(18)
O6	K2	2.831(15)
O6	Sb1	2.090(6)
O7	Ge1	1.770(8)
O7	Ge3	1.741(8)
O7	K1	3.612(12)
O7	K2	3.054(15)
O8	Ge2	1.762(8)
O8	Ge3	1.759(9)
O8	K1	3.463(17)
O8	K2	2.833(13)
O9	Ge1	1.745(8)
O9	Ge2	1.788(8)
O9	K2	3.087(16)
O9	K2	3.412(18)
K1	Zr1	3.679(8)
K1	Zr1	4.004(7)
K1	Ge1	4.080(8)
K1	Ge2	4.085(8)
K1	Ge2	3.844(8)
K1	Ge3	3.678(7)
K1	Ge3	3.796(8)
K1	O1	3.279(19)
K1	O3	2.936(15)
K1	O4	2.922(18)
K1	O4	3.661(18)
K1	O5	2.845(15)
K1	O6	3.019(18)
K1	O7	3.612(12)
K1	O8	3.463(17)
K1	K1	4.990(9)
K1	K1	4.990(9)
K1	K2	4.180(9)
K1	K2	4.359(10)
K1	K2	4.496(9)
K1	O10	2.306(16)
K1	Sb1	3.679(8)
K1	Sb1	4.004(7)
K2	Zr1	3.794(7)
K2	Ge1	3.614(7)
K2	Ge1	4.008(6)
K2	Ge2	3.988(8)
K2	Ge3	4.042(6)
K2	Ge3	3.711(6)
K2	O2	3.302(18)
K2	O3	3.511(24)

K2	O4	2.946(14)
K2	O6	2.831(15)
K2	O7	3.054(15)
K2	O8	2.833(13)
K2	O9	3.087(16)
K2	O9	3.412(18)
K2	K1	4.180(9)
K2	K1	4.359(10)
K2	K1	4.496(9)
K2	O10	3.117(18)
K2	Sb1	3.794(7)
O10	K1	2.306(16)
O10	K2	3.117(18)
Sb1	O1	2.081(6)
Sb1	O2	2.077(6)
Sb1	O3	2.030(6)
Sb1	O4	2.058(6)
Sb1	O5	2.085(6)
Sb1	O6	2.090(6)
Sb1	K1	3.679(8)
Sb1	K1	4.004(7)
Sb1	K2	3.794(7)

Appendix 9: Full CIF information for the refinement of the Germanogermanium pharmacosiderite, figure 5.5.

_cell_length_a 15.41756(6)

_cell_length_b 15.41756

_cell_length_c 15.41756

_cell_angle_alpha 90.0

_cell_angle_beta 90.0

_cell_angle_gamma 90.0

_cell_volume 3664.77(4)

_symmetry_cell_setting cubic

_symmetry_space_group_name_H-M "I 2 3"

loop_ _symmetry_equiv_pos_site_id _symmetry_equiv_pos_as_xyz

1 +x,+y,+z

2 +z,+x,+y

3 +y,+z,+x

4 +x,-y,-z

5 -z,+x,-y

6 -y,-z,+x

$$7 -z, -x, +y$$

$$8 +y, -z, -x$$

$$9 -y, +z, -x$$

$$10 -x, -y, +z$$

$$11 +z, -x, -y$$

$$12 -x, +y, -z$$

$$101 +x+1/2, +y+1/2, +z+1/2$$

$$102 +z+1/2, +x+1/2, +y+1/2$$

$$103 +y+1/2, +z+1/2, +x+1/2$$

$$104 +x+1/2, -y+1/2, -z+1/2$$

$$105 -z+1/2, +x+1/2, -y+1/2$$

$$106 -y+1/2, -z+1/2, +x+1/2$$

$$107 -z+1/2, -x+1/2, +y+1/2$$

$$108 +y+1/2, -z+1/2, -x+1/2$$

$$109 -y+1/2, +z+1/2, -x+1/2$$

$$110 -x+1/2, -y+1/2, +z+1/2$$

$$111 +z+1/2, -x+1/2, -y+1/2$$

$$112 -x+1/2, +y+1/2, -z+1/2$$

ATOMIC COORDINATES AND DISPLACEMENT PARAMETERS

Ge

Ge1 0.9996(4) 0.24324(28) 0.25853(24) 1.0 Uiso 0.00502(14) 24

Ge

Ge2 0.18123(33) 0.18123(33) 0.18123(33) 1.0 Uiso 0.00502(14) 8

Ge

Ge3 0.18459(23) 0.17782(22) 0.68080(35) 1.0 Uiso 0.00502(14) 24

O

O1 0.1760(10) 0.1949(9) 0.0595(11) 1.0 Uiso 0.0047(9) 24

O

O2 0.8046(11) 0.8192(13) 0.5652(13) 1.0 Uiso 0.0047(9) 24

O

O3 0.6755(10) 0.1935(10) 0.0570(8) 1.0 Uiso 0.0047(9) 24

O

O4 0.1737(12) 0.6801(10) 0.0674(9) 1.0 Uiso 0.0047(9) 24

O

O5 0.3060(12) 0.3060(12) 0.3060(12) 1.0 Uiso 0.0047(9) 8

O

O6 0.3029(9) 0.3131(9) 0.8066(10) 1.0 Uiso 0.0047(9) 24

K

K1 0.2174(9) 0.5 0.0 0.617 Uiso 0.0725(20) 12

K

K2 0.2845(14) 0.5 0.0 0.383 Uiso 0.0725(20) 12

K

K3 0.2464(25) 0.0 0.0 0.712 Uiso 0.0725(20) 12

K

K4 0.3540(21) 0.0 0.0 0.288 Uiso 0.0725(20) 12

O

O7 0.9204(6) 0.9204(6) 0.9204(6) 1.0 Uiso 0.0047(9) 8

O

O8 0.3857(9) 0.4373(8) 0.9064(10) 0.7125 Uiso 0.0047(9) 24

If you change Z, be sure to change all 3 of the following

_chemical_formula_sum "Ge7 K3.00 O19.14"

_chemical_formula_weight 931.60

_cell_formula_units_Z 8

MOLECULAR GEOMETRY

Bond	Distance Å
Ge1 O1	1.699(16)
Ge1 O2	1.671(16)
Ge1 O3	1.827(13)
Ge1 O4	1.764(12)
Ge1 K1	3.744(4)
Ge1 K1	3.976(5)
Ge1 K2	3.777(5)
Ge1 K2	4.014(5)
Ge1 K3	3.986(4)
Ge1 K3	3.755(5)
Ge1 K4	4.029(12)
Ge2 Ge3	3.000(6)
Ge2 Ge3	3.000(6)
Ge2 Ge3	3.000(6)
Ge2 O1	1.891(17)
Ge2 O1	1.891(17)
Ge2 O1	1.891(17)
Ge2 O6	1.950(15)
Ge2 O6	1.950(15)
Ge2 O6	1.950(15)

Ge2	K3	4.077(11)
Ge2	K3	4.077(11)
Ge2	K3	4.077(11)
Ge3	Ge2	3.000(6)
Ge3	Ge3	3.012(6)
Ge3	Ge3	3.012(6)
Ge3	O2	1.790(19)
Ge3	O3	1.869(13)
Ge3	O4	1.809(14)
Ge3	O5	1.951(16)
Ge3	O6	1.935(14)
Ge3	O6	2.011(14)
Ge3	K1	4.030(4)
Ge3	K2	3.939(4)
Ge3	K3	4.108(12)
Ge3	K4	3.988(6)
O1	Ge1	1.699(16)
O1	Ge2	1.891(17)
O1	K3	3.324(20)
O1	K3	2.973(17)
O2	Ge1	1.671(16)
O2	Ge3	1.790(19)
O2	K1	3.226(18)
O2	K1	3.254(21)
O2	K2	3.556(20)
O2	K2	2.980(21)
O3	Ge1	1.827(13)
O3	Ge3	1.869(13)
O3	K1	3.158(18)
O3	K2	2.865(16)
O3	K3	3.336(21)
O3	K4	3.144(15)
O4	Ge1	1.764(12)
O4	Ge3	1.809(14)
O4	K1	3.040(17)
O4	K2	3.421(21)
O4	K3	3.087(24)
O4	K4	2.919(18)
O5	Ge3	1.951(16)
O5	Ge3	1.951(16)
O5	Ge3	1.951(16)
O6	Ge2	1.950(15)
O6	Ge3	2.011(14)
O6	Ge3	1.935(14)
K1	Ge1	3.744(4)
K1	Ge1	3.744(4)

K1	Ge1	3.976(5)
K1	Ge1	3.976(5)
K1	Ge3	4.030(4)
K1	Ge3	4.030(4)
K1	O2	3.226(18)
K1	O2	3.226(18)
K1	O2	3.254(21)
K1	O2	3.254(21)
K1	O3	3.158(18)
K1	O3	3.158(18)
K1	O4	3.040(17)
K1	O4	3.040(17)
K1	K2	1.034(23)
K1	K2	4.720(16)
K1	K2	4.720(16)
K1	K3	5.150(33)
K1	K3	5.150(33)
K1	K4	4.038(24)
K1	K4	4.038(24)
K1	K4	4.903(16)
K1	K4	4.903(16)
K1	O8	3.121(19)
K1	O8	3.121(19)
K1	O8	3.299(17)
K1	O8	3.299(17)
K2	Ge1	3.777(5)
K2	Ge1	3.777(5)
K2	Ge1	4.014(5)
K2	Ge1	4.014(5)
K2	Ge3	3.939(4)
K2	Ge3	3.939(4)
K2	O2	3.556(20)
K2	O2	3.556(20)
K2	O2	2.980(21)
K2	O2	2.980(21)
K2	O3	2.865(16)
K2	O3	2.865(16)
K2	O4	3.421(21)
K2	O4	3.421(21)
K2	K1	1.034(23)
K2	K1	4.720(16)
K2	K1	4.720(16)
K2	K3	5.13(4)
K2	K3	5.13(4)
K2	K4	4.930(22)
K2	K4	4.930(22)

K2	K4	4.013(27)
K2	K4	4.013(27)
K2	O8	2.334(20)
K2	O8	2.334(20)
K3	Ge1	3.755(5)
K3	Ge1	3.986(4)
K3	Ge1	3.986(4)
K3	Ge1	3.755(5)
K3	Ge2	4.077(11)
K3	Ge2	4.077(11)
K3	Ge3	4.108(12)
K3	Ge3	4.108(12)
K3	O1	3.324(20)
K3	O1	2.973(17)
K3	O1	3.324(20)
K3	O1	2.973(17)
K3	O3	3.336(21)
K3	O3	3.336(21)
K3	O4	3.087(24)
K3	O4	3.087(24)
K3	K1	5.150(33)
K3	K1	5.150(33)
K3	K2	5.13(4)
K3	K2	5.13(4)
K3	K4	1.66(5)
K3	O7	3.102(32)
K3	O7	3.102(32)
K3	O8	3.182(34)
K3	O8	3.182(34)
K4	Ge1	4.029(12)
K4	Ge1	4.029(12)
K4	Ge3	3.988(6)
K4	Ge3	3.988(6)
K4	O3	3.144(15)
K4	O3	3.144(15)
K4	O4	2.919(18)
K4	O4	2.919(18)
K4	K1	4.038(24)
K4	K1	4.038(24)
K4	K1	4.903(16)
K4	K1	4.903(16)
K4	K2	4.930(22)
K4	K2	4.930(22)
K4	K2	4.013(27)
K4	K2	4.013(27)
K4	K3	1.66(5)

K4	K4	4.50(6)
K4	O8	2.166(19)
K4	O8	2.166(19)
O7	K3	3.102(32)
O7	K3	3.102(32)
O7	K3	3.102(32)
O8	K1	3.121(19)
O8	K1	3.299(17)
O8	K2	2.334(20)
O8	K3	3.182(34)
O8	K4	2.166(19)

Appendix 10: Full CIF information for the refinement of the Titanogermanium pharmacosiderite, figure 5.9.

_cell_length_a	11.1503(5)
_cell_length_b	11.1503
_cell_length_c	7.9237(4)
_cell_angle_alpha	90.0
_cell_angle_beta	90.0
_cell_angle_gamma	90.0
_cell_volume	985.15(7)
_symmetry_cell_setting	tetragonal
_symmetry_space_group_name_H-M	"P -4 b 2"

loop_ _symmetry_equiv_pos_site_id _symmetry_equiv_pos_as_xyz

1 +x,+y,+z

2 +y,-x,-z

3 -x,-y,+z

4 -y,+x,-z

5 -x+1/2,+y+1/2,+z

6 +y+1/2,+x+1/2,-z

7 +x+1/2,-y+1/2,+z

8 -y+1/2,-x+1/2,-z

ATOMIC COORDINATES AND DISPLACEMENT PARAMETERS

Ti

Ti1 0.1372(4) -0.0081(10) 0.1426(8) 1.0 Uiso 0.0186(16) 8

Ge

Ge1 0.2571(4) 0.2429(4) 0.0 1.0 Uiso 0.0356(10) 4

Ge

Ge2 0.0 0.0 0.5 1.0 Uiso 0.0356(10) 2

O

O1 0.1418(14) 0.2571(18) 0.8657(25) 1.0 Uiso 0.0261(29) 8

O

O2 0.2444(18) 0.1111(14) 0.1032(24) 1.0 Uiso 0.0261(29) 8

O

O3 0.1453(12) -0.0186(17) -0.0998(17) 1.0 Uiso 0.0261(29) 8

O

O4 0.8819(10) 0.018(4) 0.3688(12) 1.0 Uiso 0.0261(29) 8

O

O5 0.3409(11) -0.0141(18) 0.7493(15) 1.0 Uiso 0.0261(29) 8

K

K1 0.2896(6) 0.2104(6) 0.5 1.0 Uiso 0.1060(32) 4

K

K2 0.5 0.0 0.0 1.0 Uiso 0.1060(32) 2

If you change Z, be sure to change all 3 of the following

_chemical_formula_sum "Ge3 K3 O20 Ti4"

_chemical_formula_weight 846.64

_cell_formula_units_Z 2

MOLECULAR GEOMETRY

Bond	Distance Å
Ti1 Ti1	3.131(7)
Ti1 Ti1	3.064(9)
Ti1 Ti1	3.131(7)
Ti1 Ge1	3.222(10)
Ti1 Ge2	3.219(7)
Ti1 O1	2.004(16)
Ti1 O2	1.814(12)
Ti1 O3	1.927(12)
Ti1 O3	2.339(21)
Ti1 O3	2.188(21)
Ti1 O4	1.808(10)
Ti1 K1	4.104(8)
Ti1 K2	4.202(6)
Ge1 Ti1	3.222(10)
Ge1 Ti1	3.222(10)
Ge1 O1	1.677(10)
Ge1 O1	1.677(10)
Ge1 O2	1.688(10)
Ge1 O2	1.688(10)
Ge1 K1	3.9948(16)
Ge1 K1	3.9948(16)
Ge1 K2	3.830(7)
Ge1 K2	4.054(7)
Ge2 Ti1	3.219(7)
Ge2 O4	1.690(9)
Ge2 O4	1.690(9)
Ge2 O4	1.690(9)

Ge2	O4	1.690(9)
Ge2	K1	3.9913(16)
O1	Ti1	2.004(16)
O1	Ge1	1.677(10)
O1	K1	3.374(26)
O1	K2	3.312(26)
O2	Ti1	1.814(12)
O2	Ge1	1.688(10)
O2	K1	3.371(20)
O2	K2	3.213(24)
O3	Ti1	1.927(12)
O3	Ti1	2.188(21)
O3	Ti1	2.339(21)
O4	Ti1	1.808(10)
O4	Ge2	1.690(9)
O4	K1	3.351(33)
O4	K1	3.362(33)
O5	K1	3.240(18)
O5	K2	2.668(14)
K1	Ti1	4.104(8)
K1	Ti1	4.104(8)
K1	Ge1	3.9948(16)
K1	Ge1	3.9948(16)
K1	Ge2	3.9913(16)
K1	Ge2	3.9913(16)
K1	O1	3.374(26)
K1	O1	3.374(26)
K1	O2	3.371(20)
K1	O2	3.371(20)
K1	O4	3.362(33)
K1	O4	3.351(33)
K1	O4	3.351(33)
K1	O4	3.362(33)
K1	O5	3.240(18)
K1	O5	3.240(18)
K2	Ti1	4.202(6)
K2	Ge1	3.830(7)
K2	Ge1	4.054(7)
K2	Ge1	3.830(7)
K2	Ge1	4.054(7)

K2	O1	3.312(26)
K2	O2	3.213(24)
K2	O5	2.668(14)

Appendix 11: Full CIF information for the refinement of the caesium exchanged

Germanogermanium pharmacosiderite, figure 5.12.

_cell_length_a 10.92814(7)

_cell_length_b 10.92814

_cell_length_c 7.79598(8)

_cell_angle_alpha 90.0

_cell_angle_beta 90.0

_cell_angle_gamma 90.0

_cell_volume 931.029(16)

_symmetry_cell_setting tetragonal

_symmetry_space_group_name_H-M "P -4 b 2"

loop_ _symmetry_equiv_pos_site_id _symmetry_equiv_pos_as_xyz

1 +x,+y,+z

2 +y,-x,-z

3 -x,-y,+z

4 -y,+x,-z

5 -x+1/2,+y+1/2,+z

6 +y+1/2,+x+1/2,-z

7 +x+1/2,-y+1/2,+z

8 -y+1/2,-x+1/2,-z

ATOMIC COORDINATES AND DISPLACEMENT PARAMETERS

Ge

Ge1 0.13797(11) -0.00801(13) 0.13897(18) 1.0 Uiso 0.00023(17) 8

Ge

Ge2 0.26621(9) 0.23369(9) 0.0 1.0 Uiso 0.00023(17) 4

Ge

Ge3 0.0 0.0 0.5 1.0 Uiso 0.00023(17) 2

O

O1 0.1412(6) 0.2523(7) 0.8616(10) 1.0 Uiso 0.0139(10) 8

O

O2 0.2708(7) 0.1037(6) 0.1265(9) 1.0 Uiso 0.0139(10) 8

O

O3 0.1186(6) -0.0217(8) 0.8926(9) 1.0 Uiso 0.0139(10) 8

O

O4 0.8675(5) 0.0090(10) 0.3777(8) 1.0 Uiso 0.0139(10) 8

Cs

Cs1 0.29528(9) 0.20472(9) 0.5 0.897(4) Uiso 0.0316(5) 4

K

K1 0.29528(9) 0.20472(9) 0.5 0.103(4) Uiso 0.0316(5) 4

K

K2 0.5 0.0 0.0 1.0 Uiso 0.0218(15) 2

O

O5 0.3547(7) -0.0423(6) 0.7039(10) 1.0 Uiso 0.0142(10) 8

If you change Z, be sure to change all 3 of the following

_chemical_formula_sum "Cs1.79 Ge7 K1.21 O20"

_chemical_formula_weight 1113.78

_cell_formula_units_Z 2

MOLECULAR GEOMETRY

Bond	Distance Å
Ge1 Ge1	3.0425(21)
Ge1 Ge1	3.0206(25)
Ge1 Ge1	3.0425(21)
Ge1 O1	1.918(6)
Ge1 O2	1.899(6)
Ge1 O3	1.938(7)
Ge1 O3	2.137(8)
Ge1 O3	1.894(8)
Ge1 O4	1.862(6)
Ge1 Cs1	4.0351(14)
Ge1 Cs1	4.2789(15)
Ge1 K1	4.0351(14)
Ge1 K2	4.1029(13)
Ge2 O1	1.752(6)
Ge2 O1	1.753(6)
Ge2 O2	1.730(6)
Ge2 O2	1.731(6)
Ge2 Cs1	3.92371(22)
Ge2 Cs1	3.92371(22)
Ge2 K1	3.92371(22)
Ge2 K1	3.92371(22)
Ge2 K2	3.6124(14)
Ge2 K2	4.1149(14)
Ge3 O4	1.736(6)
Ge3 Cs1	3.92654(24)
Ge3 Cs1	3.92654(24)
Ge3 Cs1	3.92654(24)

Ge3	Cs1	3.92654(24)
Ge3	K1	3.92654(24)
O1	Ge1	1.918(6)
O1	Ge2	1.752(6)
O1	Cs1	3.324(8)
O1	K1	3.324(8)
O1	K2	3.298(8)
O2	Ge1	1.899(6)
O2	Ge2	1.730(6)
O2	Cs1	3.125(8)
O2	K1	3.125(8)
O2	K2	2.921(8)
O3	Ge1	1.938(7)
O3	Ge1	1.894(8)
O3	Ge1	2.137(8)
O4	Ge1	1.862(6)
O4	Ge3	1.736(6)
O4	Cs1	3.087(9)
O4	Cs1	3.364(10)
O4	K1	3.087(9)
O4	K1	3.364(10)
Cs1	Ge1	4.0351(14)
Cs1	Ge1	4.2789(15)
Cs1	Ge1	4.2789(15)
Cs1	Ge1	4.0351(14)
Cs1	Ge2	3.92371(22)
Cs1	Ge2	3.92371(22)
Cs1	Ge3	3.92654(24)
Cs1	Ge3	3.92654(24)
Cs1	O1	3.324(8)
Cs1	O1	3.324(8)
Cs1	O2	3.125(8)
Cs1	O2	3.125(8)
Cs1	O4	3.364(10)
Cs1	O4	3.087(9)
Cs1	O4	3.087(9)
Cs1	O4	3.364(10)
Cs1	Cs1	5.55296(34)
Cs1	K2	5.0204(8)
Cs1	K2	5.0204(8)

Cs1	O5	3.199(7)
Cs1	O5	3.586(8)
Cs1	O5	3.586(8)
Cs1	O5	3.199(7)
K1	Ge1	4.0351(14)
K1	Ge1	4.0351(14)
K1	Ge2	3.92371(22)
K1	Ge2	3.92371(22)
K1	Ge3	3.92654(24)
K1	Ge3	3.92654(24)
K1	O1	3.324(8)
K1	O1	3.324(8)
K1	O2	3.125(8)
K1	O2	3.125(8)
K1	O4	3.364(10)
K1	O4	3.087(9)
K1	O4	3.087(9)
K1	O4	3.364(10)
K1	K2	5.0204(8)
K1	K2	5.0204(8)
K1	O5	3.199(7)
K1	O5	3.586(8)
K1	O5	3.586(8)
K1	O5	3.199(7)
K2	Ge1	4.1029(13)
K2	Ge2	3.6124(14)
K2	Ge2	4.1149(14)
K2	Ge2	3.6124(14)
K2	Ge2	4.1149(14)
K2	O1	3.298(8)
K2	O2	2.921(8)
K2	Cs1	5.0204(8)
K2	K1	5.0204(8)
K2	K1	5.0204(8)

K2	K1	5.0204(8)
K2	K1	5.0204(8)
K2	O5	2.839(8)
O5	Cs1	3.199(7)
O5	Cs1	3.586(8)
O5	K1	3.199(7)
O5	K1	3.586(8)
O5	K2	2.839(8)

Appendix 12: Full CIF information for the refinement of the caesium exchanged

Titanogermanium pharmacosiderite, figure 5.13.

_cell_length_a	11.2473(7)
_cell_length_b	11.2473
_cell_length_c	7.9386(8)
_cell_angle_alpha	90.0
_cell_angle_beta	90.0
_cell_angle_gamma	90.0
_cell_volume	1004.26(11)
_symmetry_cell_setting	tetragonal
_symmetry_space_group_name_H-M	"P -4 b 2"

loop_ _symmetry_equiv_pos_site_id _symmetry_equiv_pos_as_xyz

1 +x,+y,+z

2 +y,-x,-z

3 -x,-y,+z

4 -y,+x,-z

5 -x+1/2,+y+1/2,+z

6 +y+1/2,+x+1/2,-z

7 +x+1/2,-y+1/2,+z

8 -y+1/2,-x+1/2,-z

ATOMIC COORDINATES AND DISPLACEMENT PARAMETERS

Ti

Ti1 0.1408(6) 0.0005(9) 0.1416(13) 1.0 Uiso 0.025 8

Ge

Ge1 0.25150(21) 0.24850(21) 0.0 1.0 Uiso 0.0267(11) 4

Ge

Ge2 0.0 0.0 0.5 1.0 Uiso 0.0267(11) 2

O

O1 0.1229(12) 0.2328(13) 0.8504(23) 1.0 Uiso 0.0049(26) 8

O

O2 0.2421(14) 0.1324(13) 0.1466(23) 1.0 Uiso 0.0049(26) 8

O

O3 0.1068(11) -0.0091(16) -0.0944(20) 1.0 Uiso 0.0049(26) 8

O

O4 0.8676(9) 0.0040(20) 0.3833(15) 1.0 Uiso 0.0049(26) 8

O

O5 0.3867(12) -0.0119(13) 0.7311(18) 1.0 Uiso 0.0049(26) 8

K

K1 0.28072(24) 0.21928(24) 0.5 0.258(11) Uiso 0.0658(26) 4

K

K2 0.5 0.0 0.0 0.260(20) Uiso 0.0477(27) 2

Cs

Cs1 0.28072(24) 0.21928(24) 0.5 0.742(11) Uiso 0.0658(26) 4

Cs

Cs2 0.5 0.0 0.0 0.740(20) Uiso 0.0477(27) 2

If you change Z, be sure to change all 3 of the following

_chemical_formula_sum "Cs2.22 Ge3 K0.78 O20 Ti4"

_chemical_formula_weight 1055.22

_cell_formula_units_Z 2

MOLECULAR GEOMETRY

Bond	Distance Å
Ti1 Ti1	3.174(11)
Ti1 Ti1	3.167(14)
Ti1 Ti1	3.174(11)
Ti1 O1	1.733(14)
Ti1 O2	1.871(11)
Ti1 O3	1.916(15)
Ti1 O3	2.107(21)
Ti1 O3	1.940(21)
Ti1 O4	1.922(12)
Ti1 K1	4.078(8)
Ti1 K2	4.194(9)
Ti1 Cs1	4.078(8)
Ti1 Cs1	4.345(10)
Ti1 Cs2	4.194(9)
Ge1 O1	1.880(10)
Ge1 O1	1.880(10)
Ge1 O2	1.753(10)
Ge1 O2	1.753(10)
Ge1 K1	3.9964(7)
Ge1 K1	3.9964(7)
Ge1 K2	3.9527(33)
Ge1 K2	4.0003(33)
Ge1 Cs1	3.9964(7)
Ge1 Cs1	3.9964(7)

Ge1	Cs2	3.9527(33)
Ge1	Cs2	4.0003(33)
Ge2	O4	1.754(10)
Ge2	K1	4.0064(5)
Ge2	Cs1	4.0064(5)
O1	Ti1	1.733(14)
O1	Ge1	1.880(10)
O1	K1	3.303(21)
O1	K2	3.515(18)
O1	Cs1	3.303(21)
O1	Cs2	3.515(18)
O2	Ti1	1.871(11)
O2	Ge1	1.753(10)
O2	K1	3.003(20)
O2	K2	3.462(18)
O2	Cs1	3.003(20)
O2	Cs2	3.462(18)
O3	Ti1	1.916(15)
O3	Ti1	1.940(21)
O3	Ti1	2.107(21)
O4	Ti1	1.922(12)
O4	Ge2	1.754(10)
O4	K1	3.154(20)
O4	K1	3.391(21)
O4	Cs1	3.154(20)
O4	Cs1	3.391(21)
O5	K1	3.398(14)
O5	K2	2.490(14)
O5	Cs1	3.398(14)
O5	Cs1	4.006(15)
O5	Cs2	2.490(14)
K1	Ti1	4.078(8)
K1	Ti1	4.078(8)
K1	Ge1	3.9964(7)
K1	Ge1	3.9964(7)
K1	Ge2	4.0064(5)
K1	Ge2	4.0064(5)

K1	O1	3.303(21)
K1	O1	3.303(21)
K1	O2	3.003(20)
K1	O2	3.003(20)
K1	O4	3.391(21)
K1	O4	3.154(20)
K1	O4	3.154(20)
K1	O4	3.391(21)
K1	O5	3.398(14)
K1	O5	3.398(14)
K1	Cs2	5.2840(26)
K1	Cs2	5.2840(26)
K2	Ti1	4.194(9)
K2	Ge1	3.9527(33)
K2	Ge1	4.0003(33)
K2	Ge1	3.9527(33)
K2	Ge1	4.0003(33)
K2	O1	3.515(18)
K2	O2	3.462(18)
K2	O5	2.490(14)
K2	Cs1	5.2840(26)
Cs1	Ti1	4.078(8)
Cs1	Ti1	4.345(10)
Cs1	Ti1	4.345(10)
Cs1	Ti1	4.078(8)
Cs1	Ge1	3.9964(7)
Cs1	Ge1	3.9964(7)
Cs1	Ge2	4.0064(5)
Cs1	Ge2	4.0064(5)
Cs1	O1	3.303(21)
Cs1	O1	3.303(21)

Cs1	O2	3.003(20)
Cs1	O2	3.003(20)
Cs1	O4	3.391(21)
Cs1	O4	3.154(20)
Cs1	O4	3.154(20)
Cs1	O4	3.391(21)
Cs1	O5	3.398(14)
Cs1	O5	4.006(15)
Cs1	O5	4.006(15)
Cs1	O5	3.398(14)
Cs1	K2	5.2840(26)
Cs1	K2	5.2840(26)
Cs1	Cs1	5.6660(8)
Cs1	Cs2	5.2840(26)
Cs1	Cs2	5.2840(26)
Cs2	Ti1	4.194(9)
Cs2	Ge1	3.9527(33)
Cs2	Ge1	4.0003(33)
Cs2	Ge1	3.9527(33)
Cs2	Ge1	4.0003(33)
Cs2	O1	3.515(18)
Cs2	O2	3.462(18)
Cs2	O5	2.490(14)
Cs2	K1	5.2840(26)
Cs2	Cs1	5.2840(26)